Fakultät für Mathematik und Naturwissenschaften | RWTH AACHEN UNIVERSITY

Growth, structure, and superconductivity–ferromagnetism interplay in $YBa_2Cu_3O_{7-x}/SrRuO_3$ thin films and heterostructures

Von der Fakultät für Mathematik und Naturwissenschaften der RWTH Aachen University zur Erlangung des akademischen Grades eines Doktors der Naturwissenschaften genehmigte Dissertation

Vorgelegt von

Vítor Alexandre de Oliveira Lima, Master of Science

aus

Arcoverde, Brasilien

Berichter*:* *Privatdozent Dr. Shibrabata Nandi*

Prof. Dr. rer. nat. Joachim Mayer

Tag der mündlichen Prüfung*: 11.05.2026*

No meu peito a mesma dor que afoga,
faz lembrar tudo o que sou.
Sou mais.

Todo choro de rancor se apague...

Ouça essa voz:
sonho sob meus pés, que as minhas mãos só toquem ouro;
oração dos meus pais, e bem mais atrás, nosso tesouro.

Que essa pele marrom suba o tom, se for preciso.
Muito além dessa dor, bem mais amor —
eu sei pelo que vivo.

— Jota.pê, "Ouro Marrom"

In my chest, the same pain that drowns
reminds me of all that I am.
I am more.

May every tear of bitterness fade away...

Listen to this voice:
a dream beneath my feet, may my hands touch only gold;
my parents' prayer, and long before them, our treasure.

May this brown skin rise in tone, if needed.
Far beyond this pain, much more love —
I know what I live for.

— Jota.pê, "Ouro Marrom"

Zusammenfassung

Hybrid-Nanostrukturen, die verschiedene physikalische Eigenschaften in einer einzigen Plattform vereinen, bilden die Grundlage für die Entwicklung zukünftiger elektronischer und quantenbasierter Geräte. Besonders Heterostrukturen, die supraleitende und ferromagnetische Oxide kombinieren, sind von großem Interesse, da ihre antagonistischen Ordnungsparameter eine Vielzahl neuartiger Grenzflächenphänomene hervorrufen können. Wenn ein Supraleiter mit einem Ferromagneten in Kontakt gebracht wird, treten verschiedene gekoppelte Prozesse auf, die zusammen als Näheeffekte (proximity effects) bezeichnet werden. Beim direkten Näheeffekt dringen spin-polarisierte Cooper-Paare in die ferromagnetische Schicht ein, während beim umgekehrten Näheeffekt magnetische Korrelationen in den Supraleiter eindringen und dort den Ordnungsparameter schwächen. Indirekte Näheeffekte, vermittelt durch Austauschkopplung oder strukturelle Unvollkommenheiten, können die Grenzflächenmagnetisierung zusätzlich beeinflussen. Das Zusammenspiel dieser konkurrierenden Phänomene hängt stark von der atomaren, chemischen und magnetischen Struktur der Grenzfläche ab und eröffnet neue Möglichkeiten für supraleitende Spintronik und Quanten-elektronik. Aktuelle Neutronenstreu- und Magnetotransportstudien haben gezeigt, dass Näheeffekte in konventionellen (niedrig-T_c) metallischen Heterostrukturen durch magnetische Anisotropie auf der Nanometerskala steuerbar sind. Ähnliche Beobachtungen wurden in unkonventionellen (hoch-T_c) oxidischen Systemen mit In-Plane-Anisotropie gemacht, während der Einfluss der senkrechten magnetischen Anisotropie bislang kaum untersucht wurde. Vor diesem Hintergrund untersucht die vorliegende Arbeit epitaktische Dünnschichten und Heterostrukturen aus dem Hoch-T_c-Supraleiter $YBa_2Cu_3O_{7-x}$ (YBCO) und dem Ferromagneten $SrRuO_3$ (SRO). Dieses System eignet sich ideal, um Näheeffekte in stark korrelierten Oxiden mit senkrechter magnetischer Anisotropie zu erforschen. Die Proben wurden mittels Hochsauerstoffdruck-Sputtern hergestellt, was eine präzise Kontrolle von Kristallstruktur und physikalischen Eigenschaften ermöglicht. Durch Optimierung der Wachstumsparameter entstanden einkristalline Schichten und Multilagen mit scharfen Grenzflächen, glatter Oberfläche und hervorragender Epitaxie auf $SrTiO_3$-Substraten. Magnetotransportmessungen an YBCO/SRO-Doppelschichten zeigten eine deutliche Anomalie in der Nähe der supraleitenden Übergangstemperatur, was auf eine durch Näheeffekte induzierte Wechselwirkung zwischen den supraleitenden und ferromagnetischen Schichten hinweist. Neutronenstreuexperimente lieferten mikroskopische Einblicke in die magnetischen Tiefenprofile von Rudefizienten SRO-Filmen und ihrer Grenzflächen zu YBCO. Die Ergebnisse zeigen, dass selbst kleine Abweichungen von der Stöchiometrie den Grenzflächenmagnetismus deutlich beeinflussen, während kein eindeutiger Nachweis einer induzierten Magnetisierung in der supraleitenden Schicht erbracht werden konnte. Diese Befunde bilden jedoch eine solide experimentelle Grundlage für die Untersuchung magnetischer Näheeffekte in Oxid-Heterostrukturen mit senkrechter magnetischer Anisotropie und unterstreichen die entscheidende Rolle von Stöchiometrie, Anisotropie und Grenzflächenqualität für das Zusammenspiel zwischen Supraleitung und Ferromagnetismus.

Abstract

Hybrid nanostructures integrating distinct physical properties within a single platform are key to the development of next-generation electronic and quantum devices. Among them, superconducting (S) and ferromagnetic (F) oxide heterostructures have attracted particular attention due to the antagonistic nature of their order parameters and the rich spectrum of interfacial phenomena that can emerge from their coexistence. When a superconductor is interfaced with a ferromagnet, their order parameters interact through correlated phenomena collectively known as proximity effects. These include the penetration of spin-polarized Cooper pairs into the F layer (direct effect), the diffusion of magnetic correlations into the S layer (reverse effect), and indirect couplings mediated across nonmagnetic spacers or structural imperfections. The balance among these competing mechanisms gives rise to unconventional superconducting states and emergent magnetic textures at the interface. This work focuses on epitaxial thin films and heterostructures composed of the high-T_c superconductor $YBa_2Cu_3O_{7-x}$ (YBCO) and the itinerant ferromagnet $SrRuO_3$ (SRO), a model oxide system combining strong electronic correlations and perpendicular magnetic anisotropy (PMA). The samples were grown by high-oxygen-pressure sputtering, which enables precise control of stoichiometry and crystallinity under strongly oxidizing conditions. Optimized deposition parameters yielded single-layer films and multilayers with sharp interfaces, smooth morphology, and excellent epitaxial alignment on $SrTiO_3$ substrates. Magnetotransport measurements on bilayer YBCO/SRO heterostructures revealed an anomalous feature near the superconducting transition, attributed to a proximity-induced interaction between the S and F layers governed by the competition between their anisotropies. Neutron scattering experiments provided microscopic insight into the depth-dependent magnetic structure of Ru-deficient SRO and its interfaces with YBCO. The results show that small deviations in stoichiometry strongly influence the interfacial magnetism, while no unambiguous evidence of induced magnetization within the superconducting layer was detected. These findings establish a robust experimental framework for probing magnetic proximity effects in oxide heterostructures with PMA and highlight the key role of stoichiometry, anisotropy, and interfacial quality in governing the interplay between superconductivity and ferromagnetism.

Preface

This Ph.D. thesis was carried out as part of my doctoral studies at the Jülich Centre for Neutron Science for Quantum Materials and Collective Phenomena (JCNS-2), Forschungszentrum Jülich GmbH.

I would like to express my deepest gratitude to the Tasso Springer Fellowship for funding my Ph.D. position. Part of the work presented in this thesis was performed in collaboration with the Ernst Ruska-Centre for Microscopy and Spectroscopy with Electrons, within the Physics of Nanoscale Systems division (ER-C-1), under the project numbers FZJ-JCNS-2-LV1 and FZJ-JCNS-2-LV2.

This research also made use of resources at the Spallation Neutron Source (SNS), a DOE Office of Science User Facility operated by Oak Ridge National Laboratory (ORNL). The allocated beamtime corresponded to the Magnetism Reflectometer, under proposal number IPTS-32745.1.

Some parts of this thesis have been revised for spelling, grammar, and sentence formulation using the generative AI service Grammarly.

Acknowledgments

I would like to express my sincere gratitude to all those who, directly or indirectly, contributed to the realization and completion of this doctoral thesis. In particular, I would like to thank:

Prof. Dr. Thomas Brückel, for accepting me as a Ph.D. student at the Jülich Centre for Neutron Science (JCNS-2). Even through brief conversations after his retirement, he continued to play a fundamental role in my scientific growth and in the completion of my doctoral studies. I also thank Prof. Karen Friese, current acting director of JCNS-2, for providing all the necessary support for my participation in beamtimes and conferences, as well as for being a great listener and an excellent advisor.

Privatdozent Dr. Shibrabata Nandi, for accepting to be my *Doktorvater* at RWTH Aachen University, and for always asking the right questions and making the right comments at the right moments, providing the necessary guidance to move forward with my research despite all limitations. I also thank Prof. Dr. Joachim Mayer for kindly reviewing my thesis.

Dr. Emmanuel Kentzinger and Dr. Connie Bednarski-Meinke, scientific advisors at JCNS-2. Although we occasionally had differing views on the direction of the research, I deeply acknowledge their important contributions, especially during the initial stages of this work. Their comments definitely made me more resilient, independent, and confident in my own work.

Prof. Dr. Michael Faley, who initially joined as a collaborator in the growth of superconducting thin films and heterostructures, but became much more than that. I am sincerely grateful for your continuous support since the very beginning, for the time and knowledge you shared throughout the numerous sample preparations, electrical transport measurements, and the long hours dedicated to lamella preparation, corrective alignments, and image acquisition in the transmission electron microscopes, regardless of weekdays, weekends, or holidays. Thank you also for reviewing my writing, for taking me to inspiring conferences and for involving me in discussions with your colleagues at ER-C-1, all of which greatly enriched my experience and scientific growth. You definitely gave me the push I needed (sometimes a hard one) to keep moving forward and ensure that a good work was done. Thank you very much! I truly would not have made it this far without you.

To Berthold Schmitz, Frank Gossen, Lidia Kibkalo, Norbert Bernard, Jens Schnitzler, Sylvia de Waal, and Grigory Potemkin, for all the technical support provided with the characterization instruments, sputtering system, and clean room facilities. There would have been no samples or results to present without your cooperation and dedication.

To our secretary, Mrs. Barbara Daegener, for her constant support and for always helping me handle every administrative challenge with kindness and efficiency.

I also thank Dr. Egbert Wessel and Dr. Daniel Grüner for kindly characterizing the sputtering targets by scanning electron microscopy and energy-dispersive X-ray spectroscopy at the Institute of Energy and Climate Research – Materials Synthesis and Processing (IMD-1). I will always be grateful for your help and generosity, and I will be

forever in debt to you.

I would like to thank Prof. Dr. Regina Dittmann from the Peter Grünberg Institute for Electronic Materials (PGI-7) for allowing me to use their clean room facilities to etch the $SrTiO_3$ substrates, as well as their wire bonding machine and SEM instruments. I also wish to express my gratitude to Dr. Felix Gunkel for the valuable discussions regarding the thermal treatment of substrates and the growth of $SrRuO_3$ thin films. My thanks also go to other members of PGI-7 with whom I had the opportunity to interact: Lisa Heymann, Suqin He, Kalle Goß, Kapil Nayak, and Judith Knabe.

I would like to thank Prof. Dr. Detlev Grützmacher from the Peter Grünberg Institute for Semiconductor Electronics (PGI-9), Dr. Dan Buca and his entire group, and especially Dr. Omar Concepción, for their assistance with the measurements of all the samples presented in this thesis by high-resolution X-ray diffraction, X-ray reflectivity, and Rutherford backscattering spectroscopy. Their availability and willingness to collaborate were essential for obtaining fundamental data, and I am truly grateful for their constant support throughout this work.

I would like to thank Prof. Dr. Milan Radović for visiting Jülich in 2023 to discuss my results and for sharing his valuable insights into all aspects of my research, particularly regarding the growth of $YBa_2Cu_3O_{7-x}$ and $SrRuO_3$ thin films. I am especially grateful for his ability to teach me to look at my results from a different perspective, turning challenges into opportunities. His advice and encouragement truly motivated me to keep moving forward. Unfortunately, I could not join him for the preparation of $SrRuO_3$ thin films by pulsed laser deposition, but one day I hope to return that visit.

I would like to thank Dr. Valeria Lauter, Dr. Asmaa Qdemat, and Dr. Haile Ambaye from the Spallation Neutron Source at Oak Ridge National Laboratory (ORNL) for all their support with the proposal preparation and data analysis, as well as for the pleasant and productive beamtime at ORNL. Their expertise, patience, and collaborative spirit were invaluable for the success of the neutron scattering experiments and for deepening my understanding of the results.

I would like to thank Dr. Julio C. Cezar, Dr. Thiago Mori, Dr. Ricardo D. dos Reis, Dr. Pedro Schio, and Dr. Tanna Fiuza from the Brazilian Synchrotron Light Laboratory and the National Nanotechnology Laboratory, both part of the Brazilian Center for Research in Energy and Materials, for all their support during the proposal preparation for X-ray magnetic circular dichroism (XMCD) and X-ray linear dichroism (XLD) experiments, possible growth of $YBa_2Cu_3O_{7-x}/SrRuO_3$ films and for the assistance with Transmission electron microscopy analysis. Unfortunately, the beamtime could not be carried out during my Ph.D. due to several beamline issues, but I am confident it will be realized in the near future.

I would like to thank Dr. Klára Uhlířová, Martin Žáček, and the entire team at the Materials Growth and Measurement Laboratory (MGML) in Prague for their assistance during the low-temperature magnetic force microscopy experiments. Unfortunately, due to the reduced magnetism of the samples, we could not obtain reliable results, but I will always remember this experiment and the valuable experience I gained working with all of you.

I would like to thank Dr. Oleg Petracic (JCNS-2), Dr. Michael Schneider (SwissNeutronics), Dr. Anton Zubayer (Quantum Beam Optics Sweden AB), Dr. Annika Stellhorn (European Spallation Source), Dr. Venus Rai (University of Luxembourg), Dr. Ulrich Rücker (JCNS-2), Dr. Patrick Schöffmann (Zeiss), Dr. Mai H. Hamed (Helwan University), and Dr. Steffen Tober (Deutsches Elektronen-Synchrotron) for all the valuable

discussions and scientific exchanges throughout my Ph.D. Their insights and perspectives greatly enriched this work and contributed to my scientific development.

I once read in Dr. Dan Buca's thesis that "There are times when even a full-grown man needs a shoulder to cry on." In this sense, Dr. Pulkit Prakash and Dr. Asmaa Qdemat were that shoulder for me. I am deeply grateful to both of you for your friendship, your advice, and all the enjoyable moments and countless coffees we shared over these almost four years. I would also like to thank all my friends and colleagues at JCNS-2 — Hend, Yifan, Norberto, Dori, Viliam, Komal, Ankita, Amala, Indrajeet, and Chenyang, for the good times and the moments we shared throughout this journey.

Aos amigos e colegas brasileiros em Jülich — Helen e Saimon, Amir e Andreyna, Paula e Leandro, Tania, Joel, Tanna, Amanda, Marília, Rodrigo e Tássia, Marilaine, com os quais tive a oportunidade de compartilhar excelentes momentos sempre que me permiti estar disponível e (tentei) não pensar em trabalho. Agradeço, em especial, a Alessandra e Vincenzo, Mariana e Marc, e Higor, que foram fundamentais nos meus primeiros meses na Alemanha e são, consequentemente, inesquecíveis. Agradeço também à psicóloga Gabriela Paixão e ao psiquiatra Dr. Thiago Brandão, por me ajudarem a encontrar força, clareza e equilíbrio mesmo nos momentos mais difíceis desta caminhada.

Aos meus melhores amigos, Rodrigo, Carlos e Eduardo Rogério, agradeço por se fazerem presentes, mesmo estando em diferentes lugares do mundo. Agradeço também por todas as conversas (especialmente pela escuta), pelas doses de motivação e pelas brincadeiras, que acabam tornando o fardo um pouco mais leve. Agradeço ainda ao Eduardo Guedes, Prof. Márcio Medeiros Soares e ao José Suassuna Filho, que sempre acreditaram no meu potencial e que eu chegaria até aqui.

À Dra. Carolina Gismene, minha esposa e companheira, por todo o seu amor, cuidado e paciência comigo, mesmo nos meus piores momentos, independentemente da distância que possa existir entre nós. Carol trouxe sentido ao meu caos, mostrando-me que há um mundo lá fora que vai muito além do trabalho e dos problemas do trabalho. Obrigado por não desistir de mim, mesmo quando até eu já havia desistido, e por continuar me amando cada dia mais.

E, por fim, mas não menos importante, a toda a minha família, em especial, aos meus pais, Jairo e Míriam, e aos meus tios-padrinhos, Valda e Dadá (*in memoriam*). Não sei como expressar minha gratidão a vocês, que abriram mão de tantos prazeres da vida e, fazendo o possível — e muitas vezes o impossível —, sempre se esforçaram para oferecer aos filhos o maior legado que pais (e padrinhos) podem deixar: amor e educação. Obrigado pelo cuidado e por sempre me apoiarem, mesmo estando do outro lado do oceano e sem entender nada do que faço no meu dia a dia. Vocês são minha força motriz. Amo vocês mais que tudo e sou feliz por poder retribuir, ao menos, 1% do que fizeram por mim. Por essa razão, dedico esta tese a vocês.

Contents

Chapter 1

Introduction

In recent decades, complex oxide thin films have emerged as a fertile ground for discovering and manipulating novel electronic, magnetic, and superconducting phenomena [1]. Their remarkable range of functionalities, including high-temperature superconductivity, ferroelectricity, colossal magnetoresistance, and multiferroicity, emerge from the strong interplay among charge, spin, orbital, and lattice degrees of freedom [2–4]. When synthesized as epitaxial thin films, these materials do not merely retain their bulk properties; rather, they often exhibit enhanced or entirely new behavior as a consequence of reduced dimensionality, epitaxial strain, interface-induced symmetry breaking, and confinement effects [5, 6]. This makes oxide heterostructures a compelling platform for the design of quantum materials with emergent properties that are otherwise inaccessible in bulk compounds [7].

Superconductivity was discovered by Heike K. Onnes in 1911 [8]. Onnes observed that metals such as Hg, Pt, Pb and Bi undergo a transition from a normal metal state (with finite resistance) to a state with zero resistance (the superconducting state) below a certain critical temperature (T_c). In 1933, Meissner and Ochsenfeld discovered that a superconductor is a perfect diamagnetic material and therefore totally expels applied magnetic fields [9]. Furthermore, when the superconductor T_c is measured in the presence of an applied magnetic field, the value of T_c decreases as the magnetic field increases, to the point where the superconducting state is destroyed for a given value of magnetic field, called the critical magnetic field (B_c). This field is related to the difference in free energy between the normal and superconducting states at zero field. A microscopic theory explaining this phenomenon was only developed after more than 30 years by John Bardeen, Leon Cooper, and John Robert Schrieffer in 1957. This theory is known as BCS theory [10].

The central concept of BCS theory is that two electrons near the Fermi surface can form a bound state — called a Cooper pair — through an effective attractive interaction mediated by phonons, the quanta of lattice vibrations. As one electron moves through the crystal lattice, it distorts the surrounding positive ions, generating a region of enhanced positive charge. This distortion can attract a second electron with opposite spin and momentum, leading to Cooper pair formation. As a result, Cooper pairs typically exhibit zero orbital angular momentum and zero total spin (spin-singlet).

Despite the natural Coulomb repulsion between electrons, the phonon-mediated attraction can dominate under certain conditions, particularly at low temperatures, facilitating this pairing mechanism. In the superconducting state, Cooper pairs condense into a collective quantum ground state that is energetically more favorable than the normal metallic phase. The transition into this state is marked by the opening of an energy gap at the Fermi level, representing the energy required to break a Cooper pair. Within this gap, no electronic states are available, preventing scattering processes and thereby eliminating electrical resistance. This energy gap is also responsible for distinct anomalies in thermodynamic properties, such as sharp changes in specific heat at the critical temperature T_c [10–12].

The year 1986 marked the beginning of a new era for superconductivity with the discovery of an oxide based on La, Ba and Cu in a ceramic mixed phase. Bednorz and Muller observed that $La_{1-x}Ba_xCuO_4$ for $x \approx 0.2$ became superconducting at a temperature of 30 K [13]. They were awarded the Nobel Prize in physics in 1987, the fastest ever offered by the Academy since its inception. Also in 1987, Paul Ching Wu Chu's group announced the discovery of a new superconducting material with a critical temperature close to 92 K. It was a mixed-phase compound containing Yttrium, Barium, Copper and Oxygen: $YBa_2Cu_3O_{7-x}$ (YBCO). This discovery was confirmed in several research laboratories around the world, definitively establishing the highest critical temperature of superconductivity up to that point as being $T_c = 92$ K [14]. The BCS theory effectively explains the properties of most traditional superconducting materials. However, the discovery in 1986 of a new class of materials exhibiting superconductivity at high temperatures continues to pose a challenge for theorists, and a clear theoretical explanation for this phenomenon remains elusive.

While superconductors exhibit perfect diamagnetism, ferromagnetic materials exhibit spontaneous magnetization even in the absence of an applied magnetic field. This means that all magnetic moments of atoms or electrons align their spins along the same direction (or in the direction of an external applied magnetic field). The microscopic origin of ferromagnetism lies in the exchange interactions, where the Heisenberg exchange constant J is positive [15]. Ferromagnetic exchange interactions favor the parallel alignment of electron spins, causing a shift in the majority spin band relative to the minority spin band. This results in different occupation probabilities for each band, creating a distinct spin imbalance that produces a net magnetization [16]. A ferromagnetic ordering appears just below a critical temperature called Curie temperature (T_{Curie}).

In metallic systems, two sources of magnetism can be found: (i) localized magnetic moments and (ii) the "sea" of conduction electrons [17]. Local magnetism in metals, particularly in rare-earth metals such as Gd, Tb, Dy, and Ho, refers to the magnetic moments that arise from unpaired electrons localized on specific atoms rather than being spread across the metal. In rare-earth metals, the $4f$ electrons are relatively shielded by outer electron shells ($5s$ and $5p$), so they do not strongly interact with neighboring atoms. This shielding keeps the magnetic moments of the $4f$ electrons localized on each atom, resulting in local magnetic moments. This is why, despite the local nature of these magnetic moments, rare-earth metals can exhibit overall magnetic properties like ferromagnetism or antiferromagnetism depending on the type of exchange interaction between neighboring moments. The second type of magnetism, known as band magnetism (as seen in materials like Fe, Ni, Co, and Ruthenates), originates from the magnetic moments of the conduction electrons. These electrons are itinerant, meaning they can move freely between atomic sites, and they tend to align their magnetic moments with

the direction of an applied magnetic field [15, 18].

Among the broad family of oxide materials, high-temperature (high-T_c) superconductors and ferromagnetic oxides stand out due to their fundamentally antagonistic ground states. Despite this apparent incompatibility, the strong electronic correlations inherent in both phases allow for the emergence of intriguing physical effects when these materials are brought into contact. The integration of superconducting and ferromagnetic oxides into thin film heterostructures creates a fertile environment for exploring the physics of competing order parameters and interfacial coupling. At the interfaces between these materials, proximity effects — characterized by the penetration of Cooper pairs from the superconductor into the ferromagnet, for example — can give rise to novel phenomena such as spin-polarized supercurrents [19], generation of spin-triplet Cooper pairs [20, 21], domain superconductivity [22], and interface-driven suppression or enhancement of magnetism or superconductivity [23, 24]. The extent of Cooper pair penetration depends on parameters such as temperature, disorder, and the magnetic properties of the ferromagnet [19, 25].

Proximity effects in superconductor/ferromagnet systems can be broadly categorized into direct and indirect types. The direct proximity effect occurs when the superconductor is in direct contact with the ferromagnet, allowing Cooper pairs to diffuse into the ferromagnetic region and, reciprocally, enabling magnetic exchange fields to influence the superconducting layer. This mutual interaction can modify both magnetic and superconducting properties near the interface, giving rise to phenomena such as oscillations in the T_c and the emergence of spin-triplet pairing states [26]. In contrast, the indirect proximity effect arises in structures where the superconductor and ferromagnet are separated by an intermediate non-magnetic layer. In such cases, coupling between the layers is mediated by long-range spin, orbital, or charge interactions, enabling proximity-induced modifications without direct electronic overlap [27]. In addition to the conventional proximity effect, superconductor/ferromagnetic hybrid systems can also exhibit a reverse proximity effect, in which magnetic order from the ferromagnet extends into the superconducting region. This leads to local spin polarization, partial suppression of the superconducting gap near the interface with a consequent reduction of T_c and a possible magnetization induction in the superconductor [23, 28, 29].

Proximity effects are highly sensitive to the structural, chemical, and magnetic nature of the interface, and the ability to engineer such interfaces with atomic precision opens pathways toward novel functionalities with relevance to superconducting spintronics, fluxonic devices, and future quantum electronic systems [30, 31]. In this context, oxide-based superconductor/ferromagnet heterostructures represent both a challenge and an opportunity: they pose fundamental questions about the coexistence and/or competition of superconductivity and ferromagnetism at the atomic scale [32], and offer a platform to investigate unconventional pairing mechanisms, symmetry-breaking effects [33], and long-range quantum coherence in correlated systems.

This thesis is dedicated to the investigation of proximity effects in thin film oxide heterostructures composed of high-T_c superconductors and ferromagnets with perpendicular magnetic anisotropy, such as YBCO and $SrRuO_3$ (SRO), respectively. These materials exhibit strong anisotropy due to their layered crystal structures, which give rise to direction-dependent transport and magnetic properties. The rich interplay between electron correlations, crystal structure, and magnetic anisotropy in such systems provides a fertile ground for the emergence of novel proximity-induced phenomena.

1.1. Motivation and aim of the research problem

Recent magnetotransport and neutron scattering experiments on Nb/FePd heterostructures have shown proximity effects linked to the strength of the perpendicular magnetic anisotropy (PMA) in the ferromagnetic layer [22, 34, 35]. Heterostructures with FePd layers exhibiting high PMA and a maze-like magnetic domain structure display domain-wall and reverse domain superconductivity, while those with low PMA and a stripe domain structure exhibit long-range supercurrents through the FePd layer. These findings demonstrate that the superconducting order parameter can be modulated at the nanoscale by adjusting PMA. This effect appears due to the comparable energy and length scales involved: specifically, the similar magnitudes of the ferromagnet stray fields and the superconductor's second critical field (B_{c2}), as well as the generation of spin-triplet Cooper pairs that penetrate deeply into the ferromagnet, matching the typical dimensions of the ferromagnetic layer's in-plane magnetic texture [19, 36–38].

In ferromagnet/superconductor/ferromagnet and multilayer heterostructures based on conventional superconductor and ferromagnetic metals and alloys, proximity effects typically appear as T_c oscillations and infinite magnetoresistance, and are associated with the ferromagnetic layer thickness [39, 40]. Unique proximity effects are also observed in superconductor/ferromagnet heterostructures based on high-T_c superconductors with ferromagnetic spin valves, usually showing in-plane magnetic anisotropy, as in YBCO/$La_{1-x}Ca_xMnO_3$ (LCMO) systems [28]. In these heterostructures, a magnetic proximity effect above T_c results in the formation of a "dead" or depleted magnetic layer at the superconductor/ferromagnetic interface, suppressing the magnetic moment in the ferromagnetic layer [29]. Below T_c, superconducting proximity effects allow spin-triplet Cooper-pairs to penetrate the ferromagnetic layer, causing a reduction in T_c. In oxide multilayers and tunnel junctions with uniform magnetization, antiferromagnetic alignment of ferromagnetic layers has been observed, leading to the induction of a small magnetic moment in the superconductor via charge transfer driven by orbital ordering and resulting in giant magnetoresistance [23, 24, 41, 42]. Furthermore, long-range spin-triplet correlations have been detected in superconductor/ferromagnet mesastructures with noncollinear magnetization, where one ferromagnetic oxide layer exhibits PMA and the other shows in-plane magnetic anisotropy. Here, superconducting currents persist up to heterostructure thicknesses of 50 nm, linked to spin-polarized (spin-triplet) Cooper-pairs generated by the noncollinear magnetization of the ferromagnetic layers [43–45].

Although substantial progress has been made in studying proximity effects in heterostructures based on high-T_c superconductors and ferromagnetic materials with in-plane magnetic anisotropy, detailed investigations of proximity effects involving high-T_c superconductors coupled to ferromagnets showing PMA are still lacking. To address this gap, we initially explored proximity effects in thin film heterostructures of FePd/YBCO, grown using a combination of Molecular Beam Epitaxy (MBE) and High Oxygen Pressure Sputtering (HOPS). Specifically, we aimed to investigate whether phenomena such as domain superconductivity and/or the generation of spin-triplet Cooper pairs could also appear in this metal/oxide heterostructure. Given the similar lattice parameters of FePd and YBCO, epitaxial growth of FePd on YBCO was expected. However, the usually rough YBCO surface, combined with its tendency to absorb moisture during transfer between the HOPS and MBE systems, significantly compromised the interface quality. This degradation, driven primarily by the difference in surface energies between the two materials, led to droplet-like growth of FePd rather than a smooth, layer-by-layer

deposition, characteristic of the FePd $L1_0$ phase [46]. As a result, the FePd films were polycrystalline and exhibited in-plane magnetic anisotropy instead of the desired PMA. Furthermore, a rapid deterioration of YBCO's superconducting properties was observed, particularly a sharp reduction in T_c, attributed to oxygen imbalance at the metal-oxide interface. This study was conducted in collaboration with Mengying Tang and is detailed in her Master's thesis [47]. Despite attempts to perform a comprehensive analysis of the experimental results, the presence of the initially targeted proximity effects could not be confirmed, largely due to the challenges in fabricating high-quality and stable samples.

Due to considerable interest in SRO as a promising material for the development of quantum electronics — a novel field based on quantum degrees of freedom — and its structural compatibility with other technologically relevant oxides such as YBCO and $SrTiO_3$ (STO), the focus of this work shifted towards oxide-based heterostructures. SRO was for many years considered solely as an electrode in ferroelectric capacitors and superconducting junctions [48, 49]. However, as the only known $4d$ transition metal oxide that exhibits both itinerant ferromagnetism and metallic conductivity below $T_{\text{Curie}} \approx 160$ K, SRO has recently attracted significant attention. When epitaxially grown on STO substrates, it exhibits PMA, narrow magnetic domain walls, and strong spin-orbit coupling, along with emergent phenomena such as the anomalous Hall effect and Berry curvature effects, making it a key material for emerging applications in both conventional and quantum technologies [31, 50]. In addition to its favorable physical properties, SRO's perovskite crystal structure enables good lattice matching with STO (0.64% mismatch) and YBCO (YBCO/STO: 1.66%, YBCO/SRO: ≈2%) [51], facilitating the epitaxial growth of high-quality heterostructures. All-oxide YBCO/SRO and SRO/YBCO heterostructures were successfully fabricated on STO substrates using HOPS, allowing for the systematic investigation of proximity effects. The insights gained into the sample preparation process and the comprehensive characterization of the morphological, structural, transport, and magnetization properties of these heterostructures are presented in detail throughout this thesis.

1.2. Outline of the thesis

This thesis is organized into eight chapters, each addressing a specific stage of the research conducted during this doctoral work.

Chapter 1 provides a general introduction to the motivation, objectives, and scientific context of this study, emphasizing the relevance of oxide-based heterostructures combining ferromagnetic and superconducting materials.

Chapter 2 provides an overview of the fundamental concepts and material-specific properties relevant to this work. It examines the structural, electronic, and magnetic characteristics of YBCO, SRO, and STO, which serve respectively as the ferromagnetic, superconducting, and substrate components of the studied heterostructures.

Chapter 3 details the experimental methods and instrumentation used throughout this work, including the HOPS system, thin film growth procedures, and the structural, magnetic, and transport characterization techniques employed.

Chapter 4 presents the growth of YBCO thin films on MgO and STO substrates. These reference samples were fabricated using the HOPS instrument at ER-C-1 by Prof. Dr. Michael Faley, and their structural and physical properties are discussed in detail.

Chapter 5 describes the optimization and growth of SRO thin films by HOPS at JCNS-2. As no prior expertise in SRO deposition was available at the institute, this work involved an extensive optimization of growth parameters. The resulting high-quality epitaxial films provided a solid basis for subsequent studies on SRO/YBCO and YBCO/SRO heterostructures. The chapter also discusses the effect of Ru deficiency, PMA, and transport behavior under different growth conditions.

Chapter 6 focuses on the study of proximity effects in YBCO/SRO and SRO/YBCO thick heterostructures grown on STO substrates. It presents a concise analysis of their growth conditions, morphology, crystallinity, and electronic transport properties. Particular emphasis is placed on the observation of an anomalous magnetoresistance near the superconducting transition, providing evidence of proximity-induced interactions between the superconducting and ferromagnetic layers.

Chapter 7 presents the results of neutron scattering experiments performed on Ru-deficient SRO thin films and thinner YBCO/SRO heterostructures. These measurements provide detailed insight into the magnetic structure and depth-dependent magnetization of the SRO layers, offering complementary information on the interfacial magnetic properties and enabling the evaluation of possible proximity effects at the nanoscale in superconductor/ferromagnet systems.

Finally, Chapter 8 offers a summary of the main findings and provides an outlook on future research directions.

Chapter 2

Investigated materials

Thin films and heterostructures of the high-temperature (high-T_c) superconductor $YBa_2Cu_3O_{7-x}$ and the itinerant ferromagnet $SrRuO_3$ were prepared on single-crystalline $SrTiO_3$ (001) substrates. This chapter presents the fundamental structural, electronic, and magnetic properties of these materials, emphasizing their relevance for the investigation of proximity effects in oxide-based heterostructures.

2.1. $YBa_2Cu_3O_{7-x}$

$YBa_2Cu_3O_{7-x}$ is one of the most renowned and extensively studied high-T_c superconductors. It serves as a model system for investigating the structural, chemical, electronic, and magnetic properties of high-T_c superconductors [52]. Moreover, its thin films are widely used in both small- and large-scale high-T_c superconducting devices, including Direct Current Superconducting Quantum Interference Devices (DC SQUID) magnetometers, superconducting magnets, coated conductor tapes, power transmission cables, transformers, and generators, underscoring the technological significance of this material [53].

$YBa_2Cu_3O_{7-x}$, where x is the oxygen deficiency, belongs to the cuprate family, a group of high-T_c transition metal oxides characterized by CuO_2 planes in their crystal structure. Cuprates are unconventional type-II superconductors that, in their undoped state, are Mott insulators exhibiting antiferromagnetic spin ordering of Cu^{2+} ions within the CuO_2 planes. $YBa_2Cu_3O_6$ is the parent compound of $YBa_2Cu_3O_7$, with the former adopting a tetragonal crystal structure (space group P4/mmm; $a = b = 3.870$ Å, $c = 11.801$ Å) and the latter an orthorhombic crystal structure (space group Pmmm; $a = 3.8185$ Å, $b = 3.8856$ Å, $c = 11.6804$ Å) [52, 54], as illustrated in Fig. 2.1.

The fully oxygenated ideal structure ($x = 0$) consists of a stack of layers in the sequence BaO - CuO - BaO - CuO_2 - Y - CuO_2 - BaO - CuO - BaO. The CuO_2 layers, which are separated by a single Y^{3+} atom and surrounded by pyramidal oxygen arrangements, are essential to the superconducting behavior. Notably, $YBa_2Cu_3O_{7-x}$ is the only high-T_c cuprate to feature CuO chains along the b-axis. These one-dimensional CuO chains, along with the BaO layers, stabilize the structure and serve as charge reservoirs, doping electrons or holes into the CuO_2 layers.

The CuO_2 layers become superconducting only for a suitable hole-doping, p, which is

indirectly tuned by the oxygen stoichiometry (i.e. by oxygen deficiency, x) in the CuO chains. The oxygen stoichiometry can be reversibly adjusted between 6 and 7 through annealing processes that pump oxygen into or out of the CuO chains along the b-axis.

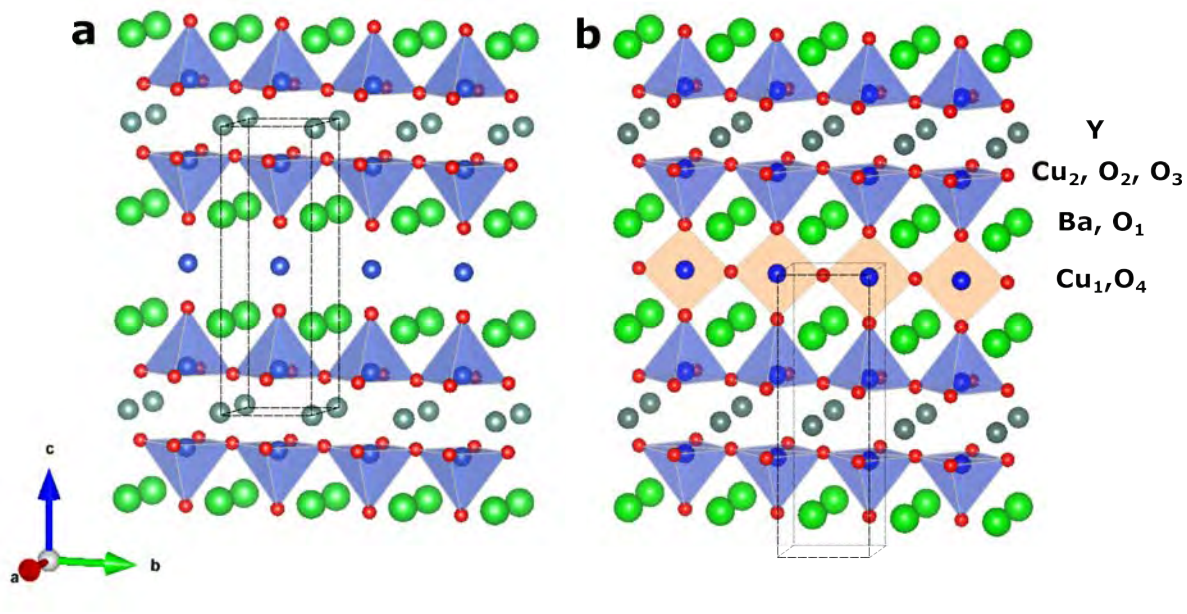

Figure 2.1.: Crystallographic structures of (a) $YBa_2Cu_3O_6$ and (b) $YBa_2Cu_3O_7$. The rectangle indicate the primitive unit cell of each material. The Y, Ba, Cu and O atoms are represented by gray, green, blue, and red spheres, respectively. Adapted from Refs. [55, 56].

The relationship between the critical temperature, T_c, and oxygen deficiency, x, in $YBa_2Cu_3O_{7-x}$ is depicted in Fig. 2.2(a) [52, 57, 58]. For $x > 0.65$, the material loses its superconducting properties entirely. A plateau near 60 K is observed in the range $0.3 < x < 0.4$, attributed to the emergence of charge ordering (charge-density wave order) rather than oxygen vacancy ordering. Fig. 2.2(b) provides a schematic of the sheet resistivity of high-T_c cuprates as a function of oxygen doping. The sharp rise in resistivity in both underdoped and overdoped cuprates likely arises from charge ordering along the charge reservoir planes. In optimally doped cuprates, the resistivity, $\rho(T)$, exhibits a clear drop to zero, consistent with superconducting behavior.

The electronic phase diagram of cuprates is complex and reveals far more than a simple T_c versus oxygen deficiency plot. Fig. 2.3 illustrates the electronic phase diagram of $YBa_2Cu_3O_{7-x}$ as a function of the hole doping p, which is representative of most cuprate compounds. At low doping levels, $YBa_2Cu_3O_{7-x}$ behaves as an antiferromagnetic insulator, similar to its parent compound. This behavior is attributed to a strong on-site Coulomb repulsion, U, acting on the Cu $3d$ electrons, resulting in a gap at the Fermi energy [59]. The antiferromagnetic order is short-ranged and changes to a spin glass phase at higher doping levels. Superconductivity emerges when the doping level exceeds $p > 0.05$/Cu atom, with optimal doping occurring at $p \approx 0.16$/Cu atom, yielding the universal T_c dome-shaped curve. At doping levels beyond the superconducting dome and at low temperatures, the material exhibits typical Fermi liquid behavior, characterized by the expected T^2 dependence of resistivity. However, in the region above the superconducting dome, known as the strange metal phase, the metallic behavior diverges from Fermi liquid theory, displaying an anomalous T-linear resistivity [60].

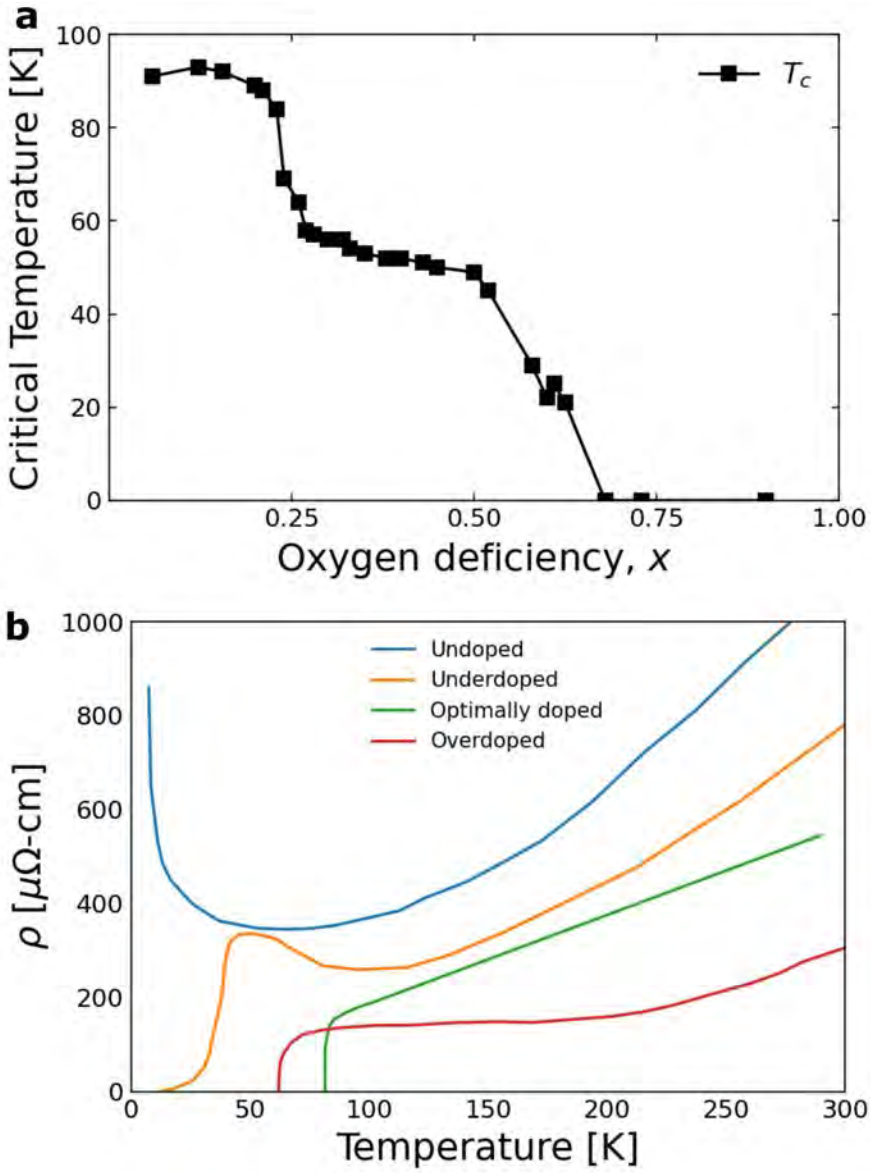

Figure 2.2.: (a) Variation of the superconducting transition temperature T_c of $YBa_2Cu_3O_{7-x}$ with the oxygen stoichiometry x and (b) a schematic overview of the resistance vs temperature $\rho(T)$ of cuprates for different doping levels. Adapted from Ref. [52, 57, 58].

At temperatures near 50 K, the charge-density wave order, responsible for the 60 K plateau in T_c, competes with the superconducting phase. Between the antiferromagnetic and superconducting regions lies the pseudogap phase, a topic of considerable debate, which appears below a temperature T^*. Although an energy gap is observed in the electronic excitation spectra and by several techniques, such as nuclear magnetic resonance (NMR), angle-resolved photon emission spectroscopy (ARPES), scanning tunneling microscopy (STM), transport and specific heat measurements, the nature of the pseudogap remains unclear [60, 61]. It may represent either an order competing with superconductivity or preformed Cooper pairs without phase coherence [53, 62]. The pseudogap disappears abruptly at $p \approx 0.17$/Cu atom, signaling a transition where the Fermi surface evolves from hole pockets in the underdoped regime to a large hole-like Fermi surface in the overdoped region [52, 53, 63, 64].

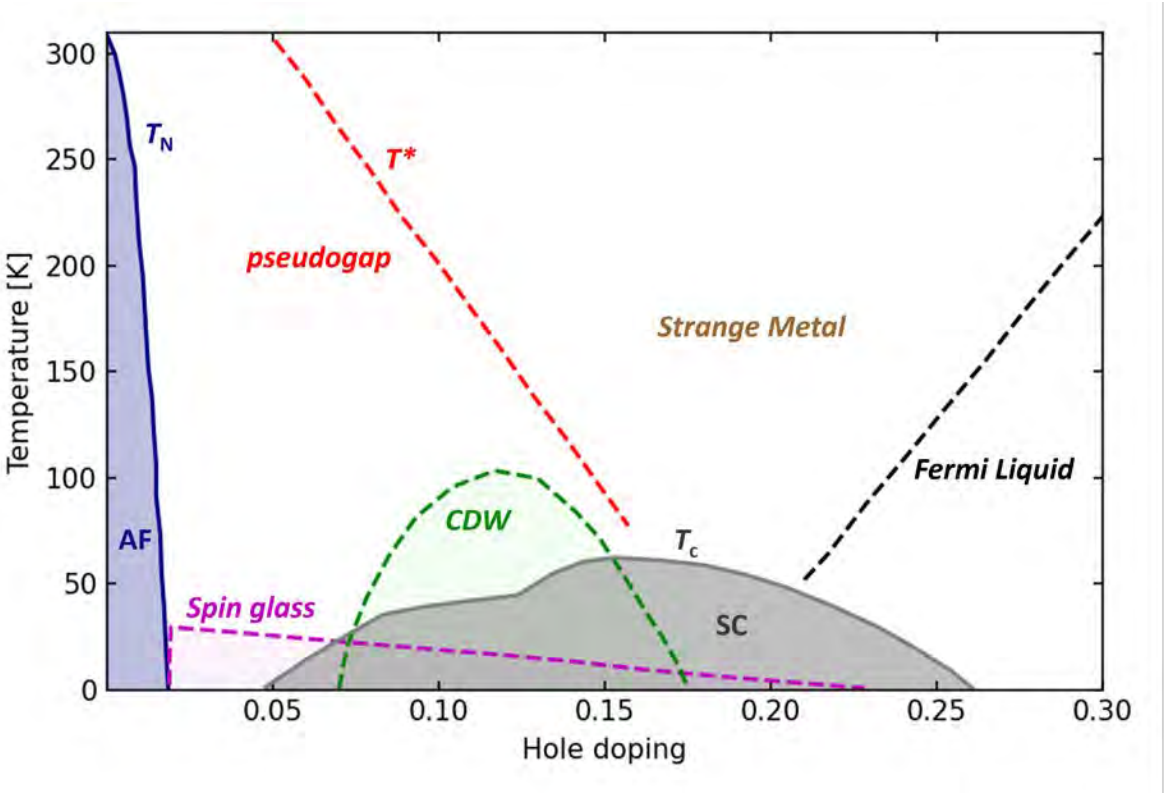

Figure 2.3.: Electronic phase diagram of $YBa_2Cu_3O_{7-x}$. Adapted from Ref. [63, 64].

It is important to emphasize that the doping level, p, and the oxygen deficiency, x, are inversely related parameters. Specifically, the highest oxygen deficiency ($x = 1$) in the CuO chain plane corresponds to the lowest doping level ($p = 0$) in the CuO_2 plane. Conversely, an oxygen deficiency of $x = 0.125$ corresponds to the optimal doping level of $p = 0.16$, where superconductivity reaches its peak performance. Therefore, for $YBa_2Cu_3O_{7-x}$, an empirical relationship between the doping level p and the oxygen content $7 - x$ can be approximated as:

$$p \approx 1 - x - \Delta, \tag{2.1}$$

where Δ accounts for additional factors such as structural and chemical variations in specific materials.

High-T_c superconductors are well known for their pronounced anisotropy, which originates in its layered crystallographic structure. As the superconductivity mainly occurs in the CuO_2 planes, linked by a weak interlayer coupling, the crystal structure affects superconducting properties. In this sense, superconducting parameters such as the London penetration depth λ, coherence length ξ, critical current J_c, lower and upper critical fields can show a considerable difference with respect to the crystallographic directions [65–67]. Table 2.1 presents fundamental superconducting parameters values obtained by magnetization and Muon spin relaxation measurements [65–67].

Furthermore, the superconducting gap is anisotropic in unconventional superconductors. In cuprates, this anisotropy arises from the Cooper pair wavefunction, where the spin component is a singlet state with $S = 0$, and the orbital component is characterized by $L = 2$, corresponding to a $d_{x^2-y^2}$ orbital symmetry. As a result, the Fermi surface exhibits fourfold symmetry, with nodes where the superconducting gap vanishes. In con-

trast, conventional superconductors feature an isotropic superconducting gap, as their wavefunction consists of a spin singlet state with $S = 0$ and an orbital component with $L = 0$ [60, 68]. Figure 2.4 illustrates this anisotropic behavior of the superconducting gap in unconventional superconductors.

Table 2.1.: Fundamental superconducting parameters values for $YBa_2Cu_3O_7$ (fully oxygenated, $T_c = 87$ K): London penetration depth λ, coherence length ξ, critical current J_c, lower and upper critical field (B_{c1} and B_{c2}). Adapted from Refs. [52, 65–67].

Parameter	Value	Temperature
λ_{ab}	125 nm	2.5 K
λ_c	450 nm	projected to T = 0 K
ξ_{ab}	1.3 nm	projected to T = 0 K
ξ_c	0.2 nm	projected to T = 0 K
B_{c1} (ab)	18 mT	projected to T = 0 K
B_{c1} (c)	53 mT	projected to T = 0 K
B_{c2} (ab)	256 T	projected to T = 0 K
B_{c2} (c)	53 T	projected to T = 0 K

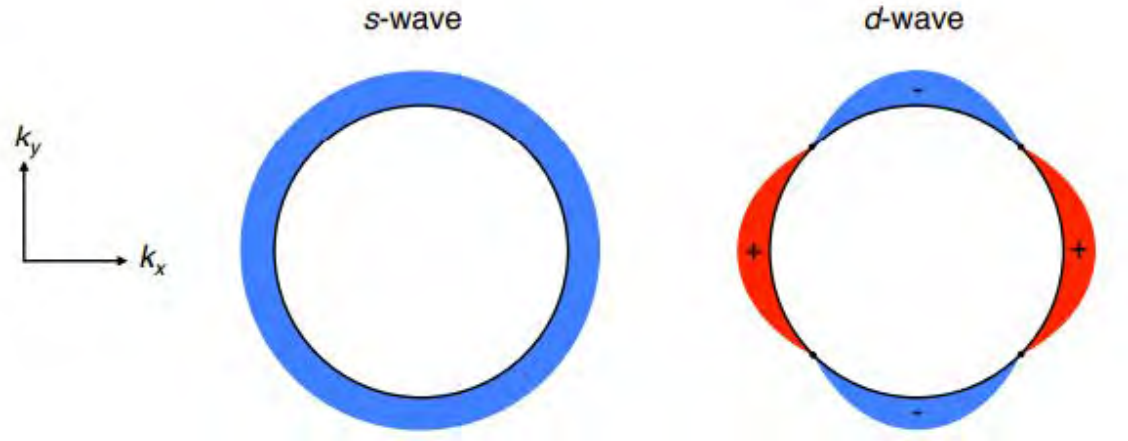

Figure 2.4.: Schematic illustrations of the superconducting gap symmetry for conventional and unconventional superconductors. Left: isotropic s-wave gap, characterized by a constant amplitude around the Fermi surface. Right: anisotropic $d_{x^2-y^2}$-wave gap, where the magnitude of the order parameter varies with momentum and changes sign between the lobes, as indicated by the + and – regions. This sign change produces nodes along the Fermi surface where the superconducting gap vanishes. Adapted from Ref. [60].

High quality $YBa_2Cu_3O_{7-x}$ thin films can be grown using several different techniques, where each one has its own advantages and disadvantages. The most frequently used growth techniques are pulsed laser deposition [68, 69], reactive co-evaporation [70] and high oxygen pressure sputtering (used in this work, described in 3.1.1) [71, 72]. In general, $YBa_2Cu_3O_{7-x}$ and all cuprates have a strong defective structure, which show anti-phase

boundaries, oxygen and cation vacancies, twin boundaries, stacking faults, interstitials and etc. Those defects act as pinning centers: regions that serves to pin or immobilize magnetic flux vortices [52]. Considering the small coherence length and anisotropic properties of high-T_c superconductors, defect-based pinning centers are essential for improving critical current J_c values and performance under magnetic fields for applications in magnets and power cables [53].

2.2. $SrRuO_3$

$SrRuO_3$ (SRO) is a complex oxide with a perovskite structure described by the general formula ABX_3. In this structure, A and B are cations, where the A-site cation typically has a larger ionic radius than the B-site cation, and X is an anion, commonly oxygen [73, 74]. SRO can also be interpreted as the limiting composition of the Ruddlesden-Popper (RP) phases $AO(AO\text{-}RuO_2)_n$, where $n \to \infty$ and A = Sr. These RP structures are formed by the repeated stacking of AO and RuO_2 planes. Fig. 2.5 illustrates the crystallographic structure of SRO, which adopts an orthorhombic crystal structure (space group *Pbnm*) at room temperature. Unstrained SRO shows two phase transitions with temperature, exhibiting crystallographic structures of higher symmetry, such as tetragonal at 547 °C and cubic at 677 °C [75].

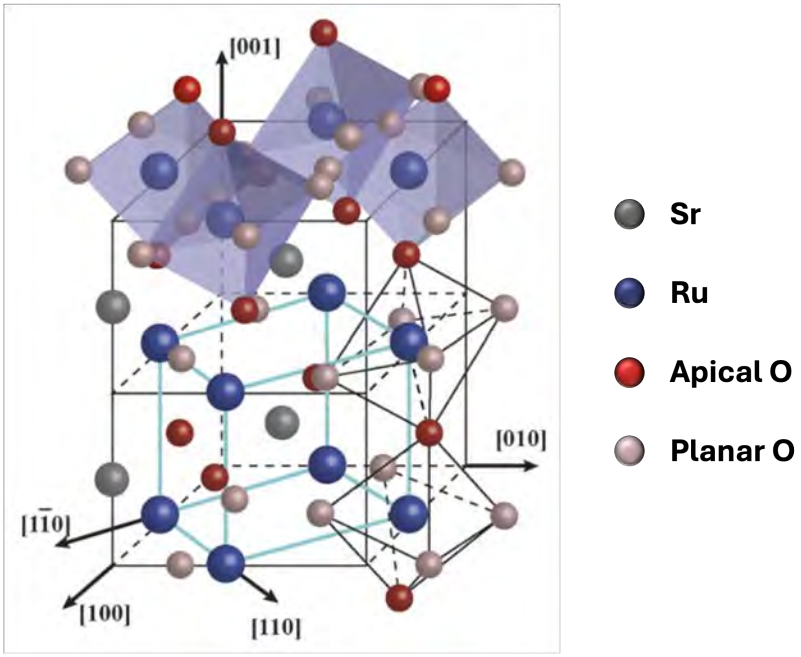

Figure 2.5.: Crystallographic structure of $SrRuO_3$. Orthorhombic unit cell is shown in black and the pseudocubic is shown in blue. The Sr, Ru, apical O, and planar O atoms are represented with gray, blue, red, and pink spheres, respectively. Taken from Ref. [31].

A notable distortion of the RuO_6 octahedra is observed in Fig. 2.5, which is attributed to the significant difference in bond lengths, with the Ru–O bond approximately twice as short as the Sr–O bond. The lattice parameters of the orthorhombic unit cell are a_{or} = 5.53 Å, b_{or} = 5.57 Å and c_{or} = 7.85 Å. Since SRO has an aristotype perovskite structure [73], its orthorhombic unit cell comprises four units derived from the perfect

cubic perovskite structure, isostructural with $GdFeO_3$. This arrangement leads to a pseudocubic lattice constant $a_{pc} = 3.93$ Å [75–77]. The pseudocubic unit cell is shown in blue in Fig. 2.5. Note that, in reciprocal space notation, the pseudocubic $(00l)$ reflections correspond to the orthorhombic $(hh0)$ reflections. The relation between the lattice parameters of the orthorhombic unit cell and the pseudocubic unit cell is given by the equation below [76]:

$$a_{pc} = \left[\left(\frac{a_{or}}{\sqrt{2}}\right)\left(\frac{b_{or}}{2}\right)\left(\frac{c_{or}}{\sqrt{2}}\right)\right]^{\frac{1}{3}}. \tag{2.2}$$

SRO is the first oxide identified as a ferromagnet driven by itinerant electrons, with a Curie temperature (T_{Curie}) of about 160 K and a saturation moment of 1.6 μ_B per Ru atom at $T = 0$ K. When epitaxially grown under compressive strain [on a $SrTiO_3$ (001) substrate, for example], it often exhibits perpendicular magnetic anisotropy (PMA), although this property depends on substrate-induced strain and orientation [78–80]. The material displays excellent metallicity at low temperatures ($T < 10$ K) due to Fermi liquid behavior, but its metallicity decreases with rising temperature as it approaches room temperature.

The electronic structure of SRO is shaped by the splitting of Ru 4d orbitals in its octahedral crystal field, where the higher-energy 4d (e_g) levels are above the 4d (t_{2g}) levels. Filling the 4d (t_{2g}) orbitals with four electrons according to Hund's rules yields a low-spin state of $S = 1$ [79, 81], as shown in Fig. 2.6. First-principles band structure calculations by Allen et al. (1996) and Singh (1996) confirmed SRO's itinerant ferromagnetism and predicted a ground-state magnetic moment of 1.5–1.6 μ_B, consistent with experimental observations. These insights form the basis for exploring its band structure, electron itinerancy, and correlation effects [75, 82, 83]. Typical electric transport and magnetization measurements of a stoichiometric SRO thin film grown on $SrTiO_3$ substrates are depicted in Fig. 2.7.

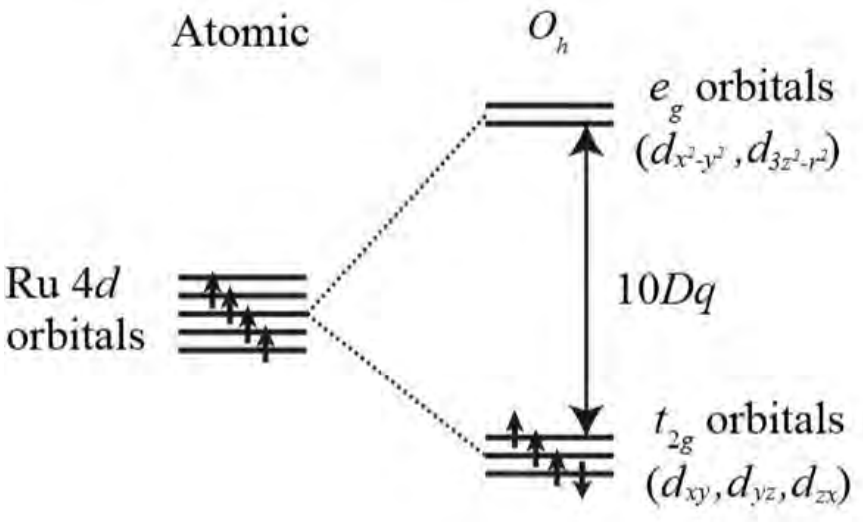

Figure 2.6.: The electron and spin configurations in the degenerate Ru 4d orbitals of an isolated Ru atom, along with their splitting under the influence of the octahedral crystal field (O_h) in SRO, are shown. The crystal-field splitting parameter is represented by 10Dq, while black arrows on the energy levels indicate electrons with their respective spins. Adapted from Ref. [84].

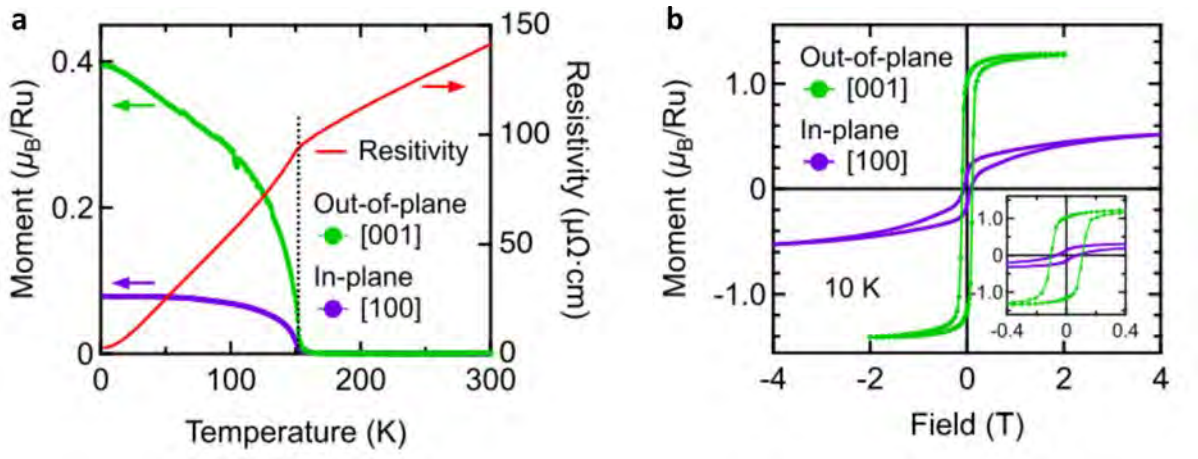

Figure 2.7.: (a) Temperature dependence of the electronic transport and magnetization of a stoichiometric SRO (65 nm thick) thin film grown on $SrTiO_3$ substrate. The magnetization curves were acquired with field cooling process with a magnetic field of 100 Oe applied parallel to [001] (green, out-of-plane) and [100] (purple, in-plane) crystallographic directions. (b) Magnetic hysteresis curves at 10 K. Adapted from Ref. [85].

The above mentioned physical properties of SRO are usually investigated in its thin film form. This is due to the difficulty in preparing high-quality bulk single crystals of SRO, since Ru starts evaporating at temperatures near 300 °C [86]. High-quality SRO bulk single crystals can still be prepared using the floating zone growth method with the installation of a cold trap (to avoid RuO_2 condensation on the walls of quartz tube) and with feed rods that present an enrichment of RuO_2, to compensate for Ru losses during the growth [87]. Molecular beam epitaxy (MBE), reactive evaporation, pulsed laser deposition (PLD) and 90° off-axis magnetron sputtering are growth techniques usually employed on the growth of high quality SRO thin films, with films prepared on MBE showing a residual resistivity ratio [RRR = $\rho(T_{\text{high}})/\rho(T_{\text{low}})$] over 50 [85, 88–95]. The RRR provides quantitative information on the number of crystallographic defects and impurities inside a material. Fig. 2.8 illustrates the RRR, the full width at half maximum of the rocking curve of the $(001)_{pc}$ or $(002)_{pc}$ peaks and the T_{Curie} of SRO thin films grown on several substrates and techniques.

SRO has attracted considerable interest as a promising material in the emerging field of quantum electronics, a novel form of electronics based on the quantum degrees of freedom [30, 31]. This new application of SRO would move it beyond consideration as only an electrode in ferroelectric capacitors and superconducting junctions [48, 49]. Moreover, it exhibits strong spin–orbit coupling, as well as an anomalous Hall effect that originates from Berry curvature, making it a promising platform for Berrytronics and topological superconductivity [31, 85, 88, 96–98]. The structural compatibility and subsequent interplay of physical properties between SRO and other technologically relevant oxides are being explored, paving the way for applications in various fields such as electronics, catalysis, energy storage, and more [50].

In addition to its metallic and ferromagnetic characteristics, SRO thin films display a remarkably rich magnetotransport behavior that is highly sensitive to stoichiometry, crystalline quality, and defect concentration. Stoichiometric and ultrahigh-quality epitaxial films, particularly those grown by MBE [85], exhibit unsaturated linear positive

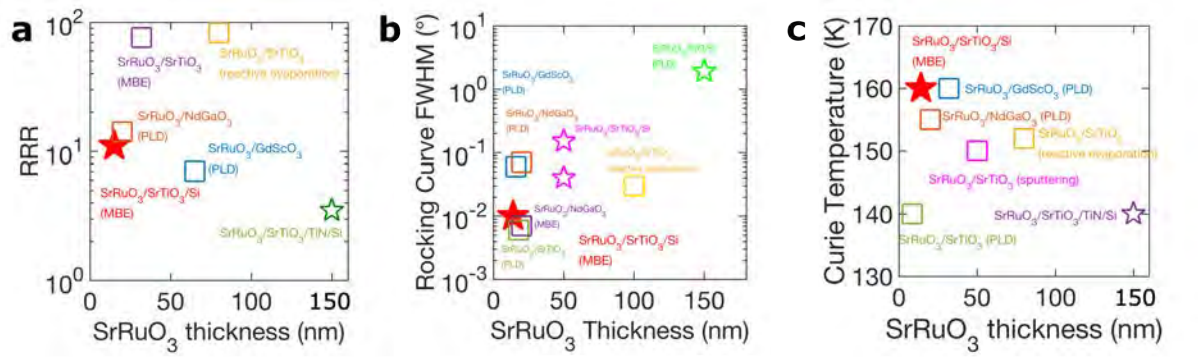

Figure 2.8.: (a) Residual resistivity ratio, rocking curve full width at half maximum and Curie temperature of SRO thin films grown on several substrates using different techniques. Adapted from the supplementary material of Ref. [89] and the references therein.

magnetoresistance at high magnetic fields, quantum oscillations of the Shubnikov–de Haas type with a Berry phase close to π, and exceptionally high carrier mobilities [98]. These findings are interpreted as evidence of Weyl-fermion transport arising from the strong spin–orbit coupling and topological features of the Ru $4d$ (t_{2g}) bands near the Fermi level. In this regime, the linear positive magnetoresistance does not originate from conventional orbital motion or weak anti-localization effects, which are negligible above 0.5 T [98]. Instead, it reflects a topological quantum contribution associated with Weyl nodes and the chiral anomaly in the electronic structure of SRO.

By contrast, Ru-deficient SRO thin films exhibit qualitatively different behavior. The RRR is markedly reduced, the T_{Curie} slightly decreases ($\approx$ 140 K), and the high-field magnetoresistance becomes negative or non-linear [99]. These features are attributed to enhanced scattering from Ru vacancies, which shorten the quasiparticle lifetime and suppress the quantum oscillations observed in stoichiometric films. Early studies have also shown that the magnetoresistance contains both orbital and spin-dependent contributions, depending on the measurement geometry (transverse or longitudinal) and on the magnetic domain configuration (i.e. single- or multi-domain SRO film) [95, 100–102]. Therefore, distinguishing intrinsic topological transport from other mechanisms, such as conventional orbital magnetoresistance, spin-disorder scattering, or effects related to structural defects and magnetic domain configurations, requires careful structural, compositional, and geometrical control. The contrasting behaviors discussed above are summarized in Fig. 2.9, which compiles representative magnetoresistance data from stoichiometric, Ru-deficient, and single-domain SRO films.

The SRO narrow domain wall width of 3 nn, together with a magnetic periodicity ranging from 200 nm to 1 μm [91], can provide a favorable environment for the generation of spin-triplet correlations when SRO is interfaced with high-T_{c} cuprates. This has motivated a more detailed study of its interfacial proximity effects and the role of magnetization in hybrid SRO/YBCO heterostructures.

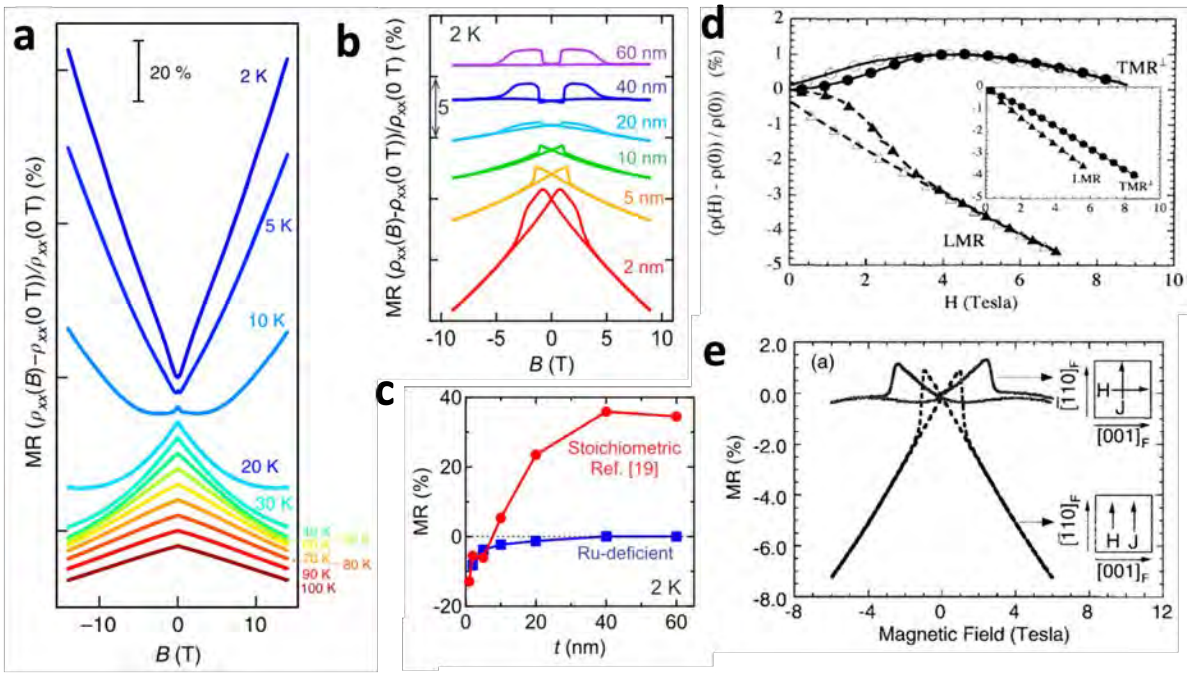

Figure 2.9.: Panels illustrating the crossover from classical orbital and spin-disorder dominated magnetoresistance to quantum topological transport in high-quality SRO thin films. (a) Linear, non-saturating positive magnetoresistance reported for stoichiometric, ultra-high quality films in the clean transport regime, where Weyl-fermion transport has been proposed on the basis of multiple quantum-transport signatures (adapted from Ref. [98]). (b) Evolution of the magnetoresistance as a function of film thickness for Ru-deficient SRO, showing suppression of the linear behavior and appearance of negative MR in thinner or more disordered films. (c) Comparison of the MR amplitude versus thickness for stoichiometric and Ru-deficient films at 2 K, illustrating the compositional dependence of the transport regime (adapted from Ref. [99]). (d, e) Magnetoresistance of epitaxial single-domain SRO measured in transverse (TMR) and longitudinal (LMR) geometries, showing opposite signs corresponding to orbital (positive) and spin-disorder (negative) contributions (adapted from Refs. [100, 101]).

2.3. $SrTiO_3$

$SrTiO_3$ (STO) is a perovskite material considered the standard substrate for the epitaxial growth of complex oxides [103, 104], such as $YBa_2Cu_3O_{7-x}$ (YBCO) and SRO, because above 105 K it has cubic perovskite crystal structure with a lattice parameter of 3.905 Å [105, 106]. The STO substrate consists of alternating layers of SrO and TiO_2, as depicted in Fig. 2.10.

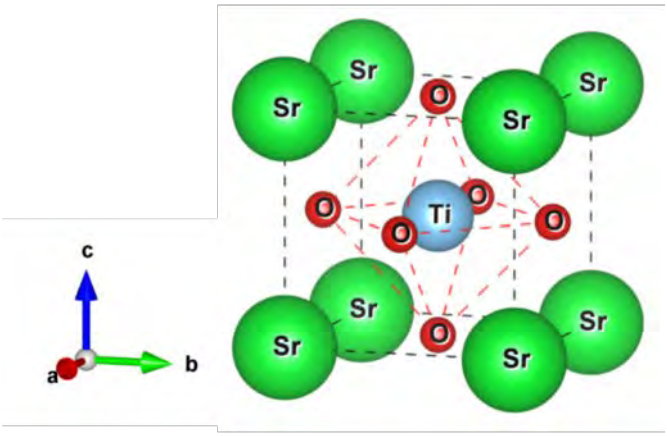

Figure 2.10.: Crystallographic structure of $SrTiO_3$. Adapted from Ref. [16].

Commercially available STO substrates present a mixture of SrO and TiO_2 layers and this surface is usually flat. However, having singly terminated surfaces (TiO_2-terminated STO substrates are more common) has been found to be important, as it minimizes crystal imperfections during the thin film growth resulting in films with sharp interfaces. After etching with buffered hydrofluoric acid (BHF), the SrO reacts strongly with the BHF solution and forms a product that dissolves easily in water [103]. The etched substrates are annealed and the TiO_2-terminated surface, characterized by the terraces with straight step edges that usually have one unit cell height, become visible, as shown in Fig. 2.11.

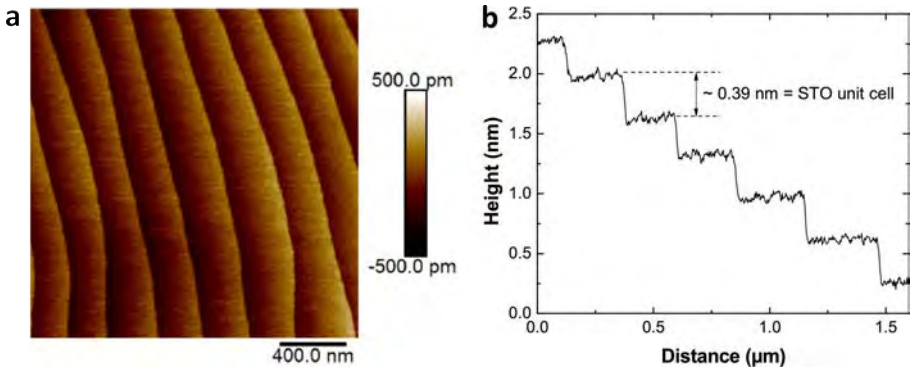

Figure 2.11.: (a) AFM topographic image (2×2 µm^2) of an STO(001) substrate treated with a BHF solution, and (b) cross-sectional profile revealing a step height of 0.39 nm between adjacent terraces, corresponding to the lattice parameter of STO. Adapted from Ref. [107].

In this context, two definitions become important: the substrate miscut angle (α) and the angle of miscut direction (ϕ). The substrate miscut angle α refers to the deviation of the substrate's surface from a perfectly flat or ideal crystallographic plane. Specifically, it

is the angle between the actual surface normal of the substrate and the normal to a chosen crystallographic plane (e.g., the (001) plane). This angle is introduced intentionally or may occur naturally due to imperfections during the preparation of the substrate.

Substrates with a miscut are commonly referred to as vicinal substrates. When terraces form on such surfaces, they are typically distributed uniformly across the substrate. In addition, the terraces are aligned along a specific direction. The inclination or orientation of the terraces is characterized by the angle between the normal to the terrace edges and the crystallographic [100] direction. This angle, denoted as ϕ, is referred to as the miscut direction angle [102, 103]. Figures 2.12 and 2.13 illustrate these two definitions.

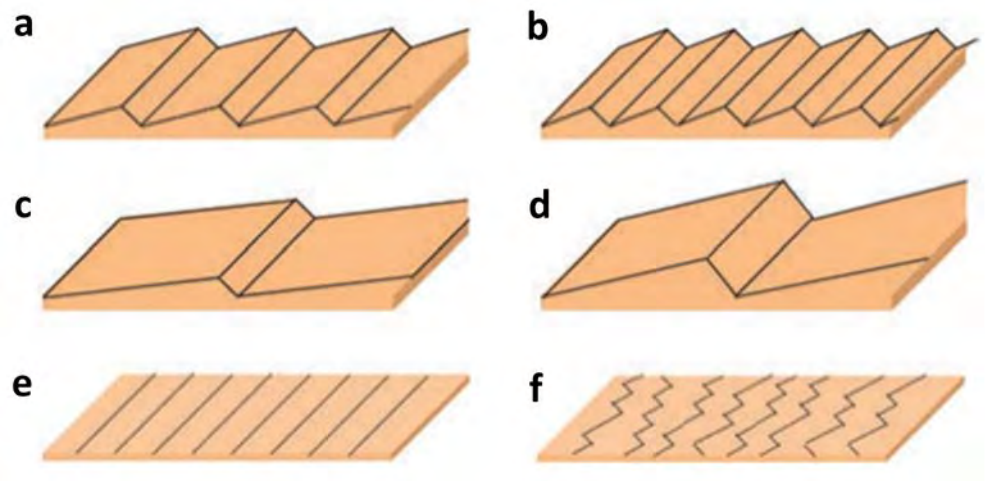

Figure 2.12.: Illustrations of various substrate types showing (a) intermediate miscut, (b) large miscut or vicinal surface, (c) low miscut or exact, (d) step bunching, (e) straight steps (low ϕ), and (f) kinked steps (high ϕ). Taken from Ref. [103].

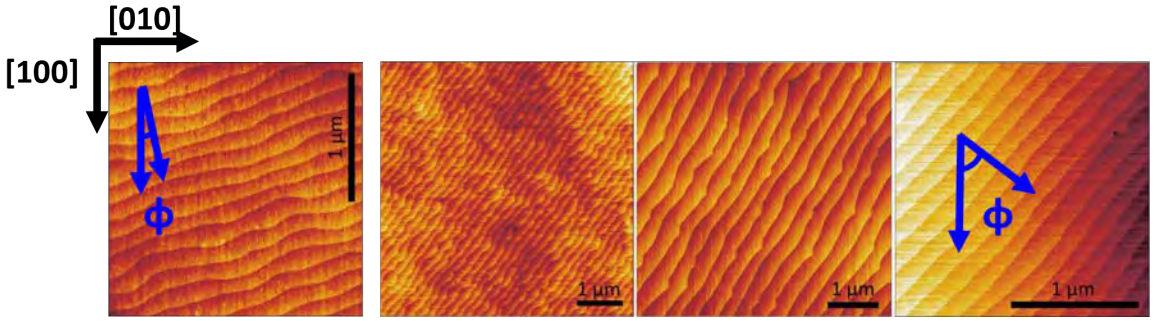

Figure 2.13.: Surface morphology of as-prepared STO substrates with varying miscut angles (ranging from 0.06° to 0.16°, categorized as low miscut) and miscut direction angles (ϕ). The miscut direction angle ϕ varies from 10° to 45°. The figure has been adjusted to ensure consistent crystallographic orientation across the AFM micrographs. Adapted from the supplementary material of Ref. [102].

As mentioned in subsection 2.2, SRO exhibits PMA and metallic properties when grown under compressive strain. In this case, STO substrates are particularly suitable, as it also has a perovskite structure with lattice parameters very close to those of SRO ($a_{pc} = 3.93$

Å). SRO thin films can be epitaxially grown on STO substrates due to the small lattice mismatch of 0.64%. The growth mechanism of SRO thin films on exact and vicinal STO substrates has been extensively investigated by various research groups [78, 92, 94, 95].

It is well established that the step-flow growth of thin films on vicinal substrates promotes the formation of preferential structural domains, as illustrated in Fig. 2.14(a–b). The terraced structure of the STO substrate, where either (100) or (010) facets are exposed, gives rise to distinct vertical interfaces between different orthorhombic SRO domains and the STO substrate at the step edges, as indicated by the arrows in Fig. 2.14(a). This asymmetry in the interfacial structure breaks the growth symmetry, making one particular domain energetically more favorable.

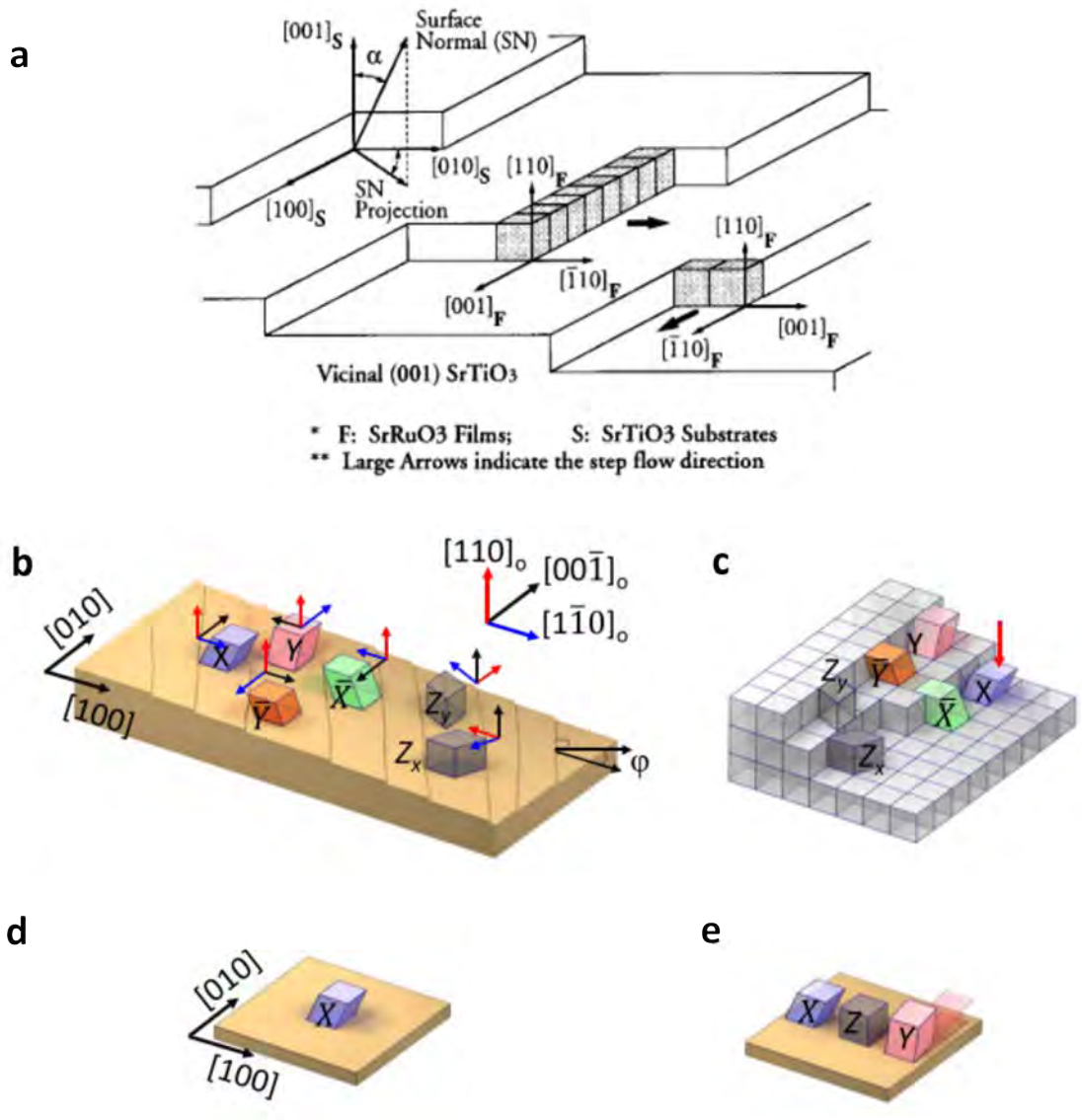

Figure 2.14.: (a) A schematic diagram of a vicinal $SrTiO_3$ (001) substrate illustrating the miscut angle (α) and miscut direction (ϕ), along with the epitaxial arrangement for two types of step-flow growth. (b) The six possible orthorhombic domains and (c) their interface with the STO substrate. (d) Single and (e) multi-domain SRO thin film on a STO substrate. Adapted from Ref. [95, 102].

There are six possible orthorhombic domains, as schematically shown in Fig. 2.14(b-c). These domains originate from the slight distortion of the orthorhombic unit cell, in which the angles between the crystallographic axes deviate slightly from 90°, leading to a small tilt of the lattice. When SRO is epitaxially grown on STO (001), the *c*-axis can be oriented either in-plane (along one of the two principal directions of STO) or out-of-plane. For the X-domain, the (100) plane tilts away from the STO substrate, whereas for the $\bar{X}$ domain, it tilts toward the STO unit cell. In the case of the Y and $\bar{Y}$ domains, their (100) planes are parallel to the STO (100) plane, but their [001] axes are slightly tilted relative to the STO [001] axis.

A similar situation occurs for the Z_x and Z_y domains, where their principal axes are misaligned with those of STO at the (001) interface. When step flow occurs predominantly in a single direction without two-dimensional nucleation, the resulting thin films will form a single domain, as illustrated in Fig. 2.14(d). The presence of single-domain or multi-domain structure is usually investigated through ϕ-scan and reciprocal space mapping measurements. It is known that single-domain SRO films exhibit better magnetic and electric transport properties in comparison to multi-domain SRO thin films. The STO substrate miscut can also play a role in the morphological and physical properties of SRO thin films [94, 95, 102, 108].

STO substrates undergo structural phase transitions at low temperatures, as shown in Table 2.2. Epitaxial growth on the STO surface can result in complex behavior due to strain-induced interactions between the thin film and the near-surface region of STO. In extreme cases, this strain may induce structural phase transitions in the epitaxial layers. X-ray and neutron data reveal strongly anisotropic, micrometer-sized facets [105]. As temperature decreases, structural domains form near the STO surface, with phase separation into tetragonal and cubic crystallites. These domains extend into the thin film but not into the deeper substrate layers. Hoppler et al. [105] show that strain effects from the STO substrate can occur at temperatures distinct from the antiferrodistortive phase transition of bulk STO, which is also observed in magnetization measurements as a function of temperature. The formation of these facets, which affect thin film quality, presents a significant challenge for low temperature scattering studies [105, 106, 109, 110]. While alternatives like Nb-doped STO substrates are commonly used to minimize or avoid these structural phase transitions, their effectiveness remains scientifically unproven.

Table 2.2.: Structural phase transition in STO substrates. Adapted from Ref. [106].

Temperature range [K]	Structure type
110 - 300	Cubic (possible pseudocubic)
65 - 110	Tetragonal
35 - 65	Orthorhombic
10	Possibly rhombohedral

In this work, STO substrates with miscut angles of $0.05° < \alpha < 0.1°$ were used to grow SRO and YBCO thin films and YBCO/SRO and SRO/YBCO heterostructures. The STO substrates were chemically etched during 30 seconds using a buffered hydrofluoric acid (NH_4F–HF) solution and annealed at 950 ˚C for 2 h. This process was performed at the clean room of Peter Grünberg Institute for electronic materials (PGI-7) following the procedure developed by Rene Borowski and accordingly to the supervision of Sylvia de Waal and Grigory Potemkin.

Chapter 3

Methods and instrumentation

All thin films and heterostructures discussed in this work were grown using High Oxygen Pressure Sputtering (HOPS). This chapter describes the principles of the HOPS technique, the experimental procedures employed during film growth, and the methods used for structural, transport, and magnetic characterization.

3.1. Crystal growth modes in thin films

Thin epitaxial growth of crystalline films depends both on material properties, such as the lattice mismatch between film and substrate, sticking coefficient, surface diffusivity, and on thermodynamic parameters, i.e. external conditions tuned during deposition that control the system's energy balance, such as substrate temperature, oxygen partial pressure, and plasma power [111, 112]. The growth modes are generally classified into four categories, determined by the mobility of adatoms on the substrate surface, as illustrated in Fig. 3.1.

The concept of surface energy balance as the determinant of epitaxial growth was first formalized by Ernst Bauer in 1958, who introduced a thermodynamic criterion based on the surface energies of the film (σ_f), the substrate (σ_s), and the film–substrate interface (σ_i) [113]. The key parameter is the change in surface energy,

$$\Delta\sigma = \sigma_f + \sigma_i - \sigma_s, \tag{3.1}$$

which quantifies the degree of substrate wetting by the film material.

For incomplete wetting ($\Delta\sigma > 0$), i.e. when the combined surface energies of the film and interface exceed that of the substrate, the system minimizes its energy through the nucleation of three-dimensional islands, known as Volmer–Weber (VW) growth. When $\Delta\sigma \leq 0$ and the lattice mismatch is negligible, the equilibrium island height approaches zero and two-dimensional islands form, giving rise to layer-by-layer or Frank–van der Merwe (FM) growth. Finally, when $\Delta\sigma < 0$ but the lattice mismatch is finite, growth begins with the formation of a thin wetting layer, after which three-dimensional islands nucleate on top, a mechanism known as Stranski–Krastanov (SK) growth. Thus, $\Delta\sigma \leq 0$ (or equivalently, $\sigma_s > \sigma_f + \sigma_i$) implies a complete wetting at least in the first epitaxial

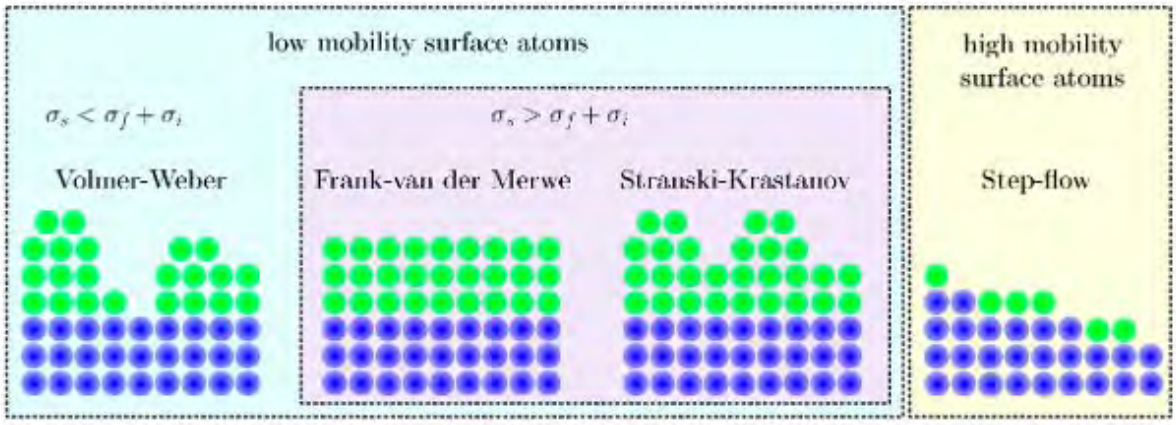

Figure 3.1.: Schematic representation of thin film growth modes. For low surface mobility and low interfacial energy, growth proceeds via three-dimensional islands (Volmer–Weber). For high interfacial energy, layer-by-layer (Frank–van der Merwe) or layer-plus-island (Stranski–Krastanov) growth can occur. At high surface mobility, step-flow growth is possible. Adapted from Ref. [111].

layers, while the lattice mismatch determines whether FM or SK occurs [114].

A fourth mechanism, step-flow growth, occurs under conditions of high adatom mobility, typically achieved at elevated substrate temperatures and moderate fluxes. In this regime, atoms diffuse to the step edges of a vicinal substrate and incorporate into the advancing terraces, leading to smooth, single-domain films with fewer defects [111].

3.1.1. High Oxygen Pressure Sputtering

High Oxygen Pressure Sputtering (HOPS) is a method to grow thin films at oxygen pressures greater than 0.5 mbar, instead of normal sputtering process with very low pressures. The HOPS technique was developed in the early 80's by Prof. Dr. Ulrich Poppe and Prof. Dr. Michael Faley [Ernst Ruska-Centre for Microscopy and Spectroscopy with Electrons (ER-C-1)] at Forschungszentrum Jülich GmbH, with the purpose of preparing High-T_c superconductors, such as $YBa_2Cu_3O_{7-x}$ and $Bi_2Sr_2CaCu_2O_{8+x}$. Over time, these machines began to be used for the deposition of other types of materials, such as, complex oxides and multiferroics systems [71, 115, 116].

The HOPS system described here is located in laboratory room 65 of Jülich Centre for Neutron Science for Quantum Materials and Collective Phenomena (JCNS-2). The instrument setup is shown in Fig. 3.2. This setup is composed of a deposition chamber, a (99.99% purity) oxygen bottle, mass flow controller MKS Type 250E pressure/flow controller, oil-free backing pump and turbomolecular pump, and a Direct Current (DC) and Radio Frequency (RF) power supply. The instrument can be controlled manually or with the help of a computer. With this technique, thin films and multilayered structures can be prepared using DC and RF sputtering and with high process gas pressures up to 3.5 mbar. Generally, DC sputtering is used for materials that have considerably good electrical conductivity while RF sputtering can be used for insulating as well as poorly conductive materials. Thin films prepared by HOPS have layers with good homogeneity over the surface of the substrate, where the thin film stoichiometry is pre-determined by the target stoichiometry. The deposition temperature as well as the base pressure used during the film growth can also play a role in the film stoichiometry.

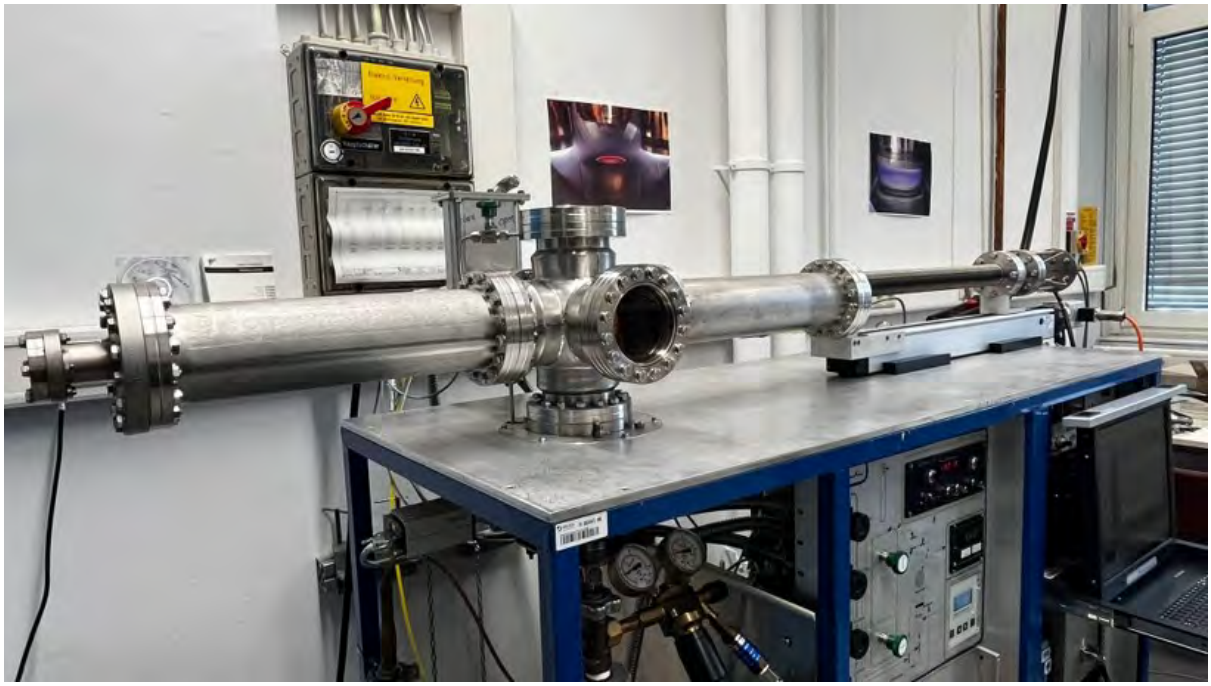

Figure 3.2.: High Oxygen Pressure Sputtering system instrument.

Sputtering is a physical vapor deposition growth technique. In the sputtering process, a target material, composed of the desired deposition substance, is bombarded with ionized atoms of a process gas, such as oxygen, in our case. A negative electrical potential applied to the target (magnetron cathode) accelerates free electrons, which ionize the process gas through collisions. These ions strike the target with sufficient energy to eject/sputter material atoms, forming a plasma or plume. The sputtered material is directed toward a heated substrate, where it condenses to form a thin film. Magnets behind the target can enhance the plasma's directionality in a process called magnetron sputtering. The plasma emits a characteristic glow as ions recombine with electrons, releasing excess energy as light. The thin film growth continues at a controlled rate by regulating deposition parameters such as gas pressure, substrate temperature, and applied power until the desired film thickness is achieved [117, 118].

During a deposition process with HOPS, the selected substrate is positioned on the block heater, ensuring precise alignment within the frames (which protects deposition into the block heater). To achieve the highest possible level of cleanliness and reduce contamination, the chamber is then sealed and pumped to achieve a base pressure of approximately 1×10^{-6} mbar. Once this vacuum level is reached, the process gas is introduced into the chamber, and its pressure is controlled using the mass flow controller to establish optimal conditions. Prior to initiating the actual deposition, the target material undergoes a pre-sputtering process for a minimum duration of one day [71, 115, 116]. In other research groups, such as at J. Santamaria's group in Complutense University of Madrid, this process is realized for at least one week prior to deposition or are under constant pre-sputtering process. This step helps to clean the target surface and stabilize a good sputtering process. After this pre-sputtering phase, the deposition process can start. An illustration schematic of a general sputtering deposition at HOPS is shown in Fig. 3.3.

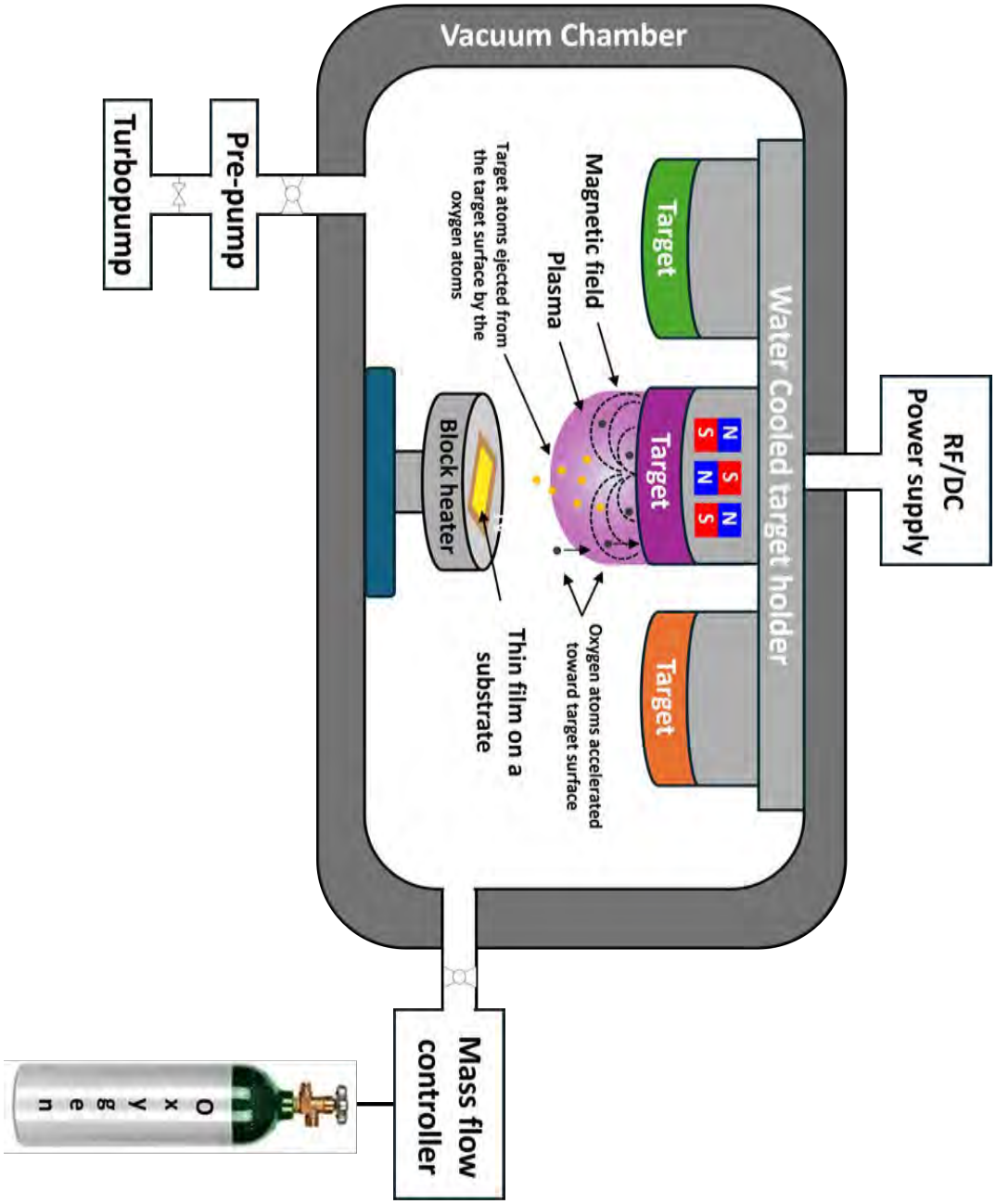

Figure 3.3.: Schematic of a general sputtering deposition at HOPS.

The growth parameters must be adjusted in order to obtain an optimal plasma and subsequent homogeneous films. These parameters include deposition temperature (T_{dep}), target-substrate distance (D_{TS}), oxygen partial pressure (P_{O_2}), forward power (FWDP), and reflected power (REFP). For DC sputtering processes, the current and voltage are also precisely controlled. Finally, the thickness of the films are controlled by deposition time. The growth parameters used for DC and RF sputtering at HOPS are summarized on the tables 3.1 and 3.2. Precise pyrometer measurements of the substrate temperature show that is is about 80 – 110 °C lower than block heater temperature, therefore, here we define the temperature of the heater block as T_{dep}. This is in agreement with Ref. [119].

Table 3.1.: DC sputtering adjustable parameters.

DC Sputtering parameter	Value
Current	0.001 – 3 A
Voltage	1 – 600 V
Oxygen partial pressure (P_{O_2})	0.1 – 2.5 mbar
Target-substrate distance (D_{TS})	0.5 – 2.5 cm
Block heater temperature (T_{dep})	20 °C – 1100 °C

Table 3.2.: RF sputtering adjustable parameters.

RF Sputtering parameter	Value
Forward Power (FWDP)	0 – 100 W
Reflected Power (REFP)	must be kept at 0 W
Variable capacitor (Tune, Ct)	0 – 999 a. u.
Variable capacitor (Load, Cl)	0 – 999 a. u.
Oxygen partial pressure (P_{O_2})	0.1 – 2.5 mbar
Target-substrate distance (D_{TS})	0.5 – 2.5 cm
Block heater temperature (T_{dep})	20 – 1100 °C

Each parameter in the thin-film deposition process plays a vital role in determining plasma quality and film uniformity. To ensure high-quality samples and gain better insights into their physical properties, a growth optimization process is typically performed. This involves fine-tuning growth parameters to identify optimal conditions. Figure 3.4(a) illustrates an optimal plasma state for an SRO target achieved after such optimization. It shows a homogeneous plasma achieved after optimizing growth parameters, which ensures a stable and efficient deposition process. In contrast, Fig. 3.4(b) depicts an unstable, non-homogeneous plasma with visible sparks resulting from target damage, highlighting the critical importance of proper parameter tuning to prevent equipment damage and ensure high-quality film growth.

At the start of my Ph.D. project, the HOPS machine lacked an established protocol or user manual, leading to inconsistent usage. Through collaboration with Prof. Dr. Michael Faley (ER-C-1), we developed a standardized protocol for growing complex oxides, such as SRO, along with a comprehensive user manual. These resources are now available to ensure consistent and reliable operation, reflecting the commitment to improving research practices and facilitating the effective use of this advanced equipment. The protocol and

user manual can be find at the Appendix A. An online logbook was also developed in collaboration with Florian Rhiem from the Technical and administrative infrastructure (JCNS-TA), allowing the integration of the HOPS machine with the JCNS instruments.

The SRO thin films discussed in this work were prepared using RF sputtering in the HOPS system of JCNS-2 accordingly to this protocol and following the steps presented in the prepared manual. The YBCO samples were prepared in collaboration with Prof. Dr. Michael Faley, given his many years of experience with high- T_c superconductors. The YBCO thin films were deposited using DC sputtering in a dedicated HOPS system for YBCO growth. Heterostructures of YBCO/SRO and SRO/YBCO were prepared by a two-step process that combines the deposition of SRO and YBCO separately.

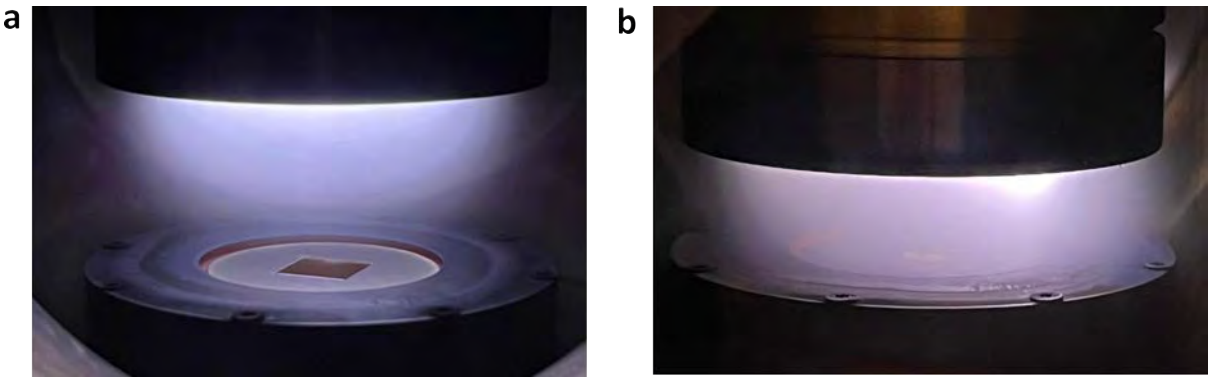

Figure 3.4.: (a) Homogeneous plasma obtained after the growth optimization process and (b) not homogeneous plasma with a spark caused by target damage.

3.2. Characterization techniques

3.2.1. Atomic force microscopy

Atomic force microscopy (AFM) is a powerful technique for studying material surfaces, providing a detailed topographical visualization. Developed in the mid-1980s to address the limitations of scanning tunneling microscopy (STM) in examining insulating materials, AFM has become an indispensable tool in surface science. It enables researchers to assess the quality of substrate surfaces termination, such as for the TiO_2-terminated STO substrates as well as to investigate the presence of surface contamination/impurities and defects prior to the thin film deposition. Furthemore, it allows one to analyze the surface quality of the deposited thin films and heterostructures, and to measure local surface roughness profiles with remarkable precision [120–122].

An AFM instrument is usually composed of a tip or probe with a radius of a few nanometers located at the end of a flexible cantilever, a piezoelectric scanner, a laser, and a four-quadrant photodetector. The system is controlled by the microscope's controller, typically consisting of a lock-in amplifier, micro-controllers, and other necessary electronic components. Finally, a computer is used to process the data and visualize the information. A schematic diagram of an AFM is shown in Fig. 3.5 [121].

During an AFM experiment, the cantilever is brought close to the sample so that the tip is in contact with or very near the surface to be studied. Depending on the microscope, the piezoelectric component can either move the sample laterally while keeping the tip stationary, or vice versa. This allows a specific area to be scanned. The separation

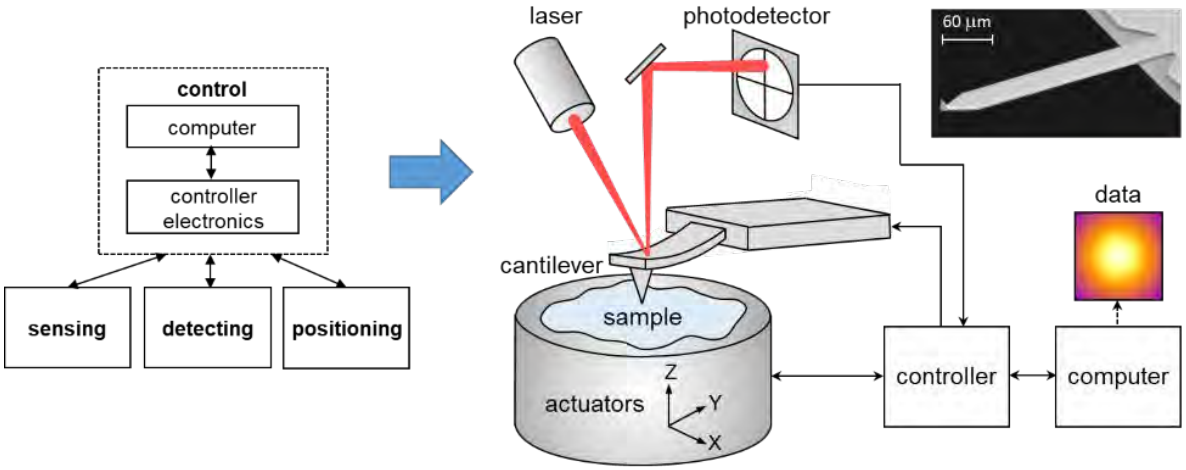

Figure 3.5.: A schematic diagram of an atomic force microscope. The tip on the cantilever is shown in the figure top right. Taken from Ref. [121].

between the tip and the sample is typically on the order of few nanometers. At this scale, localized interactions occur between the tip and the surface, which are sensitive to the morphological profile of the sample.

The cantilever is monitored using an optical lever, where a laser is focused on the back of the cantilever, and the reflected light is directed onto a photodetector. A differential amplifier records the variations in position and laser intensity caused by the deflections of the cantilever as it interacts with the surface. Additionally, a closed-loop control system is employed to maintain a constant interaction between the tip and the sample during the scanning process. The system detects the cantilever's motion during scanning by monitoring the vertical deflection (in contact mode) or oscillation amplitude (in intermittent contact mode). The difference between the setpoint value and the measured value at the photodetector is determined and taken as the error. To correct this error and maintain the setpoint value, a piezoelectric actuator moves the tip/cantilever in the z-direction. The Z-piezo movement, which has a reliable calibration (a relationship between nm and V), allows the conversion of electrical signals into topographical images [16, 122].

There are three main measurement modes in AFM: contact mode, non-contact mode and intermittent contact mode (or tapping mode). Contact mode in AFM operates with a tip-surface separation of less than 0.5 nm, making it ideal for rapid scans and analyzing friction on rough samples. In this mode, the interaction between the tip and sample transitions from attractive to repulsive as their distance decreases. Initially, Van der Waals forces dominate, pulling the tip toward the sample. As the distance reduces further, the electron clouds of the atoms overlap, causing a strong Pauli repulsion that compensates the attraction and the total force becomes positive.

This interaction is well described by the Lennard-Jones potential curve, shown in Fig. 3.6(a), which illustrates the interplay of attractive and repulsive forces. The potential decreases ($U \propto r^{-6}$) in the attractive regime and steeply rises ($U \propto r^{-12}$) in the repulsive regime. In this context, the cantilever's behavior is given by the Hooke's law for small deflections, allowing precise measurements of forces at the atomic scale during surface interactions. The magnitude of the force depends on the cantilever's spring constant and the setpoint, which are defined in a way to maintain a precise feedback. However, the force exerted by the cantilever in contact mode can damage or deform the surface of soft samples [123, 124].

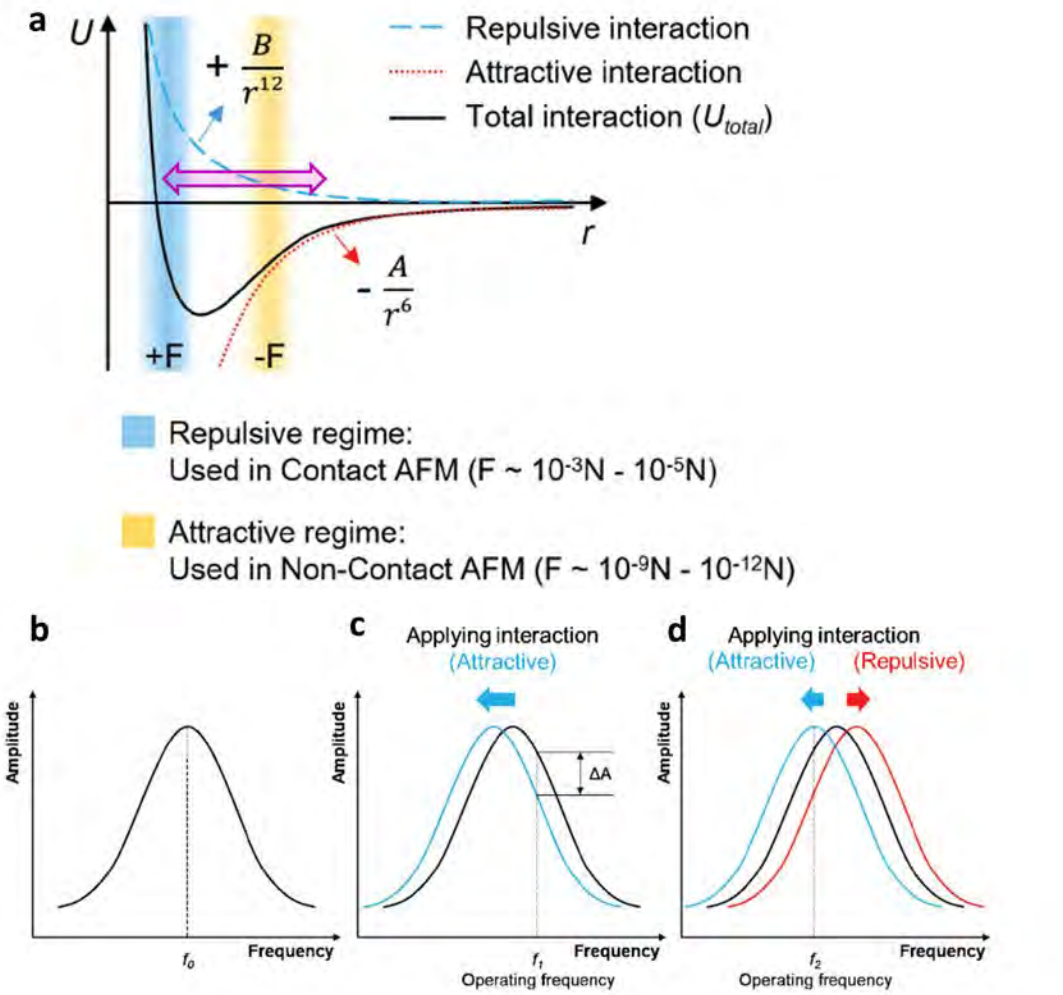

Figure 3.6.: (a) Interatomic interaction potential U as a function of distance r. The blue curve depicts a purely repulsive force, while the red curve represents a purely attractive interaction. The black curve illustrates the Lennard-Jones potential, combining short-range repulsion and long-range attraction. At larger distances, the net force is attractive ($-F$). At smaller distances, the net force is repulsive ($+F$). The pink region illustrates the operation regime of the tapping mode (or intermittent contact). (b) Oscillation frequency far apart of any tip-sample interaction. Shift in the oscillation frequency for (c) non-contact and (d) intermittent contact modes. Adapted from: [123, 124].

In non-contact mode, the cantilever oscillates with a small amplitude, typically just a few nanometers above the sample surface, in the attractive regime of the Lennard-Jones potential curve [Fig. 3.6(a)]. As the tip moves closer to the sample surface, Van der Waals forces between the tip and surface influence the cantilever's amplitude and phase. These changes are tracked by a Z-servo feedback system, which keeps the tip at a stable distance from the surface. This precise control ensures that both the tip and the sample remain undamaged [123, 124].

Intermittent contact mode (or tapping mode) involves a cantilever that oscillates up and down at a frequency between 5 and 400 kHz, with the tip gently touching the surface of the sample. Tapping mode operates in the transitional force regime between attractive and repulsive forces [the region indicated by the pink arrow in the Lennard-Jones potential curve in Fig. 3.6(a)]. Similarly to non-contact mode, the tapping mode uses the amplitude of the cantilever oscillation to detect changes in the tip-sample interaction forces, which correspond to the sample topography [123].

In non-contact and tapping modes, a shift in the oscillation frequency exists and depends upon the operating regime. The oscillation frequency f_0 is usually measured prior to the experiment and at a larger tip-sample distance, as shown in Fig. 3.6(b). For the non-contact mode, a shift to lower frequencies is observed in the oscillation frequency f_1, as pointed out by the blue curve in Fig. 3.6(c). As the tapping mode works on transitional force regime between attractive and repulsive forces, a shift to lower or higher oscillation frequencies f_2 is observed, as shown in Fig. 3.6(d). The detected change in the oscillation amplitude is indicated as ΔA [123].

In the tapping mode, the phase difference between drive and detected signal contains information about material-specific mechanical properties. The drive signal refers to the oscillation of the cantilever at a fixed amplitude near the resonant frequency. This amplitude is controlled through the feedback system, which adjusts the drive to maintain the oscillation at the desired level. As the amplitude and phase of the cantilever's oscillation are influenced by the interactions between the tip and the sample surface, the phase signal carries information that are sensitive to material-specific interactions such as elasticity, adhesion and stiffness. Therefore, the phase signal can reveal variations in mechanical properties and material composition within a sample. However, due to the influence of multiple factors on the phase signal, phase imaging primarily provides qualitative insights into the mechanical and material distribution, rather than precise quantitative measurements [123].

In this work, a surface characterization of STO substrates was carried out using AFM to verify the formation of a TiO_2-terraces surface termination. Additionally, the thin films and heterostructures deposited on these substrates were analyzed to assess its topography quality and local roughness profile. Phase imaging was employed on the investigation of multiple *a*-axis and *c*-axis growth of the YBCO/SRO and SRO/YBCO heterostructures. Given the characteristic roughness of YBCO films, the surface morphology is better visualized though phase imaging rather than topography, even though in a qualitative way. The measurements were carried out using an Agilent 5400 AFM/SPM microscope in intermittent contact mode with Mikromash type HQ:NSC15 cantilevers located at the Jülich Centre for Neutron Science (JCNS-2).

3.2.2. Scattering

Scattering is the process where a particle or wave changes direction from its initial path as a result of interacting with matter or a potential field. Diffraction (or elastic scattering) is the name given for scattering process where the energy or wavelength of the scattered particles or waves, respectively, is the same as before the scattering process. Considering that atoms in crystals are organized in an ordered manner, with interatomic spacing on the order of a few angstroms, X-ray (photons), thermal neutrons (with energy around 25 meV) and electrons are particularly suitable radiation probes employed for scattering experiments, as their wavelengths are comparable to the characteristic distances of atomic ordering in crystals. Electrons are charged particles and, therefore, is a less common probe since it can suffer from reduced penetration and multiple scattering events [125]. Figure 3.7 shows the dispersion relation of wavelength and energy for these probes.

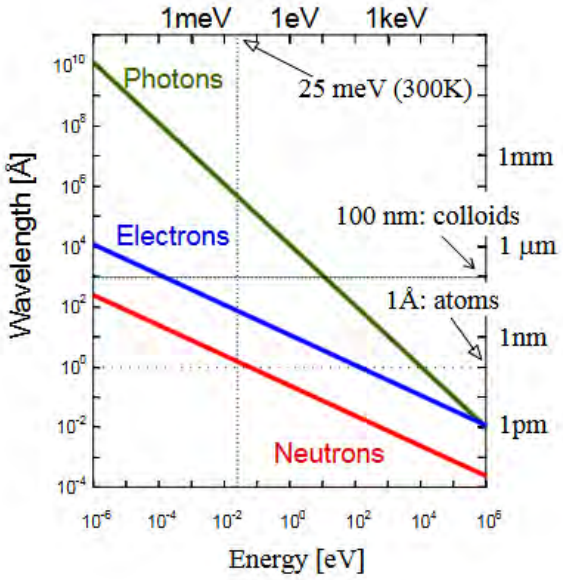

Figure 3.7.: A double logarithmic energy-wavelength diagram compares the probes neutrons, electrons, and photons by plotting their energy against their corresponding wavelengths. Taken from Ref. [125].

Although X-rays have a larger scattering cross section for structural (Thomson) scattering than neutrons, both probes are strongly used in the investigation of magnetism at the atomic scale. While neutrons scatter based on the magnetic induction within a sample, X-rays interact differently by scattering from both spin and orbital momentum. This distinction allows X-rays to separately measure form factors associated with each type of interaction [125, 126]. In this work, several scattering methods were employed to characterize the sample's crystal structure, layer thickness and interfacial roughness, epitaxial growth, elastic deformation of lattice parameters (strain), and to investigate interfacial magnetism and proximity effects. Given the Jülich Centre for Neutron Science (JCNS-2) institute's focus on scattering techniques, the description of scattering experiments will be presented in greater detail to align with its specialized research priorities and expertise.

3.2.2.1. Scattering in a periodic lattice

A crystal is a three-dimensional structure where atoms are arranged in a periodic fashion. This can be simplified by describing the crystal using a fundamental repeating unit, called the (primitive) unit cell. The unit cell is characterized by three vectors (primitive vectors), $\boldsymbol{a}$, $\boldsymbol{b}$, and $\boldsymbol{c}$, which have lengths a, b, and c, along with the angles α, β, and γ between them. These values, known as lattice parameters, provide a complete description of the crystal's structure. This concept is illustrated in Fig. 3.8. Every atom in a material can have its relative position, or coordinate, within the unit cell described by a position vector $\boldsymbol{r}$ given by:

$$\boldsymbol{r} = x\boldsymbol{a} + y\boldsymbol{b} + z\boldsymbol{c}, \tag{3.2}$$

where x, y, and z are fractions of the lattice parameters.

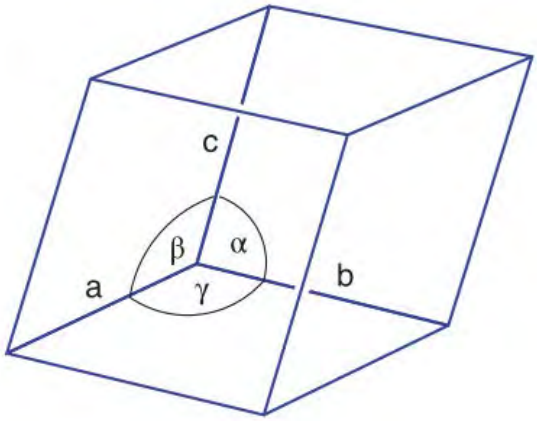

Figure 3.8.: A unit cell of a crystal can be defined by the parameters a, b, c, α, β, and γ. Taken from Ref. [127].

In a unit cell, crystallographic planes can be formed. A crystallographic plane is defined by any three non-collinear points in the unit cell volume. The orientation of a crystal plane, determined by three lattice points, is described using Miller indices (hkl). These indices are derived by finding the plane's intercepts with the crystal axes (a, b, and c), taking the reciprocals of these intercepts, and reducing them to the smallest integers that maintain the same ratio. An illustration of several crystallographic planes in a cubic unit cell and their respective Miller indices is given in Fig. 3.9.

The intensity of a diffraction pattern arises from the square of the Fourier transform of the scattering potential, which describes how incoming waves interact with a material's structure. For a crystalline material, its periodic atomic arrangement causes X-rays/neutrons/electrons to scatter in specific directions, creating sharp diffraction peaks corresponding to constructive interference. These peak positions are described by the Bragg's Law:

$$n\lambda = 2d_{hkl}\sin(\theta), \tag{3.3}$$

where n is the diffraction order, λ is the wavelength of the probe used in the scattering experiment, d_{hkl} is the distance between the crystal planes of the same family of planes hkl and θ is the incidence angle, as depicted in Fig. 3.10. This law explains that constructive interference occurs when the optical path difference between waves scattered from adjacent planes equals an integer multiple of the wavelength.

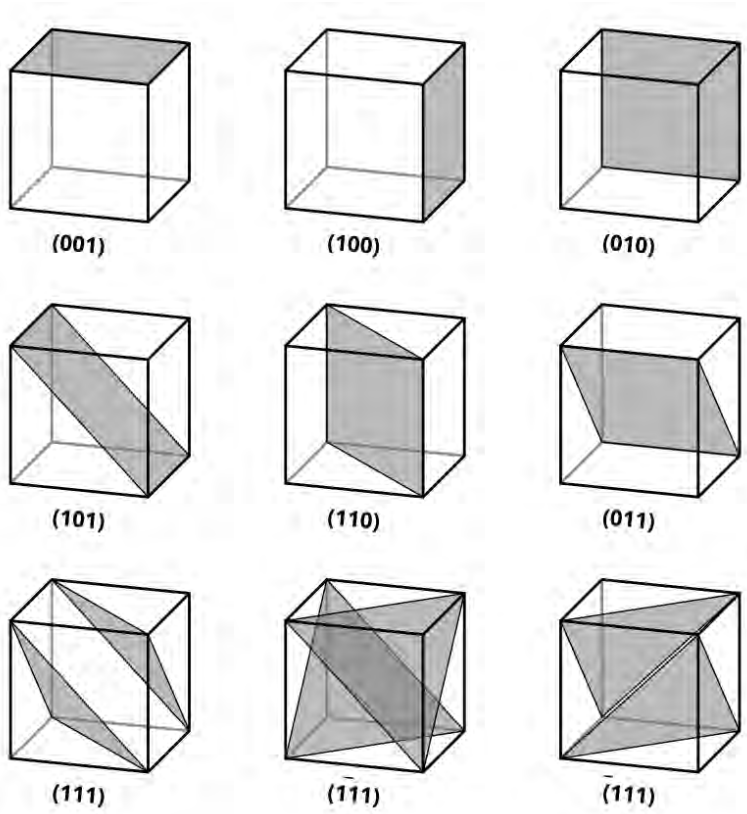

Figure 3.9.: Planes with different Miller indices in cubic crystals.

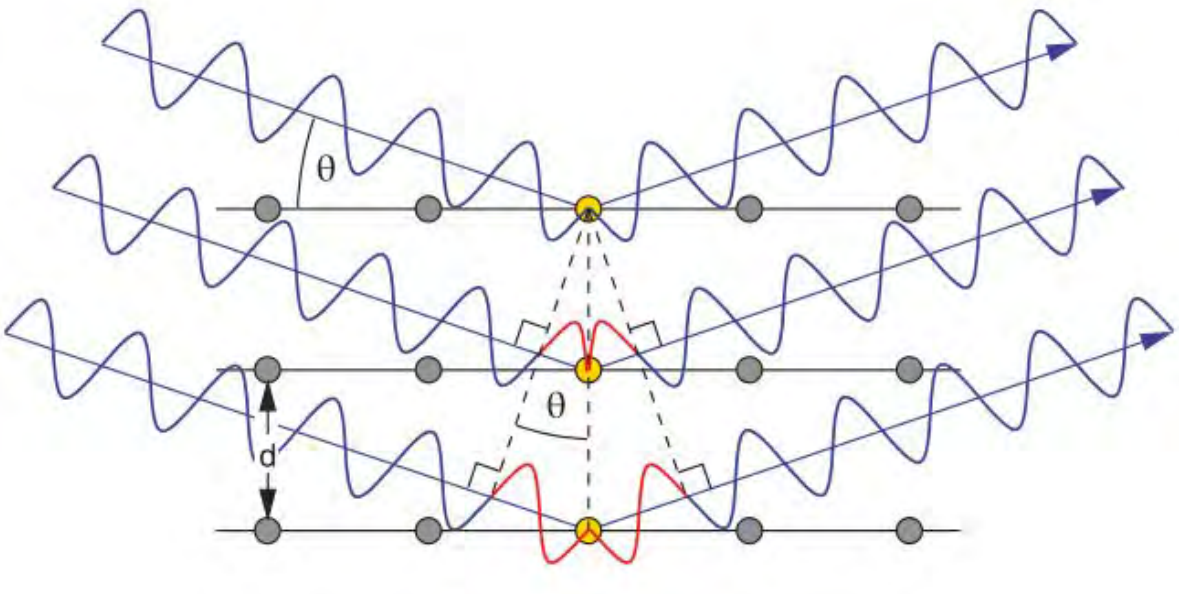

Figure 3.10.: Adjacent waves interfere constructively when the phase difference (shown in red) between them is an integer multiple (n) of their wavelength (λ), accordingly to the Bragg's Law. Taken from Ref. [127].

As the wavelength λ, which characterizes the radiation, is a scalar quantity, the vector quantity associated with the propagation direction of the wave is the wave vector $\boldsymbol{k}$, whose magnitude is inversely proportional to the wavelength ($|\boldsymbol{k}| \approx \frac{1}{\lambda}$). Therefore, it is convenient to describe the crystal structure in a space proportional to the wave vector dimensions. This space is known as reciprocal space. The set of vectors that defines a three-dimensional lattice are defined according to [11]:

$$\boldsymbol{a}^* = 2\pi \frac{\boldsymbol{b} \times \boldsymbol{c}}{\boldsymbol{a} \cdot (\boldsymbol{b} \times \boldsymbol{c})}; \quad \boldsymbol{b}^* = 2\pi \frac{\boldsymbol{c} \times \boldsymbol{a}}{\boldsymbol{a} \cdot (\boldsymbol{b} \times \boldsymbol{c})}; \quad \boldsymbol{c}^* = 2\pi \frac{\boldsymbol{a} \times \boldsymbol{b}}{\boldsymbol{a} \cdot (\boldsymbol{b} \times \boldsymbol{c})}, \tag{3.4}$$

where $\boldsymbol{a}$, $\boldsymbol{b}$ and $\boldsymbol{c}$ are the primitive vectors of the crystal lattice in the real space. Therefore, one can say that the periodicity and lattice symmetry are conserved in the reciprocal lattice, with the crystal planes being represented now as points in the lattice. An illustration of real and reciprocal space can be observed in Fig. 3.11 [128, 129].

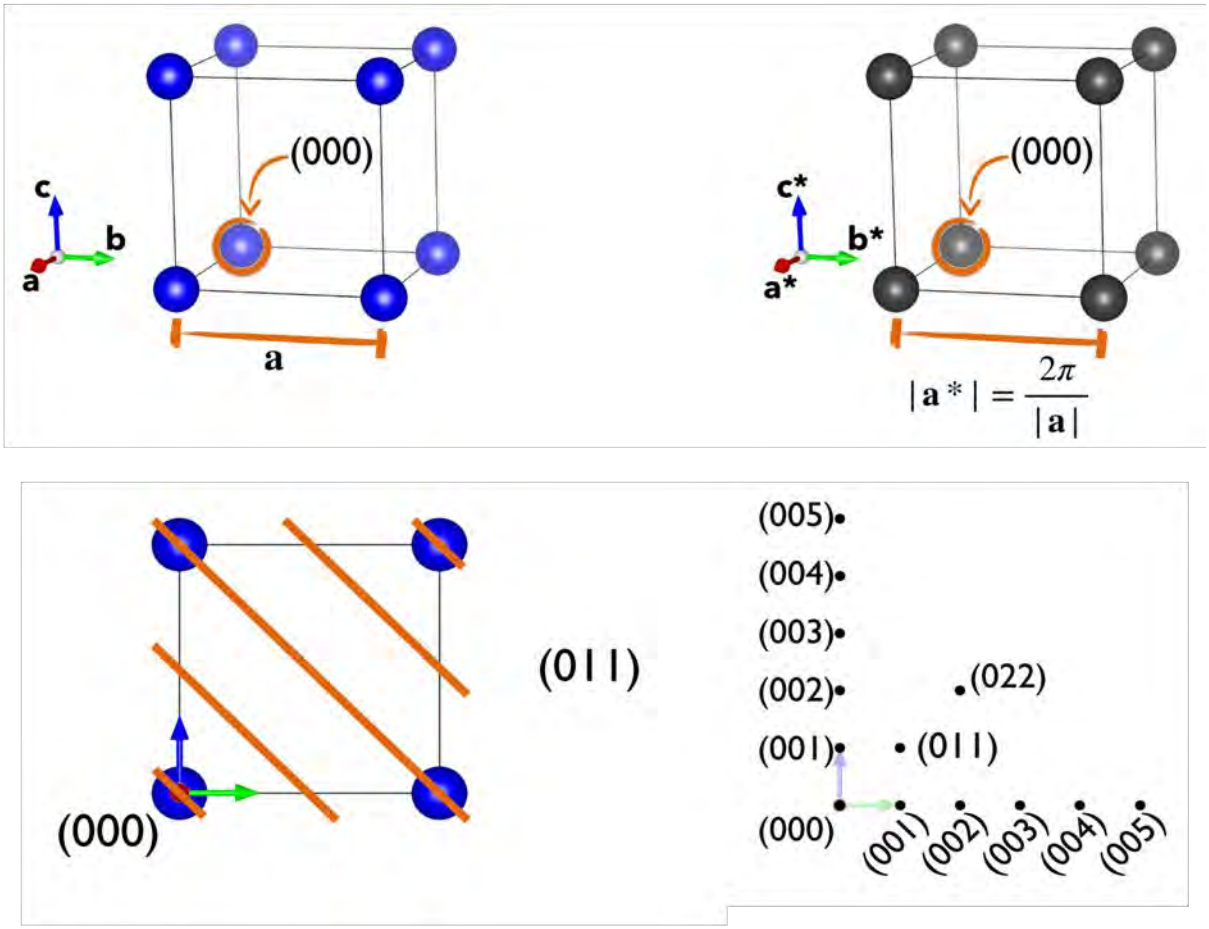

Figure 3.11.: Cubic unit cell and the lattice parameter in real space (top left) and reciprocal space (top right). {011} family of planes in the real space (bottom left) and in the reciprocal space (bottom right). Adapted from Ref. [128].

In a scattering experiment, the intensity distribution is measured as a function of the scattering vector, $\mathbf{Q}$, or scattering angle, 2θ. Using the far-field or Fraunhofer-approximation, the incident and scattered waves are described in terms of plane waves with wavelengths of λ and λ' and propagation direction k and k', respectively. Therefore,

the scattering vector $\mathbf{Q}$ is defined as:

$$\boldsymbol{k}' - \boldsymbol{k} = \Delta\boldsymbol{k} = \boldsymbol{Q}, \tag{3.5}$$

where $\boldsymbol{k}$ and $\boldsymbol{k}'$ are the wave vectors of the incident and scattered waves, respectively, and $\Delta\boldsymbol{k}$ is the reciprocal lattice vector.

For elastic scattering (diffraction) $|\boldsymbol{k}'| = |\boldsymbol{k}|$, there is no change in energy (λ remains the same), only the momentum changes, and consequently the scattering vector is equal to the reciprocal lattice vector [126]. This is the Laue condition for diffraction. The relationship between $\boldsymbol{Q}$ and the crystal structure is crucial, as it defines the conditions for constructive interference based on the reciprocal lattice geometry. The reciprocal lattice vector $\boldsymbol{Q}$ is always perpendicular to the crystal plane represented by the Miller indices (hkl) and the magnitude of this vector is equivalent to the reciprocal of the distance between consecutive planes in the crystal.

The Ewald's sphere is a geometric method in reciprocal space to visualize diffraction conditions. This concept is illustrated in Fig. 3.12. In the Ewald's construction, the incident wave vector, $\boldsymbol{k}$, originates at the (000) point, and the diffracted wave vector, $\boldsymbol{k}'$, terminates at a reciprocal lattice point (hkl). Both vectors lie on an Ewald's sphere, whose radius equals the wave vector's magnitude, $|\boldsymbol{k}| = 2\pi/\lambda$. Diffraction occurs when reciprocal lattice points intersect the sphere. Rotating the crystal in real space rotates the diffraction maxima equivalently in reciprocal space, defining angles θ and 2θ by the magnitude of $\boldsymbol{Q}$ [127]. $\boldsymbol{Q}$ is mathematically expressed by:

$$\boldsymbol{Q} = 2|k|\sin(\theta) = \frac{4\pi\sin\theta}{\lambda}. \tag{3.6}$$

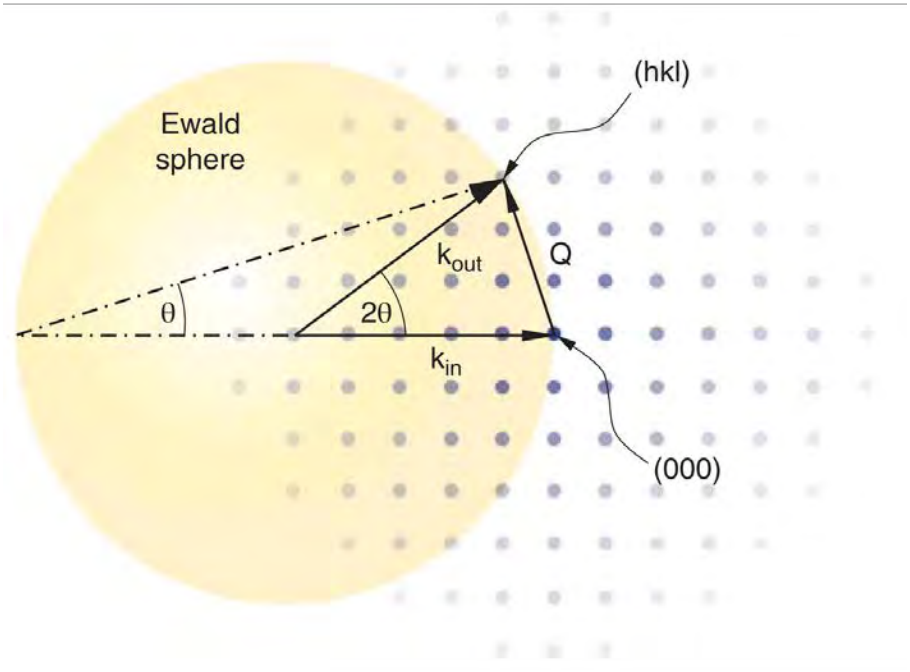

Figure 3.12.: The Ewald construction illustrates the diffraction condition using the incident wave vector $\boldsymbol{k}_{\text{in}}$ ($\boldsymbol{k}$) at the origin (000) and the diffracted wave vector $\boldsymbol{k}_{\text{out}}$ ($\boldsymbol{k}'$) ending at the reciprocal lattice point (hkl), both lying on the Ewald sphere. Taken from Ref. [127].

3.2.2.2. Scattering cross section and basics of diffraction

The term cross section refers to the probability of a scattering interaction between incident particles (such as neutrons, photons, or electrons) and a target material. The cross section has units of area, and represents an effective region within which a scattering process occurs. Larger cross sections correspond to higher interaction probabilities. Cross sections can encompass elastic, inelastic, or total scattering events, providing crucial insights into the structural, electronic, or magnetic characteristics of materials [125, 126].

The scattered intensity (or scattering strength) depends on the cross section (σ) of the scatterer as well as on the experimental setup. Considering an experimental geometry as shown in Fig. 3.13, let us assume that n' particles are scattered per second into the solid angle $d\Omega$ observed by the detector at a scattering angle 2θ, and within the energy range between E' and $E' + dE'$. In this case, the so-called double differential cross section can be defined as:

$$\frac{d^2\sigma}{d\Omega dE'} = \frac{n'}{j d\Omega dE'}, \tag{3.7}$$

where j denotes the incident particle flux, i.e. the number of particles crossing a unit area per unit time [126].

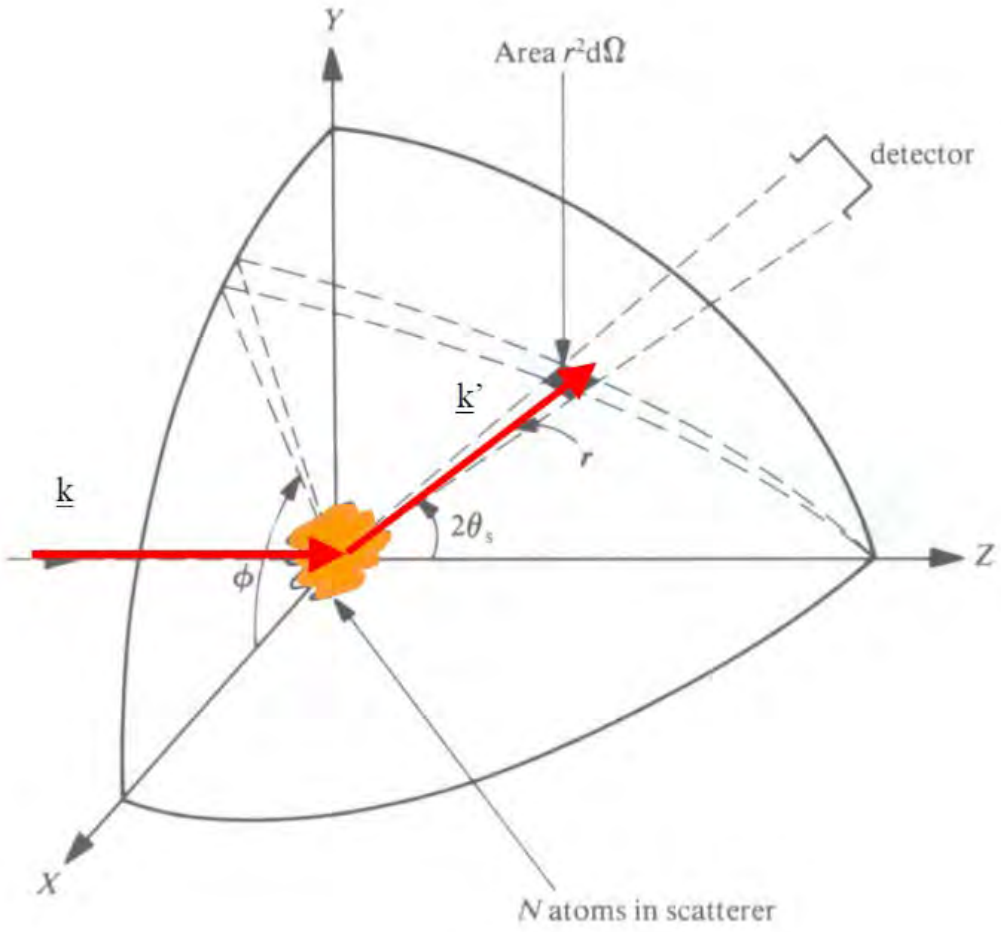

Figure 3.13.: Geometry used for the definition of the scattering cross section and scattering vector **Q**. Taken from Ref. [126].

In the case of elastic scattering, where there is no energy change in the radiation during the scattering process, or when using a detector incapable of resolving energy changes, the angular dependence is described by the differential cross section:

$$\frac{d\sigma}{d\Omega} = \int_0^{\infty} \left(\frac{d^2\sigma}{d\Omega dE'} \right) dE'. \tag{3.8}$$

By integrating the differential cross section over the entire 4π solid angle, we obtain the total scattering cross section σ, which represents the overall probability of scattering events, regardless of energy or angle variations:

$$\sigma = \int_0^{4\pi} \left(\frac{d\sigma}{d\Omega} \right) d\Omega. \tag{3.9}$$

Scattering from more than one scatterer causes interference effects. Waves scattered from different points within the sample travel along different paths, resulting in phase difference at the point of observation, as shown in Fig. 3.14.

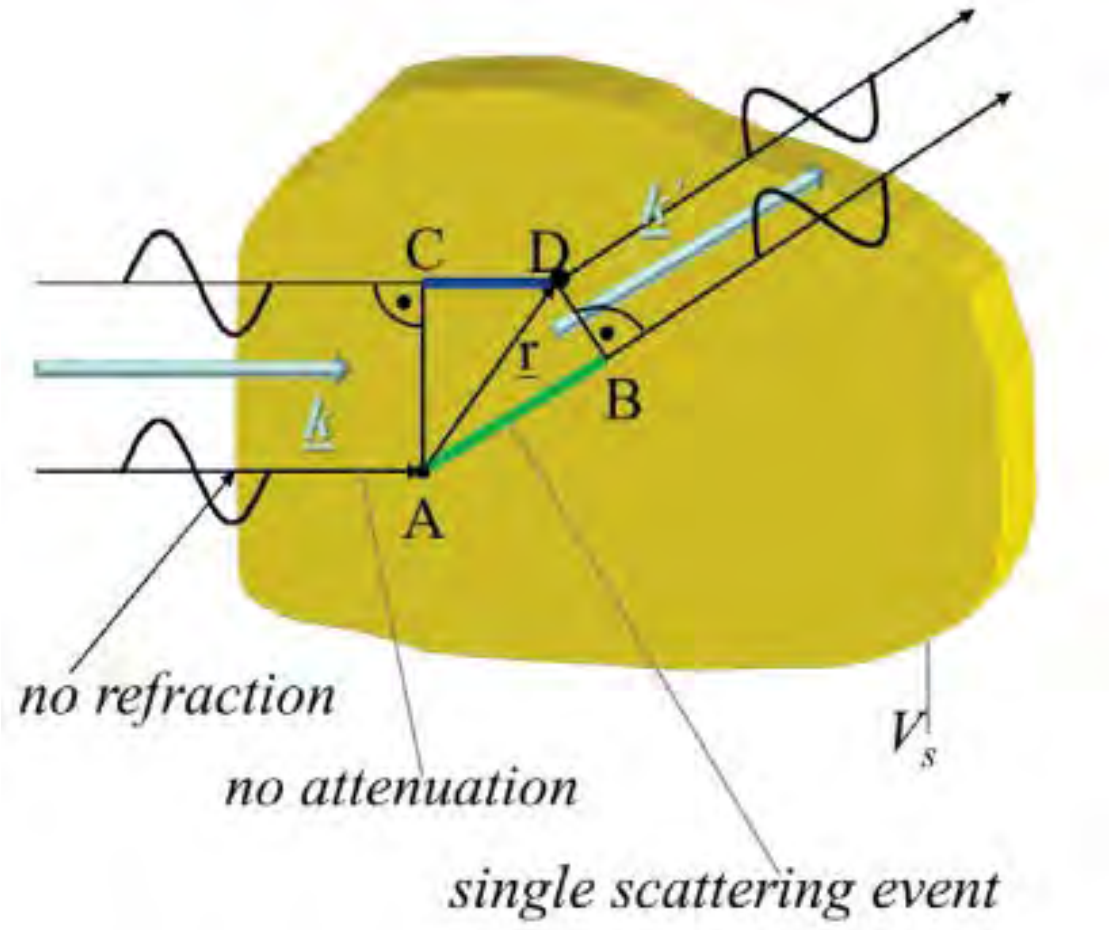

Figure 3.14.: A diagram illustrating the phase difference between a beam scattered at the origin (A) and a beam scattered at position $\boldsymbol{r}$ (D). The yellow shape represents the sample from which incoming waves undergo scattering. Taken from Ref. [126].

The phase difference is given by Eq. 3.10. These phase differences are crucial in determining the interference patterns observed during the scattering process. As a result, the overall scattering amplitude is influenced by the relative phases of the scattered waves, which depend on the relative path differences between waves scattered from different positions in the sample. This phase shift contributes to the interference effects observed in coherent scattering experiments [130].

$$\Delta\Phi = 2\pi \cdot \frac{\overline{AB} - \overline{CD}}{\lambda} = \boldsymbol{k}' \cdot \boldsymbol{r} - \boldsymbol{k} \cdot \boldsymbol{r} = \boldsymbol{Q} \cdot \boldsymbol{r}. \tag{3.10}$$

The contribution to the scattered amplitude from position $\boldsymbol{r}$ is proportional to the local interaction potential $V(\boldsymbol{r})$ between the radiation and the sample. In the case of coherent scattering, where scattered waves interfere, the total scattering amplitude results from the linear sum of the waves scattered from all points within the sample volume V_s, and this is mathematically represented by the integral:

$$A(\boldsymbol{Q}) \propto \int_{V_s} V(\boldsymbol{r}) e^{i\boldsymbol{Q}\cdot\boldsymbol{r}} d^3r. \tag{3.11}$$

The equation above demonstrates that the scattering amplitude is directly related to the interaction potential, $V(\boldsymbol{r})$, which, depending on the probe, is proportional to the relevant scattering density $\rho(\boldsymbol{r})$, by means of Fourier transform. Therefore, scattering can be regarded as a probe of reciprocal space, through its dependence on $\boldsymbol{Q}$.

Accordingly, the scattered intensity is given by the squared modulus of the scattered amplitude,

$$I(\boldsymbol{Q}) \propto |A(\boldsymbol{Q})|^2 \propto \left| \int_{V_s} V(\boldsymbol{r}) e^{i\boldsymbol{Q}\cdot\boldsymbol{r}} d^3r \right|^2, \tag{3.12}$$

where $V(\boldsymbol{r})$ is the interaction potential and $\boldsymbol{Q}$ is the scattering vector.

Usually, only the scattered intensity, $I(\boldsymbol{Q})$, is measured in a diffraction experiment, while the phase of the complex scattering amplitude is lost. This is the so-called phase problem. This problem refers to the challenge of determining the phase information of all diffracted waves, which is essential for reconstructing the object being studied. This missing phase data makes it difficult to accurately determine the atomic or molecular structure of the sample, but several techniques can be used to overcome this issue [126, 130].

For a periodic crystal, the scattering density can be decomposed into a periodic repetition of unit cells, allowing the scattered amplitude to be factorized into a lattice sum and a unit-cell contribution. Thus, the total scattered amplitude can be written as:

$$A(\boldsymbol{Q}) \propto F_{\text{u.c.}}(\boldsymbol{Q}) \sum_{\boldsymbol{T}} e^{i\boldsymbol{Q}\cdot\boldsymbol{T}}, \tag{3.13}$$

so that the scattered intensity becomes:

$$I(\boldsymbol{Q}) \propto \left| F_{\text{u.c.}}(\boldsymbol{Q}) \sum_{\boldsymbol{T}} e^{i\boldsymbol{Q}\cdot\boldsymbol{T}} \right|^2, \tag{3.14}$$

where $\boldsymbol{T}$ denotes the lattice vectors pointing to the illuminated unit cells within the sample.

Here, $F_{\text{u.c.}}(\boldsymbol{Q})$ is the unit-cell structure factor, which in a more complete formulation is written as:

$$F_{\text{u.c.}}(\boldsymbol{Q}) = \sum_{i \in \text{u.c.}} o_i f_i(\boldsymbol{Q}, E) e^{-W_i(\boldsymbol{Q},\tau)} e^{i\boldsymbol{Q}\cdot\boldsymbol{r}_i}, \tag{3.15}$$

where the sum runs over all atoms i within the unit cell, o_i is the site occupancy, $f_i(\boldsymbol{Q}, E)$ is the atomic scattering factor, $e^{-W_i(\boldsymbol{Q},\tau)}$ is the Debye–Waller factor accounting for thermal atomic displacements with τ representing the temperature, and $\boldsymbol{r}_i$ is the atomic position within the unit cell. For X-rays, f_i may also depend on the photon energy when the incident photon energy approaches an absorption edge of the element, owing to anomalous-dispersion corrections.

The lattice sum in Eq. 3.13 gives rise to sharp maxima when the scattering vector satisfies the Laue condition, $\boldsymbol{Q} = \boldsymbol{G}$, where $\boldsymbol{G}$ is a reciprocal-lattice vector. This condition is equivalent to the Bragg condition and expresses the requirement for constructive interference from the periodic lattice. In an ideal infinite crystal within the kinematic approximation, the diffraction pattern therefore consists of discrete reciprocal-lattice points weighted by the corresponding structure factor.

In real crystals, however, the measured diffraction intensity is modified by several additional effects. First, the finite size and shape of the diffracting volume broaden the reciprocal-space maxima and give rise to finite-thickness oscillations or Scherrer-like broadening. Second, strain and structural disorder introduce an additional distribution of lattice spacings, leading to peak broadening and, in some cases, asymmetric peak profiles. Third, absorption reduces the detected intensity through attenuation of the incident and diffracted beams inside the sample. Fourth, extinction and multiple scattering effects may become relevant in sufficiently perfect or thick crystals, such that the measured intensity deviates from the purely kinematic $|F|^2$ behavior. In addition, mosaic spread leads to an angular distribution of slightly misoriented crystallites or blocks, while the instrumental resolution introduces an additional convolution of the intrinsic scattering profile.

Accordingly, the experimentally observed diffraction profile may be expressed in a schematic form as:

$$I_{\text{obs}}(\boldsymbol{Q}) = \left[I_{\text{kin/dyn}}(\boldsymbol{Q}) A_{\text{abs}}(\boldsymbol{Q}) y_{\text{ext}}(\boldsymbol{Q}) \right] \otimes R(\boldsymbol{Q}) \otimes M(\boldsymbol{Q}) + B(\boldsymbol{Q}), \tag{3.16}$$

where $I_{\text{kin/dyn}}$ denotes the intrinsic scattering intensity within either a kinematic or dynamical description, A_{abs} is an absorption correction, y_{ext} accounts for extinction effects, $R(\boldsymbol{Q})$ is the instrumental resolution function, $M(\boldsymbol{Q})$ describes broadening associated with mosaic spread, and $B(\boldsymbol{Q})$ represents background contributions. Finite-size and strain broadening are typically included in the intrinsic profile $I_{\text{kin/dyn}}$.

In the present work, these expressions are introduced to provide the general crystallographic framework connecting the real-space structure of the sample to the measured scattering signal. However, the main focus of this thesis is not the full refinement of bulk diffraction data, but rather the structural and interfacial characterization of epitaxial thin films and heterostructures, particularly by X-ray and neutron reflectivity. Therefore, unless explicitly stated otherwise, the discussion below adopts the kinematic and ideal periodic approximation as a physically transparent starting point.

3.2.2.3. Atomic scattering factors for X-ray and neutron scattering

The atomic scattering factor, denoted as f_i, quantifies the magnitude of the scattering amplitude for an isolated atom. The atomic scattering factors (also called atomic form

factor) differ from the probe used in the scattering experiment, given their fundamental differences in the scattering process and it is unique to each element. For X-ray, neutron nuclear and magnetic scattering, f_i corresponds to the atomic form factor (f_0), neutron scattering length density (b), and magnetic form factor (f_m), respectively. These values depend on the scattering vector, $\boldsymbol{Q}$, or scattering angle, 2θ, as depicted in Fig. 3.15 [131].

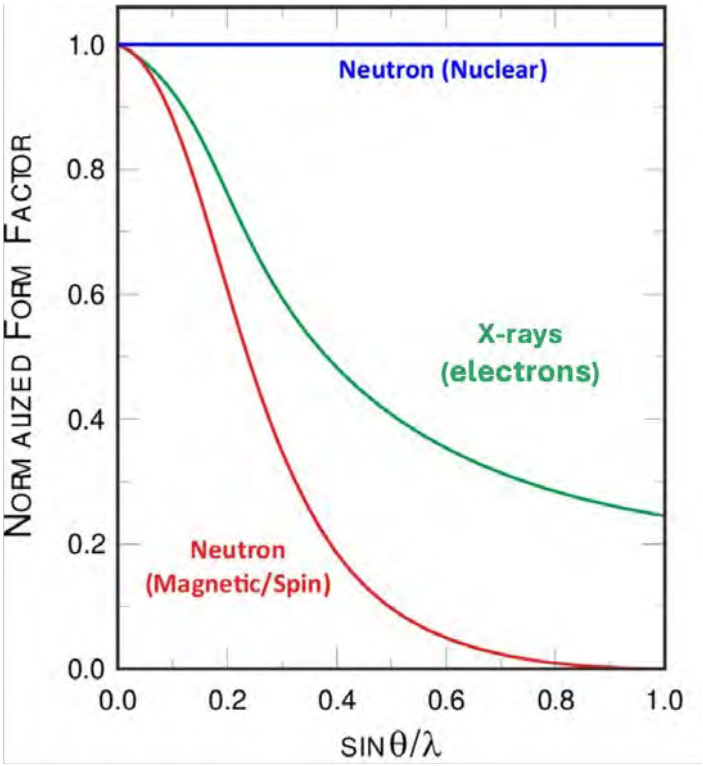

Figure 3.15.: Diagram illustrating the normalized form factors for X-rays, nuclear neutron scattering, and magnetic/spin neutron scattering, plotted as a function of $\sin\theta/\lambda$. Taken from Ref. [132].

X-rays

For X-rays, electrons play a fundamental role as the scattering particles in a sample. A neutral atom, with Z electrons, scatters X-rays across the volume occupied by its electron cloud rather than acting as a point source. Evaluating the scattering amplitude equation for a single atom yields the atomic form factor $f_0(Q)$, representing the atom's scattering strength as a function of scattering vector (or scattering angle). At $Q \to 0$, all volume elements scatter in phase, and f_i equals the atomic form factor (or form factor) $f_0(Q)$, the total electron count of the atom [127, 131].

It is generally assumed that an atom's electron density is spherically symmetric, so the atomic form factor $f_0(Q)$ depends only on the magnitude of $\boldsymbol{Q}$, not its orientation relative to the atom. However, this approximation may break down for materials with covalent bonding and orbital hybridization, where electron density deviates from perfect spherical symmetry [127]. Values for $f_0(Q)$ are available in the International Tables for Crystallography or can be calculated using the following expression:

$$f_0(Q) = \int \rho_e(\boldsymbol{r}) e^{i\boldsymbol{Q}\cdot\boldsymbol{r}} d\boldsymbol{r}, \tag{3.17}$$

in which $\rho_e(\boldsymbol{r})$ is the atom electronic density.

As illustrated in Fig. 3.15, the atomic form factor f_0 decreases with increasing scattering angle (an expression for f_0 as a function of the scattering angle can be found in Ref. [127]). Additionally, f_0 increases with the atomic number Z, as it is proportional to the number of electrons in an atom. This creates challenges in X-ray scattering experiments involving light elements with similar Z or samples containing both heavy and light elements. In such cases, light elements are more difficult to detect due to their lower scattering contribution relative to heavy elements. The magnetic form factor for X-rays is significantly smaller compared to the electron charge form factor, making it challenging to extract magnetic information from standard X-ray diffraction experiments. However, advances in synchrotron radiation sources, particularly high-flux and high-brilliance of 3rd and 4th generation synchrotrons, have enabled the successful application of X-ray (resonant) magnetic scattering techniques. These advancements allow researchers to determine also the magnetic structure of materials with greater precision, opening new possibilities for studying magnetic materials with X-rays.

Neutrons

Neutrons are a versatile probe for studying the fundamental properties of matter due to their unique characteristics. Their neutral charge allows deep penetration into materials, making them ideal for bulk property analysis, unlike other particles or even X-rays, which are limited to electronic density distributions. Neutrons interact via strong nuclear forces, enabling sensitivity to both heavy and light atoms, such as hydrogen. Moreover, their intrinsic spin and magnetic moment make them exceptionally suitable for probing magnetism, revealing details about spin arrangements, magnetic moments, and coupling in various materials. In neutron scattering, two primary interactions are observed: nuclear scattering, resulting from the strong interaction between neutrons and atomic nuclei, and magnetic scattering, arising from the magnetic dipole-dipole interaction between the neutron's magnetic moment and the spin or orbital moments of unpaired electrons in the material. Nuclear and magnetic scattering have different scattering factors [133].

The nuclear scattering can be approximated considering the interaction between a neutron and a nucleus using a delta function potential, which assumes the scattering occurs over an extremely small range (the so-called Fermi-pseudo-potential approximation). In this picture, the interaction potential presented in Eq. 3.11 now takes the following form:

$$V(\boldsymbol{r}, \boldsymbol{r}_j) = \frac{2\pi\hbar^2}{m_n}[b_j\delta(\boldsymbol{r} - \boldsymbol{r}_j)], \tag{3.18}$$

where $\boldsymbol{r}$ is the neutron coordinate, $\boldsymbol{r}_j$ is the coordinate of the nucleus, m_n is the mass of the neutron and b_j is the neutron scattering length (density), a phenomenological parameter as measure of the strength of the interaction potential.

Considering that the nucleus can be described as a point-like object given the wavelength of thermal neutrons (see Fig. 3.7), the nuclear neutron scattering is isotropic and independent of the scattering vector or scattering angle. This explains the straight line of nuclear scattering shown in Fig. 3.15. In this sense, the differential cross section and cross section for the nuclear scattering are given by:

$$\frac{d\sigma}{d\Omega} = |b^2| \implies \sigma = 4\pi b^2. \tag{3.19}$$

The value of b depends not only on the atomic number but also on the isotope and the relative orientation of the nuclear spin to the neutron spin [133]. Isotopes may vary

significantly in natural abundance, and the nuclear spin tends to align randomly unless influenced by an external magnetic field. Since b differs for each isotope, it leads to both coherent and incoherent scattering [131]. In neutron scattering experiments involving isotopes, the coherent and incoherent contributions to the cross-section must be averaged, as outlined below [134]:

$$\left.\frac{d\sigma}{d\Omega}\right|_{\text{nuclear}} = \langle b\rangle^2 \left|\sum_r e^{i\boldsymbol{Q}\cdot\boldsymbol{r}}\right|^2 + N\left\langle (b-\langle b\rangle)^2\right\rangle. \tag{3.20}$$

The first term in the equation 3.20 represents the coherent scattering contribution, incorporating phase information and therefore gives rise to interference effects. The second term corresponds to incoherent scattering, which includes the mean square scattering length for all N atoms but lacks phase information. This leads to an additive effect on the scattered neutrons, resulting in an isotropic background that is proportional to the number of atoms (N), appearing uniformly across the measured scattering vector/angle range [133, 134]. For this reason, the incoherent scattering contribution is not often considered during neutron scattering experiments and the nuclear cross section can be approximated using only the coherent scattering part.

Neutrons can also be scattered by the magnetic moments of unpaired electrons, a process known as magnetic neutron scattering. This interaction arises from the magnetic dipole-dipole potential between the neutron's magnetic dipole moment ($\boldsymbol{V}_m$) and the magnetic field of the unpaired electrons ($\boldsymbol{B}$). The magnetic field $\boldsymbol{B}$ is composed of contributions from spin ($\boldsymbol{B}_{\text{spin}}$) and orbital ($\boldsymbol{B}_{\text{orbital}}$) components. The interaction potential, $\boldsymbol{V}_m$, can be mathematically described as [134]:

$$\boldsymbol{V}_m = -\boldsymbol{\mu}_n \cdot \boldsymbol{B}, \quad \boldsymbol{\mu}_n = -(\gamma_n \mu_N \boldsymbol{\sigma}), \tag{3.21}$$

where $\boldsymbol{\mu}_n$ is the magnetic moment of the neutron, γ_n is the gyromagnetic ratio of neutron, $\boldsymbol{\sigma}$ is the neutron spin operator and μ_N is the nuclear magneton [134].

The magnetic scattering cross-section for a process in which a neutron changes its wave vector from $\boldsymbol{k}$ to $\boldsymbol{k'}$ and its spin projection along a quantization axis z from σ_z to σ_z' can be described using the first Born approximation. This formalism considers the interaction potential between the neutron's magnetic moment and the magnetic field of the sample, and the resulting cross-section is derived by evaluating the overlap of the initial and final neutron states while accounting for the scattering potential [134]. Thus magnetic scattering cross-section assumes the form below:

$$\left.\frac{d\sigma}{d\Omega}\right|_{\text{mag.}} = \left(\frac{m_n}{2\pi\hbar^2}\right)^2 |\langle \boldsymbol{k}'\sigma_z'|\boldsymbol{V}_m|\boldsymbol{k}\sigma_z\rangle|^2. \tag{3.22}$$

In magnetic neutron scattering, the neutron beam does not probe only a magnetic moment localized at a single point of the crystal, but rather the real-space distribution of the sample magnetization vector $\mathbf{M}(\mathbf{r})$. Accordingly, the magnetic scattering amplitude is determined by the Fourier transform of this magnetization distribution,

$$\mathbf{M}(\mathbf{Q}) = \int \mathbf{M}(\mathbf{r})\, e^{i\mathbf{Q}\cdot\mathbf{r}} d^3r, \tag{3.23}$$

where $\mathbf{r}$ is the real-space position vector and $\mathbf{Q}$ is the scattering vector. Thus, magnetic

neutron scattering probes the spatial Fourier components of the sample magnetization selected by the experimental scattering geometry.

Moreover, magnetic neutron scattering is sensitive only to the component of the magnetization perpendicular to the scattering vector $\mathbf{Q}$, since the magnetic interaction is transverse with respect to $\mathbf{Q}$. In practical terms, if the magnetization is parallel to $\mathbf{Q}$, it does not contribute to the magnetic scattering signal, whereas a magnetization component perpendicular to $\mathbf{Q}$ contributes maximally, as shown in the Fig. 3.16. Therefore, the relevant quantity is the transverse magnetization $\mathbf{M}_\perp(\mathbf{Q})$, defined as:

$$\mathbf{M}_\perp(\mathbf{Q}) = \mathbf{M}(\mathbf{Q}) - \left[\mathbf{M}(\mathbf{Q}) \cdot \hat{\mathbf{Q}}\right] \hat{\mathbf{Q}}, \tag{3.24}$$

where $\hat{\mathbf{Q}}$ is the unit vector along $\mathbf{Q}$.

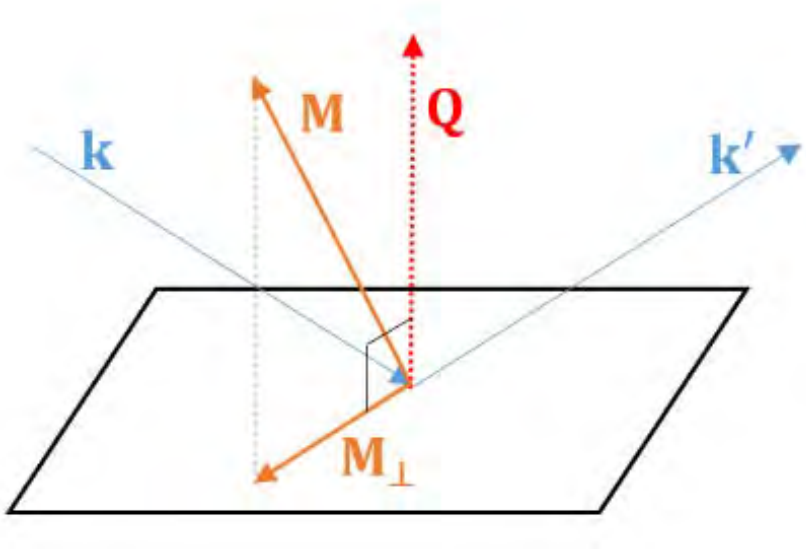

Figure 3.16.: Illustration of magnetic scattering, where only the magnetization component perpendicular to the scattering vector, $\boldsymbol{Q}$, contributes to the magnetic scattering signal. The vector $\mathbf{M}_\perp$ corresponds to the projection of the magnetization $\mathbf{M}$ onto the plane perpendicular to $\mathbf{Q}$. Taken from Ref. [131].

In other words, Eq. 3.24 removes the component of $\mathbf{M}(\mathbf{Q})$ parallel to $\mathbf{Q}$, retaining only the part that contributes to the magnetic scattering signal. With this definition, the magnetic scattering cross section in Eq. 3.22 can be simplified by considering the elastic-scattering case only. Substituting the interaction potential from Eq. 3.21 into Eq. 3.22, one obtains:

$$\left.\frac{d\sigma}{d\Omega}\right|_{\text{mag.}} = (\gamma_n r_0)^2 \left| \frac{-1}{2\mu_B} \langle \sigma_z' | \boldsymbol{\sigma} \cdot \boldsymbol{M}_\perp(\boldsymbol{Q}) | \sigma_z \rangle \right|^2, \tag{3.25}$$

where the factor $\gamma_n r_0$ is a constant and $\boldsymbol{M}_\perp(\boldsymbol{Q})$ denotes the component of the Fourier-transformed sample magnetization $\mathbf{M}(\mathbf{r})$ that is perpendicular to the scattering vector $\mathbf{Q}$.

To relate the general reciprocal-space magnetization $\mathbf{M}(\mathbf{Q})$ to the microscopic magnetic structure of the crystal, it is convenient to express it as a sum over the atomic magnetic moments. For many transition-metal systems with partially filled d shells, the orbital

contribution is often largely quenched by the crystal field, so that the electron spin provides the dominant contribution to magnetic neutron scattering. In this case, the reciprocal-space magnetization can be written as:

$$\boldsymbol{M}(\boldsymbol{Q}) = -2\mu_B f_m(\boldsymbol{Q}) \sum_j e^{i\boldsymbol{Q}\cdot\boldsymbol{R}_j} \boldsymbol{S}_j, \tag{3.26}$$

where $\mathbf{R}_j$ is the position vector of the j-th atom, $\mathbf{S}_j$ is its spin contribution, and $f_m(\mathbf{Q})$ is the magnetic form factor. Unlike nuclear scattering, magnetic neutron scattering arises from the interaction of the neutron magnetic moment with the spatial distribution of magnetization associated with the electronic cloud. Therefore, the magnetic form factor plays a role analogous to the atomic form factor in X-ray scattering, by accounting for the spatial distribution of the spin density. In the present case, it can be defined in terms of the spin density $\rho_{\text{spin}}(\mathbf{r})$ as:

$$f_m(\boldsymbol{Q}) = \int_{Atom} \rho_{\text{spin}}(\boldsymbol{r}) e^{i\boldsymbol{Q}\cdot\boldsymbol{r}} d^3r. \tag{3.27}$$

Consequently, the magnetic differential cross section can be simplified by taking into account only the expectation value of the spin component perpendicular to the scattering vector, $\boldsymbol{S}_\perp$, yielding:

$$\left.\frac{d\sigma}{d\Omega}\right|_{\text{mag.}} = (\gamma_n r_0)^2 \left| f_m(\boldsymbol{Q}) \sum_j \langle S_{j\perp} \rangle e^{i\boldsymbol{Q}\cdot\boldsymbol{R}_j} \right|^2. \tag{3.28}$$

Magnetic neutron scattering arises from unpaired electrons in partially filled shells, in contrast to X-ray scattering, which probes the overall electron density. Consequently, the magnetic form factor decreases much more rapidly with increasing scattering angle (or Q) than the X-ray atomic form factor [134], as illustrated in Fig. 3.15. In elastic neutron scattering, the nuclear and magnetic contributions are present simultaneously and add coherently at the amplitude level. Therefore, the total scattered neutron intensity is determined by the combination of the nuclear scattering amplitude $N(\mathbf{Q})$ and the magnetic scattering amplitude $\boldsymbol{\sigma} \cdot \mathbf{M}_\perp(\mathbf{Q})$. Accordingly, the differential cross section for elastic neutron scattering can be written as [131]:

$$\left.\frac{d\sigma}{d\Omega}\right|_{\text{neutron}} = |N(\boldsymbol{Q}) + \boldsymbol{\sigma} \cdot \boldsymbol{M}_\perp(\boldsymbol{Q})|^2, \tag{3.29}$$

where $\boldsymbol{\sigma}$ is the neutron spin operator.

3.2.2.4. X-ray scattering techniques

In the context of thin films, high-resolution X-ray diffraction and X-ray reflectivity are of great importance. While the former encompasses measurements in which the movement of the scattering vector $\boldsymbol{Q}$ is accurately measured and provides information about the thin film growth (epitaxial or polycrystalline growth) and its crystal structure, including the size of the lattice parameters, their alignment with the substrate and possible elastic deformations (strain), the second is based on the variation of the scattering length density (electronic density) of the thin film layers as a function of depth and is sensitive to the

thickness and interlayer roughness of the film.

High-resolution X-ray diffraction and X-ray reflectivity measurements were carried out at the Peter Grünberg Institute for Semiconductor Electronics (PGI-9) using a Rigaku SmartLab X-ray diffractometer. The measurements were carried out by Dr. Omar Concepcion using a measurement flow/sequence prepared by Dr. Christoph Ringkamp.

High resolution X-ray diffraction

For a given film/substrate system where the film grows epitaxially, the film's single-crystal structure is generally expected to match that of the substrate. In this case, the diffraction pattern will exhibit contributions from both the substrate and the film. Depending on their lattice parameters and interplanar distances, the resulting Bragg peaks may be very close. The precision required to study epitaxial layers is achieved using the differential form of Bragg's law:

$$\frac{\Delta d_{hkl}}{d_{hkl}} = \frac{\Delta\lambda}{\lambda} + \frac{\Delta\theta}{\theta}, \tag{3.30}$$

emphasizing the need for monochromatic and low-divergence X-ray beams [135].

Such precision is present in the high-resolution X-ray scattering, considering its triple-axis geometry. In this geometry, the X-ray beam is scattered three times: once in the monochromator, once in the sample, and finally in the analyzer crystal after the sample. The triple-axis geometry is illustrated in the Fig. 3.17. Therefore, high-resolution X-ray diffraction serves as a natural alternative to techniques using double-crystal geometry (monochromator and sample), which often lack the resolution required to detect subtle structural changes in single crystals under analysis [136].

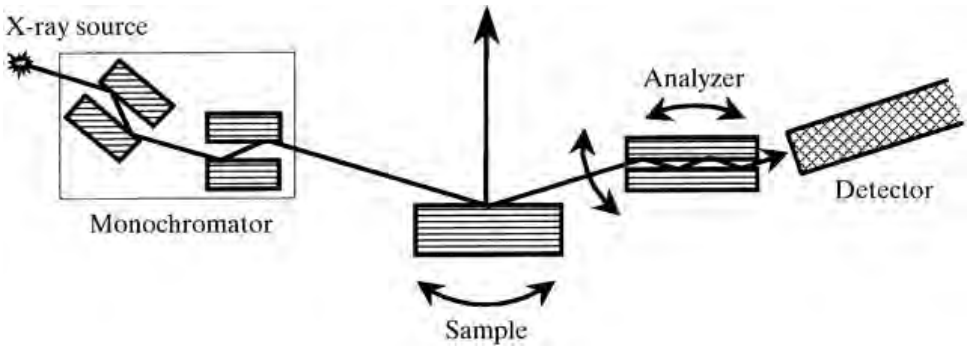

Figure 3.17.: Schematic illustration of the triple-axis X-ray diffraction geometry. Taken from Ref. [137].

X-ray diffraction serves as a tool to translate movements in real space (laboratory frame) into measurements in reciprocal space, enabling indirect detection of structural changes through modifications in the reciprocal lattice. The relationship between real and reciprocal space is expressed by Eq. 3.4. The scattering vector $\boldsymbol{Q}$ can be determined solely by the angular positions ω and 2θ. By defining the perpendicular and parallel directions of the thin film as Q_z and $Q_{x,y}$, respectively, the following expressions can be derived:

$$Q_z = \frac{1}{\lambda}\left[\cos\omega - \cos(2\theta - \omega)\right] \quad \text{and} \tag{3.31}$$

$$Q_{x,y} = \frac{1}{\lambda}\left[\sin\omega - \sin(2\theta - \omega)\right], \tag{3.32}$$

where $|\boldsymbol{Q}| = \sqrt{Q_z^2 + Q_{x,y}^2}$ and therefore the degrees of freedom in the diffraction plane are represented by the angles ω and 2θ [129, 136].

The movement of $\boldsymbol{Q}$ in reciprocal space associated with these angles can be described as follows [136]:

- **Rocking curve (ω):** consists of aligning the detector to a specific family of planes (hkl) so that Bragg's Law is satisfied. Once aligned, the detector remains fixed while ω is varied. In reciprocal space, the motion of a rocking curve corresponds to a circular trajectory around the origin within the diffraction plane. Since it does not involve the detector position (i.e., 2θ), the magnitude of the scattering vector remains constant throughout the motion.

- **2θ scan (detector scan):** Describes a circular motion with a radius of $1/\lambda$ around the origin of the $\boldsymbol{k}$ vector. It changes the magnitude of the scattering vector according to the equation Eq. 3.6.

However, these types of scans do not provide information about the parallel or perpendicular directions of the thin film (i.e. in-plane and out-of-plane lattice parameters). Therefore, other types of reciprocal space scans, which are linearly dependent on ω and 2θ, are often used to better describe the characteristics of both the thin film and the substrate. These include:

- **$\omega/2\theta$ scan:** in this type of measurement, an X-ray beam is incident at an angle ω relative to the surface of the sample, and the detector is positioned at an angle 2θ relative to the incident beam. The scan is performed by incrementing 2θ at twice the rate of the increment in ω, which corresponds to simultaneously moving the detector and the source (or sample in synchrotrons) while maintaining the angular velocity of the detector at twice the angular velocity of the source (or sample in synchrotrons). When $\omega = \theta$, the scan is referred to as symmetric, and only crystal planes parallel to the sample surface, with reciprocal lattice points along the normal, will be investigated. This scan occurs along the Q_z direction and provides information about the lattice parameter perpendicular to the sample plane (out-of-plane), as well as information about the epitaxial layer–substrate relationship. When $\omega \neq \theta$, the scan is called asymmetric, and the scattering vector is tilted with respect to the normal of the sample surface. In this case, there is an offset between ω and the Bragg angle. This type of scan provides information about both in-plane and out-of-plane lattice parameters.

- **Q-scan:** a type of measurement in reciprocal space along a chosen Q-direction. Unlike a strictly symmetric $\omega/2\theta$ scan, its angular motion is adjusted to probe a selected trajectory in reciprocal space. Such scans are particularly useful for thin films, since they provide information on the reciprocal-space profile of a reflection, including peak broadening, strain, and finite coherent thickness.

- **Reciprocal space mapping (RSM):** a type of measurement that involves multiple $\omega - 2\theta$ scans, where only the magnitude of $\boldsymbol{Q}$ changes, for different ω values, modifying the direction and orientation of the scattering vector. This process maps a region around a reciprocal lattice point (hkl) by converting angular coordinates

$(\omega - 2\theta)$ into reciprocal space coordinates $(Q_{x,y}, Q_z)$ using equations 3.32 and 3.31. RSM provides insights into finite-size effects and defects in the crystalline structure, particularly in epitaxial layers.

- **Phi-scan:** in this type of measurement, the sample is rotated around its surface normal (ϕ) while keeping the X-ray beam and detector aligned to a fixed reciprocal lattice point. This scan probes the in-plane rotational symmetry of the crystal lattice, providing information about grain orientation, epitaxial alignment, and crystal twinning. Phi-scans are particularly useful for characterizing azimuthal relationships between the epitaxial film and the substrate.

An illustration of all the above described scans in the reciprocal space is shown in Fig. 3.18.

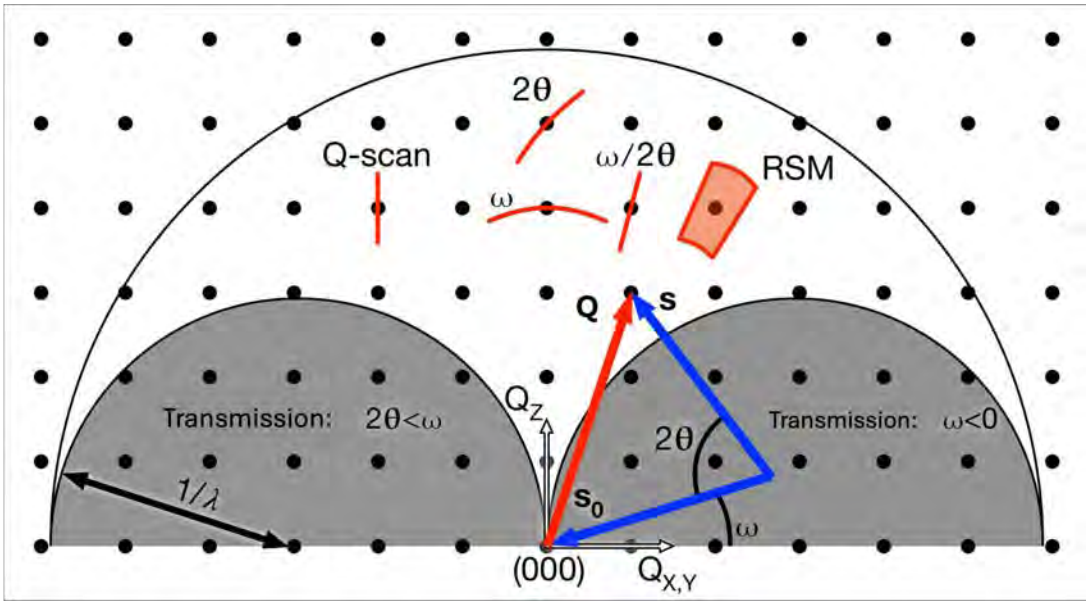

Figure 3.18.: Direction of different measurement types in reciprocal space. $\boldsymbol{S}_0$ and $\boldsymbol{S}$ are the incident and scattered wave vectors (similar to $\boldsymbol{k}$ and $\boldsymbol{k'}$). The reflections inaccessible by the reflection technique are located in the darker regions of reciprocal space. Adapted from Ref. [136].

In this work, $\omega/2\theta$ scans and reciprocal space maps were performed to obtain the information about the sample's crystal structure quality, their crystalline thickness (obtained from the fit of the Laue oscillations) and epitaxial growth. The Cu-Kα radiation (λ = 1.5406 Å) and a HyPix-3000 high-energy-resolution 2D multidimensional semiconductor detector were used. All the samples prepared were aligned using the STO (002) Bragg peak for the measurements of $\omega/2\theta$ scans. The epitaxial growth and in-plane alignment of crystalline grains or domains of the SRO thin film were verified through a ϕ-scan. In this experiment, the detector was fixed at the asymmetric (103) reflection of the SRO/STO while the polar angle of 18.4° (the angle between the [001] and [103] directions in a cubic crystal lattice) was added to the incident beam (source arm). This way the sample can remain flat in the quartz plate mounted in the goniometer. After that, the sample was rotated around the azimuthal angle ϕ. The in-plane elastic strain was studied through reciprocal space mapping around the (103) reflection of the SRO/STO. YBCO/SRO and SRO/YBCO were characterized only by means of $\omega/2\theta$ scans.

X-ray reflectivity

X-ray reflectivity (XRR) is a non-destructive technique used to analyze the surface and near-surface structures of materials, particularly thin films and multilayers. In an XRR measurement, the X-ray beam strikes a thin film or multilayer sample at low angles (0-5°) and the intensity of the scattered X-rays is measured as a function of scattering vector (or angle). The scattering vector (angle) remains in the specular condition, meaning that this technique is sensitive only to the depth of the material, and no lateral (in-plane) information can be obtained. In thin films and multilayers, the X-ray is reflected at interfaces, with total or partial reflection occurring at boundaries between materials with different refraction indices. Constructive interference of the scattered X-rays leads to an oscillatory pattern in the reflected intensity. This pattern, resulting from the modulation of electron density in thin-layer structures, provides information on layer thickness and surface roughness.

Heinz Kiessig was one of the first to observe the interference patterns, known as Kiessig fringes, in X-ray reflectivity measurements of thin nickel films on glass substrates [138, 139], from where he could obtain the film thickness. The theoretical understanding of the technique was later on advanced by Lyman G. Parratt, which developed a formalism for applying and calculating the reflectivity of multilayer structures, allowing one to obtain the electronic density profile of the superficial layers. His contributions established a systematic method for interpreting XRR data, enabling the analysis of more complex layered systems [140]. The technique was not strongly used until the 1990s, when methods were developed to account for surface roughness, interfacial roughness, and interdiffusion in analytical procedures. From that point onward, XRR gained significantly more attention as a powerful tool for morphological characterization of surfaces and thin films. However, its application is limited to relatively smooth and flat surfaces, as roughness on the order of tens of nanometers attenuates the X-ray beam and no information can be obtained [141]. An example of a XRR pattern and the information provided by an XRR profile is shown in Fig. 3.19.

The periodicity of the modulation in the reflected intensity as a function of the scattering angle is directly related to the thickness of the film layer. The position of the critical angle (up to which total external reflection of the incident radiation occurs) corresponds to the surface density. Additionally, the amplitude of the modulation and the decay of reflected intensity are associated with the roughness and quality of the film's interfaces and layers. The reflectivity of a perfect interface is proportional to the difference in electron densities between the layer constituents, but it decreases due to disorder caused by interdiffusion or roughness at the interfaces [141, 142].

The thickness of a given layer can be determined from the reflectivity pattern using the following expression:

$$Q = \left(\frac{2\pi}{d}\right) n, \tag{3.33}$$

which is derived by applying Eq. 3.3 to Eq. 3.6, with n being the indice of each Kiessig fringe in XRR pattern. However, this approach is only carried out to get a slight idea of the thickness of the sample.

A more comprehensive analysis of reflectivity curves can be achieved through simulation and fitting procedures based on structural models. These simulations typically adopt a block-like model, which represents the sample as a series of layers on a substrate. Each layer is characterized by its scattering length density (SLD) (or electronic density, ρ, in the case of X-rays), thickness (t), and the roughness or interdiffusion at the interfaces.

The SLD defines the scattering contrast between adjacent layers and is proportional to the electronic density of the material.

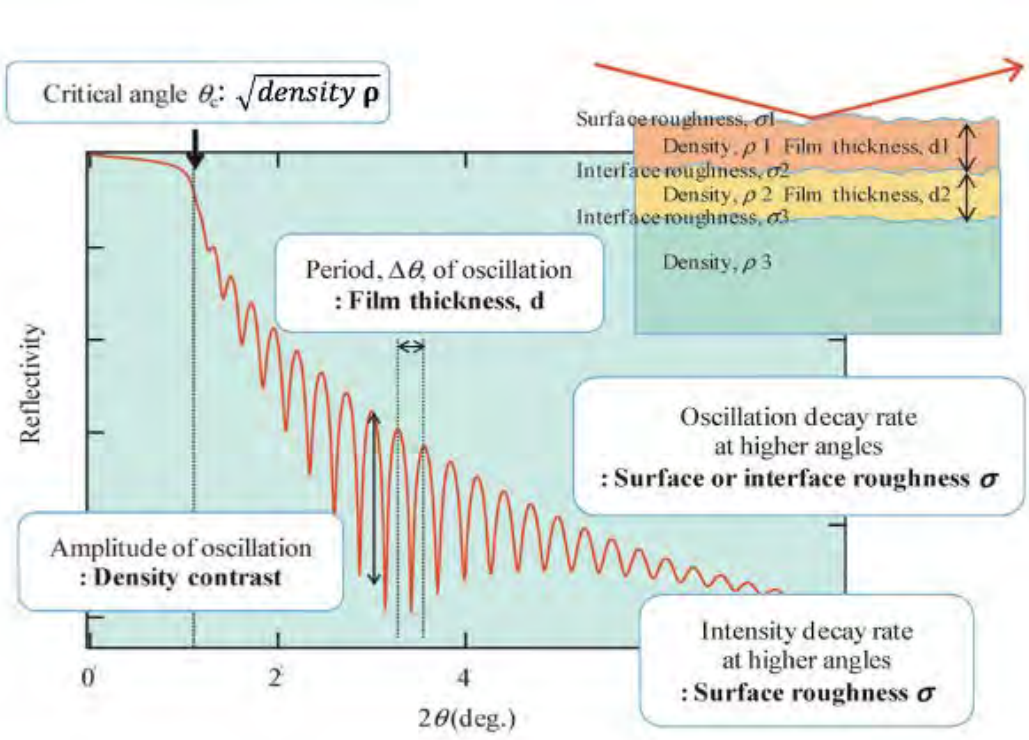

Figure 3.19.: Information provided by an XRR profile. Adapted from Ref. [142].

The disorder at an interface is modeled by connecting adjacent layers through a continuous density profile described by an error function (erf), which smooths the transition between two SLD values. This profile can be expressed as:

$$\rho(z) = \frac{\rho_1 + \rho_2}{2} + \frac{\rho_2 - \rho_1}{2} \operatorname{erf}\left(\frac{z - z_0}{\sqrt{2}\sigma}\right), \tag{3.34}$$

where ρ_1 and ρ_2 are the SLDs of the adjacent layers, z_0 is the mean position of the interface, and σ represents the root-mean-square roughness, corresponding to the width of the Gaussian derivative of the error function.

The parameters ρ, t, and σ for each layer can be quantitatively determined by fitting the experimental reflectivity curve using software such as General X-ray fitting program (GenX), which follows the Marquardt–Levenberg formalism for nonlinear least-squares minimization. In this approach, the best agreement between simulated and experimental data is achieved by minimizing the sum of squared deviations, ensuring a physically consistent description of the layer structure [141, 143].

In this work, XRR measurements were carried out using the Cu-Kα radiation (λ = 1.5406 Å) and the thin film film thickness were initially estimated accordingly to the Eq. 3.33. After that, the GenX software was used to fit the XRR data using a block-like model. The estimated thickness, local roughness obtained by AFM and theoretical nuclear SLD were used as an initial guess. The calculated X-ray SLD values for the materials considered in this work are presented in the Appendix B.

3.2.2.5. Neutron scattering techniques

Given the fact that neutron scattering is sensitive to both the structural and magnetic properties of a sample, polarized neutron reflectivity (PNR) measurements were conducted at the Spallation Neutron Source (SNS) at Oak Ridge National Laboratory. The experiments aimed to investigate the interfacial and depth-dependent magnetism of SRO thin films and a potential proximity effect, such as the induction of magnetic moments in the superconductor or the presence of a magnetic dead layer at SRO thin films and SRO/YBCO heterostructures interfaces.

Polarized Neutron reflectivity

Neutron reflectivity is a scattering technique where a neutron beam is reflected in a sample and the intensity of scattered (reflected) neutrons is recorded as a function of the scattering vector ($\boldsymbol{Q}$). It is similar to X-ray reflectivity, discussed in the section above, and allows one to get similar information, such as structural and interfacial properties of thin films, multilayers and heterostructures.

As discussed in subsection 3.2.2.3, neutrons carry a magnetic moment and are therefore sensitive to magnetic fields and magnetic moments in matter. This allows the incident beam to be spin-polarized by means of a polarizer, such as a supermirror or a ferromagnetic device, which selects neutrons according to their spin state [133]. The polarization is defined with respect to a chosen quantization axis, usually aligned with the applied external magnetic field, and the beam is then described by two possible spin states: spin-up (+) and spin-down (–). This method is called Polarized Neutron Reflectometry (PNR).

In a typical PNR experiment, the spin-polarized neutron beam is directed onto the sample at grazing incidence. After reflection, the spin state of the neutrons is analyzed, often using a dedicated spin analyzer such as an in-situ ^{3}He analyzer [133, 144]. This way, the neutron reflectivity is measured separately for the four possible combinations of incident and reflected spin states:

- R^{++}: Spin-up neutrons reflected as spin-up;
- R^{--}: Spin-down neutrons reflected as spin-down;
- R^{+-}: Spin-up neutrons reflected as spin-down;
- R^{-+}: Spin-down neutrons reflected as spin-up.

The non-spin-flip channels (R^{++} and R^{--}) and spin-flip channels (R^{+-} and R^{-+}) provide complementary information on the nuclear and magnetic depth profiles of the sample. As a result, PNR enables simultaneous access to structural and magnetic depth-dependent properties with nanometer-scale resolution, which is particularly valuable for studying interfacial magnetism and proximity effects [133, 145]. A typical PNR pattern is shown in Fig. 3.20.

In PNR, the total SLD is defined as the sum of the nuclear contribution (nuclear SLD or nSLD) and the magnetic contribution arising from the sample's magnetization component along the neutron spin quantization axis (magnetic SLD or mSLD), according to:

$$\rho_{\pm}(z) = \rho_n(z) \pm \rho_m(z), \tag{3.35}$$

where $\rho_n(z)$ is the nuclear SLD and $\rho_m(z)$ is the magnetic SLD. The signs + and – correspond to the neutron spin being parallel or antiparallel to the sample magnetization,

respectively. Thus, the total SLD profiles for spin-up and spin-down neutrons are given by $\rho_+(z) = \rho_n(z) + \rho_m(z)$ and $\rho_-(z) = \rho_n(z) - \rho_m(z)$, which define the reflectivity contrast measured in PNR experiments.

The magnetic SLD is proportional to the local magnetization $M(z)$ through a constant of proportionality C:

$$\rho_m(z) = C\,M(z), \tag{3.36}$$

where $C = 2.853 \times 10^{-9}\,\text{Å}^{-2}\,(\text{emu/cm}^3)^{-1}$ or equivalently $C = 2.91 \times 10^{-12}\,\text{Å}^{-2}\,(\text{A/m})^{-1}$. C depends exclusively on the Bohr magneton, the neutron gyromagnetic ratio, and the classical radius of the electron.

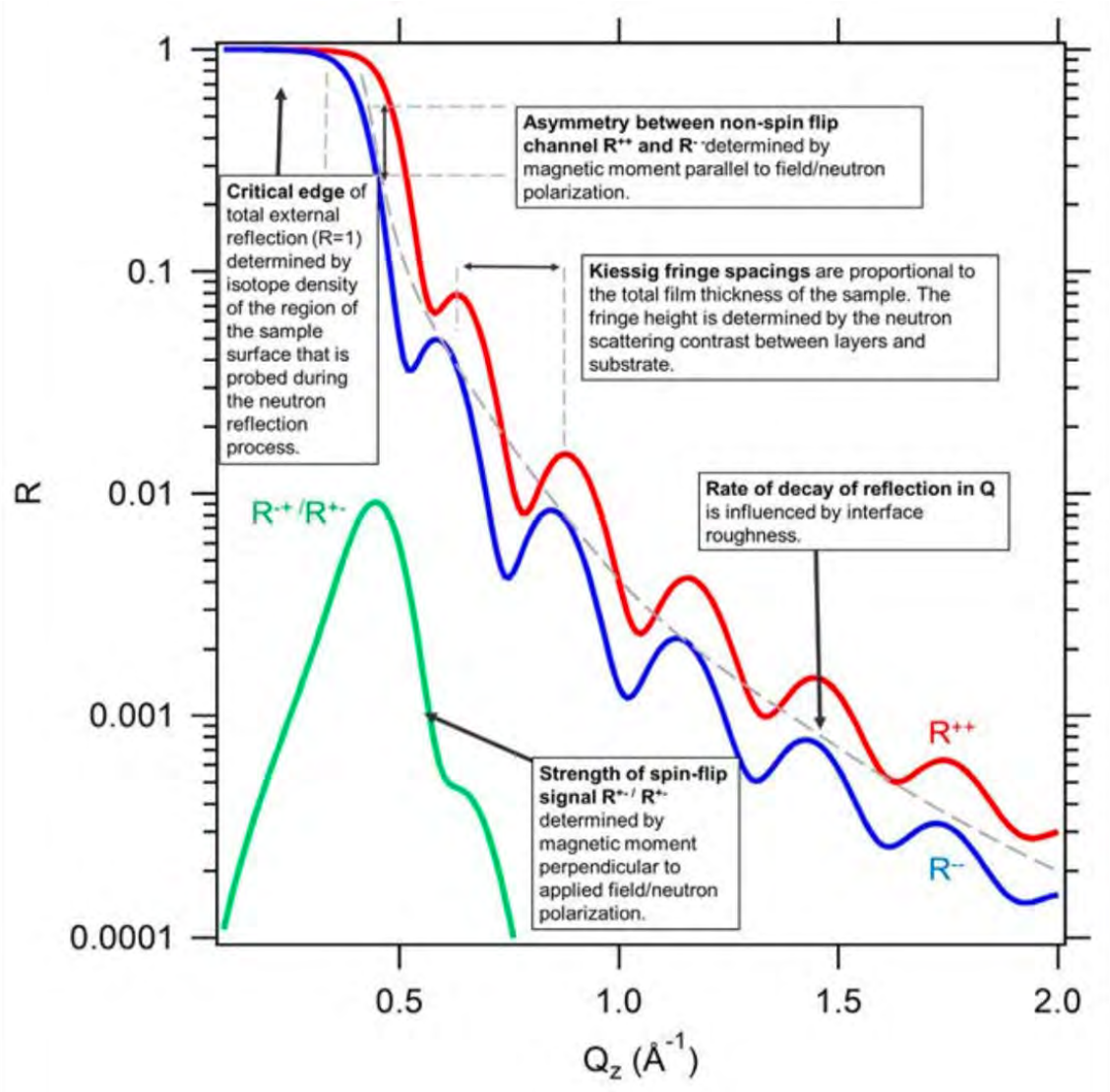

Figure 3.20.: A simplified illustration of how a neutron reflectivity profile is influenced by layer thickness, chemical composition, and magnetization. The example features a 40 nm-thick nickel film on a silicon substrate, with a magnetic moment of 0.6 μB per Ni atom, oriented at 45° relative to the in-plane applied field. The bottom curve shows R^{+-} and R^{-+}, which are identical for all but very few cases of magnetization profiles, is related to the component of the magnetization perpendicular to the applied field. Taken from Ref. [146].

To illustrate these concepts, consider a few typical cases. For a fully magnetized sample, where the magnetization vector is aligned with the external magnetic field, the non-spin-flip (NSF) reflectivity channels (R^{++} and R^{--}) exhibit different total SLDs, leading to a shift in the critical edge (see Fig. 3.20). In this case, the SLD corresponding to R^{++} is enhanced relative to R^{--}. When the magnetization is not fully aligned with the external field, only the projection of the magnetization along the field direction contributes to the magnetic SLD [133, 146].

The spin-flip (SF) reflectivity channels (R^{+-} and R^{-+}) provide direct information about magnetization components that are non-collinear with the neutron quantization axis. In specular PNR, only the magnetization component perpendicular to the scattering vector $\mathbf{Q}$ contributes to magnetic scattering. Among this magnetically active component, the part perpendicular to the neutron polarization axis gives rise to spin-flip scattering, since it can rotate the neutron spin during the scattering process. Consequently, SF reflectivity is sensitive to transverse in-plane magnetization components and can reveal canted magnetization, magnetic inhomogeneity, domain structures, or non-collinear magnetic configurations. In contrast, magnetically homogeneous regions with magnetization fully collinear with the applied field yield negligible SF intensity [133, 146].

In this work, PNR measurements were carried out in two thin films samples: SRO thin film deposited on a TiO_2-terminated Nb:STO substrate and in a YBCO/SRO thin film heterostructure deposited on a TiO_2-terminated STO substrate. Both samples were field cooled in a 4.8 T magnetic field applied parallel to sample surface (in-plane). The PNR measurements were performed at temperatures above and below the critical temperature T_c of the YBCO/STO thin film heterostructure. The PNR data were analyzed using a block-like model (similar to the one used for XRR) in the GenX software. This time, the magnetization and the magnetic SLD of the sample were considered for the fit. The calculated neutrons nuclear SLD values for the materials considered in this work are also presented in the Appendix B.

3.2.3. Scanning and transmission electron microscopy

Electron Microscopy (EM) is a powerful characterization technique used to investigate the fine structure of materials across a wide range of magnifications. In addition to providing high-resolution imaging, EM enables crystallographic and spectroscopic analyses, making it an essential tool for material characterization. Techniques such as Scanning Electron Microscopy (SEM) and Transmission Electron Microscopy (TEM) are among the most widely used methods in this field [125, 147, 148].

The principles of electron microscopy are based on the interactions between an electron beam and a sample. Similar to photons (X-rays) and neutrons, electrons can undergo both elastic and inelastic scattering processes when interacting with matter. These interactions occur within a defined interaction volume in the sample, as illustrated in Fig. 3.21. The size and shape of the interaction volume depend on the material properties (i.e. atomic number Z) and the energy of the incident electrons. Along with the escape depth of the scattered electrons, the interaction volume determines the spatial resolution and the type of information that can be extracted from each signal. These scattering events serve as the foundation for the imaging and analytical capabilities of electron microscopy. A more detailed explanation of electron-sample interactions in electron microscopy is provided below [16, 125, 147].

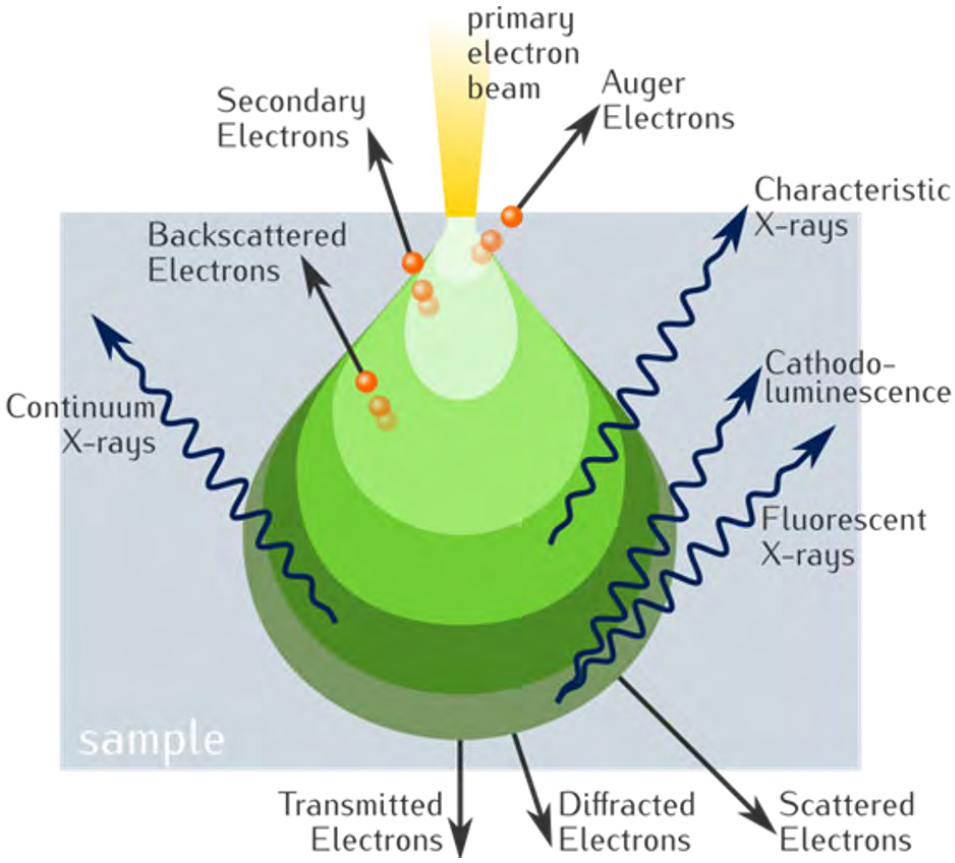

Figure 3.21.: Schematic representation of the interaction volume between the incident electron beam and the sample. The interaction volume depends on the material properties and the energy of the incident electrons. Taken from Ref. [149].

- **Backscattered Electrons (BSE):** BSEs are produced when primary beam electrons are elastically scattered by the sample at angles of up to 180°. These electrons retain an energy level similar to that of the primary electron beam. More specifically, BSEs interact with the positive electric field of the atomic nucleus in the sample (Rutherford scattering).

- **Transmitted Electrons:** These are electrons that pass through the sample without undergoing any interaction. Their transmission depends on the sample's thickness, the mean free path of electrons in the material, and the energy of the primary electron beam.

- **Diffracted Electrons:** These are electrons that interact with the crystalline lattice of the sample, undergoing elastic scattering. Due to the wave-particle duality of electrons, they also exhibit wave-like behavior. Since their momentum and energy are conserved during elastic scattering, diffraction patterns of the sample can be constructed using electron microscopy.

- **Secondary Electrons (SE):** These electrons are characteristic of inelastic interactions, where energy and momentum (phase) are exchanged between the electron beam and the sample. SEs are low-energy electrons ejected from the outermost

atomic shells (low binding energy). Because of their low energy, only those electrons near the surface and with sufficient energy to overcome the surface barrier or work function can escape the material. Examples of secondary electron signals include characteristic X-rays and Auger electrons. Auger electrons are typically emitted by elements with low atomic numbers, whereas characteristic X-rays are dominant in elements with higher atomic numbers.

- **Characteristic X-rays:** During inelastic scattering, electrons from the primary beam may interact with inner-shell electrons of the sample atoms, causing these electrons to transition to an outer shell, leaving a vacancy (hole) in the inner shell. To release the energy from this excited atom, an electron from an outer shell fills the vacancy, emitting a photon in the process. The emitted photon has a characteristic energy determined by the difference in energy levels between the outer and inner shells. These photons, known as characteristic X-rays, are unique to each element in the material. By analyzing the energy of characteristic X-rays, individual elements in the material can be identified through electron microscopy.

- **Auger Electrons:** In addition to characteristic X-ray photon emission, inelastic interactions can also result in the emission of Auger electrons. These are electrons ejected from the inner shells of an atom during electronic recombination. Specifically, when an atom is excited, an electron from an inner shell can decay to fill the vacancy left behind, transferring its energy to another electron in a nearby shell. This second electron is then ejected from the atom and is referred to as an Auger electron. Auger electron emission helps conserve the atom's energy during recombination from the excited to the ground state. The kinetic energy of the Auger electron is equal to the difference between the initial electronic transition energy and the ionization energy of the shell from which the Auger electron was ejected. The probability of Auger electron emission increases as the energy difference between the initial and final states decreases, making this process dominant in lighter elements.

- **Scattered Electrons:** These electrons also arise from inelastic scattering, which can be either coherent or incoherent. In coherent inelastic scattering, energy transfer occurs, but the phase may or may not be conserved. This type of scattering is associated with collective excitations, such as phonons or magnons, due to their comparable energy transfers. In incoherent inelastic scattering, however, the phase is completely lost. Incoherent scattering results from localized or random processes within the sample.

In scanning electron microscopy (SEM), an electron beam interacts with a sample, and images are typically obtained by detecting backscattered electrons (BSE), secondary electrons (SE), and characteristic X-rays using dedicated detectors. As briefly described earlier, BSEs are more energetic and have a deeper sampling depth, providing information from the subsurface regions of the sample. The BSE signal is proportional to the atomic number (Z), making it stronger for elements with higher Z values. Consequently, variations in material composition appear as a contrast in the image, where regions with higher Z appear brighter relative to darker regions with lower Z.

Secondary electrons, on the other hand, are more surface-sensitive, with an escape depth of approximately 10 nm. This is due to the cascade effect during electron-sample

interactions, where only electrons near the surface (low energy electrons) can escape and can be detected. As a result, SE images provide detailed surface information, offering greater sensitivity to surface features and enhanced resolution for capturing topological contrast and fine details. Additionally, spectral analysis of characteristic X-rays enables elemental identification of the sample's components. This capability is integrated into SEM systems equipped with Energy Dispersive X-ray Spectroscopy (SEM-EDS), allowing simultaneous imaging and compositional analysis, making SEM a powerful tool for both morphological and chemical characterization [125, 148].

In transmission electron microscopy (TEM), a high-energy electron beam is transmitted through an ultrathin sample (also called a lamella), allowing the investigation of the sample's structure, composition, and, depending on the imaging or spectroscopy mode, local electronic structure with atomic or near-atomic resolution. TEM images are formed when electrons interact with the sample, primarily through transmission, elastic scattering, and inelastic scattering processes. These interactions are captured using a CCD camera or a fluorescent screen. TEM operates in two primary modes: the imaging mode and the diffraction mode. In imaging mode, the transmitted electron beam is detected and magnified by the objective lenses, providing detailed information about the structure, interfaces, defects, and epitaxial relationships of the sample (in the case of thin films). In diffraction mode, the diffracted beams are detected, and the objective lenses produce a diffraction pattern, revealing information about the crystalline structure, lattice spacing, and orientation. These imaging conditions are also referred to as bright-field (BF) and dark-field (DF) modes, depending on whether the transmitted or diffracted electrons are used for image formation [147, 150].

High-Resolution Transmission Electron Microscopy (HR-TEM) images take advantage of phase contrast created by the interference of electron waves as they traverse the sample and interact with its atomic structure. In crystalline materials, HR-TEM image formation relies on the diffraction of atomic planes under specific imaging conditions. Electrons, which exhibit wave-like behavior, are elastically scattered by the atomic potentials, and the resulting phase difference between the scattered and unscattered electron waves produces interference patterns that generate contrast in the image. HR-TEM enables the investigation of interfaces, atomic-scale defects, and structural characteristics in thin films and multilayered materials with sub-angstrom resolution, typically around 1 Å [150].

Alternatively, High-Angle Annular Dark-Field Scanning Transmission Electron Microscopy (HAADF-STEM) is based on a scanning mode in which a highly focused electron probe is scanned across the sample, and the scattered electrons are collected by an annular detector at high angles. The resulting image intensity is approximately proportional to the atomic number ($Z^{1.7-2}$), yielding Z-contrast that is much less affected by electron phase-interference effects than conventional HR-TEM imaging. HAADF-STEM thus offers direct, composition-sensitive imaging with atomic resolution, complementing the structural information obtained from HR-TEM phase-contrast imaging [150].

Furthermore, EDS mapping can be performed simultaneously with STEM imaging, enabling compositional analysis. In EDS mapping, the characteristic X-rays emitted from the sample are collected at each scanning position of the focused electron probe, so that a full spectrum is acquired pixel by pixel across the image. From these spectra, the spatial distribution of elements is reconstructed, providing quantitative composition maps that can be directly correlated with the structural features observed in the STEM image. When combined with HAADF-STEM, which provides Z contrast, EDS mapping enables correlated structural and compositional analysis at the nanoscale, allowing the

identification of interfaces, diffusion profiles, and compositional gradients across thin films and multilayers [150].

SEM-EDS was applied to investigate the stoichiometry of the SRO target bought at Toshima Manufacturing. The SEM images and EDS-spectra were collected using a Zeiss Merlin Field-Emission Scanning Electron Microscope (FE-SEM) operated by Dr. Egbert Wessel and Dr. Daniel Grüner in the Institute of Energy Materials and Devices (IMD) for Structure and Function of Materials (IMD-1). To investigate compositional variation as a function of depth, HAADF-STEM images and elemental maps SRO thin films were collected using a FEI Titan G2 80-200 ChemiSTEM operated by Prof. Dr. Michael Faley in the Ernst Ruska-Centre for Microscopy and Spectroscopy with Electrons for Physics of Nanoscale Systems (ER-C-1). The YBCO/SRO and SRO/YBCO heterostructures prepared by HOPS are too thick and considerable rough to be characterized by X-ray reflectivity. Therefore, to characterize its crystal structure, epitaxial quality and layer thickness HR-TEM was employed. HR-TEM images were collected on a FEI Tecnai G2 F20 also operated by Prof. Dr. Michael Faley (ER-C-1). Lamellas along the [001] and [110] crystallographic directions were prepared by L. Kibkalo (ER-C-1).

3.2.4. Rutherford backscattering Spectroscopy

Rutherford Backscattering Spectroscopy (RBS) is an analytical technique that allows one to obtain the stoichiometry of a given material. RBS can also be used for determining the sample thickness; however, discrepancies are often observed between the thickness values obtained via RBS and those derived from techniques such as X-ray reflectivity (XRR), high-resolution X-ray diffraction (HR-XRD), and Transmission Electron Microscopy (TEM). The technique is based on the elastic collision of high-energy projectile particles with stationary target atoms in the film, governed by strong Coulomb repulsion (Rutherford scattering) [63, 111, 151, 152].

In a RBS experiment, as depicted in Fig. 3.22, a high-energy, collimated beam of alpha particles (He^{2+}) with energy E_0 and mass M_1 is projected onto the sample surface. This may result in elastic scattering of the incident α–particles by target atoms via the Coulomb interaction between the nuclei (Rutherford scattering). As a result of this scattering, the scattered projectile acquires the energy E_1 and a scattering angle θ. The stationary target particle (mass M_2) gains the kinetic energy E_2 and gets deflected at an angle Φ.

From the conservation of momentum and energy, one can calculate the so-called kinematic factor, k, which is given by [63, 151, 152]:

$$k = \frac{E_1}{E_0} = \left(\frac{M_1 \cos\theta \pm \sqrt{M_2^2 - M_1^2 \sin^2\theta}}{M_1 + M_2} \right). \tag{3.37}$$

This equation shows that, for a given scattering angle, the energy of the backscattered projectile depends on the mass of the target atom, which provides elemental sensitivity in RBS. The kinematic separation between different target masses is largest for scattering angles θ approaching 180°.

RBS is more sensitive to heavier atoms with higher atomic numbers (Z) because the scattering cross-section is proportional to the square of the stationary target particle's atomic number (Z^2). The Rutherford differential scattering cross section is given by [111,

151, 152]:

$$\frac{d\sigma}{d\Omega} \propto \left(\frac{Z_1 Z_2 e^2}{E_0}\right)^2 \frac{1}{\sin^4(\frac{\theta}{2})} d\Omega, \tag{3.38}$$

where Z_1 and Z_2 are the atomic numbers of the incident α-particle and the target element, e is the electronic charge, and θ and Ω are the scattering angle and the solid angle of the detector.

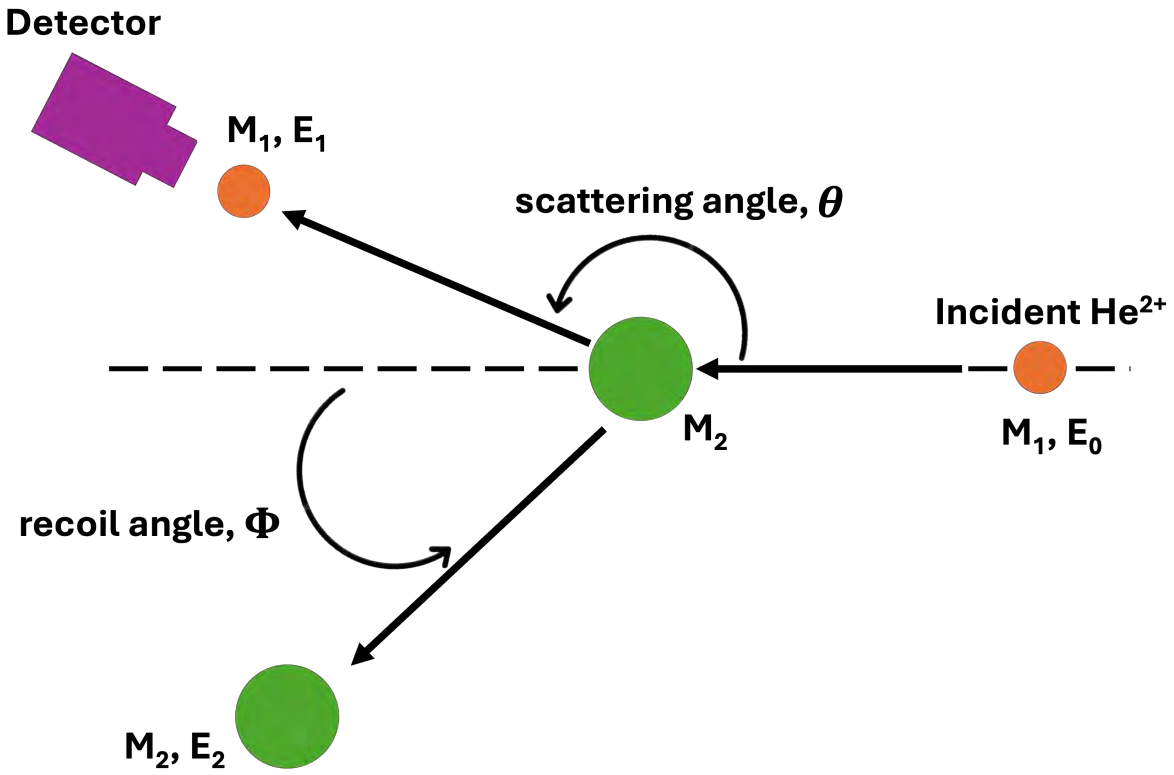

Figure 3.22.: Schematic representation of elastic Rutherford backscattering. An incident He^{2+} ion with mass M_1 and energy E_0 is scattered by a target atom of mass M_2. The scattered projectile is detected with energy E_1 at a scattering angle θ, while the recoiling target atom leaves the collision with energy E_2 at a recoil angle Φ.

In a typical RBS spectrum, the horizontal axis is divided into channels, which correspond to discrete energy intervals recorded by the multichannel analyzer (MCA) connected to the detector. Each channel represents a specific energy range of the backscattered ions, so that higher channel numbers correspond to ions with higher detected energies. The relationship between channel number and energy is determined through calibration using reference materials with well-known peaks. Consequently, the RBS spectrum displays the detected yield as a function of channel (or energy), allowing the identification of elements and depth distributions within the sample [151].

Figure 3.23 shows a simulated RBS spectra for a thin film sample. For thin samples, the signal for each element is peak like. For thicker samples, such as substrates, the ions lose energy inside the sample, leading to an elongation of the signal towards zero energy, resulting in a step-like shape [111]. RBS data can be simulated using the RUMP software, which was developed by M. Thompson, Cornell University in 1983 [153].

$SrRuO_3$ thin films were characterized by RBS to obtain its stoichiometry. The measurements were performed at Peter Grünberg Institute for Semiconductor Electronics (PGI-9) by Dr. Omar Concepción. The data analysis was performed using the RUMP software.

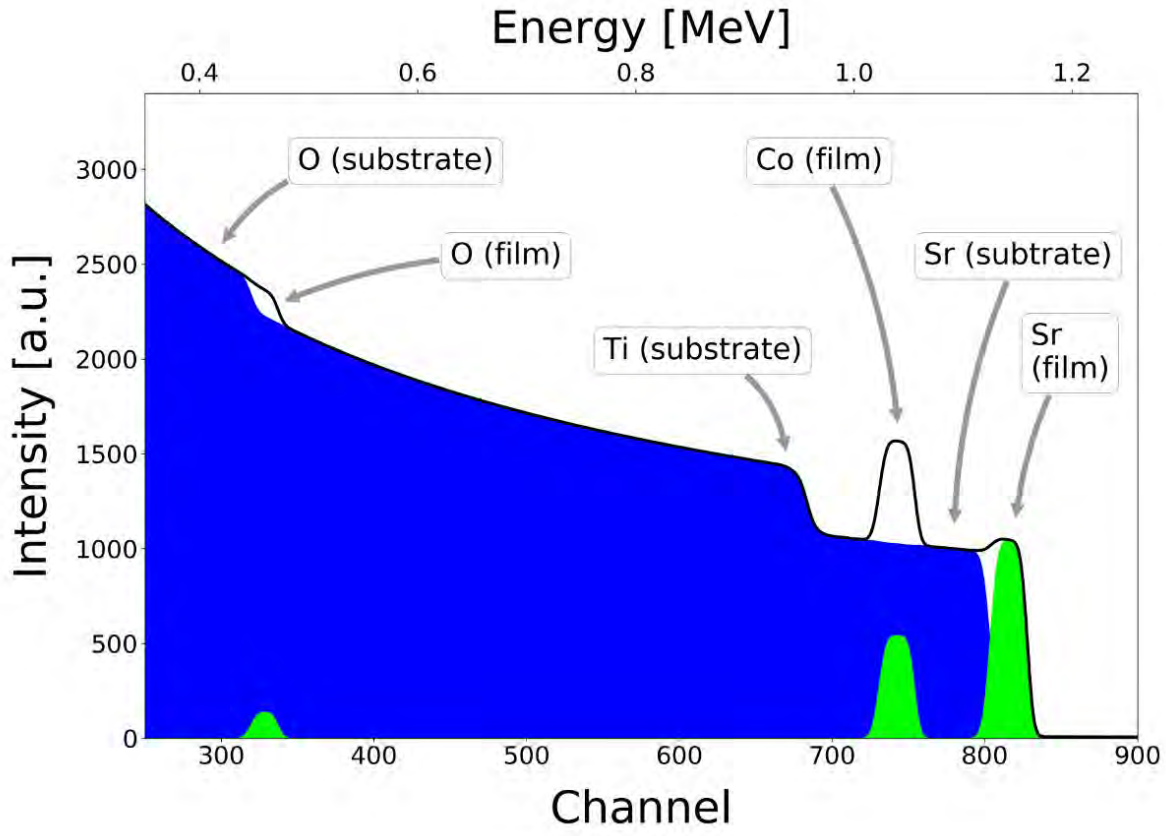

Figure 3.23.: Simulation of a $SrCoO_{3-\delta}$ film on a $SrTiO_3$ substrate. The black line represents the simulated total intensity, while the film contribution is shown in green and the substrate contribution in blue. Taken from Ref. [111].

3.2.5. Magnetization measurements

The magnetization of the samples was measured as a function of temperature and magnetic field using zero-field-cooled (ZFC) and field-cooled (FC) protocols, as well as magnetic hysteresis loops recorded at selected temperatures and magnetic fields. All measurements were carried out using a Quantum Design Magnetic Properties Measurement System (MPMS-XL) [154].

The MPMS mainly consists of a Superconducting Quantum Interference device (SQUID) and a superconducting magnet inside a liquid He Dewar vessel. This setup allows measurements in a temperature range from 2 K up to 400 K and in magnetic fields up to ±7 T. For the measurements, the thin-film samples, originally 10 mm x 10 mm, were cut into smaller pieces of approximately 4 mm x 4 mm, mounted inside a plastic straw, and inserted into the MPMS. The magnetic field generated by the superconducting magnet is applied along the z-direction and can be oriented either parallel or perpendicular to the sample surface depending on the mounting geometry. The sample mounting configuration is illustrated in Fig. 3.24.

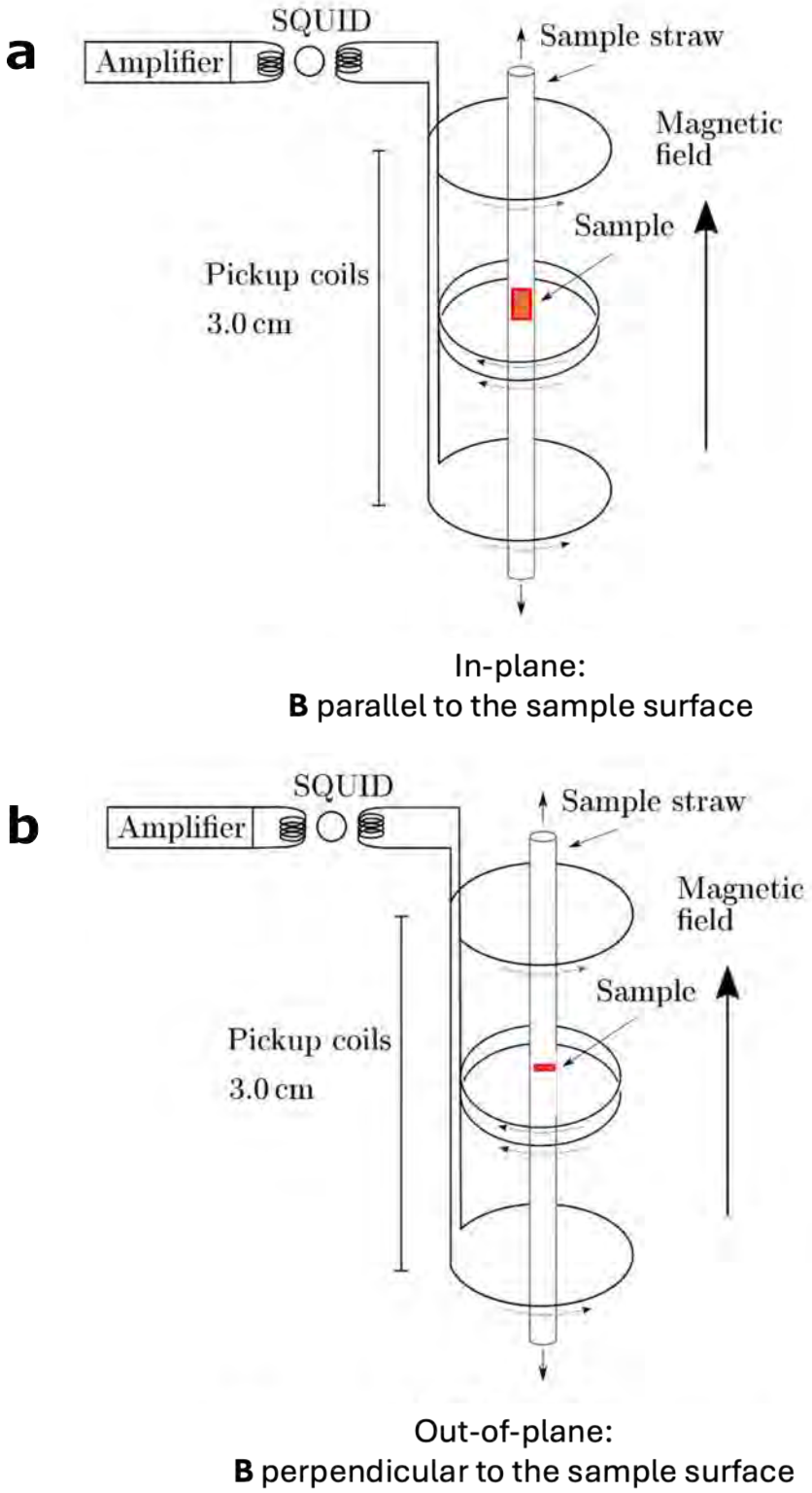

Figure 3.24.: Schematic of MPMS setup with sample mounted inside a straw for measurements with external magnetic field applied (a) parallel to the sample surface (in-plane) and (b) perpendicular to the sample surface (out-of-plane). Adapted from Refs. [111, 154].

During the measurement, the sample is moved through a set of pickup coils made of superconducting wire. These coils are arranged as a second-order gradiometer, in which the outer coils are wound in the opposite direction to the inner coils [155]. The magnetic moment of the sample induces a current in the detection coils, which is inductively coupled to the SQUID circuit. Owing to the gradiometer configuration, uniform magnetic fields are largely suppressed and do not contribute to the measured signal.

The SQUID circuit consists of a superconducting loop containing Josephson junctions [156]. In a superconductor, the Cooper pairs are described by a macroscopic wavefunction, which leads to the quantization of the phase change around the loop in integer multiples of 2π. As a consequence, the magnetic flux passing through the superconducting loop is quantized in units of the flux quantum, $\Phi_0 = 2.07 \times 10^{-15}$ Vs. Any external magnetic flux, such as that associated with the sample magnetization, modifies the phase difference across the junctions and gives rise to a compensating Josephson current [12]. By detecting this current, extremely small magnetic moments can be measured, with a sensitivity of approximately 5×10^{-12} Am^2.

ZFC and FC measurements were used to determine the temperature dependence of the magnetization. From these measurements, the Curie temperature (T_{Curie}) of the SRO thin films and the superconducting critical temperature (T_{c}) of the YBCO thin films, as well as of the SRO/YBCO and YBCO/SRO heterostructures, were determined. In addition, magnetic hysteresis loops measured at different temperatures were used to evaluate the saturation magnetization of the SRO thin films and to investigate the changes associated with the superconducting and ferromagnetic states in the SC/FM and FM/SC heterostructures. All measurements were performed at the MPMS of the Jülich Centre for Neutron Science (JCNS-2).

3.2.6. Electron transport measurements

The electrical transport properties of the samples were measured as a function of temperature and magnetic field using the four-probe method. All measurements were carried out using the resistivity and transport measurement options available in a Quantum Design Physical Properties Measurement System (PPMS) and in a Quantum Design PPMS DynaCool system.

Both instruments are equipped with an integrated cryostat, enabling transport measurements over a wide temperature range from 2 to 400 K, and with a superconducting magnet allowing the application of magnetic fields up to ±9 T. These systems enable resistivity and magnetoresistance measurements under well-controlled conditions. The conventional PPMS operates with a liquid-helium Dewar and a liquid-nitrogen radiation shield, whereas the PPMS DynaCool uses a cryogen-free cooling system based on a closed-cycle helium refrigerator. The PPMS allows both direct-current (DC) and alternating-current (AC) transport measurements, while the PPMS DynaCool operates in AC mode only.

Electrical contacts were made using a TPT HB10 Wire Bonder with automatic z-axis bonding, available at the Peter Grünberg Institute for Electronic Materials (PGI-7). For transport measurements, the thin film samples were mounted onto a PPMS puck using double-sided adhesive tape. Aluminum wire bonds were then used to connect the contact pads of the sample to the puck terminals. To minimize geometrical artifacts, samples with approximately square or rectangular shapes were used whenever possible. Depending on the mounting configuration, the sample could be measured at different orientations with

respect to the external magnetic field using a horizontal rotator. Figure 3.25 shows a sample mounted directly on the puck, allowing magnetotransport measurements with the field applied out-of-plane, and a sample mounted on the horizontal rotator, which enables measurements for field orientations between -10° to 360°.

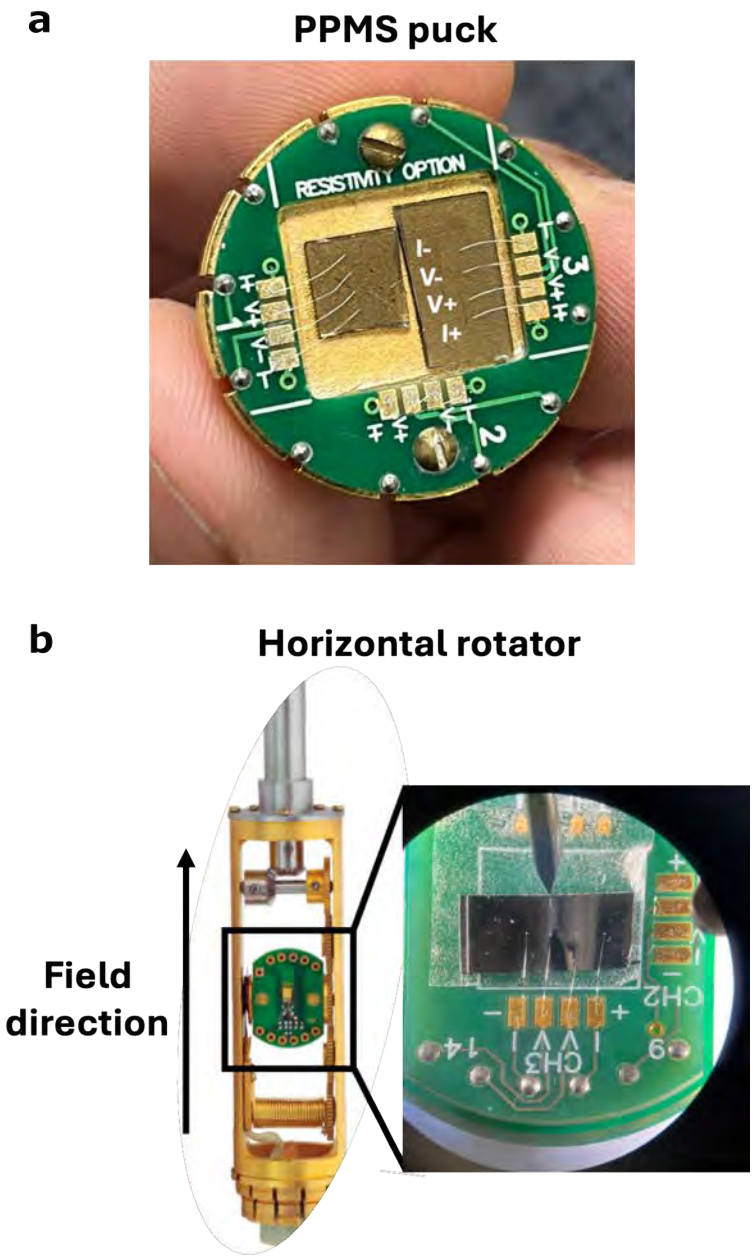

Figure 3.25.: Thin films samples bonded in the (a) PPMS puck, which allows measurements with magnetic field applied out-of-plane and in the (b) horizontal rotator, which allows measurements with magnetic field applied in angles in in a range of -10° to 360°.

For a sample of thickness t, the resistivity measured in the four-probe configuration can be written as:

$$\rho = \frac{\pi}{\ln(2)} t \left(\frac{V}{I} \right) f_1 f_2, \tag{3.39}$$

where f_1 and f_2 are correction factors accounting for the finite sample thickness and finite lateral dimensions, respectively. The thickness correction factor f_1 also depends on whether the substrate is electrically insulating or conducting. For square or rectangular samples on insulating substrates, with lateral dimension d much larger than the probe spacing s ($d/s > 1$), both correction factors are close to unity, so that $f_1 = 1$ and $f_2 \approx 1$ in the present case [157].

Transport measurements were performed to investigate the resistive behavior of the SRO thin films and to determine the superconducting critical temperature of the SC/FM and FM/SC heterostructures. Low excitation currents in the range from 1 μA to 50 μA were applied to the $I^{\pm}$ terminals in order to minimize Joule heating. In the PPMS DynaCool, the measurements were carried out in AC mode using frequencies between 6 and 20 Hz, while in the PPMS both AC and DC configurations were available.

Magnetoresistance measurements were performed with the magnetic field applied both out-of-plane and in-plane, depending on the sample mounting geometry. These measurements were used to investigate the transport response of the heterostructures and its evolution across the superconducting and ferromagnetic regimes. All electrical transport measurements were carried out at the Jülich Centre for Neutron Science (JCNS-2).

Chapter 4

Growth of $YBa_2Cu_3O_{7-x}$ thin films

$YBa_2Cu_3O_{7-x}$ (YBCO) was chosen as the high critical-temperature (high-T_c) superconductor for investigating proximity effects in high-T_c superconductor/ferromagnetic (SC/FM) thin-film heterostructures. This selection was motivated by YBCO's extensive applicability in both small- and large-scale superconducting devices, as well as its well-established growth conditions by High Oxygen Pressure Sputtering. The YBCO thin films and the superconducting layers in the SC/FM heterostructures examined in this work were grown in collaboration with Prof. Dr. Michael Faley. This chapter provides a detailed overview of the growth conditions and a summary of the characterization results obtained for the reference YBCO films.

4.1. High Oxygen pressure sputtering growth

High Oxygen Pressure Sputtering (HOPS) is a deposition technique specifically developed for the growth of high-T_c SC, the vast majority of which are oxide materials. The high oxygen pressure used during film growth plays a crucial role in mitigating the re-sputtering process, where a small fraction of high-energy sputtered ions traveling from the target to the substrate can cause the removal of already-deposited material. The high oxygen pressure acts then as a moderator by facilitating collisions between these energetic particles with the process gas (oxygen), leading to energy dissipation before they reach the substrate or are lost to the chamber walls.

In addition to the oxygen pressure, other parameters such as the target-substrate distance (D_{TS}), deposition temperature (T_{dep}) and the parameters involved in plasma generation (which depends on the source type, direct current or radio frequency power supply) play an important role on the film growth, and their structural and physical properties. In thin films growth, the deposition parameters are usually carefully optimized to achieve high-quality films.

For epitaxial films, the lattice mismatch of the thin film material and the substrate becomes a relevant parameter. In some cases, it is necessary to reduce the lattice mismatch between film and substrate and, for this reason, seed- and buffer-layers are deposited on the substrate prior to the film deposition. In the case of YBCO epitaxial films, substrates such as buffered-MgO, $SrTiO_3$ (STO), $LaAlO_3$, $LaSrAlO_4$, YSZ (Yttria-Stabilized Zirco-

nia), sapphire (with Ag, CeO_2, and MgO buffer layers) are commonly used in order to obtain epitaxial films [158].

YBCO usually grows in three possible ways, known as *c*-axis growth (or spiral growth, where the *c*-planes are oriented parallel to the substrate surface), *a*-axis growth (where the *ab*-planes are oriented perpendicularly to the substrate surface) or in a mixture of these two [159, 160]. The YBCO growth modes are strongly dependent on T_{dep}, with higher T_{dep} favoring spiral-like growth and predominant *c*-axis orientation, whereas *a*-axis-oriented grains can be stabilized at lower T_{dep}. However, the final *c*-axis/*a*-axis orientation is not determined by temperature alone, but also by substrate-induced strain, film thickness, growth kinetics, and the thermal expansion mismatch between the film and the substrate. These factors influence the density of growth spirals and can lead to substrate-dependent differences in the YBCO growth morphology [161, 162]. After growth, YBCO films undergo a thermal treatment (annealing process) in a controlled atmosphere to assure its high-T_{c} properties.

The careful optimization of growth and annealing parameters greatly enhances the crystalline quality of the deposited films and ensures optimal oxygen doping, both of which are crucial for achieving the desired superconducting properties. The YBCO growth optimization was performed by Prof. Dr. Michael Faley and Prof. Dr. Ulrich Poppe and can be found elsewhere [72, 116, 163, 164]. In this work, YBCO reference thin films were deposited on buffered-MgO and STO substrates using a DC plasma source, with nominal thicknesses of 180 nm and 85 nm, respectively. An illustration of the deposition of a YBCO thin film on a STO substrate and the schematic of the two SC reference samples are shown in Fig. 4.1.

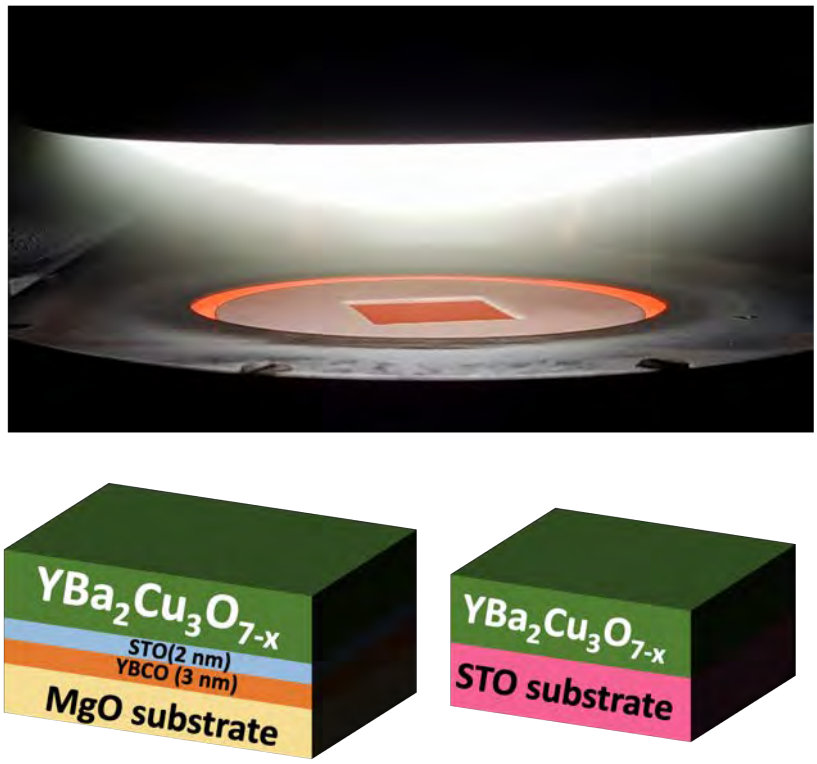

Figure 4.1.: Top: deposition of a a YBCO thin film on a STO substrate. Bottom left: schematic of a buffered-MgO substrate. Bottom right: schematic of a STO substrate.

The MgO substrate was first etched using an ion beam machine in order to induce a surface texture along the [100] and [010] directions of the substrate. After etching, the MgO substrate was buffered with a 3 nm seed-layer of YBCO followed by a 2 nm buffer-layer of STO. The YBCO seed layer promotes the structural transition from the rock-salt MgO surface to the perovskite YBCO structure, while the STO layer acts as a chemical blocking layer, preventing Mg-related contamination and favoring *c*-axis-oriented YBCO growth. The STO substrate was not subjected to any chemical treatment, such as chemical etching, since the surface termination of the STO substrate, either SrO or TiO_2, does not play an important role in the YBCO film quality [165]. Accordingly, it was only cleaned with acetone and isopropanol in an ultrasonic bath.

The substrates are placed directly onto a heater block inside the deposition chamber, which is evacuated to pressures around 10^{-6} mbar to ensure a clean environment. Prior to YBCO growth, the target undergoes pre-sputtering process at low oxygen pressure with low current and voltage values for several days to eliminate contaminants and stabilize the deposition conditions. The values of current and voltage are usually increased during the pre-sputtering process until they reach the deposition values. The YBCO thin film is deposited at an oxygen pressure of 2.5 mbar using a DC plasma generated by a current of 500 mA and a voltage of 240 V. The optimal D_{TS} was found to be 1 cm, where the plasma gently touches the substrate surface. Deviations from this distance lead to films with poor crystallinity and stoichiometry. The deposition temperature is set to 930 ˚C, as measured at the heater block. However, precise pyrometer measurements indicate that the actual substrate temperature is approximately 110 ˚C lower [119]. Film thickness is controlled by the deposition time, with a typical growth rate of approximately 100 nm/h under these conditions. After deposition, the shutter is closed, and the sample is cooled down to 500 ˚C at 2.5 mbar. The plasma is then switched off, and the pressure is immediately increased to 10 mbar, where it remains overnight to ensure proper oxygen incorporation. A summary of the pre-sputtering, growth and post-growth annealing parameters is provided in Table 4.1, while additional details about the growth procedure can be found in Appendix A.

Table 4.1.: Summary of the pre-sputtering, growth and post-growth annealing parameters used on the YBCO growth, such as oxygen partial pressure , target-substrate distance (D_{TS}), deposition temperature (T_{dep}). N/A means not applicable.

Parameter	Pre-sputtering	Growth	Post-growth annealing
Current	0.1 mA	500 mA	N/A
Voltage	280 V	240 V	N/A
P_{O_2}	0.3 mbar	2.5 mbar	10 mbar
D_{TS}	N/A	1 cm	N/A
T_{dep}	N/A	930 ˚C	500 ˚C

4.2. Topography

The surface morphology of YBCO films prepared on buffered-MgO and STO substrates was investigated by scanning electron microscopy (SEM) in secondary electron mode. Representative SEM micrographs of the films are shown in Fig. 4.2. Atomic force mi-

croscopy (AFM) in both topography and phase modes was also employed to probe the film surface. However, due to the limited response of the AFM cantilever to sharp height variations between rough and smoother regions, the acquired images appeared blurred and are therefore not presented here. Instead, the AFM topography data were used exclusively to quantify the local surface roughness of the YBCO films.

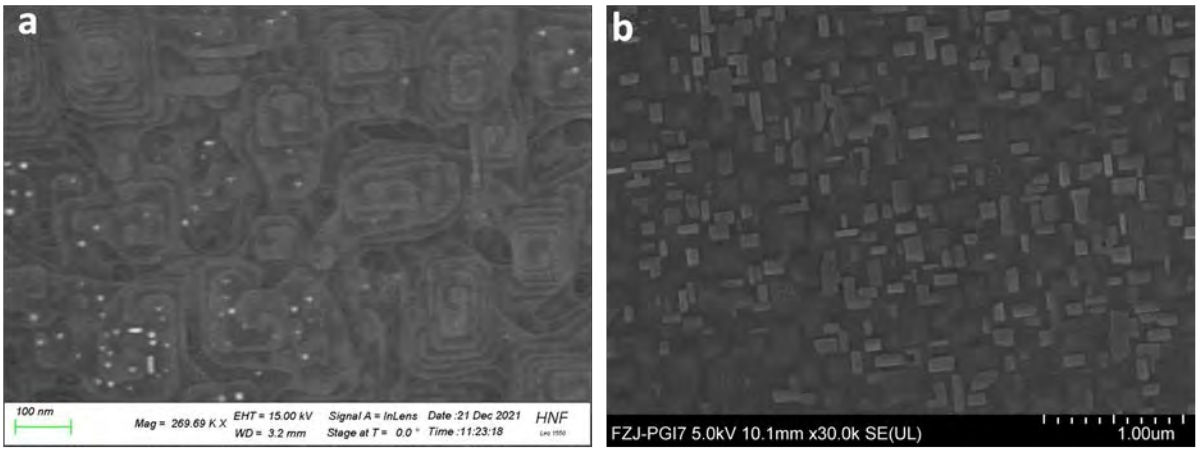

Figure 4.2.: Scanning electron microscopy micrographs of the YBCO film deposited on (a) buffered-MgO and (b) STO substrates.

The YBCO film deposited on the buffered-MgO substrate shows a predominant c-axis orientation, as evidenced by the surface spirals, as shown in Fig. 4.2(a). The film exhibits a low surface roughness of only a few nanometers, with the growth spirals showing a step-height of 1 nm. The small white dots at the film surface are related to BaCuO nanoparticles formed during the post-growth annealing process. In contrast, the YBCO film deposited on the STO substrate shows a topography characteristic of a-axis orientation. This is related to both T_{dep} and the film thickness [161], for which the density of growth spiral is already strongly suppressed in STO substrates. The root mean square roughness is 3.3 nm ± 1.7 nm, which was calculated across the 2 μm × 2 μm sample area. This value is consistent with previously reported roughness values for YBCO thin films deposited on exact and non-buffered STO substrates [166, 167].

4.3. Crystal structure

The crystalline structure of the YBCO thin films was investigated by high-resolution X-ray diffraction (HR-XRD). Figure 4.3 shows the ω–2θ diffraction scans of the films deposited on both buffered-MgO and STO substrates.

Both films exhibit excellent crystalline quality, as evidenced by the intense and well-defined diffraction peaks, which appear at consistent positions for both samples [Fig. 4.3(a)]. The observed reflections correspond to the (00l) family of planes in YBCO, indicating that the films predominantly grow with their c-axis oriented perpendicular to the substrate surface. A closer examination around the (001), (002), and (003) reflections of the STO substrate, however, reveals the presence of a small fraction of a-axis oriented grains. These grains are manifested by the additional (h00) peaks observed to the right of the YBCO (00l) reflections in the HR-XRD patterns [Fig. 4.3(b–d)]. The concentration of a-axis-oriented grains is higher for the film deposited on the STO substrate, in agreement

with the surface morphology shown in Fig. 4.2(b). Additional ϕ-scan measurements and transmission electron microscopy (not shown) confirm the epitaxial nature of both samples, with the YBCO lattice parameters aligned to those of the substrates.

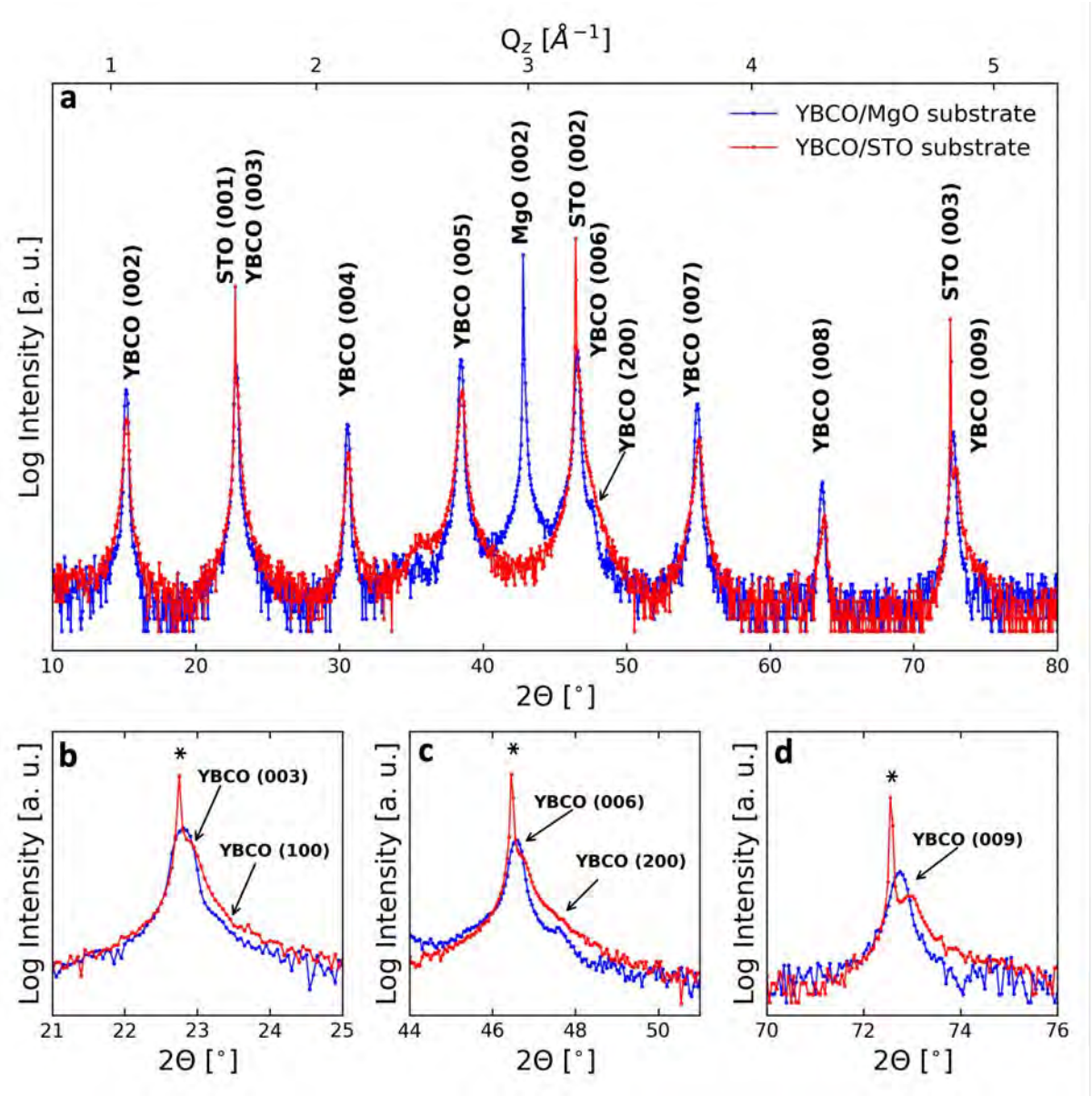

Figure 4.3.: (a) High-resolution X-ray diffraction pattern obtained for the YBCO films deposited on the buffered-MgO and STO substrates. (b-d) Detailed view around the (001), (002), and (003) crystallographic reflections of the STO substrate (indicated by the asterisks) presenting the presence of small a-axis grains in the c-axis oriented film structure.

To investigate the film thickness and interfacial roughness, the YBCO/STO sample was further characterized by X-ray reflectivity (XRR). The obtained XRR pattern is shown in Fig. 4.4. The insets show a magnified region of the XRR pattern with the corresponding fit, demonstrating good agreement with the experimental data, as well as the obtained scattering length density (SLD) profile. From the fit, a total film thickness of 85 ± 3 nm and an interfacial roughness of approximately 3 ± 2 nm were obtained. The overall fit quality is improved by including a very thin, low-SLD surface region within the YBCO

film, with an associated roughness of 2 ± 1 nm. This layer is included to better represent the surface structure of the YBCO film, likely accounting for the presence of *a*-axis grains and/or BaCuO nanoparticles formed during the post-growth annealing process.

Due to the larger thickness of the YBCO film (approximately 180 nm, as verified by cross-sectional SEM) deposited on the buffered-MgO substrate, XRR measurements for this film could not be performed.

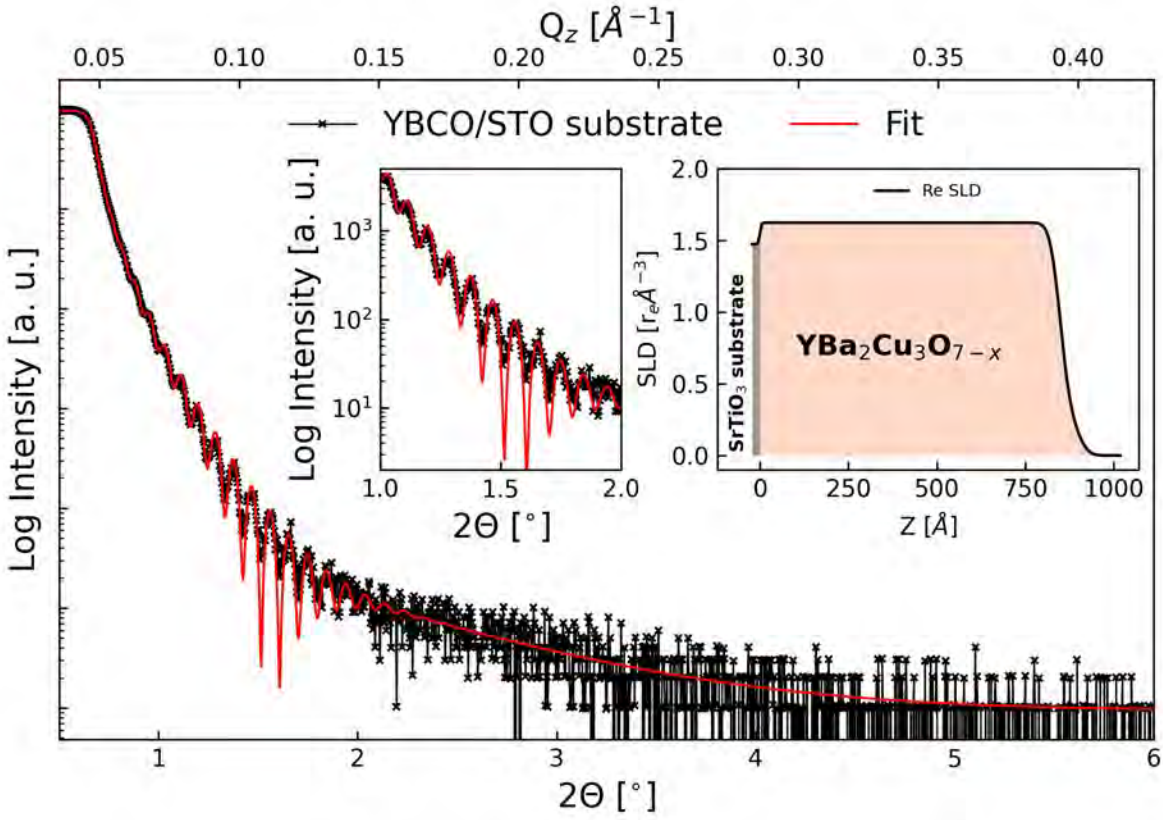

Figure 4.4.: X-ray reflectivity pattern, fit and the obtained scattering length density profile (inset) of a YBCO thin film.

4.4. Transport and magnetic properties

The superconducting properties of the samples were investigated through electrical transport and magnetization measurements as a function of temperature and applied magnetic field.

Electron transport measurements [$\rho(T, H = 0)$], carried out using the four-point probe method, are shown in Fig. 4.5 for the YBCO/buffered-MgO and YBCO/STO samples. The critical temperature (T_c) of the films was determined from the first derivative of $\rho(T)$, with the full width at half maximum (FWHM) taken as the T_c deviation. From this analysis, T_c values of 91.4 K ± 0.4 K and 87.5 K ± 0.3 K were obtained for the YBCO/buffered-MgO and YBCO/STO films, respectively.

Since the transport properties of superconducting cuprates are closely tied to the hole-doping concentration, both films can be considered nearly optimally doped, as indicated by the linear temperature dependence of the resistivity above T_c [53, 71]. At 300 K,

however, the YBCO/buffered-MgO sample shows a significantly lower resistivity (164 $\mu\Omega$-cm) compared to the YBCO/STO film (435 $\mu\Omega$-cm). This effect is consistent with enhanced electron scattering associated with the larger fraction of *a*-axis-oriented grains in this sample and the higher surface roughness of the YBCO/STO film compared with the YBCO/buffered-MgO film, although variations in oxygen stoichiometry may also play a role.

The reduced T_c and higher resistivity at 300 K observed for the YBCO/STO film are most likely related to the insufficient pre-sputtering of the replacement YBCO target used during deposition. During sample preparation, the original target broke and was replaced by a new one that had not undergone sufficiently long pre-sputtering, which likely affected the target surface condition and, consequently, the oxygen doping, structural quality, and surface roughness of the film. Subsequent films grown from the same target after extended pre-sputtering exhibited T_c values around 90 K, consistent with high-quality YBCO growth.

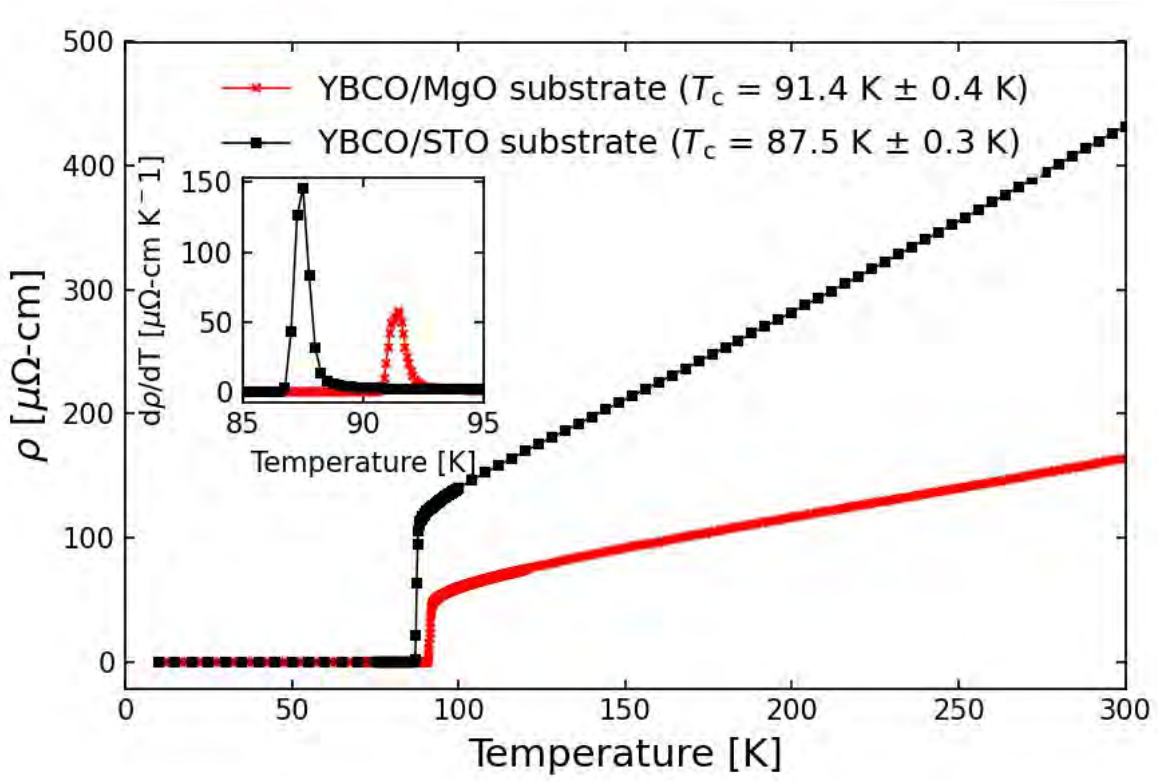

Figure 4.5.: ρ(T, H=0) dependence of YBCO thin films deposited on buffered-MgO (red) and STO (black) substrates. The T_c values were determined by taking the first derivative of ρ(T), shown in the inset figure.

Although the temperature dependence of $\rho(T)$ is widely used to determine the critical temperature of superconducting films and heterostructures, this approach is not the most precise. Magnetic susceptibility measurements, particularly under the zero-field-cooled (ZFC) protocol, provide a more direct probe of the superconducting state through the Meissner effect. In this regime, the superconductor behaves as a perfect diamagnetic material, expelling the magnetic field from its interior, which is reflected in a negative magnetic susceptibility. In a typical ZFC measurement, the sample is cooled down to low temperature in the absence of an applied field. Once the target temperature is stabilized,

an external magnetic field is applied and the magnetic response is recorded as a function of temperature while warming the sample. The raw magnetic moment measured by the SQUID, m, can be converted into magnetization by normalizing it to the sample volume, $M = m/V$. The volumetric magnetic susceptibility is then obtained as $\chi = M/H$, where H is the applied magnetic field.

ZFC susceptibility curves of the YBCO/STO film were measured under applied magnetic fields of 1 mT, 10 mT, and 1 T, with the field oriented both parallel (in-plane) and perpendicular (out-of-plane) to the film surface. The results are shown in Fig. 4.6. The onset of superconductivity is marked by a sharp drop of the susceptibility to negative values, which was taken as the definition of T_c. A comparison of T_c values obtained from transport and susceptibility measurements is presented in Table 4.2. Due to the time-consuming nature of this protocol, the YBCO/buffered-MgO film was not measured.

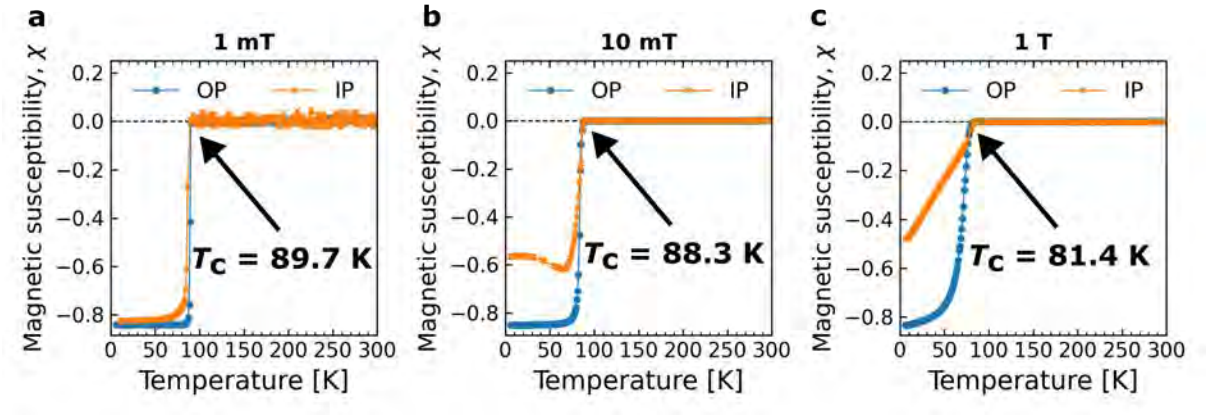

Figure 4.6.: Zero-field-cooled (ZFC) volumetric magnetic susceptibility, $\chi(T)$, of the YBCO/STO film measured under external magnetic fields of (a) 1 mT, (b) 10 mT, and (c) 1 T. Measurements were performed with the field applied both in-plane (IP, parallel to the film surface, along the [100] crystallographic direction) and out-of-plane (OP, perpendicular to the film surface). The OP data were corrected for demagnetization effects using $N \approx 1$ and the relation $\chi_{\text{real}} \approx \chi/(1-\chi)$. Magnetic susceptibility is shown in SI units (dimensionless volume susceptibility).

Table 4.2.: T_c values obtained for the YBCO/Buffered-MgO and YBCO/STO samples via transport and magnetization measurements.

Method	YBCO/Buffered-MgO	YBCO/STO
Transport	91.4 K ± 0.4 K	87.5 K ± 0.3 K
ZFC 1 mT	N/A	89.7 K ± 1.0 K
ZFC 10 mT	N/A	88.3 K ± 1.4 K
ZFC 1 T	N/A	81.4 K ± 0.5 K

The T_c, determined from the ZFC magnetic susceptibility, closely matches that obtained from $\rho(T, H = 0)$. A gradual reduction in T_c is observed with increasing applied magnetic field, regardless of its orientation. This behavior is expected, as external magnetic fields progressively suppress the superconducting state, causing a shift in T_c to lower temperatures.

For an ideal superconductor in the Meissner state, perfect diamagnetic screening implies $M = -H$, and therefore $\chi = M/H = -1$ in SI units. However, for an applied field of 1 mT, the susceptibility χ of the YBCO film deposited on the STO substrate reaches values close to −0.8 for both orientations (IP and OP). A $\chi > -1$ can arise due to geometrical effects (demagnetization in thin films) or the early penetration of vortices associated with structural defects. Considering that the lower critical fields of YBCO are $B_{c1}^{ab} \approx 18$ mT and $B_{c1}^{c} \approx 53$ mT (see Table 2.1), the applied field of 1 mT is nominally below both. Therefore, the proximity to the mixed state should be attributed not to the absolute value of the applied field, but rather to local imperfections and the underestimation of the film volume in the calculation, which can affect the calculated $\chi(T)$ response.

At higher fields (10 mT and 1 T), the shape of $\chi(T)$ below T_c progressively changes. The ideal Meissner-like diamagnetic response is increasingly suppressed as the field rises, indicating enhanced flux penetration and the transition toward a mixed/vortex state. This effect is more pronounced for fields applied parallel to the film surface (in-plane), consistent with the intrinsic anisotropy of YBCO: since $B_{c1}^{ab} < B_{c1}^{c}$, vortices penetrate more easily when the field is parallel to the CuO_2 planes, leading to a faster reduction in the magnitude of the diamagnetic susceptibility. For fields applied perpendicular to the film surface (out-of-plane), the suppression is less pronounced, reflecting the higher value of B_{c1} in this direction.

In the mixed state, quantized magnetic flux lines penetrate the superconductor in the form of Abrikosov vortices. These vortices can be pinned by defects such as point defects, voids, misfit dislocations, precipitates, grain boundaries, anti-phase boundaries, twin boundaries, and other planar defects [12, 52, 158]. Vortex pinning hinders free vortex motion, reduces dissipation, and helps sustain persistent shielding currents. This mechanism contributes to the persistence of a diamagnetic response even under relatively high applied fields.

Finally, since the investigation of proximity effects in SC/FM heterostructures relies on a combination of several experimental techniques, with magnetotransport measurements playing a central role [22, 35], we characterized the magnetoresistance response of the reference YBCO films deposited on buffered-MgO and STO substrates. The results are presented in Fig. 4.7. The data presented in Fig. 4.7(b, c) for the buffered-MgO-based sample and in Fig. 4.7(e, f) for the STO-based sample were collected at selected temperatures around the superconducting transition [colored squares marked in the resistivity curves, $\rho(T, H = 0)$, shown in Fig. 4.7(a, d)] and at low temperatures. The external magnetic field, $\mu_0 H_{ext}$, was applied both in-plane (parallel to the film surface) and out-of-plane (perpendicular to the film surface). The black curves represent the data collected with $\mu_0 H_{ext}$ swept from positive to negative values, whereas the colored curves correspond to the sweep from negative to positive values. The color code follows the temperature points marked by the squares in the $\rho(T, H = 0)$ curves.

For temperatures above T_c, the field-dependent resistivity remains finite and only weakly dependent on the applied magnetic field. This behavior is clearly observed, for example, in the curves measured well above the superconducting transition, where $\rho(T, H)$ remains close to the corresponding zero-field value $\rho(T, H = 0)$. The weak field dependence indicates that, in the normal state, the applied magnetic field produces only a small change in the resistivity of the reference YBCO films within the investigated field range.

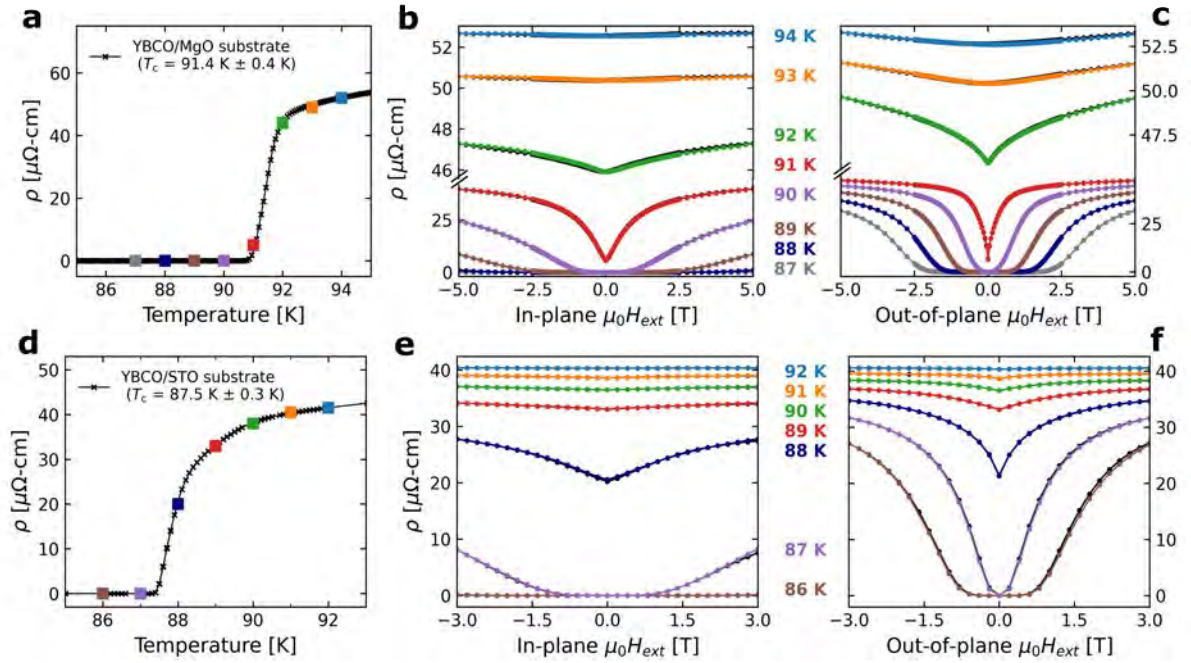

Figure 4.7.: Resistivity $[\rho(T, H = 0)]$ of YBCO thin film deposited on the (a) buffered-MgO substrate and (d) STO substrate. The colored squares represent the temperature at witch the field-dependent resistivity $[\rho(T, H)]$ measurement was performed. $\rho(T, H)$ results with the magnetic field applied in-plane (IP, parallel to the [100] crystallographic direction) of YBCO thin film deposited on the (b) buffered-MgO substrate and (e) STO substrate. $\rho(T, H)$ results performed with magnetic field applied out-of-plane (OP, perpendicular to the [100] crystallographic direction) of YBCO thin film deposited on the (c) buffered-MgO substrate and (f) STO substrate. The color code corresponds to the colors of the squares in the $\rho(T, H = 0)$ curves.

As the temperature approaches T_c, the films progressively enter the superconducting transition regime. In this temperature range, the resistivity is strongly reduced around $\mu_0 H_{ext} \approx 0$, producing a dip toward zero resistivity. This reflects the emergence of superconducting paths within the film at low fields. At higher fields, however, the superconducting contribution to the transport response is progressively suppressed, and the resistivity increases toward the normal-state value expected at the corresponding temperature.

For $T < T_c$, the films exhibit zero or nearly zero resistivity at low fields, consistent with a Meissner-like superconducting response with effective magnetic shielding. As the applied field increases, magnetic flux can penetrate the superconductor and the films enter the vortex/mixed state. In this regime, superconductivity is still present, but the zero-resistivity state can be progressively suppressed by field-induced flux penetration, vortex dynamics, and pair-breaking effects, with the relative contribution of these mechanisms depending on the field orientation and measurement geometry. Thus, the increase in resistivity at higher fields reflects the suppression of the zero-resistivity state rather than the complete destruction of superconductivity. At sufficiently high fields, complete suppression of superconductivity would lead $\rho(T, H)$ to approach the field-induced normal-state resistivity expected at that temperature. However, this high-field normal-state limit is not directly reached in the present measurements given the large upper critical fields of

YBCO.

Our results show that the same qualitative behavior is observed for both samples and for both field orientations (in-plane and out-of-plane). At the same time, the comparison between the two geometries reveals the intrinsic anisotropy of the superconducting properties of YBCO. In particular, the zero-resistivity state persists up to larger applied fields in the in-plane configuration than in the out-of-plane configuration. This behavior is consistent with the anisotropic superconducting coherence length of YBCO, with ξ_{ab} being approximately one order of magnitude larger than ξ_c. Consequently, although B_{c2} is not directly accessed within the present experimental field range, the observed field dependence follows the expected anisotropic trend reported for YBCO, where superconductivity is more robust against fields applied parallel to the CuO_2 planes than against fields applied perpendicular to them [52, 65–67]. This consistency further supports the high superconducting quality of the reference films.

4.5. Conclusions

In summary, epitaxial YBCO thin films with predominantly *c*-axis orientation were successfully deposited on buffered-MgO and STO substrates by HOPS. Both samples exhibited low local roughness; however, the surface topography of the film grown on buffered-MgO was superior to that of the film deposited on STO. A minor fraction of *a*-axis oriented grains was identified in both samples, with a more pronounced presence at the surface of the film grown on STO. Electrical transport and magnetization measurements confirmed high T_c values with sharp superconducting transitions for both films. Notably, the YBCO film grown on buffered-MgO displayed a higher T_c compared to the film on STO. The reduced T_c observed in the latter may be attributed to the use of a new target, which underwent only a limited pre-sputtering process. Finally, magnetotransport measurements revealed a consistent field-dependent resistivity behavior in both samples for external magnetic fields applied in-plane and out-of-plane. The comparison between these two geometries also probes the intrinsic anisotropy of YBCO, reflecting the different superconducting length scales and critical fields associated with the CuO_2 planes.

Chapter 5

Growth of $SrRuO_3$ thin films

$SrRuO_3$ (SRO) was chosen as the ferromagnetic layer for investigating proximity effects in high critical-temperature (high-T_c) superconductor/ferromagnet thin-film heterostructures. This material was selected because it exhibits perpendicular magnetic anisotropy (PMA) and has a good lattice match with $YBa_2Cu_3O_{7-x}$. Since SRO films had never been grown by high oxygen pressure sputtering (HOPS) at the Jülich Centre for Neutron Science (JCNS-2), a systematic optimization of the growth parameters was performed to obtain samples with high structural quality and physical properties, such as Curie temperature and PMA, consistent with the objectives of this project. To evaluate the influence of the target composition on the film stoichiometry and magnetic behavior, two different sputtering targets were employed: one with stoichiometric composition ($SrRuO_3$) and another intentionally enriched in Ru ($SrRu_{1.4}O_3$). This chapter summarizes the characterization results obtained for the reference SRO films grown from both targets.

5.1. $SrRuO_3$ thin films prepared from a stoichiometric target

5.1.1. Target and plasma stoichiometry characterization

To prepare the samples, a stoichiometric SRO target was purchased from Koshima Manufacturing Co. Ltd. with a nominal purity of 99.9% (3N). Scanning electron microscopy (SEM) and energy-dispersive X-ray spectroscopy (EDS) were performed to examine the microstructure and stoichiometry of the SRO target. These measurements were carried out by Dr. Egbert Wessel and Dr. Daniel Grüner at the Institute of Energy Materials and Devices for Structure and Function of Materials (IMD-1). SEM micrographs were acquired at 10 kV using backscattered electron detection.

The SEM images revealed that the SRO target is highly porous [Fig. 5.1(a)]. EDS measurements were performed on large and flat grains [Fig. 5.1(b)]. The representative EDS spectrum shown in Fig. 5.1(c) displays prominent Sr and Ru peaks, while the O signal appears significantly weaker. This is expected due to the low atomic number of oxygen, which limits the X-ray detection efficiency. Overall, the elemental ratios confirm that the target composition is stoichiometrically consistent with SRO.

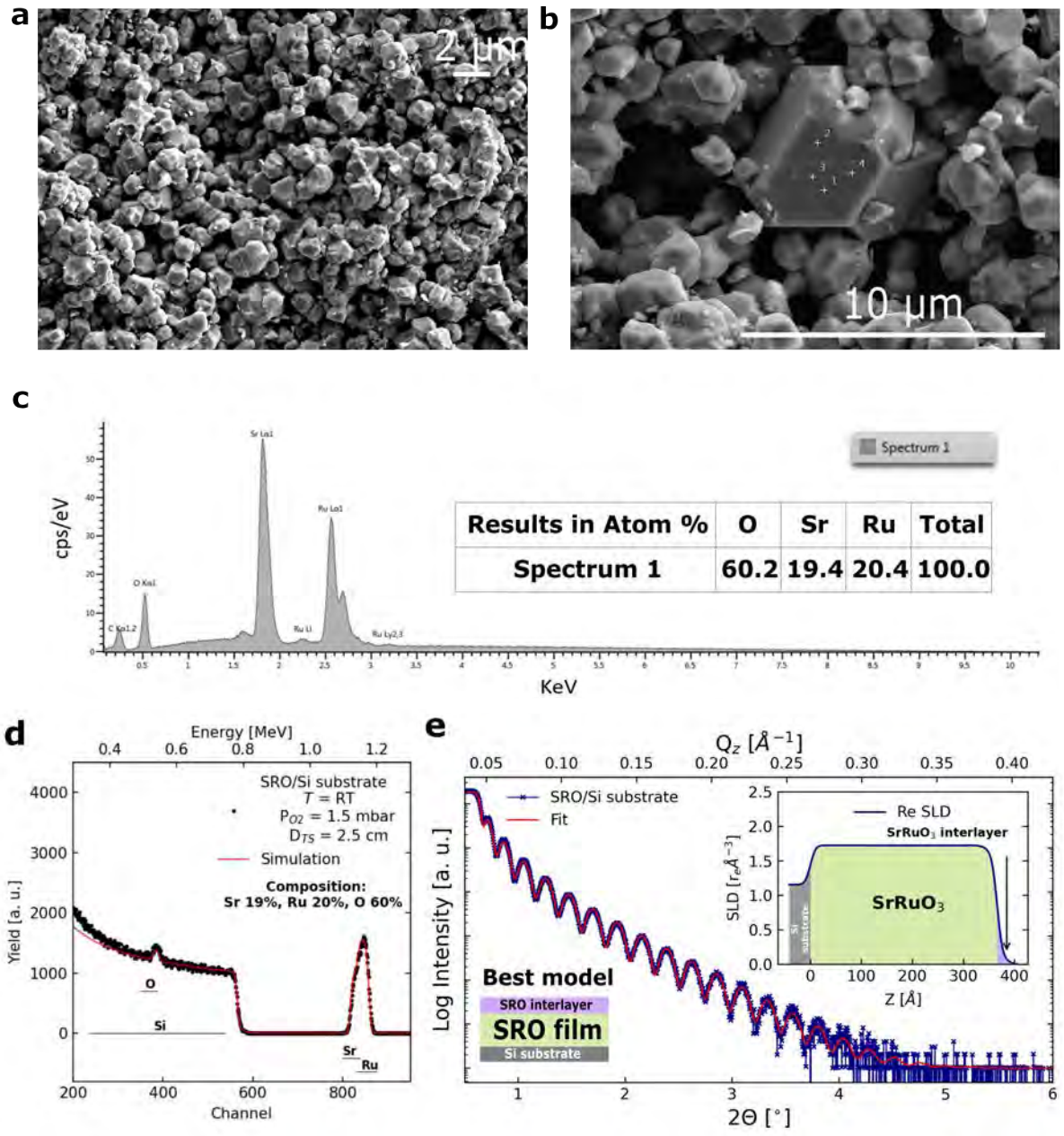

Figure 5.1.: (a) Scanning electron microscopy micrograph showing the high porosity of the SRO target. (b) Example of a large grain and Energy-dispersive X-ray spectroscopy (EDS) measurement spots. (c) EDS spectrum for one of the analyzed spots. (d) Rutherford Backscattering spectroscopy spectrum of a SRO film grown on a Si substrate at room temperature and its simulated fit. (e) Experimental X-ray reflectivity curve and corresponding fit; inset shows the derived scattering length density (SLD) profile.

During sputtering, the relative sputter yields of Sr and Ru depend on the ion energy and scattering cross sections, and the high oxygen partial pressure may further alter the stoichiometry by forming volatile RuO_x species in the plasma. Therefore, assessing whether the stoichiometry of the target is preserved in the plasma is critical for reproducible growth of SRO.

To verify whether this stoichiometry is preserved in the plasma phase during sputtering, one SRO film was deposited on a Si substrate at room temperature (RT). This choice avoided possible stoichiometric deviations caused by the high deposition temperatures (T_{dep}), typically required to grow complex oxides, and by a standard $SrTiO_3$ (STO) substrate, which presents Sr in the composition and may affect the proper determination of plasma composition. The deposition was performed using an Radio Frequency (RF) plasma source, with the target–substrate distance adjusted so that the plasma plume slightly touched the substrate surface.

The resulting film was first characterized by Rutherford Backscattering Spectroscopy (RBS). The RBS spectrum [Fig. 5.1(d)] clearly shows the characteristic peaks of Sr, Ru, O, and Si. Simulation of the spectrum, assuming an SRO film layer on Si, yielded a film thickness of approximately 32 nm and an atomic composition consistent with the stoichiometric SRO, corroborating the EDS results.

Although the film is expected to be amorphous due to the low growth temperature (T_{dep} = RT), its electronic density profile was further analyzed by X-ray reflectivity (XRR), a technique sensitive to the electronic density profile across thin layers. The experimental XRR pattern and corresponding fit [Fig. 5.1(e)] indicate a thickness of about 37 nm. The best-fitting model corresponds to a stoichiometric SRO layer with a scattering length density (SLD) close to the theoretical value of 1.746 r_eÅ^{-3} (see Appendix B), and a thin interfacial layer at the film surface exhibiting a slightly reduced SLD, related to the high-oxygen pressure deposition conditions [75]. The extracted SLD profile is shown in the inset of Fig. 5.1(e).

The combined EDS, RBS, and XRR analyses demonstrate that, under room-temperatu--re deposition, the plasma does not significantly alter the Sr:Ru ratio, indicating stoichiometric transfer from the target to the substrate. This suggests that preferential re-sputtering or volatile loss of Ru is negligible under these conditions, which establishes a reliable baseline for optimizing high-temperature growth parameters where Ru volatility becomes significant.

5.1.2. Optimization of the growth parameters

In HOPS, the main growth parameters are strongly interdependent and directly influence the plasma shape and density, the growth rate, and the resulting film quality. Therefore, optimizing the target–substrate distance, deposition temperature, oxygen partial pressure, and both forward and reflected RF power is crucial for achieving epitaxial SRO films with smooth morphology, good structural order and physical properties.

Figure 5.2 schematically illustrates the influence of these parameters on the plasma and deposition geometry. The target–substrate distance (D_{TS}) strongly affects the growth rate, crystalline structure, and surface roughness. Consequently, it was optimized to ensure that the plasma plume properly covers the substrate area without excessive ion bombardment or shadowing effects. The deposition temperature (T_{dep}) was also systematically optimized, as this parameter critically influences the volatility of Ru and the kinetic limitation of adatom incorporation into the perovskite lattice, thereby determining the

stoichiometry and crystallinity of the resulting films.

In particular, Ru is highly volatile under oxygen-rich conditions due to the possible formation of gaseous RuO_x species [74, 75, 77, 99]. Consequently, optimizing T_{dep} and oxygen partial pressure (P_{O_2}) is essential to suppress Ru loss and maintain stoichiometric film growth [85]. The forward power (FWDP) and P_{O_2} are highly correlated and jointly define the plasma's strength and shape, ranging from elongated and diffuse at low (FWDP, P_{O_2}), to compact and bright at high (FWDP, P_{O_2}) conditions. In addition, the angular distribution of sputtered species is commonly described by a cosine-type law, with the flux being highest along the target normal. However, under the high oxygen pressures used in HOPS, the mean free path of the sputtered species is strongly reduced. As a result, species ejected from the target may undergo multiple collisions with O_2 molecules before reaching the substrate, leading to angular redistribution, kinetic-energy loss, and enhanced gas-phase oxidation. This makes the effective flux arriving at the substrate dependent not only on the initial sputtering distribution, but also on P_{O_2}, FWDP, and target–substrate distance.

A schematic representation of the plasma morphology for low, high, and optimized combinations of FWDP and P_{O_2} is shown in Fig. 5.2. The following subsections discuss in detail the optimization of each of these parameters. The samples prepared during these optimization steps, together with their thicknesses and interfacial roughnesses, are summarized in Appendix C.

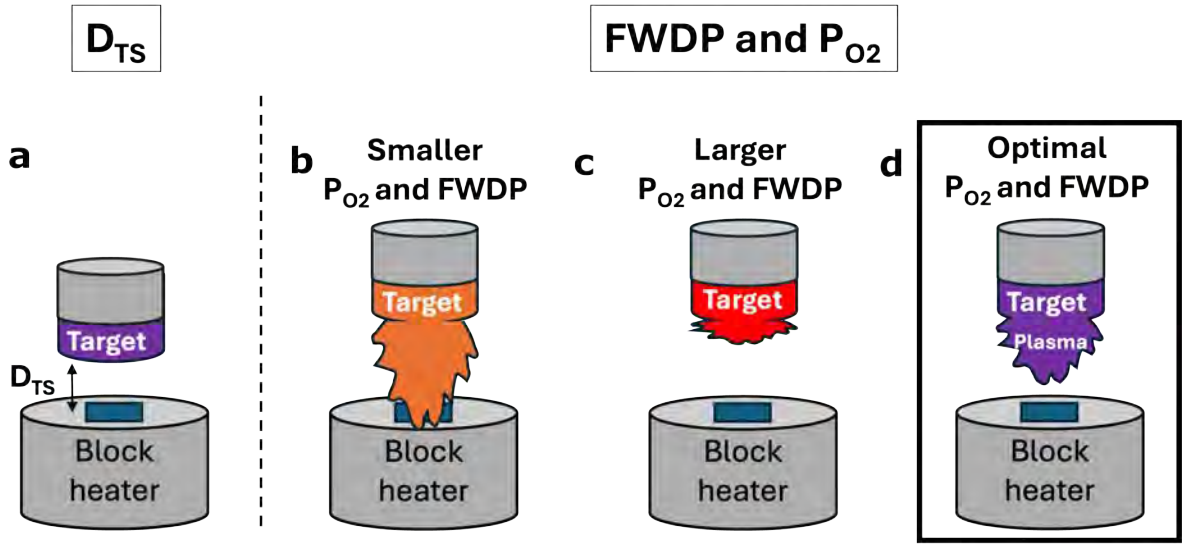

Figure 5.2.: Schematic representation of the plasma behavior during high oxygen pressure sputtering. The plasma shape and stability depend strongly on the forward power (FWDP) and oxygen partial pressure (P_{O_2}): (b) unstable, elongated plasma at low FWDP; (c) overly dense plasma at high FWDP; and (d) stable and homogeneous plasma under optimized conditions. The block heater maintains the substrate at the desired deposition temperature (T_{dep}), while (a) the target–substrate distance (D_{TS}) defines the geometry and coverage of the plasma plume.

5.1.2.1. Target–substrate distance

To optimize the target–substrate distance (D_{TS}), three SRO films were grown varying D_{TS} between 1.5 cm, 2.0 cm, and 2.5 cm, while keeping the other growth parameters constant (T_{dep} = 785 °C, FWDP = 100 W, and P_{O_2} = 1.5 mbar). The D_{TS} values were chosen considering the limits of the HOPS machine. The SRO films were deposited on low miscut TiO_2-terminated STO (001) substrates exhibiting atomically flat terraces with one unit-cell step height, as shown in the atomic force microscopy (AFM) micrographs in Fig. 5.3(a–c).

The surface topography of the deposited SRO films was also characterized by AFM, as presented in Fig. 5.3(d–f). The film grown with D_{TS} = 1.5 cm exhibits an island growth, evidenced by the formation of isolated islands across the surface. This morphology results in a considerably high local roughness (root-mean-square roughness, σ_{RMS}). In contrast, the films grown with D_{TS} between 2.0 and 2.5 cm display a smoother and more homogeneous surface ($\sigma_{RMS} \approx 1$ nm), with a terrace profile that closely replicates the substrate surface. This effect is most pronounced for the sample prepared with D_{TS} = 2.5 cm. The terraces observed on the surface of the sample grown with D_{TS} = 2.0 cm are shallower and likely correspond to mixed RuO_2- and SrO-terminated regions. Although terraces are clearly visible, these samples likely did not grow in a pure step-flow mode but rather in a mild step-bunching regime, as indicated by the irregular step edges and slight accumulation of material along the terrace boundaries.

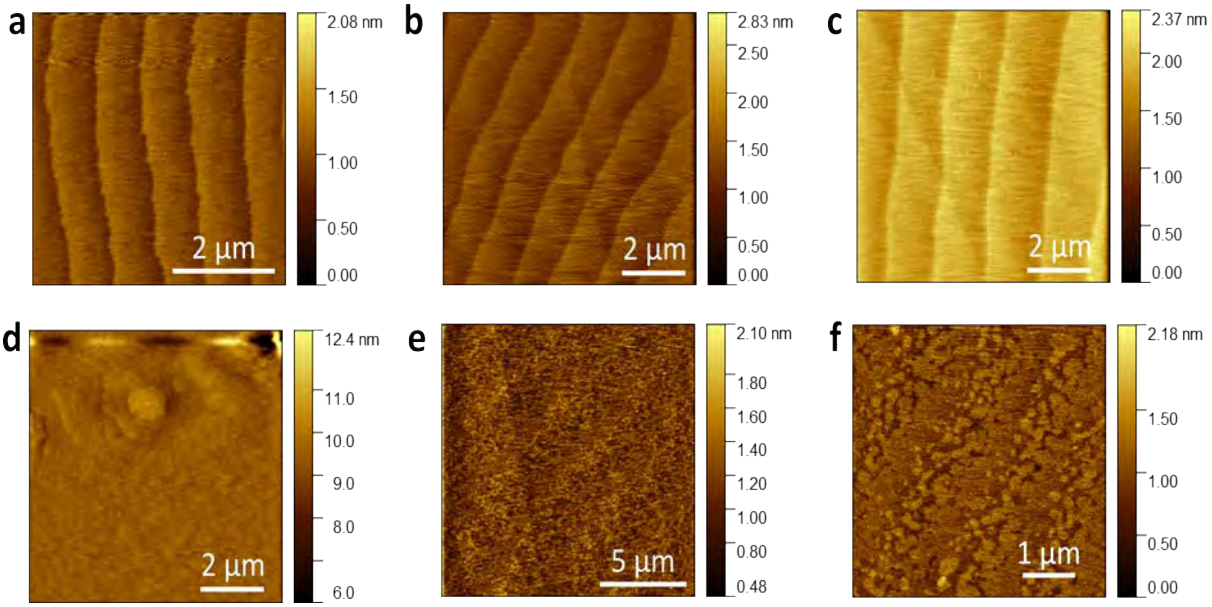

Figure 5.3.: Atomic force microscopy of (a–c) TiO_2-terminated STO substrates prior to the deposition of SRO thin films, and (d–f) corresponding SRO films grown with target–substrate distances of 1.5 cm, 2.0 cm, and 2.5 cm, respectively.

The crystalline structure of the three SRO films deposited at different D_{TS} values was analyzed by high-resolution X-ray diffraction (HR-XRD), as shown in Fig. 5.4(a). The Bragg peaks corresponding to the pseudocubic SRO_{pc} (002) reflection (indicated by triangles) gradually shift toward lower 2θ values as D_{TS} decreases, indicating that the films become thicker for shorter D_{TS}. This observation demonstrates that the deposition rate increases as D_{TS} is reduced. For reference, the diffraction pattern of the STO substrate around the (002) crystallographic direction is also included.

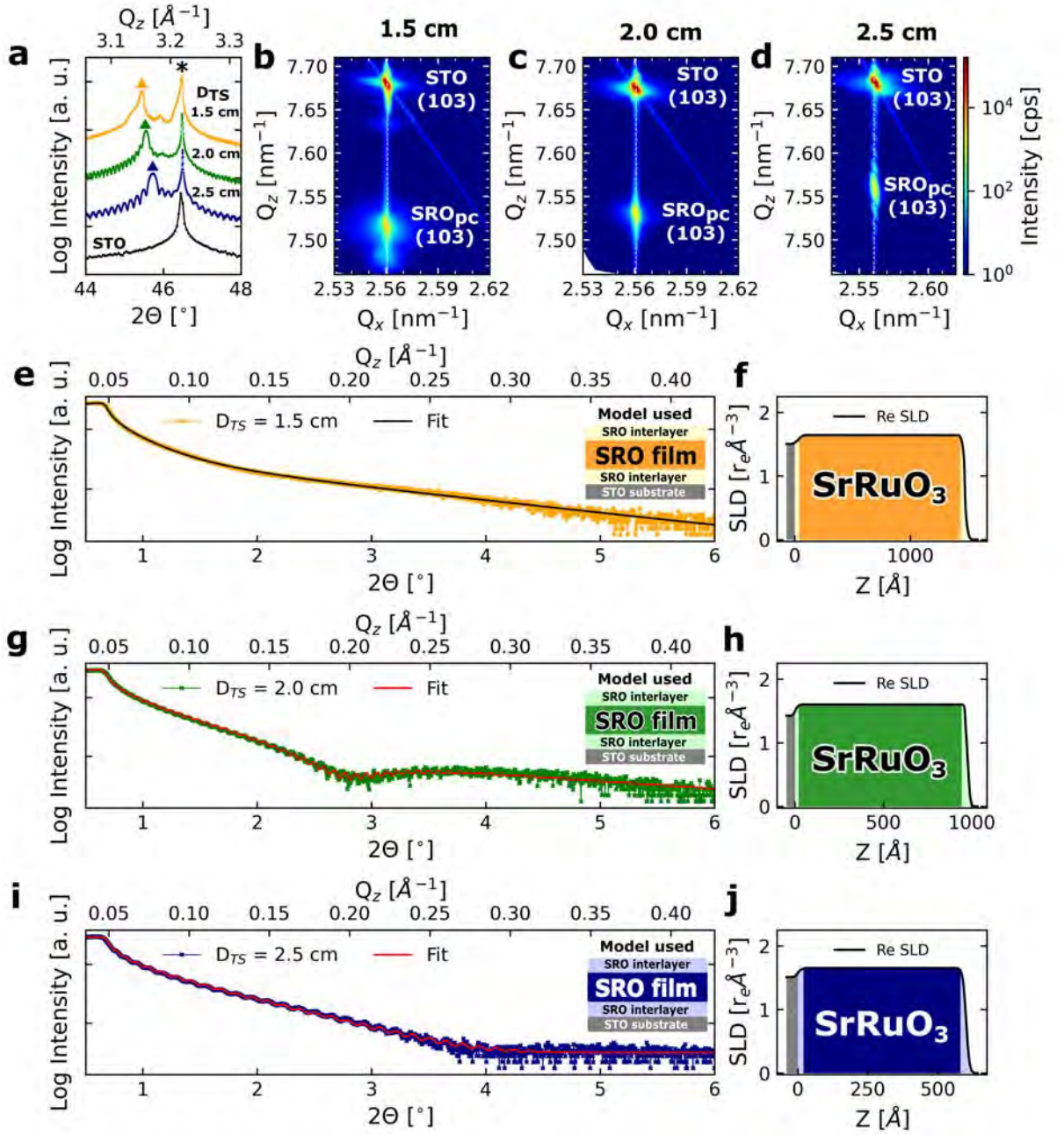

Figure 5.4.: (a) High-resolution X-ray diffraction patterns of SRO films deposited at different D_{TS} values and of the STO substrate. Triangles mark the Bragg peaks of the SRO_{pc} (002) reflection, and the asterisk indicates the STO (002) substrate peak. (b–d) Reciprocal space maps around the (103) reflection as a function of D_{TS}. The dashed white line serves as a guide to the eye. (e–j) Experimental X-ray reflectivity patterns, best-fit simulations, and corresponding scattering length density (SLD) profiles for D_{TS} values of 1.5 cm, 2.0 cm, and 2.5 cm, respectively.

The structural quality of the films is highest for the sample deposited with D_{TS} = 2.5 cm, as evidenced by the long-range Laue oscillations observed in the HR-XRD pattern. The film deposited with D_{TS} = 2.0 cm also exhibits Laue oscillations, although a small secondary peak appears on the right-hand side of the main Bragg reflection, suggesting the splitting of the SRO_{pc} (002) reflection. This effect becomes more pronounced for the film grown at D_{TS} = 1.5 cm, which does not show any Laue oscillations.

Despite these differences in out-of-plane coherence, the in-plane lattice parameters of all SRO films remain compressively strained and match those of the STO substrate, as confirmed by reciprocal space maps (RSMs) around the (103) reflections of both SRO film and STO substrate [Fig. 5.4(b–d)]. Together with ϕ-scan measurements (not shown), which exhibit fourfold symmetry with film and substrate peaks separated by 90°, these results confirm that all films are epitaxial and follow a cube-on-cube orientation relationship with the substrate.

The film thicknesses were determined by fitting the Kiessig fringes observed in the XRR patterns. Several layered models, based on stacked block-like layers on a substrate, were tested to best reproduce the reflectivity curves. Figure 5.4(e–j) shows the experimental XRR data, the fit accordingly to the best model (shown as insets), and the derived SLD profiles. The Kiessig fringes exhibit a significantly smaller periodicity for the film grown at D_{TS} = 1.5 cm compared with those at larger distances, confirming that this film is substantially thicker. This behavior further supports the dependence of deposition rate (and resulting film thickness) on the target–substrate distance.

Interestingly, the obtained SLD model reveals reduced-density interfaces at both the top (surface) and bottom (SRO/STO) boundaries of all films. Similar effects were reported by Młynarczyk et al. [74, 77], who observed Ru deficiency localized at the top and bottom interfaces of SRO films deposited by direct-current HOPS, while the central region retained stoichiometric composition. Such compositional modulation produces Sr enrichment at the interfaces, leading to a reduction of the local SLD relative to the bulk value. In contrast, for the present films, the reduced SLD extends throughout the entire thickness, with the central region exhibiting a value of 1.633 r_eÅ^{-3}, lower than the theoretical 1.746 r_eÅ^{-3}. This finding suggests a more extensive Ru deficiency rather than a confined interfacial effect, although a stronger reduction in Ru concentration is also observed at the interfaces. This interpretation is further supported by RBS measurements [Fig. 5.5(a–c)], which reveal Ru deficiencies of up to 25% [168].

It is believed that the discrepancy between the simulated and experimental RBS spectra below 1 MeV for the sample grown with D_{TS} = 2.5 cm arises from the stepped (terraced) surface morphology of the film. Since RBS detects the sample relative to its average surface plane, the terrace structure produces local variations in the effective scattering depth, leading to the observed modulation in the signal. Nevertheless, this effect does not significantly affect the quality of the fit for the Ru and Sr peaks.

Finally, the magnetic and electronic transport properties of the films were also investigated. The Curie temperature (T_{Curie}) was determined from magnetization versus temperature measurements [$M(T)$] [Fig. 5.6(a–c)]. Remarkably, $T_{Curie} \approx 150$ K was obtained for all samples by calculating the first derivative of $M(T)$ [Fig. 5.6(d–f)], even though a considerable Ru deficiency is present. However, an additional phase transition between 50 K and 100 K was observed in the samples deposited with D_{TS} = 1.5 cm and 2.0 cm. This feature is attributed to the antiferrodistortive (AFD) structural phase transition of STO substrates [105, 106], and can influence the magnetic response of the SRO layer through interfacial strain coupling.

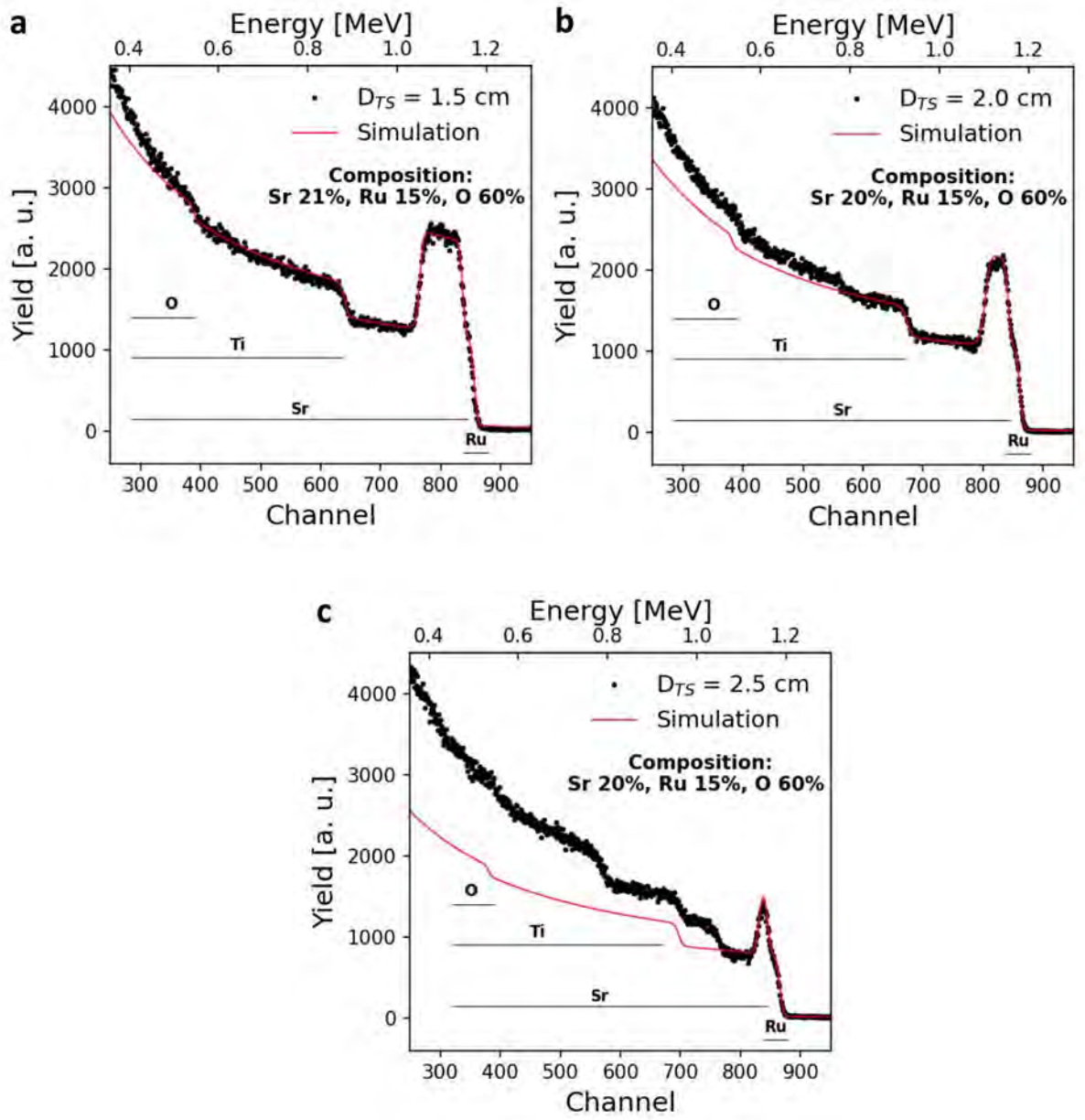

Figure 5.5.: Rutherford Backscattering spectrum and simulation of SRO thin films deposited with target-substrate distance equivalent to (a) 1.5 cm, (b) 2.0 cm and (c) 2.5 cm.

Magnetization as a function of the applied magnetic field was also measured to obtain hysteresis [$M(H)$] curves [Fig. 5.6(g–i)]. The results indicate that the films exhibit PMA, as evidenced by the slightly faster saturation and higher magnetic moment along the out-of-plane direction [field applied parallel to the crystallographic SRO_{pc} (001) axis] compared with the in-plane direction [field applied perpendicular to SRO_{pc} (001)]. Nevertheless, the saturation magnetic moment is significantly below the theoretical value of 1.63 μ_B/Ru expected for stoichiometric SRO thin films, which is a direct consequence of the Ru deficiency present in all samples.

The electronic transport properties were also strongly affected by Ru deficiency. None of the films exhibit the characteristic kink in the $\rho(T)$ curve associated with the ferromagnetic metallic transition of stoichiometric SRO near T_{Curie} [Fig. 5.6(j–l)]. Instead,

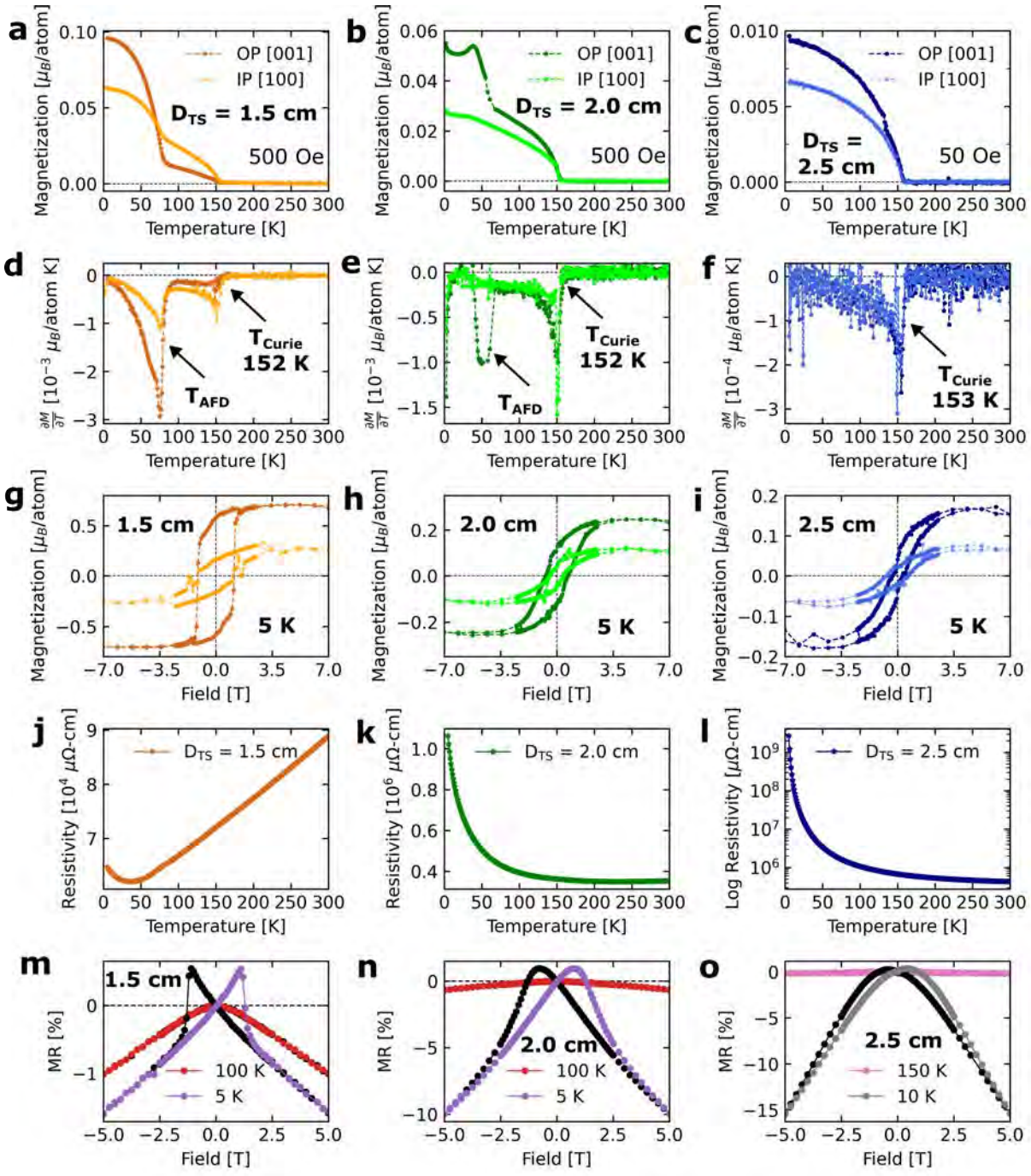

Figure 5.6.: Magnetic, transport, and magnetotransport properties of SRO thin films grown at different D_{TS}. (a–c) $M(T)$ curves. (d–f) Derivative of $M(T)$ showing $T_{Curie} \approx 150$ K for all samples and a secondary transition (50–100 K) related to the STO substrate. (g–i) $M(H)$ loops reveal perpendicular magnetic anisotropy with low saturation moments due to Ru deficiency. (j–l) $\rho(T)$ curves show no metallic transition near T_{Curie}, indicating semiconducting to insulating behavior. (m–o) Magnetoresistance is predominantly negative, dominated by spin-disorder scattering and localization from Ru vacancies. Black curves in the MR panels correspond to magnetic field sweeps from H+ to H−, and colored curves to the reverse direction (H− to H+).

$\rho(T)$ displays a semiconducting- or even insulating-like behavior, depending on D_{TS}. For the sample grown at D_{TS} = 1.5 cm, $\rho(T)$ increases monotonically with decreasing temperature, resembling a semiconducting response [Fig. 5.6(j)], whereas the samples grown at larger D_{TS} exhibit stronger localization effects and a more insulating character [Fig. 5.6(k–l)]. In addition, low residual resistivity ratios (RRR = $\rho_{300\,K}/\rho_{5\,K}$) were found. These results confirm that Ru deficiency and the associated disorder substantially suppress the metallicity and magnetic ordering of SRO films.

The magnetoresistance (MR) of the SRO films was also measured as a function of magnetic field and temperature [Fig. 5.6(m–o)]. All samples exhibit a predominantly negative MR at low temperatures, with a magnitude that increases as temperature decreases. This behavior contrasts with the linear positive MR typically observed in stoichiometric and ultrahigh-quality SRO films [85, 98], and is instead characteristic of Ru-deficient SRO [99, 101]. The disappearance of the positive linear magnetoresistance and the appearance of a negative component indicate that spin-disorder scattering becomes dominant. This behavior arises from magnetic disorder and carrier localization associated with Ru vacancies, which suppress the coherent transport characteristic of stoichiometric SRO [95, 98–100].

In summary, D_{TS} primarily controls the film morphology, crystalline quality, and deposition rate in HOPS. Among the tested conditions, D_{TS} = 2.5 cm produced the smoothest surface topography, the longest Laue oscillations, and the highest degree of epitaxial order, indicating superior structural quality. Although the magnetic and transport measurements suggest the presence of Ru deficiency, this effect originates from the high deposition temperature used in all growths rather than from D_{TS} itself. Therefore, D_{TS} = 2.5 cm was selected as the optimal geometry for subsequent optimization studies focused on the deposition temperature and oxygen pressure.

5.1.2.2. Deposition temperature

To optimize the deposition temperature (T_{dep}), four SRO films were grown at T_{dep} = 897 °C, 785 °C, 673 °C, and 560 °C, while keeping the other growth parameters constant (D_{TS} = 2.5 cm, FWDP = 100 W, and P_{O_2} = 1.5 mbar). The film grown at 785 °C was already discussed in the previous subsection. Since the substrates are placed directly on the heater block, T_{dep} is defined as the block temperature; however, the actual substrate surface temperature is approximately 80 °C lower than the indicated value, as indicated by pyrometer measurements. The SRO films were deposited on low miscut TiO_2-terminated STO (001) substrates, as shown in the AFM micrographs in Fig. 5.7(a–c).

The surface morphology of the SRO films grown at different T_{dep} values was analyzed by AFM, as shown in Fig. 5.7(d–f). Interestingly, the film deposited at 560 °C exhibits a terrace-like morphology similar to that of the STO substrate. However, the terraces are narrower and shallower than those of the substrate, likely corresponding to mixed RuO_2- and SrO-terminated regions. Although the AFM micrograph of the sample grown at 673 °C [Fig. 5.7(e)] has limited resolution, the morphology suggests a tendency toward the Stranski–Krastanov growth mode, characterized by the coexistence of continuous layers and three-dimensional islands. This is evidenced by the formation of multi-terraced islands and larger protrusions [observed as yellow spots in Fig. 5.7(e)]. As discussed in the previous subsection, the film grown at 785 °C [Fig. 5.3(e)] displays wide terraces separated by irregular step edges, consistent with a mild step-bunching growth regime. The slight accumulation of material along the terrace boundaries indicates kinetic instabilities in the

step-advance process rather than nucleation of three-dimensional islands. Finally, growth at the highest temperature (T_{dep} = 897 °C) was characterized by a pronounced island morphology (Volmer–Weber growth), with a high density of three-dimensional islands covering the surface. From these optimization results, it is clear that T_{dep} strongly affects the surface morphology of SRO films. Therefore, from a morphological point of view, T_{dep} = 785 °C represents the optimal growth temperature for obtaining smooth and continuous SRO films under such sputtering conditions.

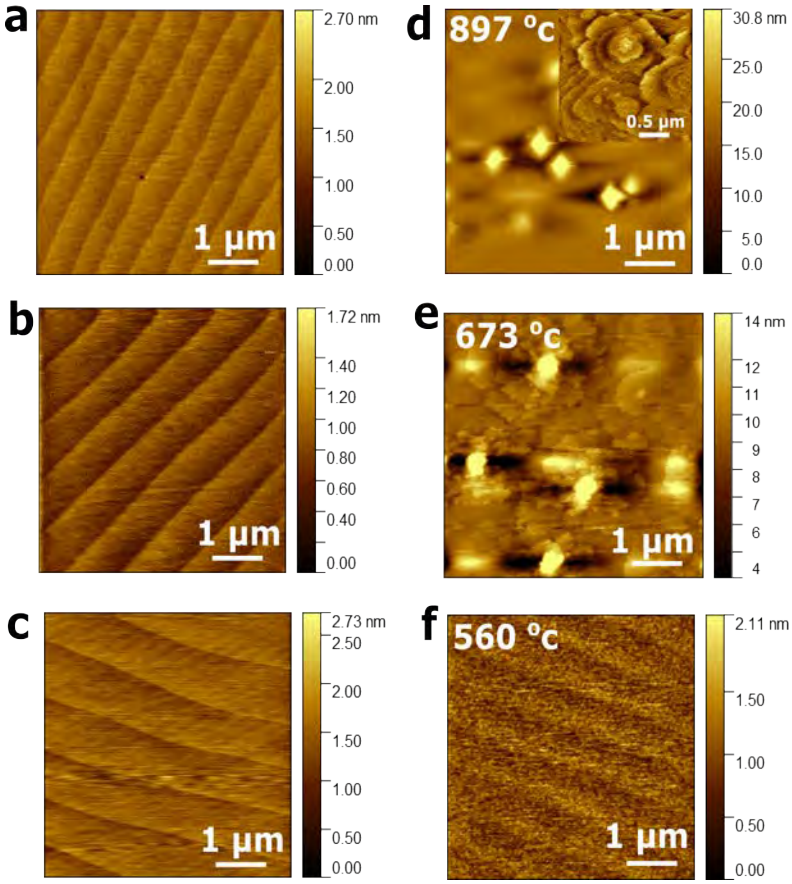

Figure 5.7.: Atomic force microscopy of (a–c) TiO_2-terminated STO substrates prior to the deposition of SRO thin films, and (d–f) corresponding SRO films grown with T_{dep} of 897 °C, 673 °C and 560 °C.

Figure 5.8(a) shows the HR-XRD patterns of the SRO films deposited at T_{dep} = 897 °C, 673 °C, and 560 °C. All films exhibit long-range Laue oscillations around the SRO_{pc} (002) reflection, with no evidence of peak splitting as observed for samples grown with $D_{TS} < 2.5$ cm. The different periodicities of the Laue oscillations arise from variations in deposition time due to experimental constraints, rather than from the deposition temperature itself. RSMs [Fig. 5.8(b–d)] and ϕ-scan measurements (not shown) confirm that all films are epitaxial, displaying cube-on-cube alignment with the STO substrate.

The XRR patterns and corresponding fits for all films investigated in this optimization step are presented in Fig. 5.8(e). The fitting procedure was carried out following the same methodology described previously, using block-like structural models with reduced SLD throughout the film thickness. This reduction in SLD is consistent with the presence of Ru deficiency, which is known to increase with deposition temperature due to the enhanced volatility of Ru.

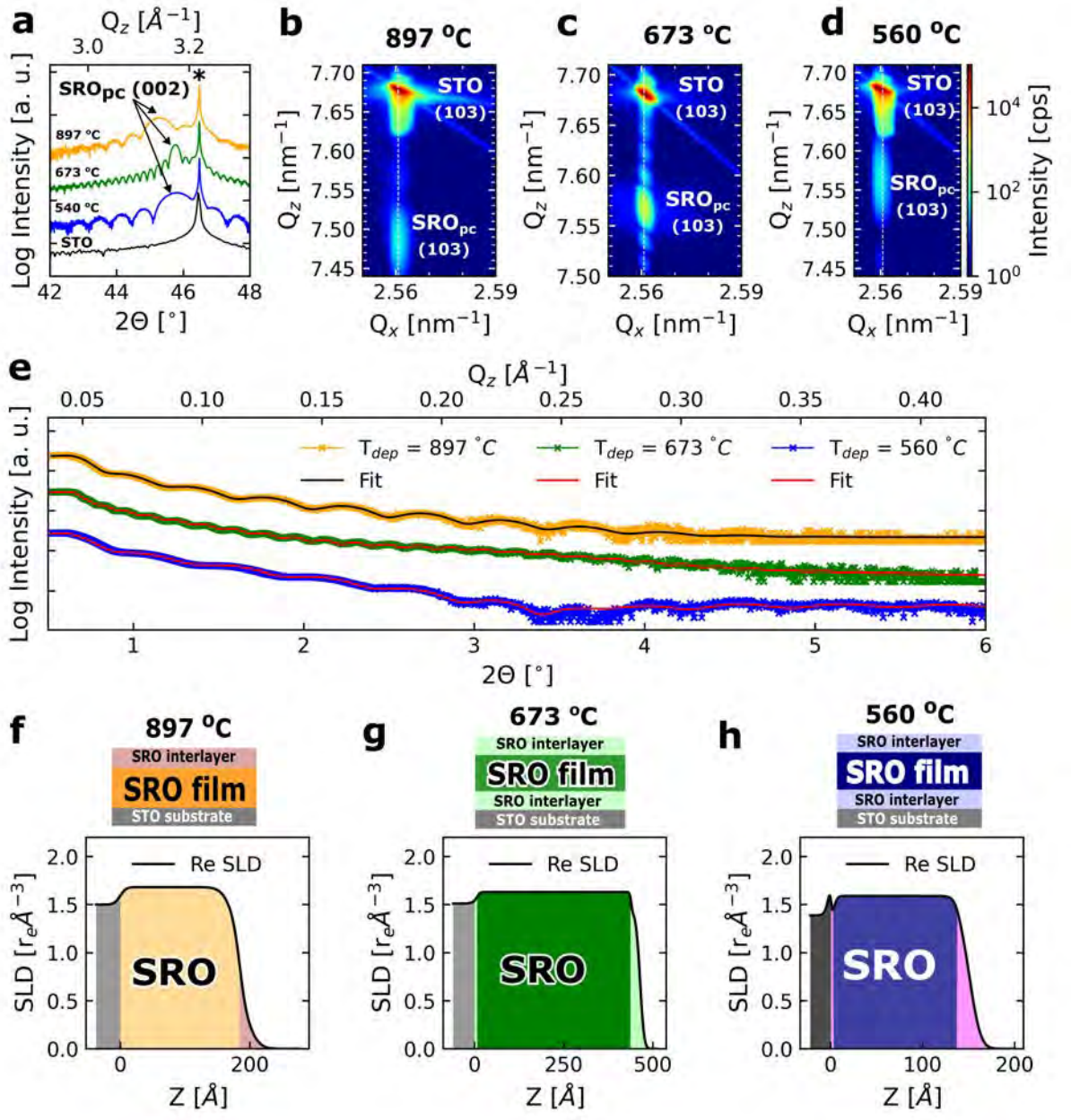

Figure 5.8.: (a) High-resolution X-ray diffraction patterns of SRO films deposited at different T_{dep} values and of the STO substrate. The asterisk indicates the STO (002) substrate peak. (b–d) Reciprocal space maps around the (103) reflection as a function of T_{dep}. The dashed white line serves as a guide to the eye. (e–j). Experimental X-ray reflectivity patterns, fit accordingly to the best block-like model (schemes), and corresponding scattering length density (SLD) profiles for T_{dep} of 897 °C, 673 °C and 560 °C.

To accurately reproduce the experimental curves, it was necessary to include interlayers at the film surface and/or at the film–substrate interface. These interlayers exhibit a strongly reduced SLD, suggesting a high concentration of Ru vacancies in these regions. Although the SLD values extracted from the fits show an overall reduction compared to the theoretical value for stoichiometric SRO, the relatively high SLD obtained for the interfaces in the film grown at 560 °C [Fig. 5.8(h)] does not fully agree with the expected strong Ru depletion. Furthermore, the quality of the fit (represented by the figure of merit in GenX) for this sample was not optimal, leaving the interpretation of these SLD variations uncertain and indicating that more accurate structural or compositional data would be required to clarify this behavior. The schematic block-like layered structures stacked on the STO substrate are also shown in Fig. 5.8(f–h).

Considering the high volatility of Ru, the T_{dep} is expected to strongly influence the structural quality of the films by promoting the formation of defects such as Ru and oxygen vacancies [75, 86]. Although the SLD profiles obtained from XRR exhibit reduced values compared with the theoretical values of a stoichiometric SRO film, the overall SLD reduction is similar for all samples grown at different T_{dep}. To further investigate this behavior, the RBS data were simulated, and the best-fitting results are shown in Fig. 5.9(a–c). Interestingly, the Ru deficiency is more pronounced in the films grown at both the highest (T_{dep} = 897 °C) and lowest (T_{dep} = 560 °C) temperatures.

At high temperature, this behavior is expected due to the thermal volatility of Ru: under oxygen-rich conditions, Ru readily forms volatile oxides such as RuO_4 and RuO_3, which desorb from the surface and lead to Ru depletion [74, 75, 77]. In contrast, the increased Ru deficiency at low temperature can be attributed to a kinetically limited incorporation regime, in which adatom mobility is reduced and RuO_x species, weakly bonded and over-oxidized, either desorb or are chemically resputtered before incorporating into the perovskite lattice. At intermediate deposition temperatures (673–785°C), the surface mobility is sufficient to promote efficient incorporation of Ru into the lattice while minimizing thermal desorption, resulting in a more stable Ru stoichiometry, even though with approximately 25% Ru deficiency [99, 168].

Despite the presence of Ru deficiency, the crystallinity of the films remains high, as evidenced by the well-defined finite-thickness (Laue) oscillations observed in the HR-XRD measurements. The only notable structural difference between stoichiometric and Ru-deficient SRO films is a slight out-of-plane lattice expansion, as previously reported by Siemons et. al [169]. These observations highlight the complex nature of disorder in SRO thin films: even in the absence of significant structural degradation, subtle deviations in stoichiometry can profoundly affect the electronic and magnetic properties. This finding is consistent with the broader understanding of SRO epitaxy, where the material's crystallinity can remain robust despite considerable Ru deficiency, while its transport and magnetic characteristics are highly sensitive to such non-stoichiometry [75].

Regarding the magnetic properties, the samples grown at 673 °C and 785 °C exhibit the same T_{Curie}, approximately 153 K, as determined from the first derivative of $M(T)$ curves [Fig. 5.10(d–f)]. The corresponding $M(T)$ curves are shown in Fig. 5.10(a–c), with additional data for the T_{dep} = 785 °C sample presented in Figs. 5.6(c, f). Because the magnetization curves obtained under an in-plane (IP) magnetic field do not display a well-defined magnetic transition, Fig. 5.10(d, f) presents only the out-of-plane (OP) data, which reveal a broad but still discernible magnetic transition. From the $M(T)$ and hysteresis $M(H)$ measurements [Figs. 5.10(g–i) and 5.6(i)], it can be concluded that all samples exhibit PMA, which is more clearly distinguished for intermediate T_{dep} values. In

this optimization step, only the SRO film grown at 673°C exhibited the AFD structural phase transition, suggesting that this transition might be substrate-dependent.

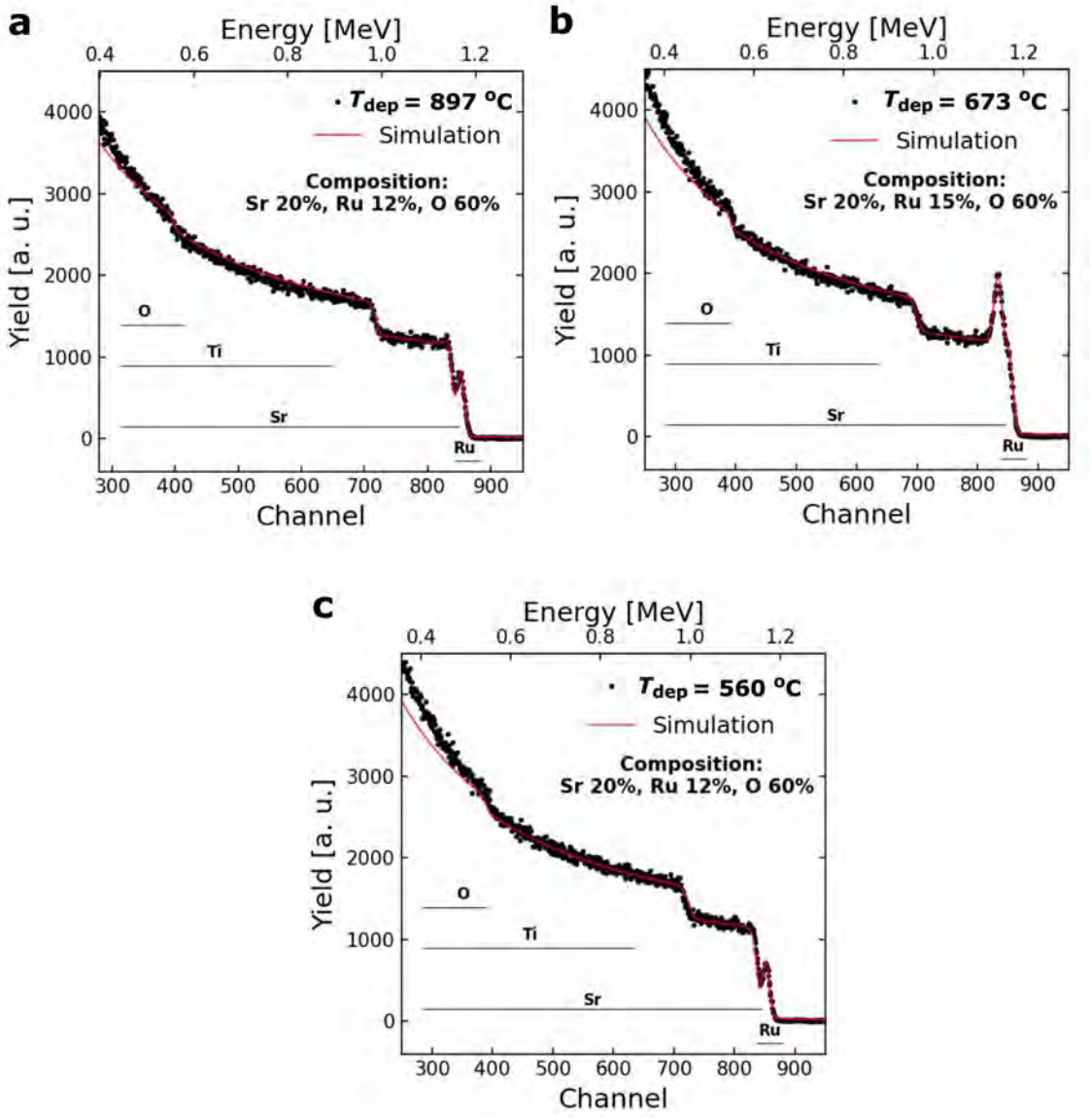

Figure 5.9.: Rutherford Backscattering spectra and simulation of SRO thin films deposited at T_{dep} equivalent to (a) 897 °C, (b) 673 °C and (c) 560 °C.

Electronic transport measurements yield similar results, characteristic of semiconducting or insulating thin films, as evidenced by the temperature dependence of the resistivity $\rho(T)$ [Fig. 5.10(j-l)]. Although subtle, the resistivity is higher at low temperatures for the films grown at 897°C and 560°C. In all cases, the RRR is extremely low, consistent with the presence of structural defects that enhance electron scattering. All samples exhibit a predominantly negative MR at low temperatures [Fig. 5.10(m-o)], with a magnitude that increases as temperature decreases, similar to the results obtained in the D_{TS} optimization. The disappearance of the positive linear MR and the emergence of a negative component indicate that spin-disorder scattering becomes dominant. As mentioned before, this behavior arises from magnetic disorder and carrier localization associated with Ru vacancies, which suppress the coherent transport characteristic of stoichiometric SRO [95, 98–100].

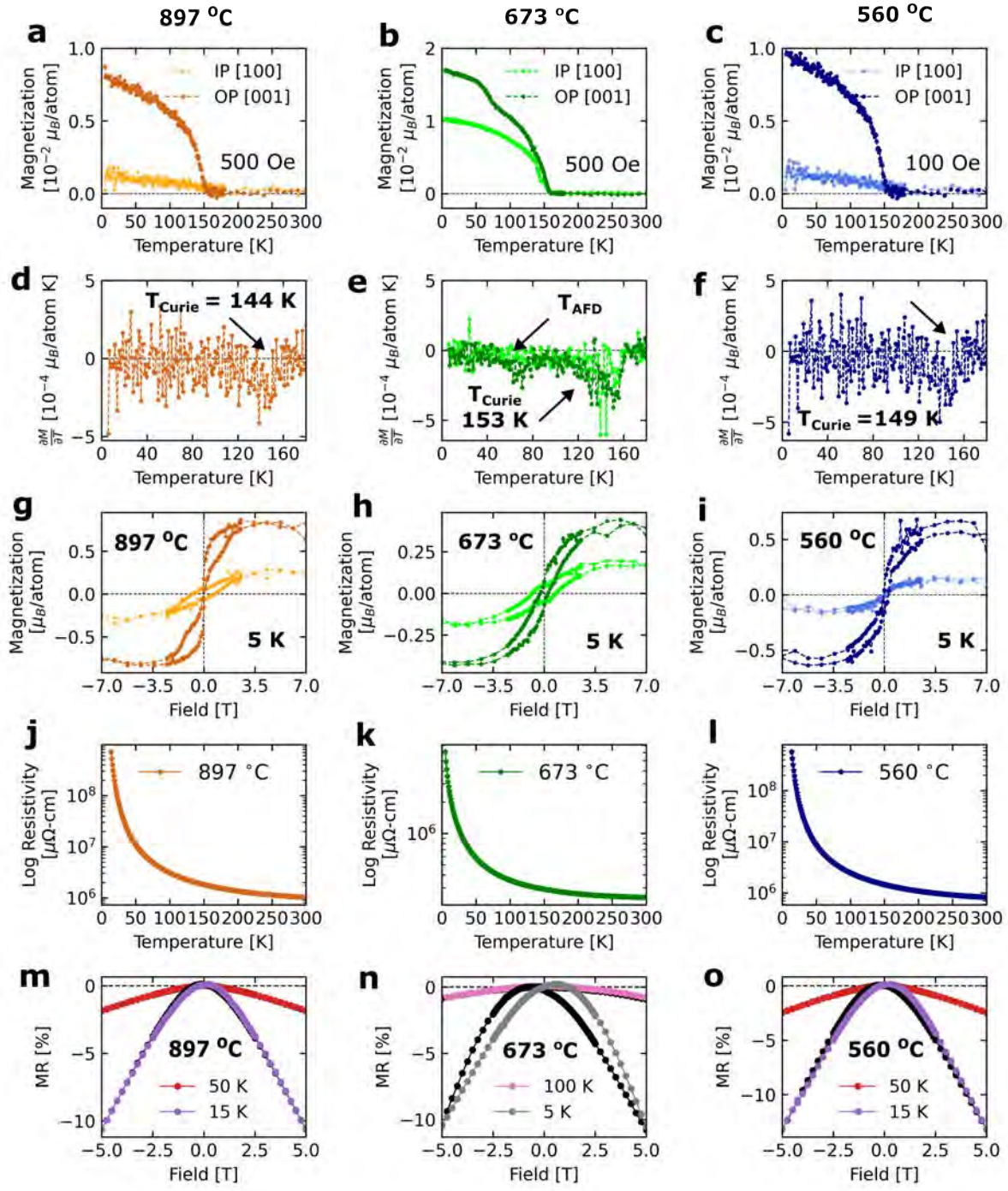

Figure 5.10.: Magnetic, transport, and magnetotransport properties of SRO thin films grown at different T_{dep} values. (a–c) $M(T)$ curves. (d–f) First derivative of $M(T)$ showing $T_{\mathrm{Curie}} \approx 153$ K for films grown at several values of T_{dep}. (g–i) $M(H)$ loops reveal perpendicular magnetic anisotropy, most pronounced for intermediate T_{dep}. (j–l) $\rho(T)$ curves indicate semiconducting to insulating behavior. (m–o) Magnetoresistance is predominantly negative and increases in magnitude at low temperatures, dominated by spin-disorder scattering and carrier localization due to Ru vacancies.

Overall, T_{dep} plays a decisive role in determining the growth mode, surface morphology, stoichiometry, and physical properties of SRO thin films. Both excessively high and low T_{dep} values lead to Ru deficiency through distinct mechanisms: at high temperature, Ru volatility and the formation of volatile RuO_x species (RuO_3, RuO_4) dominate, whereas at low temperature, limited adatom mobility and chemical re-sputtering hinder full Ru incorporation into the perovskite lattice. Between 673 °C and 785 °C lies a kinetic–thermodynamic "window of compromise", where surface diffusion is sufficient for Ru to occupy its proper lattice site before over-oxidizing or desorbing. Films grown within this temperature range exhibit the smoothest morphology, the highest structural coherence, and the most stable ferromagnetic behavior, defining the optimal growth conditions for the growth of subsequent SRO films.

5.1.2.3. Pressure and forward power

Once the parameters D_{TS} and T_{dep} were optimized, the remaining variables to be adjusted were the oxygen partial pressure (P_{O_2}) and the forward RF power (FWDP), which defines the amount of energy delivered to sustain the plasma. Because P_{O_2} and FWDP are strongly correlated, and both directly influence the plasma shape, density, and stability, they were optimized simultaneously. The reflected power (REFP), which indicates impedance mismatch between the generated plasma and the matching network circuit caused, for instance, by variations in oxygen pressure, ion density, or chamber geometry, was continuously monitored and maintained at zero during all experiments. Therefore, REFP values are not explicitly reported in this thesis.

At high oxygen pressure, Ru vacancies are unavoidable, regardless of the Sr:Ru ratio in the sputtered vapor phase [75]. Thus, this optimization step was not expected to yield stoichiometric SRO films but was performed for completeness and systematic evaluation of the growth parameters. Thin films of SRO were deposited on low-miscut TiO_2-terminated STO (001) substrates while keeping D_{TS} = 2.5 cm and T_{dep} = 785 °C fixed. Two growth conditions were investigated: (FWDP, P_{O_2}) = (150 W, 2.5 mbar) and (125 W, 2.0 mbar). Although higher FWDP values are technically achievable with the RF generator, the corresponding higher P_{O_2} values required to maintain a stable plasma could not be reached. At pressures above 2.5 mbar, the turbo pump backing the screw pump begins to stall, even when the bypass valve is almost fully closed. Therefore, higher combinations of FWDP and P_{O_2} were not explored, as they could potentially damage either the HOPS system or the SRO target.

Unfortunately, due to the temporary malfunction of the AFM, topographical characterization of the substrates and the corresponding films could not be performed. From a structural point of view, both samples exhibit long-range Laue oscillations [Fig. 5.11(a)] and are epitaxial, with in-plane lattice parameters compressively strained by the STO substrate, as shown by the RSMs [Fig. 5.11(b–c)]. The films grow in a cube-on-cube orientation, and, similar to the temperature optimization series, no splitting of the SRO_{pc} (002) reflection was observed, confirming the effective optimization of D_{TS} and T_{dep}.

Interestingly, the deposition rate increased even though the D_{TS} distance remained fixed. This effect is attributed to the higher FWDP, which enhances the ion energy and consequently the sputtering yield of the target. Analysis of the XRR patterns [Fig. 5.11(d)] shows that both films are Ru-deficient throughout their thickness, as indicated by the reduced SLD values, with a stronger deficiency near the film surface. In the best-fitting models for both samples, a single interlayer at the film surface was

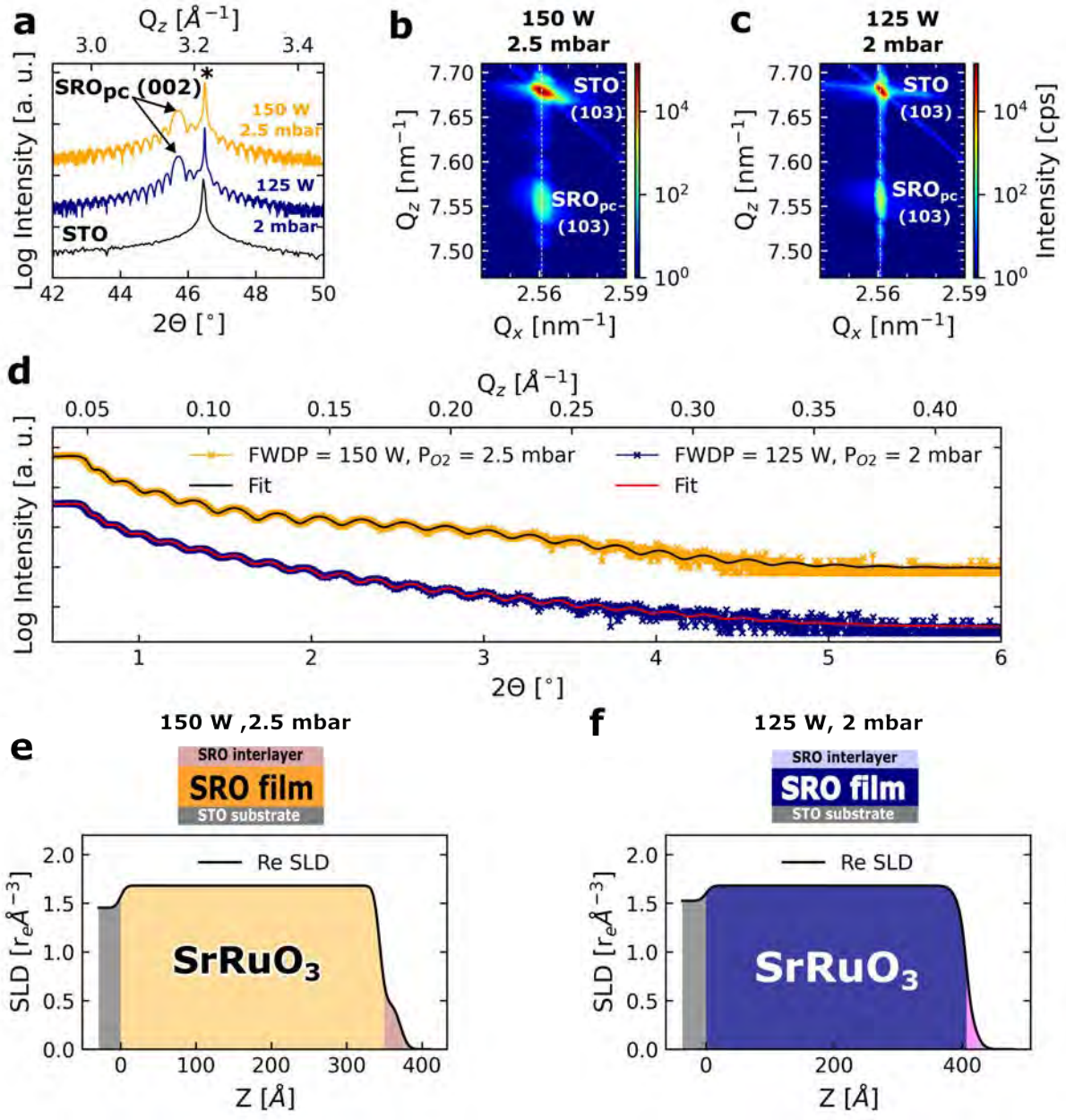

Figure 5.11.: (a) High-resolution X-ray diffraction patterns of SRO films deposited with (FWDP, P_{O_2}) = (150 W, 2.5 mbar), (125 W, 2.0 mbar), and of the STO substrate. The asterisk indicates the STO (002) substrate peak. (b–c) Reciprocal space maps around the (103) reflection. (d) Experimental and fitted X-ray reflectivity patterns, and (e, f) the corresponding SLD profiles.

sufficient to reproduce the experimental curves, suggesting that higher FWDP and P_{O_2} values may enhance the structural uniformity near the film–substrate interface and improve the overall layer definition. However, this hypothesis should be further verified by high-resolution transmission electron microscopy (HR-TEM) combined with chemical composition analysis.

The Ru deficiency was confirmed by RBS measurements [Fig. 5.12]. Interestingly, the film deposited under (FWDP, P_{O_2}) = (125 W, 2.0 mbar) exhibited a significant improvement in Ru stoichiometry, with a deficiency of approximately 17%, compared to 13% for the film deposited at (150 W, 2.5 mbar). This represents a notable enhancement when compared with the ~25% Ru deficiency observed in the D_{TS} and T_{dep} optimization series, where the films were grown with (FWDP, P_{O_2}) = (100 W, 1.5 mbar) under otherwise similar conditions. However, the origin of this improvement is not yet clear and may arise from a complex interplay between plasma density, ion energy, and oxygen activity.

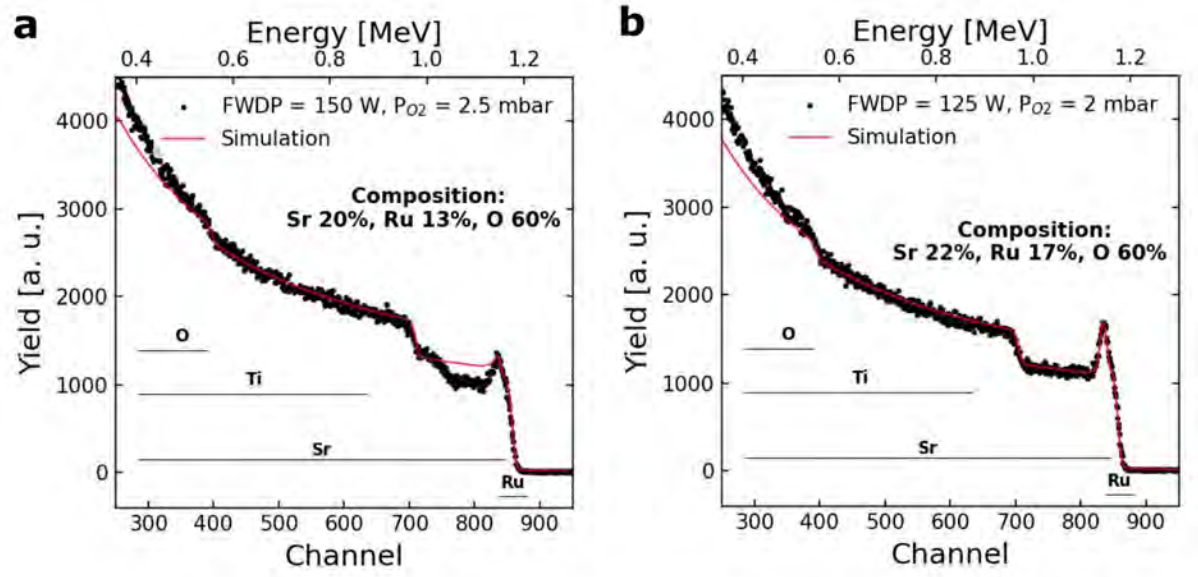

Figure 5.12.: Rutherford Backscattering spectra and simulation of SRO thin films deposited with (FWDP, P_{O_2}) of (a) (150 W, 2.5 mbar) and (b) (125 W, 2.0 mbar).

A possible explanation is that this intermediate combination of (FWDP, P_{O_2}) modifies the plasma chemistry, reducing the formation and re-sputtering of volatile RuO_x species (particularly RuO_4) from the growing surface, thereby enhancing Ru incorporation. Although the RBS results indicate an overall improvement in stoichiometry, the XRR analysis [Fig. 5.11(d)] reveals a more pronounced Ru deficiency near the film surface. This apparent discrepancy suggests that, while this combination of (FWDP, P_{O_2}) reduces global re-sputtering and improves bulk Ru incorporation, local chemical instabilities at the surface, possibly related to RuO_x desorption during post-growth oxidation (cooling), still lead to the formation of a Ru-depleted surface layer. Further high-resolution structural and compositional analyses are required to confirm this hypothesis.

Magnetic, transport, and magnetotransport properties of SRO films prepared at higher (FWDP, P_{O_2}) values were investigated [Fig. 5.13]. Similar to the optimization series discussed previously, both samples are ferromagnetic and exhibit PMA. The film deposited under (FWDP, P_{O_2}) = (150 W, 2.5 mbar) shows the highest T_{Curie} among all optimized

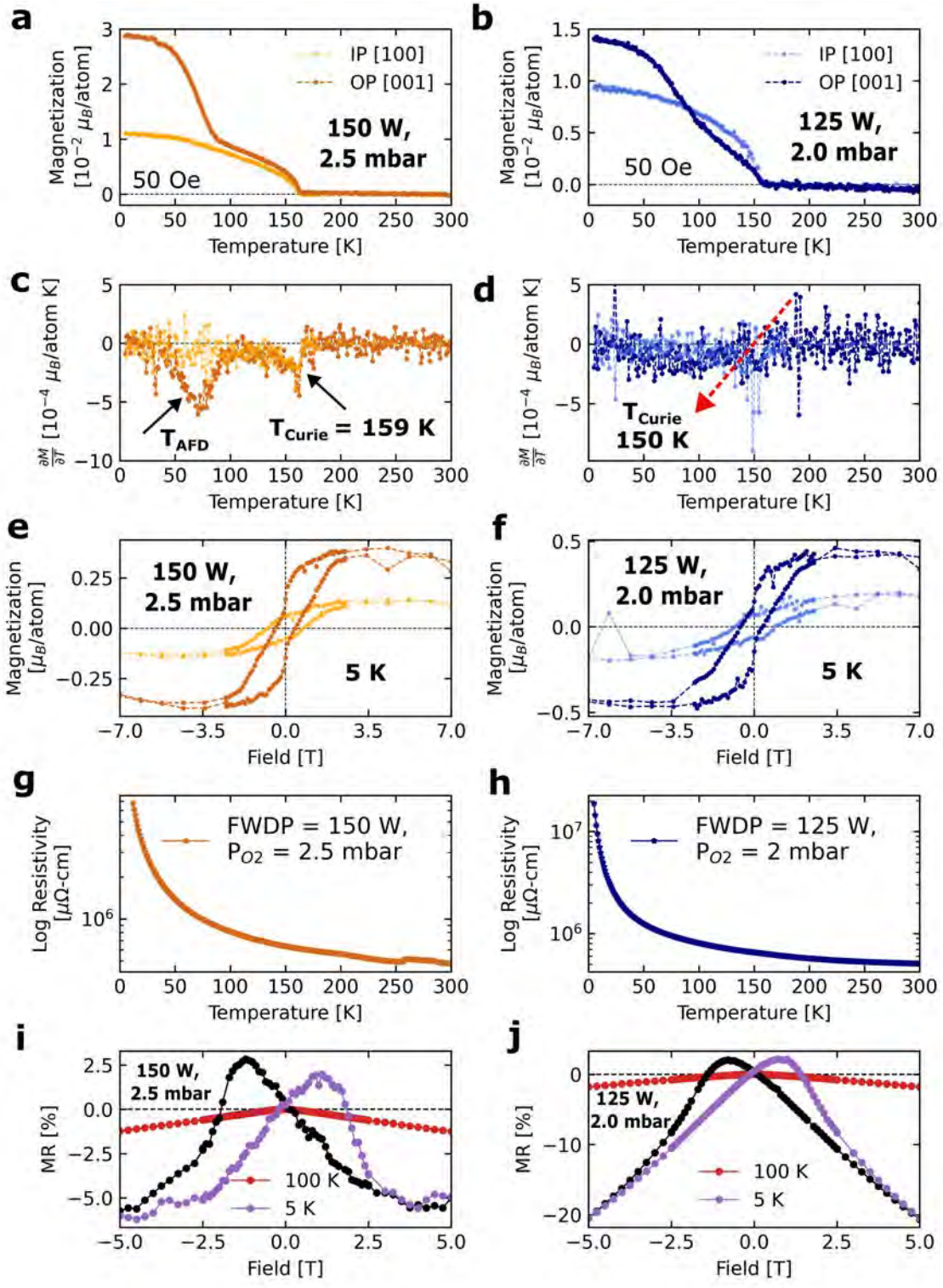

Figure 5.13.: Magnetic, transport, and magnetotransport properties of SRO thin films grown at different (FWDP, P_{O_2}). (a–d) $M(T)$ and corresponding derivatives showing T_{Curie} for both films. (e–f) $M(H)$ confirm perpendicular magnetic anisotropy. (g–h) Resistivity $\rho(T)$ curves display semiconducting or weakly insulating behavior with low residual resistivity ratios. (i-j) Magnetoresistance curves are predominantly negative and increase in magnitude at low temperatures.

samples, reaching 159 K [Fig. 5.13(a, c)]. In contrast, the sample grown at (125 W, 2.0 mbar) displays a well-defined magnetic transition near 150 K [Fig. 5.13(b, d)], although the feature is less evident in the first derivative of $M(T)$ (the dashed red arrow serves as a guide to the eye). PMA is further confirmed by the magnetic hysteresis $M(H)$ loops [Fig. 5.13(e–f)]. Similar as before, only the SRO film grown at (FWDP, P_{O_2}) = (150 W, 2.5 mbar) exhibited the AFD structural phase transition, corroborating the substrate-dependent effect.

As in the previous cases, the temperature dependence of resistivity $\rho(T)$ is characteristic of semiconducting or weakly insulating behavior, and very low RRR were obtained. The magnetotransport response is also similar to the earlier optimization series, with predominantly negative MR that increases in magnitude as the temperature decreases. Notably, the butterfly-shaped MR curves exhibit maxima at fields larger than the coercive fields extracted from the corresponding $M(H)$ loops, indicating that the MR response is not solely governed by magnetization reversal processes but also involves contributions from carrier localization, anisotropic magnetoresistance (AMR), and spin-disorder scattering associated with Ru vacancies [98, 99, 170, 171].

In summary, although the intermediate condition (FWDP, P_{O_2}) = (125 W, 2.0 mbar) resulted in a slightly improved Ru stoichiometry compared to the higher-power regime, the physical origin of this behavior remains unclear. It likely results from complex interactions among plasma chemistry, oxygen activity, and Ru volatility that are not yet fully understood. A comprehensive investigation of these effects would require detailed plasma diagnostics and systematic control of the sputtering parameters over a broad experimental range, including the deposition and characterization of a large number of samples. Such a study, while essential and scientifically valuable, is also extremely time-consuming and extends beyond the scope of this Ph.D. project, being more appropriately addressed through a dedicated instrumentation-focused investigation. For this reason, and to ensure stable and reproducible plasma conditions during subsequent growth experiments, the standard parameters (FWDP, P_{O_2}) = (100 W, 1.5 mbar) were adopted for all further depositions.

5.2. $SrRuO_3$ thin films prepared from a Ru–enriched target

The use of a Ru-enriched $SrRuO_3$ target was motivated by the aim of determining whether an excess of Ru could compensate for the losses associated with its high volatility at elevated deposition temperatures, potentially yielding films closer to stoichiometric composition.

This investigation was initiated after the growth and characterization of the superconductor/ferromagnet heterostructures for the proximity effect studies had already been completed and the corresponding results were under discussion. Consequently, the SRO ferromagnetic layers used in those heterostructures were deposited from the stoichiometric target discussed in Section 5.1 and are therefore Ru-deficient, with all the implications associated with this deficiency.

Although this study is not part of the main scope of the present work, it became a necessary effort driven by the difficulties encountered in obtaining stoichiometric SRO films with optimal physical properties. The optimization of deposition parameters and the subsequent characterization of films grown from both stoichiometric and Ru-enriched

target are highly time-consuming tasks, which could not be fully completed within the timeframe of this Ph.D. project. Nevertheless, the results presented here provide an important complementary assessment, demonstrating the extent of the efforts undertaken to improve the structural and physical quality of SRO films grown by HOPS.

5.2.1. Plasma stoichiometry characterization

A $SrRu_{1.4}O_3$ (hereafter referred to as SRO-143) target was purchased from Koshima Manufacturing Co. Ltd., with a nominal purity of 99.9% (3N). According to the manufacturer, the target composition may contain a slight excess of RuO_2, which could influence the plasma chemistry and deposition kinetics. Unfortunately, due to limited instrument access at the collaborating institutes, the microstructure and stoichiometry of the target could not be directly examined by SEM/EDS, which limits the accuracy of the subsequent stoichiometric assessment.

As mentioned before, the relative sputter yields of Sr and Ru depend on the ion energy and scattering cross sections, while the high oxygen partial pressure can further modify the cation flux by oxidizing the target surface and forming volatile RuO_x species. As a result, the plasma composition and the resulting flux toward the substrate are expected to reflect the target stoichiometry only partially. To assess this relationship, a thin SRO-143 film was deposited on a Si substrate at room temperature under the optimized conditions determined in the previous section: $D_{TS} = 2.5$ cm and (FWDP, P_{O_2}) = (100 W, 1.5 mbar), using an RF plasma generator.

Since the target composition could not be measured directly by SEM-EDS, the effective plasma stoichiometry was inferred from the composition of the film deposited at room temperature, where thermal diffusion and re-evaporation are minimized. This approach provides an indirect estimation of whether the cation flux from the plasma, and consequently the film composition, approaches the nominal stoichiometry reported by the manufacturer, corresponding to approximately 40% excess Ru.

The deposition rate using the SRO-143 target was lower than that obtained with the stoichiometric target under identical HOPS conditions, even though the overall appearance of the plasma was very similar in both cases [see Fig. 3.4(a)]. The lower deposition rate may reflect differences in target microstructure and/or electrical conductivity that influence the sputtering yield. The RBS spectrum and corresponding fit for a film grown on Si at room temperature are shown in Fig. 5.14(a). From the extracted composition (20% Sr, 26% Ru, and 60% O), the Sr:Ru ratio indicates an effective Ru enrichment of approximately 30%, somewhat below the nominal 40% specified for the target.

To obtain depth-dependent information, XRR was performed on the same film, as shown in Fig. 5.14(b). The best-fitting block-like model required two interlayers, one at the free surface and one at the film–substrate interface. The resulting SLD profile indicates a film with SLD closer to the theoretical SLD of stoichiometric SRO (a modest improvement relative to the stoichiometric target series), while both interfaces exhibit a pronounced reduction in SLD. This behavior suggests a lower Ru concentration near the interfaces, consistent with a compositional gradient along the film thickness. Given that the film was deposited at room temperature, such variation cannot be attributed to thermal diffusion or kinetic effects during growth, but rather to plasma-related instabilities that lead to temporal fluctuations in the Sr:Ru ratio during sputtering.

Taken together, RBS (depth-averaged) and XRR (depth-resolved) analyses indicate that the Ru content achieved with the Ru-enriched target approaches, but does not fully

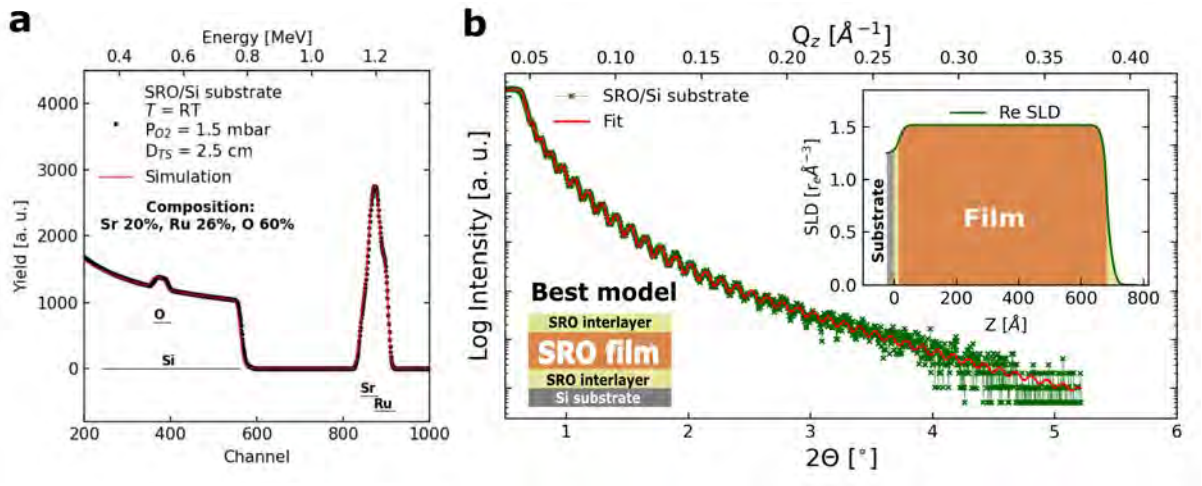

Figure 5.14.: (a) Rutherford Backscattering spectroscopy spectrum of a SRO film grown from a Ru-enriched target on a Si substrate at room temperature and its simulated fit. (b) Experimental X-ray reflectivity curve and corresponding fit; inset shows the derived scattering length density (SLD) profile.

reach, the nominal 40% excess. Therefore, the actual cation flux may differ from the nominal target composition, which must, in the future, be determined. Additional compositional probes, such as EDS in Scanning Transmission Electron Microscopy (STEM), X-ray Photo-emission spectroscopy (XPS) or Time-of-Flight Secondary Ion Mass Spectrometry (ToF-SIMS) depth profiling, and High-Resolution Transmission Electron Microscopy and Electron Energy Loss Spectroscopy (HR-TEM/EELS) at the interfaces, would be valuable to confirm the inferred compositional gradients and local oxygen content.

5.2.2. Optimization of the growth temperature

To better understand which T_{dep} defines the kinetic–thermodynamic window that best balances Ru volatility at high temperature and adatom mobility at low temperature, a quick optimization step was carried out in which T_{dep} was varied over the range 560, 673, 785, 897, and 975 °C.

Considering the similarities between the plasmas generated from the stoichiometric and Ru-enriched SRO targets, although their chemical compositions differ, the target–substrate distance, forward power, and oxygen partial pressure were kept fixed at D_{TS} = 2.5 cm and (FWDP, P_{O_2}) = (100 W, 1.5 mbar), as defined in Section 5.1. These samples were deposited on STO substrates with TiO_2-terminated surfaces exhibiting well-defined terraces [Fig. 5.15]. The substrate shown in Fig. 5.15(e) exhibits some deviation from ideal surface termination; however, the film grown on it still displayed a smooth and homogeneous morphology. During this optimization process, some experimental limitations were encountered: RBS and SQUID magnetometry were not available at that time. Therefore, the samples were characterized only by AFM, HR-XRD, and electrical and magnetotransport measurements.

The surface morphology of the SRO films grown at different T_{dep} values was analyzed by AFM, as shown to the right of the corresponding STO substrates in Fig. 5.15. The surface topography is clearly dependent on the deposition temperature. At 560 °C [Fig. 5.15(b)],

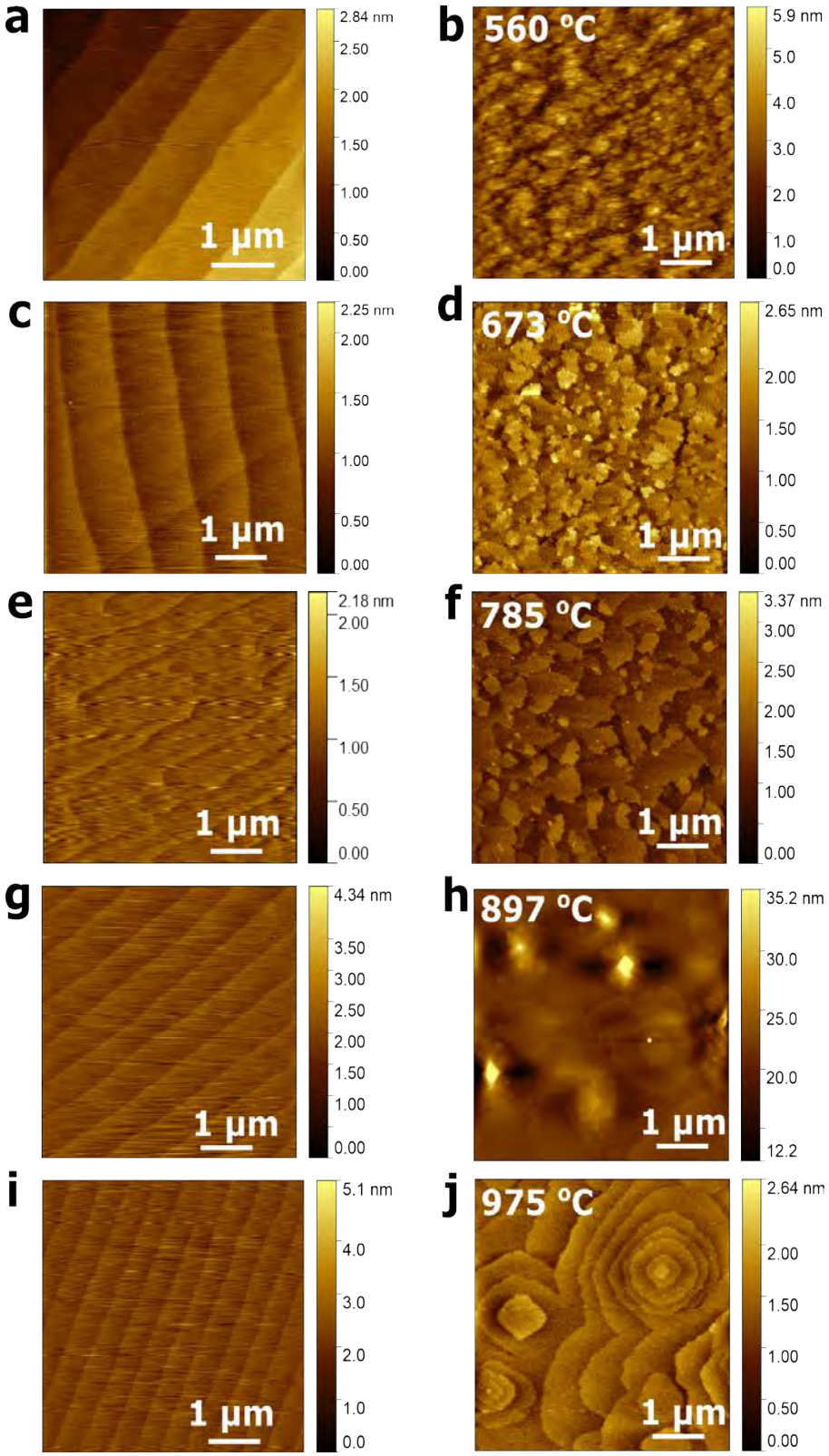

Figure 5.15.: Atomic force microscopy images of TiO_2-terminated STO substrates (a, c, e, g, i) and corresponding SRO thin films (b, d, f, h, j) grown from the SRO-143 target at different deposition temperatures (T_{dep} = 560, 673, 785, 897, and 975 °C). The surface morphology strongly depends on T_{dep}.

the film appears nearly uniform over the substrate, with no evident step edges or islands, making it difficult to identify a distinct growth mode. At 673 °C [Fig. 5.15(d)], the morphology begins to show the formation of steps and terraces, although not yet continuous or aligned in a well-defined direction. The surface at 785 °C [Fig. 5.15(f)], in contrast, exhibits a much clearer terraced structure, following the miscut direction of the substrate. The terrace edges are slightly irregular, and a small accumulation of material is observed near the step boundaries, indicating a mild step-bunching growth regime. For these three temperatures, the local roughness remains low, suggesting smooth film surfaces. At 897 °C, the local roughness increases significantly due to the presence of multi-terraced islands and larger protrusions [highlighted as yellow regions in Fig. 5.15(h)], characteristic of a transition to a Stranski–Krastanov growth mode. Finally, the film grown at the highest temperature (T_{dep} = 975 °C) shows a fully developed three-dimensional island morphology, typical of Volmer–Weber growth, with a high density of isolated crystallites covering the surface. Therefore, from a morphological point of view, T_{dep} = 785 °C still represents the optimal growth temperature for obtaining smooth and continuous SRO films under such sputtering conditions.

The crystalline structure of the SRO films grown at different T_{dep} values was characterized by HR-XRD, as shown in Fig. 5.16(a). All samples display clear Laue oscillations around the SRO_{pc} (002) reflection, confirming their high structural quality and smooth interfaces. A systematic shift of the Bragg peak position with T_{dep} is observed, indicating a dependence of the out-of-plane lattice parameter on the deposition temperature. The film grown at 785 °C exhibits a slight shift toward higher 2θ values, corresponding to a smaller lattice spacing, whereas the films deposited at other temperatures show a shift toward lower angles. These variations in lattice parameter may be related to Ru deficiency in the films [169].

Siemons et al. reported that, although the crystallinity of the films remains high, as evidenced by the Laue oscillations in the HR-XRD patterns, the only notable structural difference between stoichiometric and Ru-deficient SRO films is a slight out-of-plane lattice expansion [169]. The films are epitaxial, as confirmed by RSMs analysis [Fig. 5.16(d) for the sample deposited at 785 °C] and ϕ-scan measurements (not shown). Here is important to declare that due to the thin film thickness and to the limited dynamical range of the difractometer detector, two RSM maps (one at the STO reflection and another at the SRO film reflection) were necessary to measure the samples. This explains the two intensity color bars in Fig. 5.16(d).

In addition, a weak and broadened contribution from RuO_2 is detected only for the film grown at 785 °C [Fig. 5.16(a)], suggesting the presence of a small amount of amorphous RuO_x phase formed under this specific growth condition. This feature may be associated with the nominal RuO_2 excess in the Ru-enriched SRO target, as indicated by the manufacturer, which could favor the segregation or partial oxidation of Ru at intermediate deposition temperatures. However, no structural variation was identified in the block-like model used to fit the XRR data [Fig. 5.16(c)] as a result of this RuO_2 contribution.

The XRR data were analyzed using a block-like model consisting of a film with reduced SLD on a substrate and a surface layer with a strongly reduced SLD value. In general, all films exhibit SLD values lower than the theoretical one for stoichiometric SRO, indicating a Ru deficiency in the samples. This interpretation is consistent with the HR-XRD results [Fig. 5.16(a)], where the SRO_{pc} (002) Bragg peaks are slightly shifted toward lower 2θ angles, confirming an out-of-plane lattice expansion associated with Ru deficiency. Interestingly, in the present optimization step, the best-fitting model for all samples,

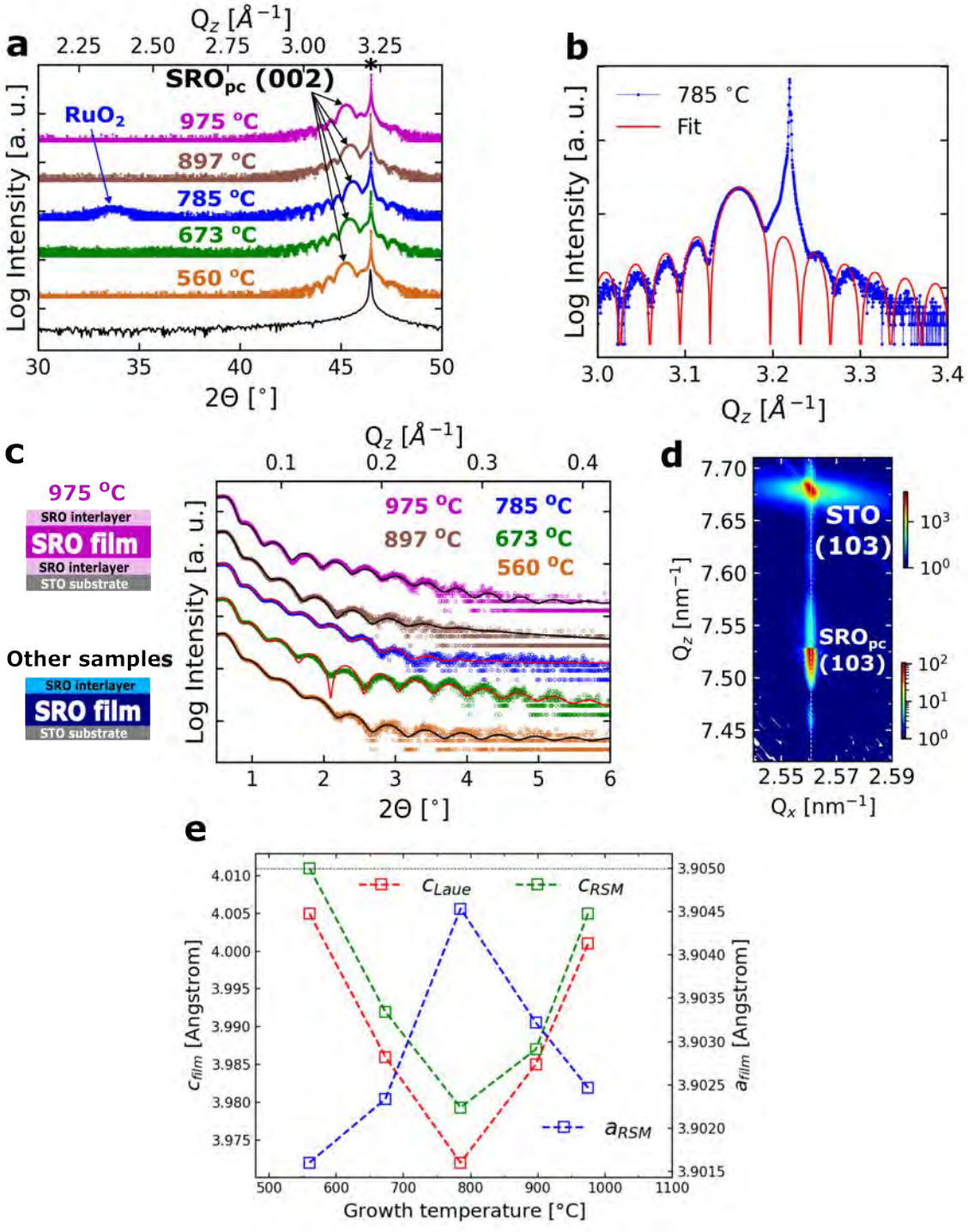

Figure 5.16.: (a) High-resolution X-ray diffraction patterns of Ru-enriched SRO films grown at different deposition temperatures (T_{dep}). (b) Fit of the Laue Oscillations performed according to the Ref. [172, 173]. (c) Experimental and fitted X-ray reflectivity curves and the corresponding block-like models used. (d) Reciprocal space map around the (103) reflection of the film prepared at 785 °C. (e) Temperature dependence of the lattice parameters a_{RSM} and c_{RSM} (from RSM) and c_{Laue} (from Laue oscillations). The dashed line in (e) indicates the STO lattice parameter value (a = 3.905 Å).

except the one deposited at the highest temperature, required only a single interlayer, located at the film surface, rather than two, as used in previous section. This observation suggests that both the Ru enrichment in the target and the deposition temperature influence the film growth mechanism and interfacial structure, possibly by modifying the way Ru incorporates during nucleation and the subsequent evolution of surface roughness and density across the film. However, such a conclusion cannot be firmly drawn based solely on this optimization step, and further investigations are required to confirm this behavior.

Since RBS measurements were not available and the reduction in SLD showed a similar dependence for all deposited samples, it was difficult to directly infer their stoichiometry. To address this limitation and indirectly evaluate the degree of Ru deficiency, an analysis similar to that performed by Siemons et al. [169] was carried out. Accordingly, the out-of-plane lattice parameter c_{Laue} was obtained from the fitting of the Laue oscillations [Fig. 5.16(b)] in the HR-XRD patterns using the methodology described in Refs. [172, 173], and its dependence on the deposition temperature is plotted in Fig. 5.16(e). To further increase the reliability of this analysis, the intensity profiles of both the asymmetric reflections of the SRO film and the STO substrate were fitted in the RSMs around the (103) reflection as a function of Q_x and Q_z. From these fits, the lattice parameters c_{RSM} and a_{RSM} for both the film and the substrate were determined. The temperature dependence of the film lattice parameters obtained from the RSM is also shown in Fig. 5.16(e).

The extracted lattice parameters reveal a clear dependence on the deposition temperature, with the film out-of-plane lattice parameter (c_{film}) expanding at both low and high T_{dep}, and reaching a minimum in the intermediate range of temperature (785 °C). This trend mirrors the behavior reported by Siemons et al. [169] and Wakabayashi et al. [99], where Ru deficiency was shown to correlate with a tetragonal distortion characterized by out-of-plane lattice expansion and in-plane lattice compression, while stoichiometric films retain a nearly cubic symmetry with $c \approx 3.949$ Å. Therefore, the correlation between the structural evolution observed here and the optimized temperature window strongly supports the interpretation that the SRO films grown at intermediate T_{dep} values exhibit the lowest Ru deficiency, whereas those deposited at the temperature extremes suffer from cation non-stoichiometry and enhanced structural distortion. Nevertheless, even the film grown at 785 °C, corresponding to the optimal growth condition within this study, still displays a slightly larger out-of-plane lattice parameter than the stoichiometric value, indicating that it remains Ru-deficient despite its improved structural and morphological quality.

As SQUID magnetometry measurements were not available, information about T_{Curie} and magnetization cannot be drawn. However, the electrical transport and magnetoresistance data provide clear evidence of the Ru-deficient character of the films [Fig. 5.17]. The temperature dependence of the resistivity, $\rho(T)$, exhibits a semiconducting to insulating behavior for all samples, consistent with enhanced scattering and carrier localization induced by Ru vacancies. At low temperatures, the magnetoresistance (MR) is predominantly negative and displays a butterfly-like shape with a small hysteretic component between the $H^+ \rightarrow H^-$ and $H^- \rightarrow H^+$ sweeps. This feature is characteristic of anisotropic magnetoresistance (AMR) arising from the rotation of the magnetization vector during field reversal and is indicative of ferromagnetic ordering dominated by spin-disorder scattering rather than the positive, linear MR typical of stoichiometric SRO. Overall, these results confirm that, despite preserving ferromagnetism, the SRO films deposited from the SRO-143 target remain Ru-deficient and exhibit a more localized electronic character.

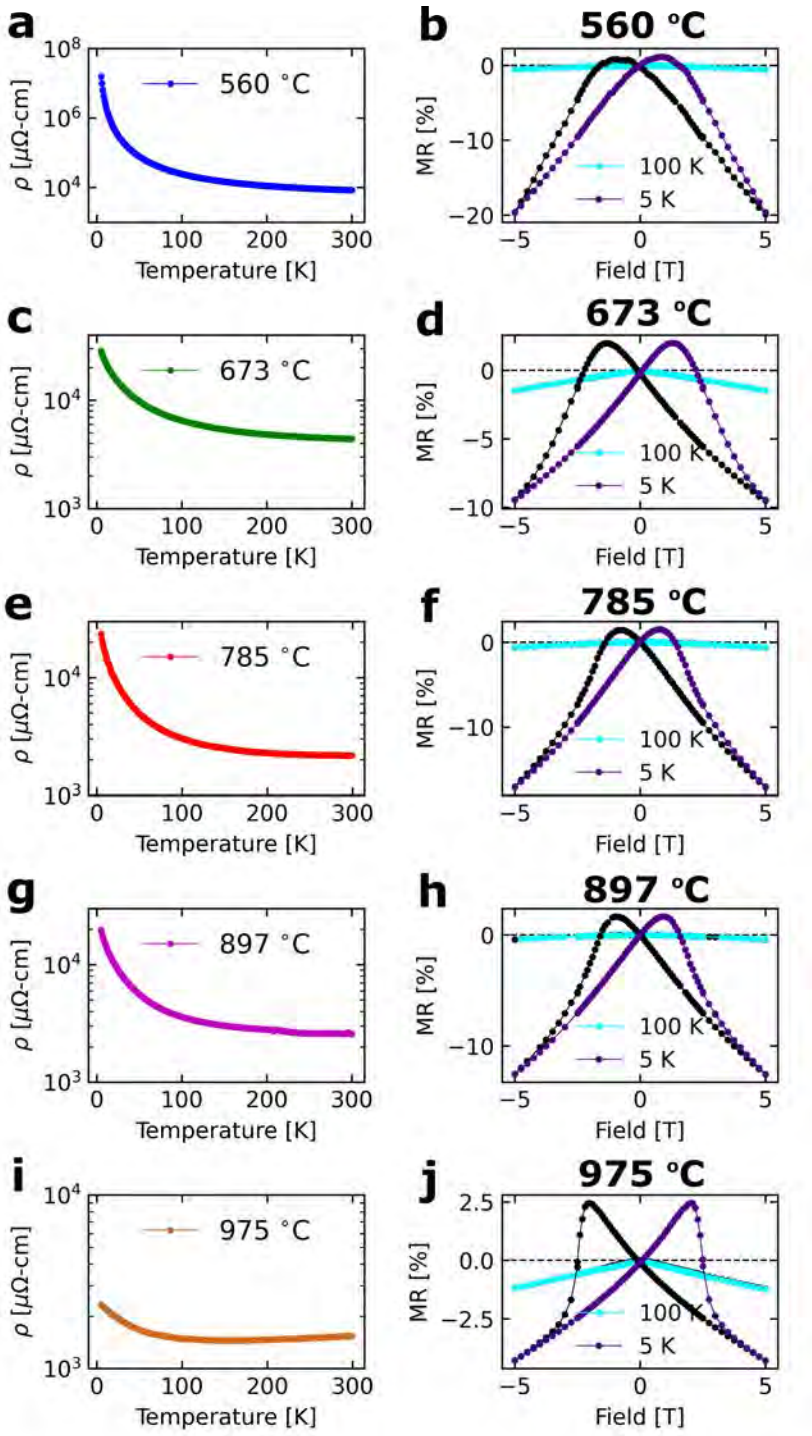

Figure 5.17.: Temperature dependence of the resistivity $\rho(T)$ and magnetoresistance (MR) of Ru-enriched SRO films grown at different T_{dep}. Black curves in the MR panels correspond to magnetic field sweeps from H+ to H−, and colored curves to the reverse direction (H− to H+).

5.3. Conclusions

In this chapter, a comprehensive optimization of the SRO thin film growth parameters by HOPS was performed at JCNS-2, where no prior experience with the deposition of SRO by this technique was available. The optimization aimed to establish reliable deposition conditions for producing epitaxial SRO films with high structural quality and physical properties suitable for subsequent studies on superconductor/ferromagnet (SC/FM) heterostructures.

Using a stoichiometric SRO target, the main growth parameters, target–substrate distance (D_{TS} = 2.5 cm), deposition temperature (T_{dep} = 785 °C), and oxygen partial pressure and forward power [(P_{O_2}, FWDP) = (1.5 mbar, 100 W)], were systematically optimized. These conditions yielded SRO films with excellent epitaxial coherence, smooth morphology, and clear PMA. However, all films exhibited a significant Ru deficiency of up to 25%, as confirmed by RBS and XRR analyses. Despite this, the $T_{Curie} \approx 150$ K remained comparable to values reported for stoichiometric SRO, in contrast to literature reports of strong T_{Curie} suppression in Ru-deficient samples prepared by molecular beam epitaxy (MBE) or pulsed laser deposition (PLD) [75, 99]. Nevertheless, a pronounced reduction of the saturation magnetization was observed, indicating the impact of cation vacancies on magnetic moment alignment. The electronic transport properties further revealed that all HOPS-grown films behave as semiconductors or weak insulators, lacking the characteristic metallic transition near T_{Curie} and exhibiting negative and anisotropic MR dominated by spin-disorder scattering and localization effects [98–101]. These features confirm that, although structurally well ordered and ferromagnetic, the HOPS-grown SRO films remain electronically localized and far from the Weyl-metallic regime reported for stoichiometric films.

In a complementary effort, a Ru-enriched $SrRu_{1.4}O_3$ (SRO-143) target was employed to test whether target enrichment could compensate for Ru volatility and kinetic losses during HOPS growth. While this study was conducted after the fabrication of SC/FM heterostructures and remains partially completed, valuable insights were obtained. Room-temperature characterization of the plasma and deposited films revealed that the Ru excess specified by the target manufacturer as nominally 40% was, in practice, closer to 30%. Nevertheless, this enrichment was not sufficient to compensate for Ru losses during HOPS growth, and the resulting films still remained Ru-deficient. Moreover, room-temperature and temperature-dependent growth experiments showed that the plasma exhibited instability, and the deposited films still displayed expanded c-axis lattice parameters, semiconducting $\rho(T)$ behavior, and negative MR – all consistent with persistent Ru deficiency. Thus, while Ru enrichment modestly improved the film stoichiometry, it did not eliminate Ru loss and subsequent overall Ru deficiency under these HOPS conditions.

Chapter 6

Anomalous magnetotransport in $YBa_2Cu_3O_{7-x}/SrRuO_3$ heterostructures

This chapter investigates the superconducting–ferromagnetic proximity effects in $YBa_2Cu_3O_{7-x}/SrRuO_3$ (YBCO/SRO) heterostructures through magnetotransport measurements. Building upon the optimized growth conditions for individual YBCO and SRO layers established in Chapters 4 and 5, the results presented here focus on thick YBCO/SRO and SRO/YBCO bilayers. Particular attention is given to how the superconducting–ferromagnetic coupling, anisotropic magnetoresistance, and layer stacking sequence influence the observed transport properties.

6.1. Scientific context

Heterostructures combining superconductors (SC) and ferromagnets (FM) offer a unique platform for investigating the competition and coexistence between two antagonistic order parameters, such as, superconductivity, characterized by the formation of Cooper pairs, and ferromagnetism, which aligns electronic spins in parallel. At their interfaces, proximity effects emerge due to the mutual penetration of the superconducting and magnetic order parameters, giving rise to a rich variety of emergent phenomena that depend sensitively on the interface quality, the strength of the magnetic anisotropy, and the characteristic energy and length scales of each material [2, 29, 30, 36].

Particularly intriguing are proximity effects involving SC coupled to FM exhibiting perpendicular magnetic anisotropy (PMA), where the magnetic easy axis is oriented normal to the film plane [22, 35]. Studies on Nb/FePd heterostructures have shown that PMA can strongly influence the spatial modulation of the superconducting order parameter, giving rise to domain-wall and reverse-domain superconductivity when the ferromagnetic stray field becomes comparable to the upper critical field (B_{c2}) of the SC [35]. These results demonstrated that the superconducting order parameter can be tuned at the nanoscale by adjusting the PMA, revealing a close relationship between magnetic anisotropy and superconducting coherence [19, 25].

Building on these findings, the present work investigates how such proximity phenomena, commonly observed in metallic systems via magnetotransport measurements [20, 21,

37, 39, 40], manifest when the high critical-temperature (high-T_c) cuprate SC, YBCO, is interfaced with SRO, a 4*d* itinerant FM exhibiting PMA. Both materials are complex oxides characterized by intrinsic anisotropies: YBCO displays a pronounced anisotropy in its superconducting coherence length ($\xi_{ab} \gg \xi_c$), London penetration depth (λ), critical current J_c, lower and upper critical field (B_{c1} and B_{c2}), while SRO presents narrow magnetic domain walls of approximately 3 nm and a periodic magnetic texture with characteristic lengths ranging from 200 nm to 1 µm [91]. These magnetic periodicities, ranging from 200 nm to 1 µm, are comparable to the magnetic penetration depth ($\lambda_{ab} \approx$ 150–200 nm) of YBCO, providing a favorable regime for magnetic coupling across the interface. However, the superconducting coherence length ($\xi_{ab} \approx$ 1.5–2 nm) remains much shorter, which confines the superconducting proximity effect to a nanometric scale.

In this context, bilayer heterostructures combining the high-T_c SC YBCO and the FM SRO were investigated to explore the interplay between superconductivity and magnetism at oxide interfaces. These systems provide an ideal oxide platform to study the effects of PMA on proximity-induced phenomena, where the competition between the superconducting coherence length of YBCO and the uniaxial magnetic anisotropy of SRO is expected to produce unconventional transport behavior. Particular emphasis is given to the anomalous magnetoresistance observed near the superconducting T_c, where distinct features, that are absent in the individual YBCO and SRO layers, appear. These anomalies are attributed to a short-range proximity effect governed by the competition between the anisotropic superconducting order in YBCO and the magnetic anisotropy of SRO [168].

6.2. Experimental details

The YBCO/SRO and SRO/YBCO bilayer heterostructures investigated in this work were grown on single-crystal $SrTiO_3$ (001) (STO) substrates with a low miscut angle between 0.05° and 0.1°. Prior to deposition, the STO substrates were chemically etched in a buffered hydrofluoric acid NH_4F–HF solution for 30 seconds and subsequently annealed at 950 °C for two hours in air to obtain atomically flat terraces with TiO_2 termination, providing ideal conditions for epitaxial growth.

The heterostructures were fabricated by High Oxygen Pressure Sputtering (HOPS), following the optimized growth parameters for YBCO and SRO detailed in Chapters 4 and 5. Stoichiometric ceramic targets of both materials were used. The base pressure before deposition was approximately 10^{-6} mbar, and high-purity oxygen (99.99%) served as the sputtering gas, with the working pressure (P_{O_2}) ranging between 1 and 3 mbar.

Each heterostructure was grown sequentially in two dedicated sputtering chambers to prevent cross-contamination. The YBCO/SRO (HS–YS) configuration was prepared by first depositing the SRO layer on the STO substrate, followed by the YBCO layer under high oxygen pressure. On the other hand, the SRO/YBCO (HS–SY) configuration was obtained by reversing the order of deposition. A schematic representation of each sample configuration is shown in Fig. 6.1(a-b). After the growth of the YBCO layer, both samples underwent a post-growth annealing treatment, in flowing oxygen at 500 °C and 10 mbar for 24 hours, to optimize oxygen stoichiometry and maximize the superconducting transition temperature. For HS–SY, an additional short annealing step (30 minutes) was applied after the top SRO deposition to recover the oxygen content in the buried YBCO layer, as oxygen diffusion through SRO is limited during high oxygen pressure deposition.

The structural and morphological characterization of the heterostructures was performed using high-resolution X-ray diffraction (HR-XRD) and X-ray reflectivity (XRR), and atomic force microscopy (AFM). The interfacial microstructure was further examined by cross-sectional high-resolution transmission electron microscopy (HR-TEM) using FEI Tecnai G2 F20. The magnetic and superconducting properties were investigated by temperature- and field-dependent magnetization measurements in a SQUID magnetometer (MPMS-XL) and a vibrating sample magnetometer (VSM) integrated into a PPMS DynaCool system, with magnetic fields applied parallel or perpendicular to the film surface. Electrical and magnetotransport measurements were carried out in a standard four-probe geometry using the PPMS system.

6.3. Morphological and structural characterization

The morphology and crystalline structure of the HS–YS and HS–SY heterostructures were analyzed to evaluate the quality of the interfaces and the epitaxial relationship between the layers. Representative topographic and phase AFM micrographs are shown in Fig. 6.1.

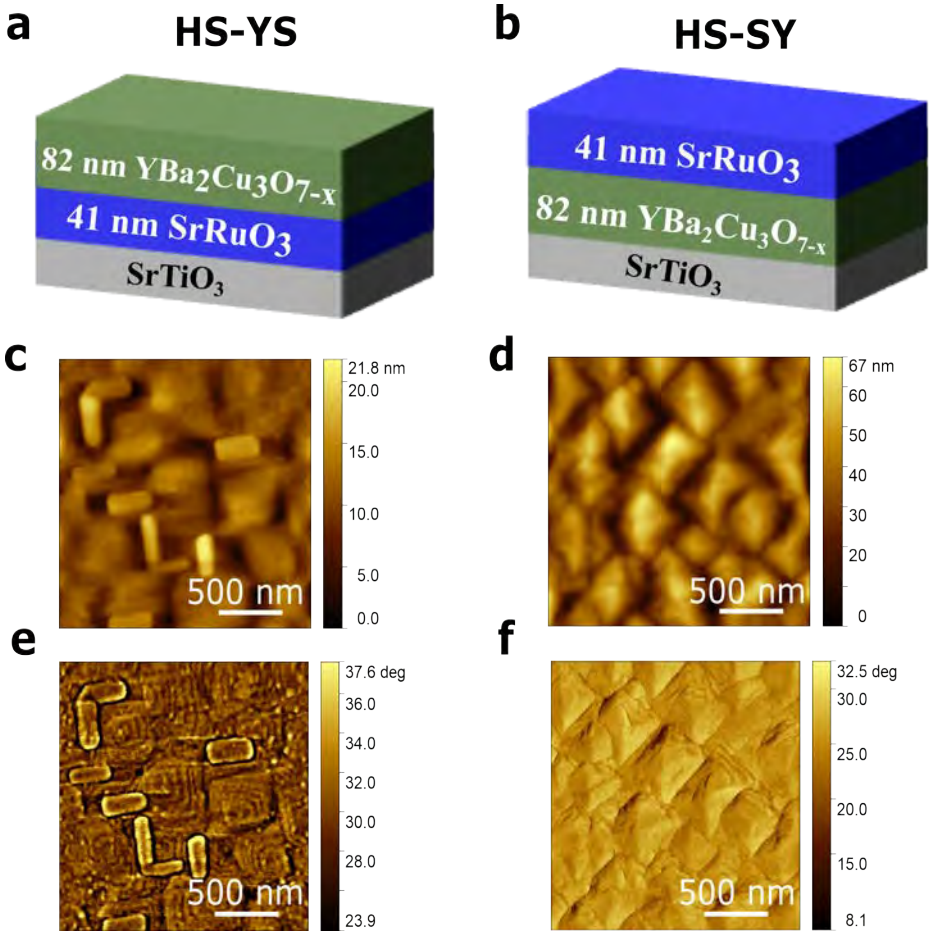

Figure 6.1.: Schematic representation of the (a) YBCO/SRO (HS-YS) and (b) SRO/YBCO (HS-SY) heterostructures deposited on low-miscut STO substrates. Atomic force microscopy topography and phase micrographs of the (c, e) HS-YS and (d, f) HS-SY heterostructures.

The surface of the HS-YS bilayer heterostructure [Fig. 6.1(c, e)] exhibits a characteristic morphology of a YBCO film, with rectangular grains and characteristic spiral features. The rectangular grains are related to the local growth of YBCO *ab*-planes oriented perpendicularly to the SRO surface (*a*-axis epitaxial growth), and the spirals are related to the growth of YBCO *ab*-planes oriented parallel to the SRO surface (*c*-axis epitaxial growth) [160, 163, 164, 174]. The average local root-mean-square (RMS) roughness of the HS–YS surface is approximately 2.9 nm ± 0.4 nm, indicating smooth growth and a well-defined interface between YBCO and the underlying SRO layer.

In contrast, the HS-SY heterostructure exhibits a significantly rougher surface, with RMS roughness values around 6.8 nm ± 0.4 nm [Fig. 6.1(d, f)]. The AFM images reveal that the top SRO layer grows in an island-like mode, consistent with the presence of twinning along the [110] direction. This behavior originates from the morphological complexity of the underlying YBCO layer, which contains mixed *a*- and *c*-axis oriented grains, growth spirals, and nanoscale CuO or $BaCuO_2$ precipitates [white dots observed on the YBCO surface in Fig. 6.1(e)] formed during the high-temperature deposition and post-growth annealing processes. These precipitates, visible as small protrusions on the YBCO surface, partially dissolve into the SRO overlayer, contributing to its increased roughness and locally disordered growth mechanism. Consequently, the structural coherence of the SRO film in the HS–SY configuration is reduced compared to the HS–YS heterostructure, where the initial SRO layer grows on a smooth TiO_2-terminated STO substrate.

Figure 6.2 shows HR-XRD measurements, confirming the high crystalline quality of both heterostructures. HR-XRD patterns of a 60 nm SRO thin film and of STO substrate are shown for comparison. In HS–YS, intense and sharp YBCO reflections indicate predominant *c*-axis orientation, although *a*-axis domains are still present. Weak reflections from secondary Ba–Cu–O phases, such as CuO and $BaCuO_2$, were also identified (indicated by triangles) and are consistent with the small nanoparticles features observed by AFM. For HS–SY, the YBCO peaks appear slightly shifted toward smaller diffraction angles, suggesting the presence of strain in the YBCO layer. The SRO reflections (open circles) in this configuration are broader and of lower intensity compared to HS–YS, indicating an SRO layer with inferior crystalline quality, possible lattice distortions, and multiple *c*-axis orientations due to the rough YBCO interface.

The total thickness of the heterostructures was controlled through the calibrated deposition rates of each layer, determined under optimized HOPS growth conditions. SRO and YBCO exhibited typical growth rates of 12.5 nm/h and 100 nm/h, respectively. To minimize possible thickness-confinement effects while maintaining the high structural and superconducting quality of YBCO, relatively thick heterostructures were grown. The SRO layer was designed to be approximately half the thickness of the YBCO layer, resulting in a nominal 2:1 thickness ratio for the bilayers. Due to the large overall thickness of the heterostructures and their relatively high surface roughness ($\sigma \geq 2.5$ nm for HS–YS and $\sigma \geq 6.5$ nm for HS–SY), Laue oscillations and Kiessig fringes could not be resolved. Therefore, quantitative determination of the layer thicknesses was performed using cross-sectional HR-TEM, as shown in Fig. 6.3 for the HS–YS heterostructure. The thicknesses measured for the SRO and YBCO layers were 40.6 ± 0.7 nm and 82.8 ± 1.9 nm, respectively, confirming the designed 2:1 ratio. These values are consistent across different regions of the micrograph, demonstrating uniform growth and good crystalline quality throughout the heterostructure. Similar structural parameters are expected for the HS–SY sample.

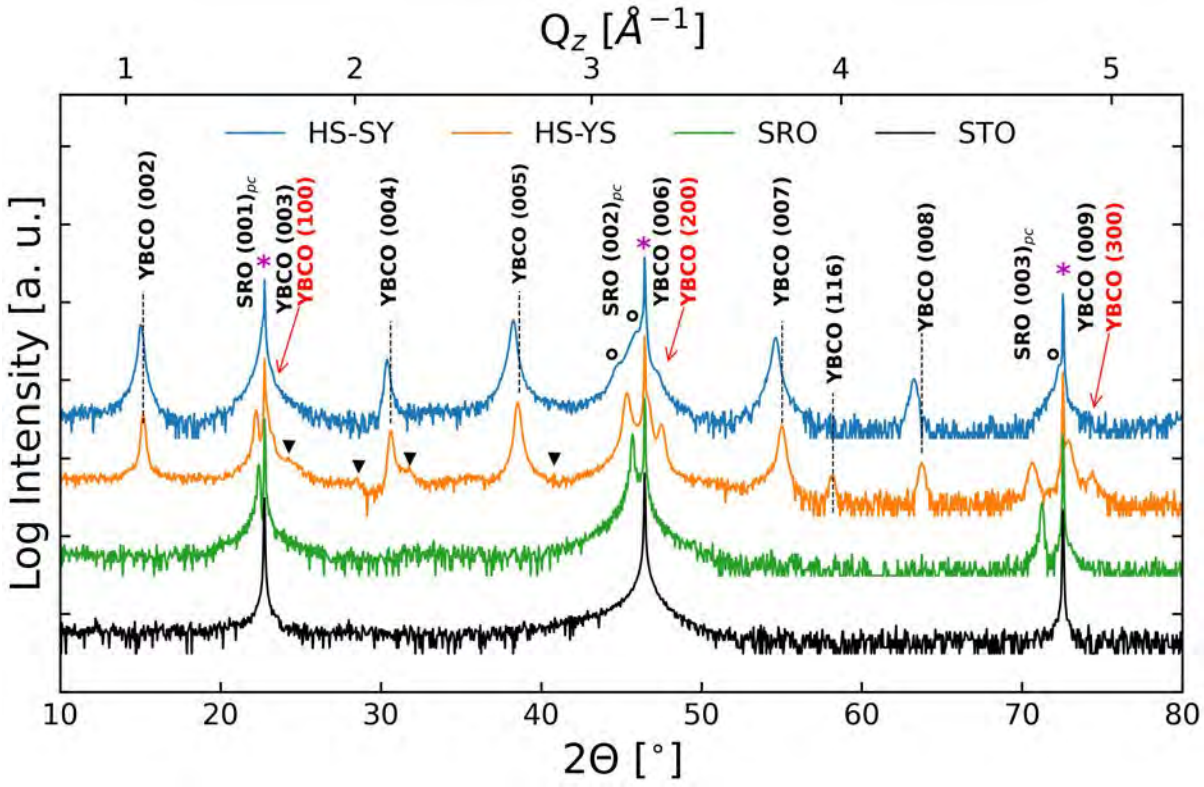

Figure 6.2.: X-ray diffraction patterns of the YBCO/SRO (HS–YS) and SRO/YBCO (HS–SY) heterostructures. Curves are vertically shifted for clarity. Asterisks mark STO peaks, triangles indicate Ba–Cu–O secondary phases in HS–YS, and open circles denote SRO reflections with multiple out-of-plane lattice parameters in HS–SY. STO substrate and SRO thin films patterns are shown as a reference.

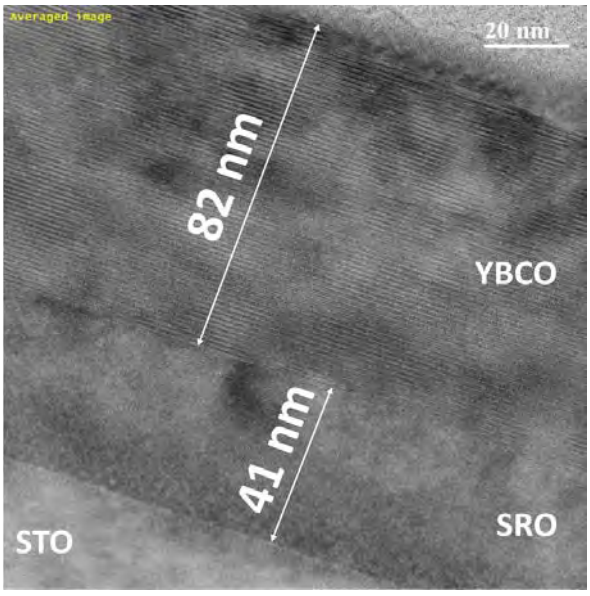

Figure 6.3.: Cross-sectional HR-TEM image of the YBCO/SRO (HS–YS) heterostructure grown on an STO substrate. The YBCO and SRO layer thicknesses of approximately 82 nm and 41 nm, respectively, confirm the designed 2:1 thickness ratio.

To further assess the crystalline structure and, in particular, the interface quality of the heterostructures, a SRO(35 nm)/YBCO(20 nm)/SRO(35 nm) trilayer was grown on a STO substrate. Cross-sectional lamellas were prepared along the [001] and [110] crystallographic directions for HR-TEM analysis. Figure 6.4 presents cross-sectional images acquired along the [110] direction.

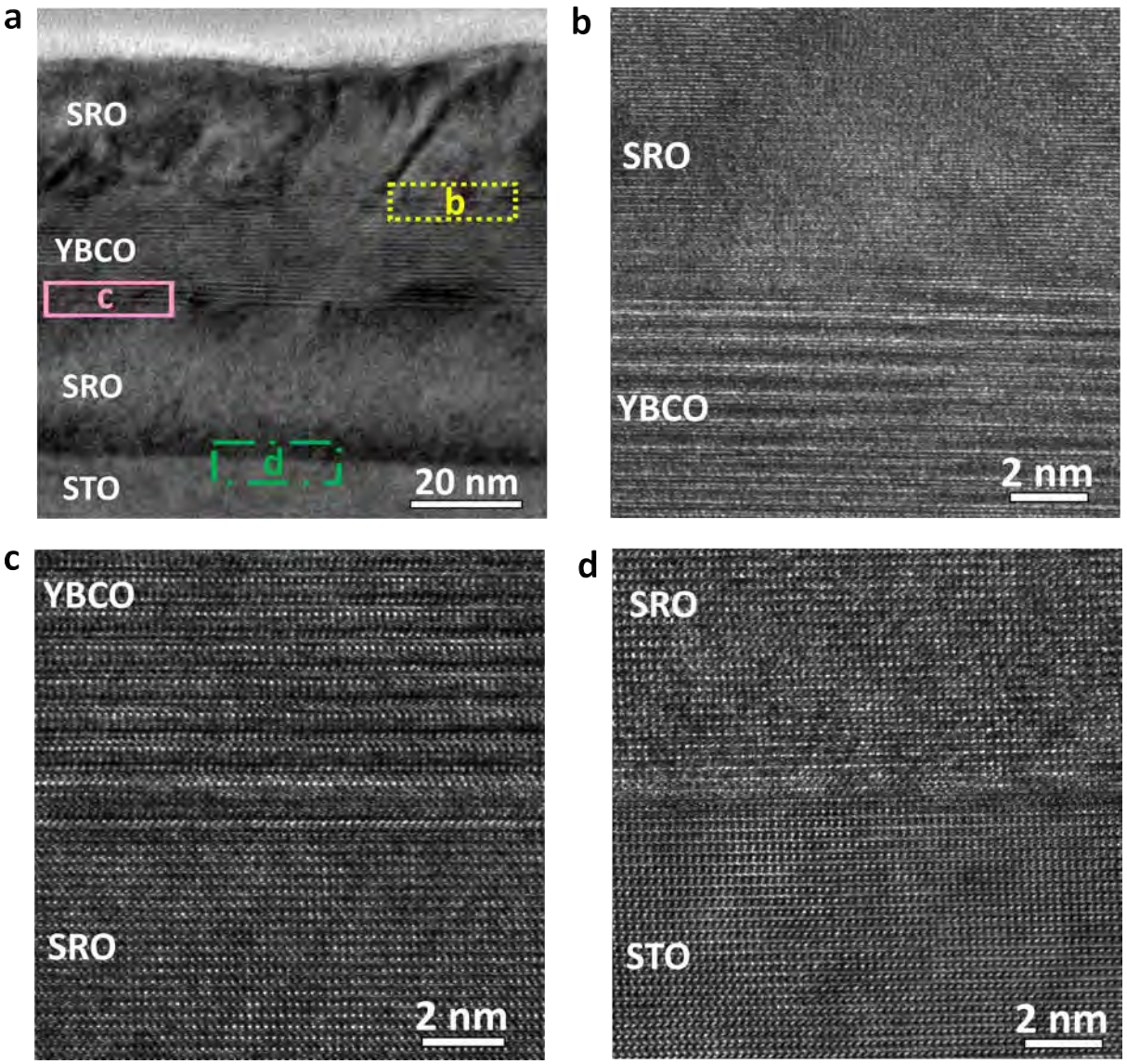

Figure 6.4.: Cross-sectional High-resolution Transmission electron microscopy images of the SRO(35 nm)/YBCO(20 nm)/SRO(35 nm) trilayer grown on a STO substrate along the [110] crystallographic direction. (a) Overview of the full heterostructure highlighting the SRO/YBCO, YBCO/SRO, and SRO/STO interfaces. (b–d) High-resolution images confirming cube-on-cube epitaxy and sharp interfaces between the layers.

The wide-field image [Fig. 6.4(a)] displays the full trilayer stack, highlighting the SRO/YBCO (top), YBCO/SRO (middle), and SRO/STO (bottom) interfaces. A clear difference in structural quality is observed between the two SRO layers: the bottom SRO layer grown directly on STO exhibits superior crystallinity and smoother interfaces compared to the top SRO layer deposited on YBCO. This difference is attributed to the

higher roughness and mixed orientation of the underlying YBCO surface, which affects the subsequent SRO growth. High-resolution images shown in Fig. 6.4(b-d) confirm the cube-on-cube epitaxial relationship across all interfaces, with well-aligned atomic planes and relatively sharp transitions between layers.

The structural and morphological characterization demonstrates that both YBCO/SRO and SRO/YBCO heterostructures exhibit epitaxial growth with well-defined layering and sharp interfaces. However, the order of deposition plays a critical role in determining the crystalline quality of the top layer: SRO deposited on YBCO (HS–SY) shows degraded crystallinity and higher roughness compared to SRO deposited directly on STO (HS–YS). This asymmetry directly impacts the magnetic and transport properties discussed in the following sections, as interface roughness and compositional inhomogeneities can locally alter the superconducting and ferromagnetic coupling across the interface.

6.4. Magnetic and electrical transport characterization

The magnetic behavior of the HS–YS and HS–SY heterostructures was investigated to evaluate the coexistence and mutual influence of superconductivity and ferromagnetism across the interface. Zero-field-cooled (ZFC) and field-cooled (FC) magnetization measurements were performed with the magnetic field applied along the out-of-plane [001] direction, corresponding to the easy axis of magnetization of the SRO layer. Before each ZFC measurement, the magnetometer coils were demagnetized to eliminate trapped flux and ensure true zero-field cooling.

The ZFC magnetization curves for both heterostructures are shown in Fig. 6.5(a). At low temperatures, a pronounced negative magnetic moment is observed, corresponding to the diamagnetic response of YBCO in the superconducting state. As the temperature increases, the magnetization gradually approaches positive values, defining the superconducting transition temperatures (T_c) of 87 K ± 0.5 K for HS–YS and 57 K ± 0.5 K for HS–SY. The inset of Fig. 6.5(a) reveals a broad magnetic feature around 100 K in the HS–SY curve, absent in HS–YS. This anomaly is attributed to the presence of residual CuO and Ba–Cu–O nanoparticles formed during the YBCO deposition and partially incorporated into the top SRO layer during subsequent growth. Similar behavior has been reported for CuO- and Y_2O_3-containing YBCO composites, where weak ferromagnetic signals appear due to nanoscale inclusions that contribute to a distributed magnetic response [175].

Field-cooled magnetization curves [Fig. 6.5(b)] confirm the ferromagnetic nature of the SRO layers and allow for accurate determination of the Curie temperature (T_{Curie}). Both heterostructures exhibit $T_{\mathrm{Curie}} = 151$ K ± 0.5 K, as determined from the derivative of the FC curves [inset of Fig. 6.5(b)]. Both heterostructures maintain ferromagnetic ordering below T_{Curie}, confirming the coexistence of superconductivity and ferromagnetism and indicating the possibility of a short-range magnetic proximity coupling across the YBCO/SRO and SRO/YBCO interfaces [51, 176, 177].

Interestingly, a magnetic field as low as 10 Oe was sufficient to overcome the superconducting diamagnetism in the FC measurements. This behavior can be explained by several factors. First, SRO exhibits uniaxial magnetic anisotropy along the out-of-plane [001] direction, so even a small external field helps preserve a net magnetization in this orientation below the superconducting T_c. Second, YBCO is a type-II SC, in which magnetic flux penetrates in the form of Abrikosov vortices once the first critical field B_{c1} is

exceeded [12]. For thin YBCO films, B_{c1} can be as low as 10 Oe due to field concentration at the sample edges. Moreover, in the HS–YS heterostructure, the mixed a- and c-axis texture observed by AFM disrupts the homogeneity of the superconducting screening currents, further reducing the effective B_{c1} and enabling flux penetration even under very small applied fields. As a result, weakly screened superconducting regions coexist with ferromagnetic domains of SRO, allowing the persistence of a positive magnetization signal in the FC curves even below T_c.

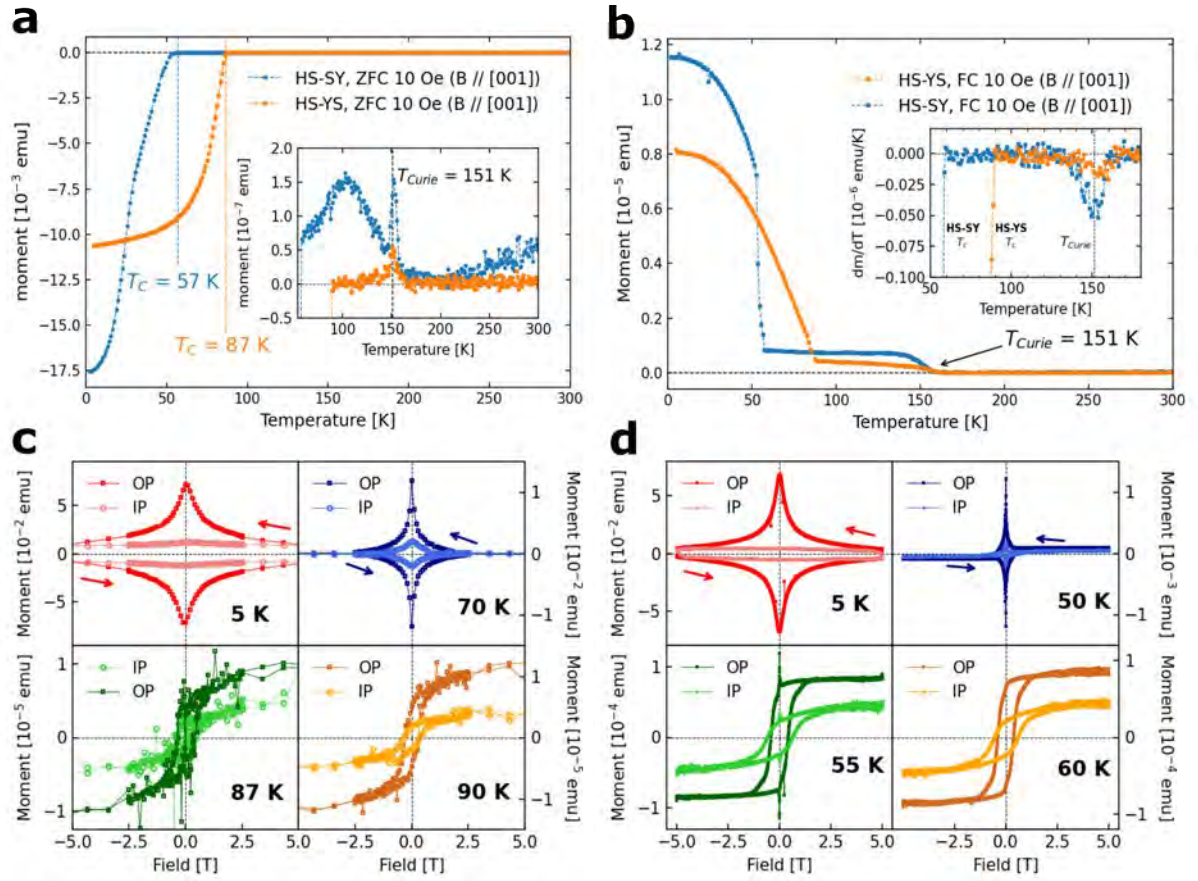

Figure 6.5.: (a) Zero-field-cooled and (b) field-cooled magnetization of YBCO/SRO (HS–YS) and SRO/YBCO (HS–SY) heterostructures measured with 10 Oe magnetic field applied along the out-of-plane [001] direction. Insets: derivative of the FC data showing $T_{\mathrm{Curie}} = 151$ K. Magnetic hysteresis loops for (c) HS-YS and (d) HS-SY at selected temperatures illustrating the transition from superconducting to ferromagnetic behavior near T_c.

Magnetic hysteresis loops measured at different temperatures [Fig. 6.5(c–d)] provide additional insight into the magnetic response near the superconducting transition. At low temperatures, both heterostructures display the characteristic hysteresis of type-II SC, dominated by a strong diamagnetic signal arising from flux pinning [12, 51]. As the temperature increases toward T_c, the loops progressively evolve from a Meissner-like superconducting behavior to a ferromagnetic shape, reflecting the direct competition between the superconducting and ferromagnetic order parameters. The pinning of magnetic flux lines is evidenced by the difference of nearly three orders of magnitude in magnetization between the superconducting and ferromagnetic states. This crossover is most evident at 87 K for the HS–YS and at 55 K for the HS–SY heterostructure, consistent

with the critical temperatures obtained from the ZFC measurements.

The temperature dependence of the electrical resistivity for the HS–YS and HS–SY heterostructures is shown in Fig. 6.6. Both samples exhibit a metallic behavior above the superconducting transition and a sharp drop in resistivity at low temperature, consistent with the onset of superconductivity. The critical temperatures, determined from the derivative of $\rho(T)$ (shown as inset) are $T_c = 87.2$ K ± 0.6 K for HS–YS and $T_c = 57.8$ K ± 0.9 K for HS–SY. The resistivity of HS–YS shows a linear temperature dependence above T_c, characteristic of optimally doped YBCO, whereas HS–SY displays a non-linear $\rho(T)$ relation typical of underdoped cuprates. This behavior reflects the limited oxygen diffusion through the SRO overlayer during growth and post-annealing, which leads to a reduced hole concentration in the buried YBCO layer.

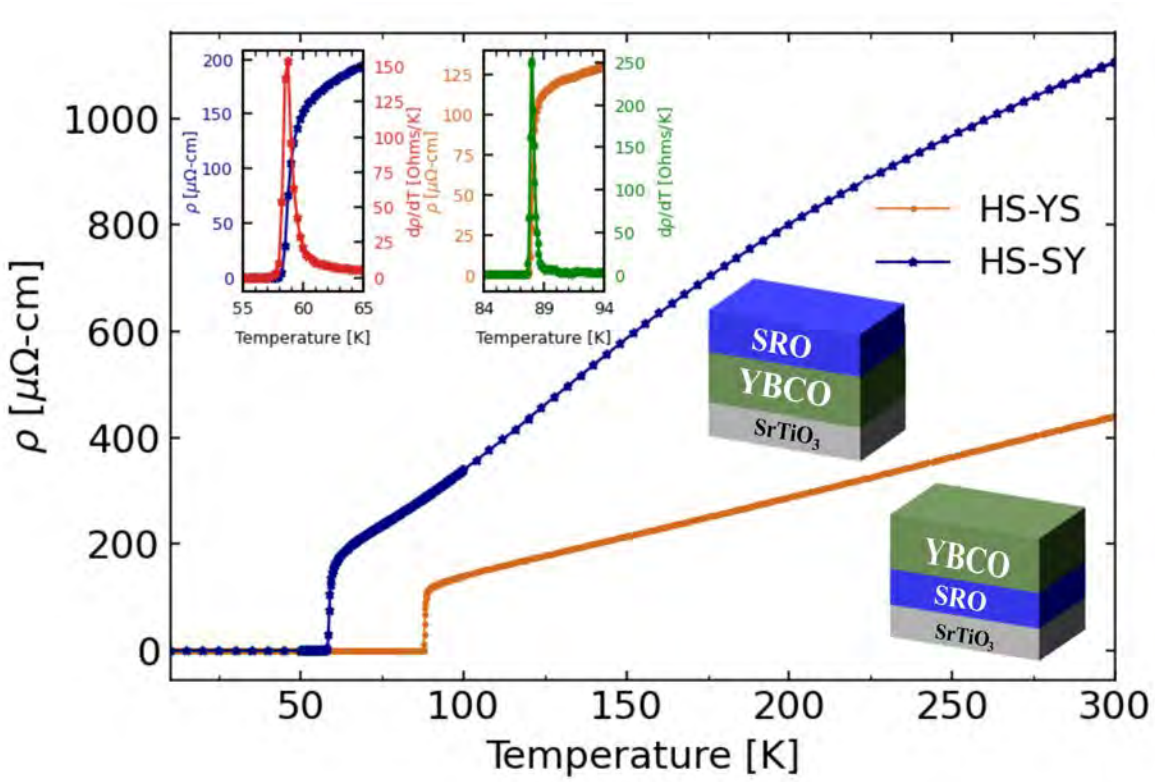

Figure 6.6.: Temperature-dependent resistivity of YBCO/SRO (HS–YS) and SRO/YBCO (HS–SY) heterostructures. The lower T_c and broader transition of HS–SY indicate underdoping and reduced superconducting coherence due to oxygen deficiency and interface disorder.

The significant difference in T_c between the two stacking configurations illustrates the sensitivity of the superconducting properties to the growth order and interface structure. In HS–YS, YBCO grows on a smooth, well-terminated SRO surface, preserving high structural and superconducting quality. In contrast, in HS–SY, the top SRO layer prevents a complete re-oxygenation of YBCO during post-annealing, resulting in an underdoped state and broader superconducting transition. Additionally, the strain and local disorder introduced at the rough SRO/YBCO interface may further degrade the superconducting coherence.

A moderate reduction of T_c in HS–YS compared to single YBCO films (approximately 4 K) can be attributed to the SC–FM proximity effect, in which the exchange field of the

ferromagnetic layer suppresses the superconducting order parameter near the interface [178, 179]. However, the much stronger suppression observed in HS–SY (approximately 35 K) cannot be explained solely by proximity coupling; it primarily results from the reduced oxygen content and altered electronic doping level of YBCO beneath the SRO layer.

It is worth noting that the characteristic kink typically observed in the resistivity of SRO thin films around T_{Curie} [85, 180], associated with the ferromagnetic and metal–insulator transition, is not visible in the $\rho(T)$ curves of the present heterostructures. This absence indicates that the SRO layers in both stacking configurations exhibit strongly suppressed metallicity and reduced magnetic ordering compared to stoichiometric SRO. As discussed in Chapter 5, this behavior originates from ruthenium deficiency inherent to the high pressure sputtering process, where Ru volatility leads to the formation of Ru vacancies even under optimized growth conditions. Consequently, the SRO layers behave as semiconducting FM rather than metallic ones, preventing the observation of the distinct resistivity transition at T_{Curie}. This limitation reflects a fundamental constraint of the deposition technique rather than the specific growth parameters employed.

These results demonstrate that the physical behavior of the heterostructures is strongly governed by the stacking order and the resulting interfacial quality. In the HS–YS configuration, where YBCO is deposited on a smooth and well-terminated SRO surface, the superconducting transition temperature remains high and the magnetic response is sharp, reflecting coherent coupling between the layers. In contrast, the HS–SY heterostructure, in which SRO is grown on a rougher YBCO surface, exhibits degraded superconductivity and a more complex magnetic signal, influenced by interfacial strain, oxygen non-stoichiometry, and increased roughness. Nevertheless, both heterostructures retain ferromagnetic ordering below T_{Curie} as well as PMA, confirming the coexistence of superconductivity and ferromagnetism and suggesting a short-range magnetic proximity coupling across the YBCO/SRO interface. The combined magnetic and electrical transport results thus highlight that structural asymmetry, oxygen diffusion, and stoichiometric balance are key parameters governing the superconducting and magnetic performance of oxide-based SC/FM hybrids.

6.5. Magnetotransport characterization

The magnetotransport behavior of the HS–YS heterostructure was investigated near the superconducting transition temperature to probe possible proximity-induced effects at the SC/FM interface. The resistivity was measured as a function of the applied magnetic field at selected temperatures close to the onset of superconductivity (84–94 K). The colors in Fig. 6.7(b–i) correspond to the colored markers in Fig. 6.7(a), indicating the temperature at which each magnetic field sweep was acquired. The external field (H_{ext}) was applied parallel (in-plane, $H_{\parallel}$) and perpendicular (out-of-plane, $H_{\perp}$) to the heterostructure surface, with the current density oriented as $\mathbf{J} \| H_{\mathrm{ext}}$ and $\mathbf{J} \perp H_{\mathrm{ext}}$, respectively. Magnetoresistance (MR) data for the SRO/YBCO (HS–SY) sample are not presented due to technical limitations during measurement.

For temperatures above 93 K, the MR curves resemble those of a single YBCO film, exhibiting a nearly linear dependence on field and no significant low-field features. However, as the temperature approaches T_{c}, distinct anomalies emerge around zero field. For $H_{\parallel}$ [Fig. 6.7(b)], a crossover from a dip to a peak in the MR signal occurs upon cooling

from 91 K to 89 K, while for $H_\perp$ [Fig. 6.7(c)], the opposite trend, from a peak to a dip, is observed. These features are reversible with field-sweep direction and occur symmetrically around zero field, ruling out experimental artifacts. The corresponding switching fields, defined as the field values where the MR begins to change sign, are approximately ±1 T for $H_\parallel$ and ±0.4 T for $H_\perp$. Importantly, these values do not coincide with the coercive field of the SRO layer, indicating that the observed anomalies are not directly linked to magnetization reversal in the ferromagnetic film.

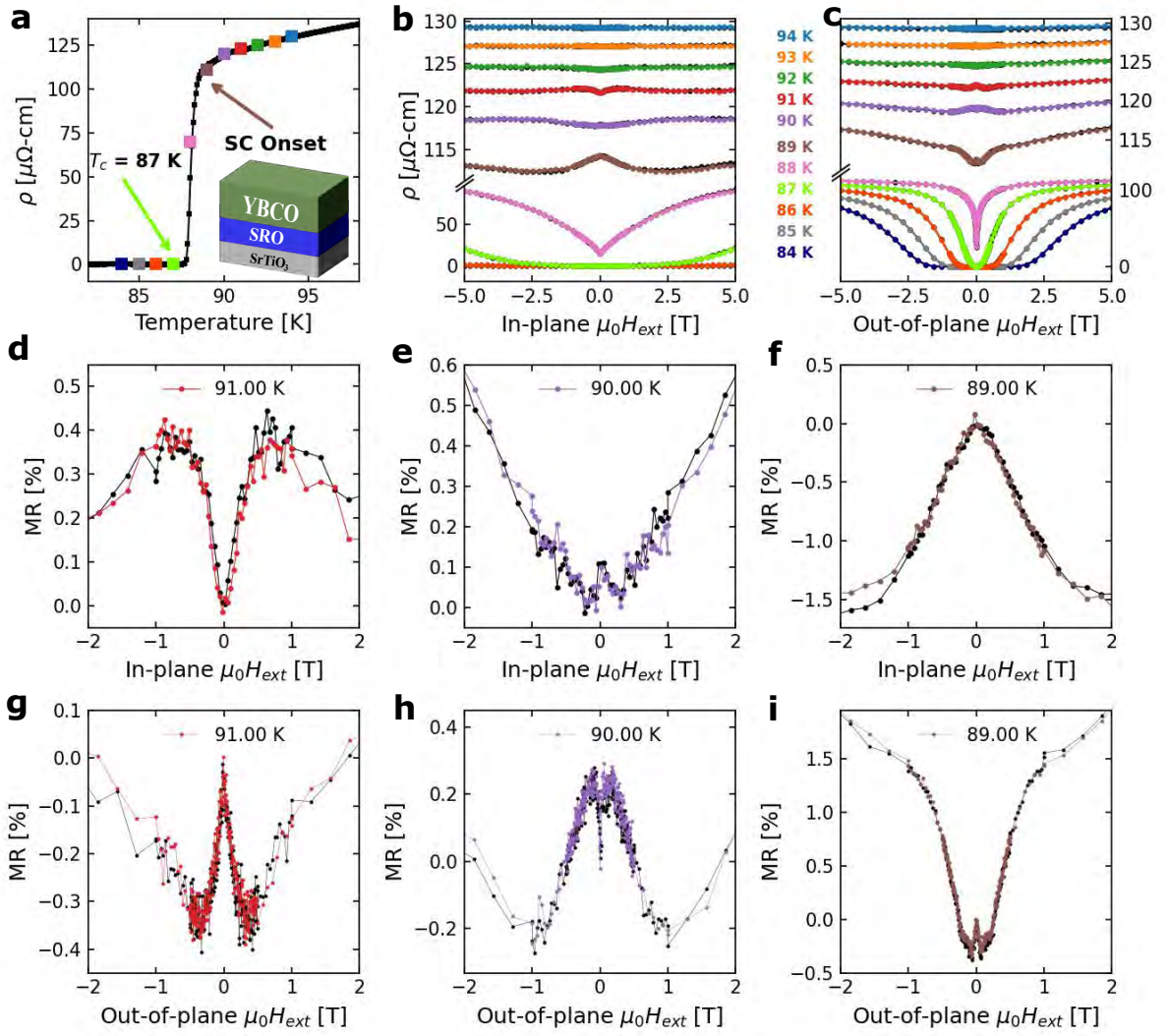

Figure 6.7.: (a) Zero-field $\rho(T)$ curve of the YBCO/SRO (HS–YS) heterostructure, with colored markers indicating the temperatures at which the magnetoresistance measurements were performed. (b–c) Full $\rho(H,T)$ magnetoresistance curves obtained under in-plane ($H_\parallel$) and out-of-plane ($H_\perp$) magnetic fields, respectively. (d–i) Corresponding normalized MR curves near zero field (-2 T ≤ H ≤ 2 T), where the anomalous features are observed. The black curves represent field sweeps from positive to negative fields, while the colored curves correspond to the reverse direction.

A closer examination of the MR behavior near zero field reveals that the amplitude and shape of these anomalies depend strongly on the field orientation. The near zero field curves, shown in Fig. 6.7(d–i), correspond to measurements performed in the range of -2

T ≤ H ≤ 2 T. The black curves represent field sweeps acquired from positive to negative fields, while the colored curves correspond to the reverse direction, from negative to positive fields. All MR curves were normalized according to the relation MR = $\frac{\rho(H)-\rho(0)}{\rho(0)}$, allowing direct comparison between different temperatures and field orientations.

When $H_\parallel$ is applied [Fig. 6.7(d–f)], the MR features are broader and less pronounced, whereas for $H_\perp$ the features become sharper and more intense [Fig. 6.7(g–i)]. This anisotropy reflects the interplay between the uniaxial PMA of SRO and the anisotropic superconducting coherence length of YBCO ($\xi_{ab} \gg \xi_c$). For out-of-plane fields, the magnetization of SRO aligns along its easy axis ([001] direction), producing stronger local magnetic fields at the interface and thus enhancing the coupling with the superconducting order parameter. In contrast, when the field is applied parallel to the surface, SRO magnetization lies along its hard axis, resulting in weaker coupling and broader MR transitions. Therefore, the contrasting responses for $H_\parallel$ and $H_\perp$ demonstrate that the observed anomalies arise from an anisotropic proximity effect governed by the relative orientation between the superconducting currents in YBCO and the magnetization in SRO.

The resistivity values of the heterostructure are significantly lower than those of standalone SRO films, confirming that the transport is dominated by the superconducting layer. This also indicates that the MR features originate from modifications of the superconducting state induced by interfacial magnetic interactions, rather than from intrinsic SRO conduction. The coexistence of positive and negative MR regions near T_c further supports this interpretation, as such mixed responses are consistent with local variations in flux pinning and vortex dynamics caused by stray magnetic fields at the interface. It is important to note that the MR of pure YBCO is always positive, as shown in Fig. 4.7, while that of SRO is consistently negative (see chapter 5), a characteristic feature of Ru-deficient ferromagnetic SRO films. Therefore, the simultaneous presence of positive and negative MR components in the YBCO/SRO heterostructure cannot originate from either layer alone but instead reflects an interfacial effect arising from the competition between superconducting and ferromagnetic order parameters.

The absence of sharp maxima or distinct double minima in the MR curves, typically associated with domain-wall superconductivity or long-range spin-triplet transport in SC/FM systems [22, 35, 37, 39–41], suggests that the proximity effect in YBCO/SRO heterostructures is short-ranged and localized at the interface. This behavior can be explained by the mismatch between the characteristic length scales of the two materials: the superconducting coherence length in YBCO ($\xi_{ab} \approx$ 1.5–2 nm) is smaller than the SRO magnetic domain-wall width (3 nm) and much smaller than domain periodicity (200 nm–1 µm). Moreover, the stray fields generated by the SRO domains are weaker than YBCO's B_{c2}, preventing the formation of extended superconducting domains or long-range triplet components [20, 21, 43]. As a result, the observed MR anomalies originate from the local competition between superconducting and ferromagnetic anisotropies rather than from long-range magnetic modulation of the superconducting order parameter.

Interestingly, there is an intriguing resemblance between the shape of the $\rho(H,T)$ curves near the superconducting onset and the characteristic field dependence of quantum corrections to conductivity, specifically weak localization (WL) and weak anti-localization (WAL) effects, commonly observed in semiconductor and disordered insulating systems [181]. In both cases, resistance dips or peaks around zero field arise from interference effects that modify the electronic diffusion. However, quantum corrections to conductivity are genuine low-temperature phenomena that occur when phase-coherent scattering dom-

inates [182, 183], typically at temperatures far below those investigated here. Therefore, while the MR curves qualitatively resemble WL and WAL behavior, these mechanisms cannot account for the features observed in our oxide heterostructures.

The magnetotransport data reveal an anisotropic and proximity-induced modification of the superconducting state near the YBCO/SRO interface. The crossover between dips and peaks in the MR signal reflects the delicate balance between superconducting coherence and magnetic anisotropy, mediated by the orientation of the applied magnetic field. These findings indicate that in oxide-based SC/FM heterostructures with PMA, such as YBCO/SRO, proximity coupling is primarily short-ranged and highly sensitive to interface morphology, strain, and the anisotropic nature of both order parameters.

6.6. Conclusions

This chapter presented a comprehensive study of the structural, magnetic, and transport properties of YBCO/SRO (HS-YS) and SRO/YBCO (HS-SY) heterostructures grown by HOPS on single-crystal STO substrates. The goal was to investigate proximity-induced interactions between superconductivity and ferromagnetism in oxide heterostructures with PMA using magnetotransport measurements as a probe.

Structural and morphological analyses confirmed that both stacking configurations exhibit epitaxial growth with sharp interfaces and coherent lattice matching. However, the growth order plays a crucial role in determining the overall crystalline quality and surface morphology. The HS–YS heterostructure (YBCO on SRO) shows smooth terraces and well-defined layering, whereas the HS–SY sample (SRO on YBCO) exhibits higher roughness and structural disorder due to the morphological complexity of the YBCO surface and partial incorporation of secondary Cu–O phases. These differences in structural quality directly impact the magnetic and superconducting properties.

Magnetization measurements revealed clear signatures of the coexistence of superconductivity and ferromagnetism. Both heterostructures exhibit a T_{Curie} of approximately 151 K, associated with the ferromagnetic ordering of SRO, while the superconducting transition temperatures were $T_{\mathrm{c}} = 87$ K for HS–YS and $T_{\mathrm{c}} = 57$ K for HS–SY. The lower T_{c} and broader transition observed in HS–SY arise from limited oxygen diffusion through the SRO overlayer and enhanced strain and roughness at the interface. Magnetic hysteresis loops demonstrated the competition between the superconducting and ferromagnetic states, with a gradual evolution from diamagnetic to ferromagnetic behavior as temperature increases. Even under small magnetic fields (10 Oe), a positive magnetization persists in the field-cooled state, attributed to flux penetration through Abrikosov vortices and the uniaxial anisotropy of SRO, which together reduce the effective superconducting screening in mixed *a*- and *c*-axis YBCO grains.

Electrical transport measurements corroborated the magnetic findings. Both heterostructures show metallic behavior above T_{c} and a sharp superconducting transition at low temperature. The modest reduction of T_{c} in HS–YS relative to single YBCO films indicates a short-range superconducting proximity effect at the YBCO/SRO interface, whereas the stronger suppression in HS–SY is mainly associated with oxygen deficiency and interfacial disorder. The characteristic kink in resistivity commonly observed in SRO films near their magnetic transition is absent here, reflecting the Ru deficiency intrinsic to the HOPS technique, which limits the metallicity of the SRO layers even under optimized growth conditions.

Magnetotransport experiments on the HS–YS heterostructure revealed anomalous features near the superconducting transition, manifesting as crossovers between dips and peaks around zero field in the $\rho(H,T)$ curves. These anomalies depend strongly on the field orientation, being sharper for out-of-plane fields and broader for in-plane ones, consistent with the interplay between the uniaxial magnetic anisotropy of SRO and the anisotropic superconducting coherence of YBCO. The coexistence of positive and negative magnetoresistance regions, together with the absence of domain-wall or long-range triplet superconductivity signatures, demonstrates that the proximity coupling in these oxide heterostructures is short-ranged and localized at the interface. The observed behavior results from the local competition between superconducting and ferromagnetic anisotropies rather than from domain-mediated effects.

In summary, the results presented in this chapter provide clear evidence of an anisotropic, short-range superconducting proximity effect in YBCO/SRO heterostructures. The interfacial coupling between superconductivity and ferromagnetism is strongly influenced by the stacking order, interface roughness, and stoichiometric balance, highlighting the importance of structural control in engineering oxide-based SC/FM systems. These findings establish YBCO/SRO as a model system for exploring the interplay between spin, charge, and anisotropy in complex oxide heterostructures and lay the groundwork for future studies aimed at tuning proximity effects through interface design and layer thickness modulation.

Chapter 7

Neutron scattering studies of $SrRuO_3$ thin films and $YBa_2Cu_3O_{7-x}/SrRuO_3$ heterostructures

This chapter focuses on neutron reflectometry experiments performed to investigate the depth-dependent magnetization profile of $SrRuO_3$ thin films and $YBa_2Cu_3O_{7-x}/SrRuO_3$ heterostructures. Building upon the structural, magnetic and transport characterization presented in the previous chapters, polarized neutron reflectivity was employed to probe the magnetic depth profile with nanometer resolution. This approach enabled the study of interfacial magnetic effects such as magnetization suppression near the interfaces and the possible emergence of a reverse proximity effect, where a magnetic moment may be induced within the $YBa_2Cu_3O_{7-x}$ layer due to its interaction with the adjacent ferromagnetic $SrRuO_3$.

7.1. Interfacial and depth-resolved magnetism in Ru-deficient $SrRuO_3$ thin films

7.1.1. Scientific context

$SrRuO_3$ (SRO) is an itinerant ferromagnetic oxide that combines metallic conductivity with strong spin–orbit coupling and pronounced perpendicular magnetocrystalline anisotropy (PMA) [31, 50, 75, 78–80]. Its Curie temperature (T_{Curie}) of about 160 K and structural compatibility with a wide range of functional oxides have made it a model system for exploring spin-polarized transport, ferroelectric coupling, and interface-driven phenomena in oxide heterostructures [31, 79, 82, 168].

As discussed in previous chapters, SRO thin films grown by high oxygen pressure sputtering (HOPS) exhibit excellent epitaxial quality and well-defined PMA, even when a considerable Ru deficiency (approximately 20–25%) is present due to the high volatility of Ru under oxidizing conditions [71, 74, 77, 99, 168, 169]. This non-stoichiometry has a relatively minor effect on T_{Curie}, in contrast with samples prepared by pulsed laser deposition or molecular beam epitaxy [99, 184], but strongly reduces the saturation mag-

netization and alters the electronic transport, driving the system away from the metallic regime characteristic of stoichiometric films [98, 99]. These findings indicate that local disorder and cation vacancies play a decisive role in determining the magnetic and electronic ground state of SRO [75, 99, 169, 185].

Despite this, the microscopic mechanisms by which Ru deficiency modifies the local magnetic environment remain poorly understood. In particular, it is still debated whether the reduction in magnetization originates from a homogeneous dilution of Ru magnetic moments throughout the film or from spatially confined, magnetically suppressed interfacial regions, often referred to as "dead" layers [186–189]. This issue is central to understanding the true magnetic depth profile of SRO and how stoichiometric imperfections and interfacial strain collectively determine the emergent magnetic anisotropy in strongly correlated oxides. A detailed microscopic picture is also essential for disentangling intrinsic interfacial phenomena, such as orbital reconstruction or exchange coupling, from extrinsic effects introduced by disorder or cation non-stoichiometry. Moreover, the interplay between stoichiometry, interfacial magnetism, and PMA is of increasing importance for the design of oxide-based spintronic and quantum devices, where even nanometric deviations in composition or interfacial structure can drastically influence spin transport and proximity effects [19, 31, 51, 88, 91, 95–97].

In this context, the present section employs polarized neutron reflectometry (PNR) and off-specular scattering (OSS), complementary to X-ray reflectivity (XRR) and scanning transmission electron microscopy (STEM-EDS), to obtain a comprehensive, depth-resolved picture of the structural and magnetic profile of Ru-deficient SRO thin films grown on Nb-doped $SrTiO_3$ substrates [190–195]. These techniques provide nanometric sensitivity to both nuclear and magnetic scattering length densities, enabling direct correlation between stoichiometric disorder, interfacial roughness, and the spatial distribution of magnetization. The results presented here elucidate how Ru deficiency governs interfacial magnetism and PMA in this correlated oxide material, offering a solid foundation for interpreting the interfacial magnetic coupling and *possible* proximity-induced phenomena later investigated in YBCO/SRO heterostructures.

7.1.2. Experimental details

Epitaxial Ru-deficient SRO thin films were grown on Nb-doped $SrTiO_3$ (Nb:STO, 0.05 wt% Nb ≈ 0.1 at%) single-crystalline (001)-oriented substrates with miscut angles between 0.05° and 0.1°. To minimize artifacts associated with the antiferrodistortive (AFD) transition of STO during neutron experiments [23], Nb:STO was selected as the substrate [196, 197]. Prior to deposition, the substrates were chemically etched in a buffered NH_4F–HF solution for 30 s and subsequently annealed at 950 °C for 2 h to obtain atomically flat, TiO_2-terminated surfaces, as verified by atomic force microscopy (AFM).

The SRO thin films were deposited from a stoichiometric SRO target using the HOPS system operating in radio-frequency (RF) mode. Before deposition, the chamber was evacuated to high vacuum and the target was pre-sputtered for 24 h to stabilize the plasma. The optimized growth parameters were deposition temperature T_{dep} = 785 °C, target–substrate distance D_{TS} = 2.5 cm, oxygen partial pressure P_{O_2} = 1.5 mbar, and forward power FWDP = 100 W. Under these conditions, the plasma remained stable and homogeneous throughout the deposition process. The typical growth rate at such deposition parameters is approximately 125 $Å h^{-1}$.

Surface morphology and roughness were analyzed by AFM. The crystalline structure,

epitaxial quality, and strain relation were investigated using high-resolution X-ray diffraction (HR-XRD). Film thickness and interfacial roughness were extracted from XRR fits. Cross-sectional Scanning Transmission Electron Microscopy coupled with Energy-Dispersive X-ray Spectroscopy (STEM-EDS) was performed on lamella prepared along the film/substrate [110] crystallographic direction using a FEI Tecnai G2 F20 and FEI Titan G2 80–200 ChemiSTEM microscope to verify interface sharpness and compositional homogeneity. Field-cooled (FC) magnetization curves were recorded under a 50 Oe field applied parallel (in-plane) and perpendicular (out-of-plane) to the [100] crystallographic direction to extract the T_{Curie}. Magnetization hysteresis loops were measured at 5, 80, and 100 K after field cooling the samples in 5 T to evaluate the magnetic anisotropy.

Neutron scattering measurements (PNR and OSS) were performed at the Magnetism Reflectometer (BL-4A) of the Spallation Neutron Source (SNS), Oak Ridge National Laboratory (ORNL). Since the SRO films have reduced magnetization, samples with an area of 10 × 10 mm^2 were measured under an in-plane magnetic field of 4.8 T applied along the [100] direction. The measurements were performed after field-cooling the samples in 4.8 T magnetic field applied in-plane to 100, 80, and 5 K. The neutron spin polarization was set either parallel (R+) or antiparallel (R–) to the field direction, which remained applied throughout the measurements. The spin-up (R+) and spin-down (R–) reflectivities were recorded up to $Q_z = 0.12$ $Å^{-1}$. Complementary off-specular maps were acquired to investigate lateral magnetic correlations and domain structures.

7.1.3. Morphological and structural characterization

The surface morphology of the Nb:STO substrate and the deposited SRO thin film is shown in Fig. 7.1(a–c). The substrate exhibits the typical terraced–step morphology characteristic of TiO_2 termination, with an average step height of approximately one unit cell. After deposition, however, the SRO film displays a multiterraced island morphology, in contrast to the smooth, step-flow surfaces observed for SRO films grown on undoped STO substrates in chapter 5.

This difference likely arises from the modified surface energy and adatom mobility associated with Nb doping [196, 197], which increases the substrate's electrical conductivity and changes its interaction with the plasma during HOPS deposition [198]. The presence of Nb may also locally alter the oxygen chemical potential near the surface, reducing surface diffusion lengths and thereby promoting the nucleation of three-dimensional islands instead of continuous terrace propagation. Consequently, the film grows through a Stranski–Krastanov mode, in which layer-by-layer growth transitions into island formation as strain and surface roughness accumulate. The appearance of multiple circular terraces around individual island nuclei indicates the occurrence of secondary nucleation on top of pre-existing islands [94, 95]. The root-mean-square (RMS) roughness determined from 2.5 × 2.5 $µm^2$ AFM scans is 37 Å ± 14 Å, consistent with moderately rough surfaces expected for films grown on low-miscut Nb:STO substrates.

The high crystalline quality of the film is confirmed by HR-XRD [Fig. 7.1(d)], which exhibits intense film reflections accompanied by well-defined Laue oscillations, indicating coherent growth and smooth interfaces over the entire thickness. Reciprocal space mapping (RSM) and ϕ-scans recorded around the (103) crystallographic reflection of SRO and Nb:STO [Fig. 7.1(e–f)] demonstrate that the film is epitaxially aligned with the substrate and laterally strained to match its in-plane lattice parameter. The out-of-plane lattice constant obtained from RSM, 3.98 ± 0.02 Å, is slightly larger than that of stoi-

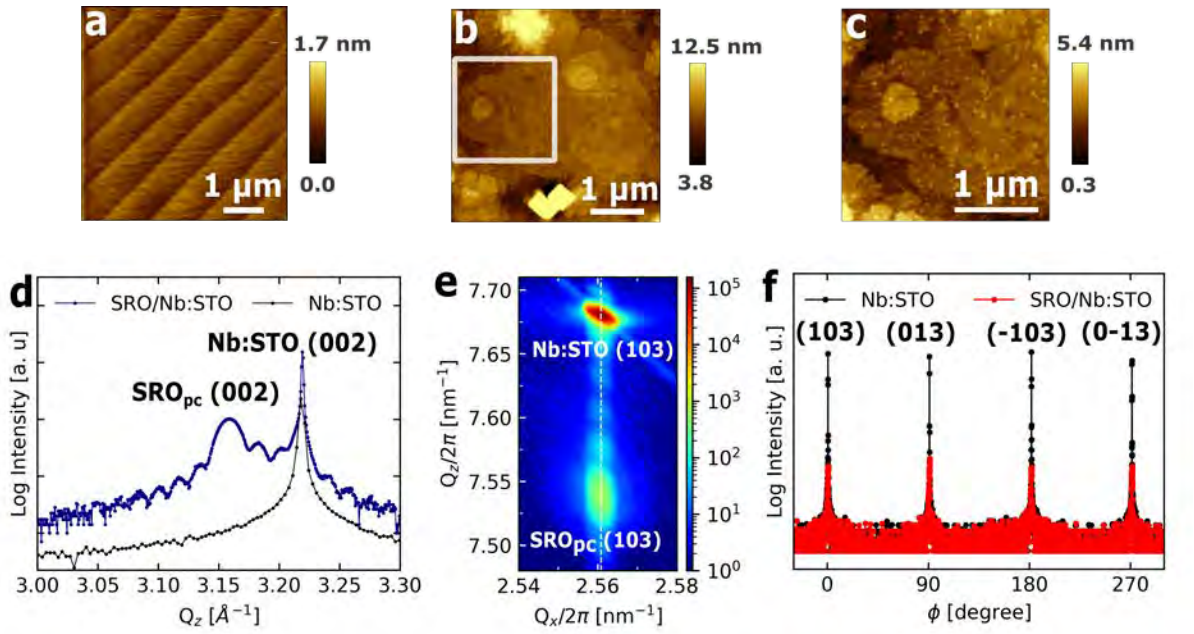

Figure 7.1.: Atomic force microscopy micrographs of (a) Nb:STO substrate and (b) SRO thin film. (c) Magnified view of the highlighted square in (b). X-ray diffraction pattern (d) around the STO (002). Reciprocal space map (e) and ϕ-scans (f) performed around the (103) crystallographic reflection of the SRO thin film and Nb:STO substrate.

chiometric SRO (3.949 Å) and represents the structural signature of Ru deficiency in the film [75, 99, 169]. The ϕ-scan peak-intensity distribution further indicates a multidomain in-plane structure, a common feature in SRO films grown on low-miscut or nominally exact STO substrates, where the terrace orientation forms large angles with the [010] crystallographic direction [95, 199].

To quantitatively evaluate the total film thickness (t) and interfacial roughness (σ), XRR data were fitted using the GenX software package [143]. The simulations were based on stacked block-like layers representing the film structure on the substrate. The models considered the presence or absence of low scattering-length-density (SLD) interlayers at the surface and/or at the film–substrate interface, similar to the analysis briefly shown in Chapter 5, as schematically illustrated in Fig. 7.2(a).

Models 1 and 2 [Figs. 7.2(b, c)] successfully reproduced the overall periodicity of the reflectivity oscillations, mainly sensitive to the total thickness, but failed to capture the finer oscillatory features related to interfacial roughness in the Q_z range of 0.07–0.15Å^{-1}. In contrast, Models 3 and 4 [Figs. 7.2(d, e)] provided an excellent agreement with the experimental data, accurately reproducing both the intensity decay and the amplitude modulation near the critical angle. Considering the AFM results, which revealed a surface composed of densely packed multiterraced islands, Model 3 appears physically representative of the actual morphology in comparison with Models 1 and 2.

Model 4, however, yielded a similarly good fit quality in comparison to Model 3, and is consistent with previous reports of Sr enrichment and Ru deficiency at both the film surface and the SRO/STO interface, attributed to Ru volatility under oxidizing growth conditions [74, 77]. The figure of merit (FOM), defined in GenX as the average absolute difference between the base-10 logarithms of the measured and simulated reflectivities,

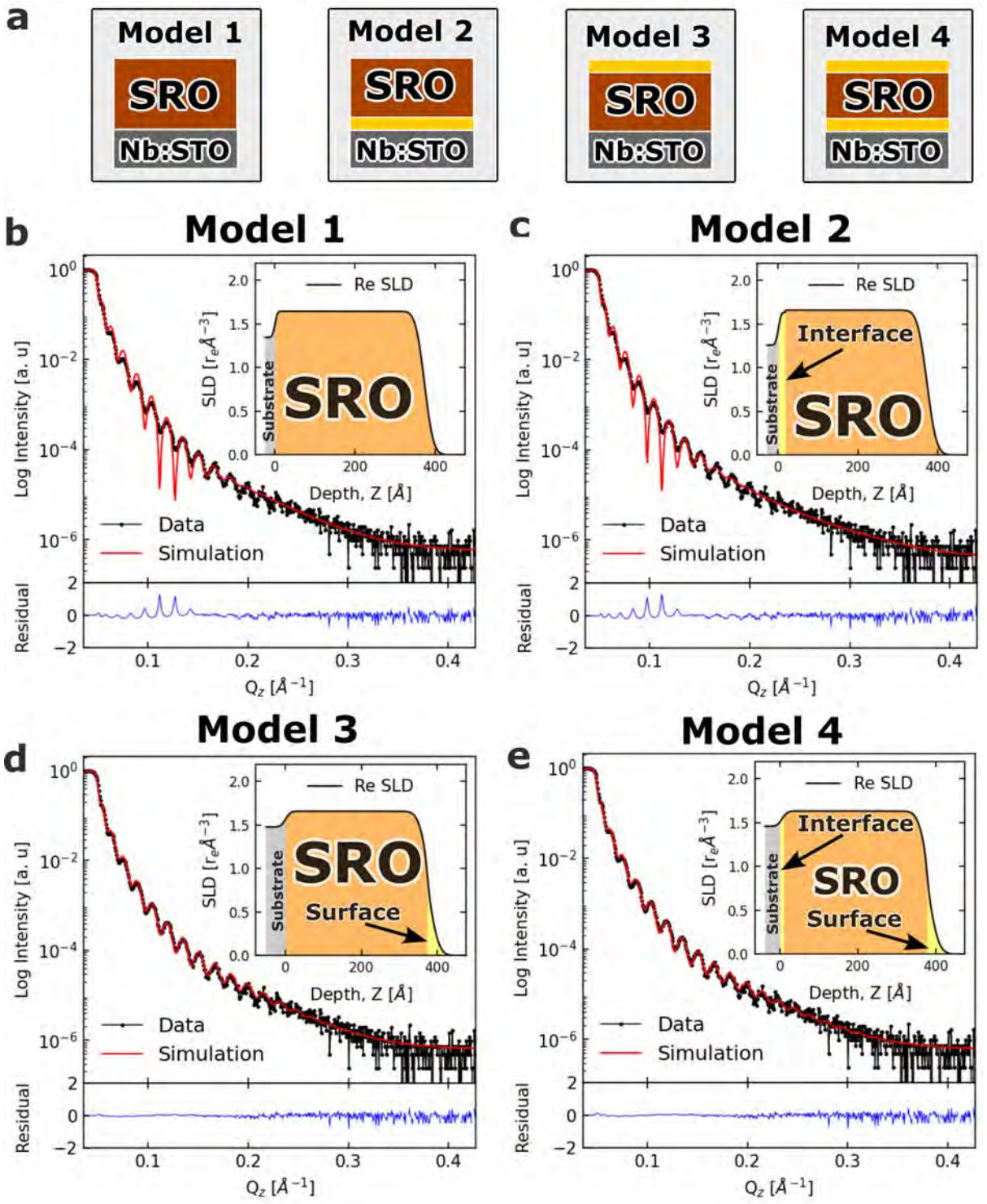

Figure 7.2.: X-ray reflectivity (XRR) data (black symbols) and GenX simulations (red lines) for all models tested in this work. The insets show the real part of the SLD profiles used in each model. Residuals (blue lines) quantify the difference between experimental data and simulations.

for Models 3 and 4 was nearly identical (on the order of 10^{-2}), leading to some ambiguity as to which configuration best represents the real structure of the sample.

To verify the reliability of the XRR-derived model and to assess whether it captures the real chemical profile, cross-sectional STEM-EDS was performed. The high-angle annular dark-field (HAADF) image [Fig. 7.3(a)] shows that the SRO film grows epitaxially on the Nb:STO substrate, forming an atomically sharp and coherent interface with no detectable secondary phases. The atomic-resolution image [Fig. 7.3(b)] clearly resolves alternating RuO_2, SrO, and TiO_2 planes across the interface, confirming the ordered perovskite stacking.

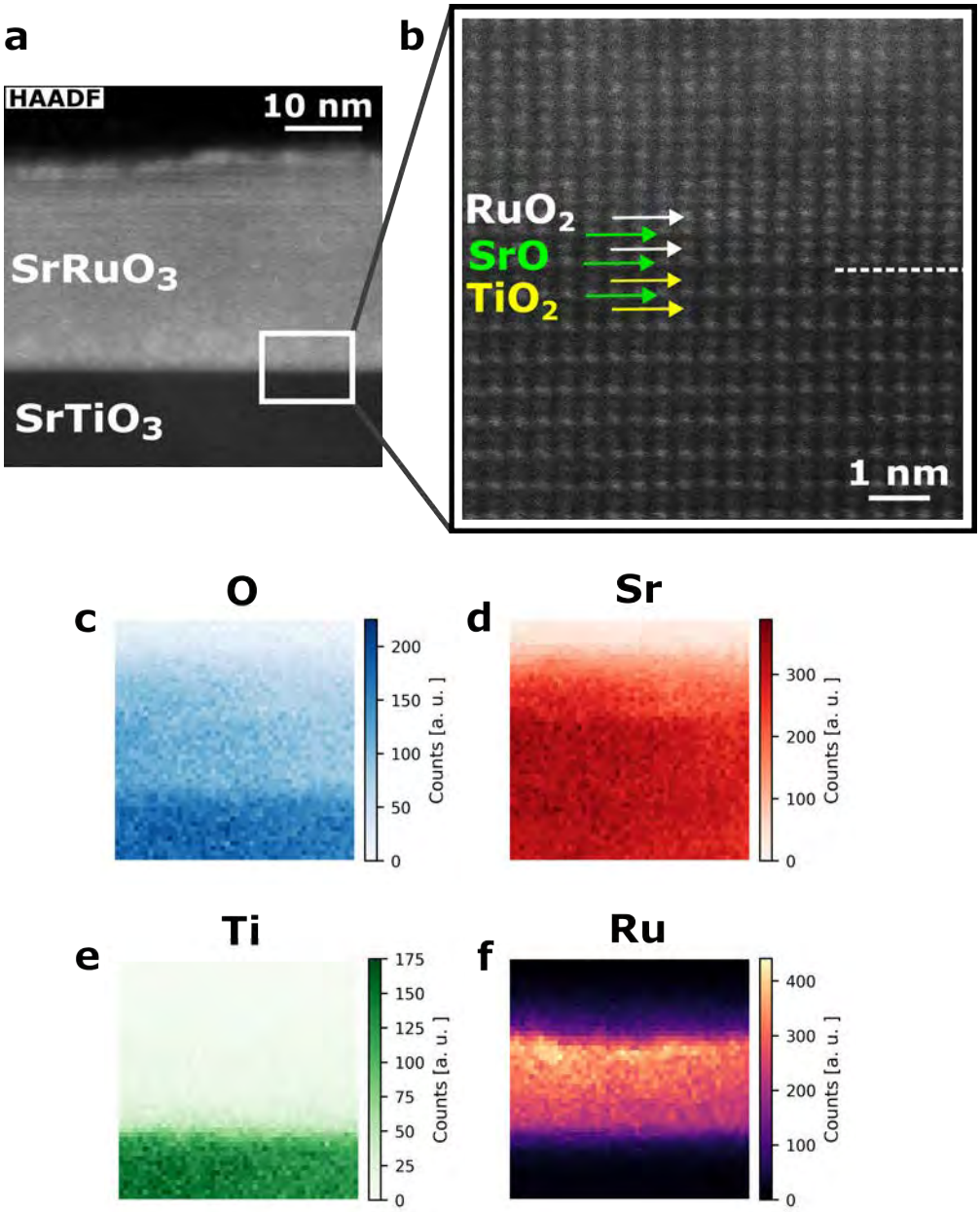

Figure 7.3.: (a) Cross-sectional HAADF-STEM image of the epitaxial SRO film on Nb:STO substrate. (b) Atomic-resolution image showing sharp interface and alternating $RuO_2/SrO/TiO_2$ planes. (c–f) EDS elemental maps for O, Sr, Ti, and Ru, evidencing Ru deficiency more pronounced at the film interfaces.

Elemental maps for O, Sr, Ti, and Ru [Figs. 7.3(c–f)] corroborate the epitaxial relationship and clearly evidence a reduction in Ru concentration near both the film surface and the buried interface. This depth-dependent compositional variation agrees with the reduced-SLD layers introduced in Model 4, confirming that this is the most physically consistent sample description. Values of thickness and average effective interfacial roughness (σ_{eff}) obtained in Model 4 are shown in Table 7.1. The RMS roughness σ_{eff} was calculated by combining the individual roughness values of the substrate/film, film, and surface interfaces, and provides a single representative parameter that captures the overall morphological contribution of multiple interfaces, facilitating direct comparison between XRR and PNR results.

The EDS maps indicate a moderate Ru deficiency even in the film bulk, suggesting that the non-stoichiometry extends throughout the entire thickness, though more pronounced at the interfaces. Such a reduction in Ru content within the film bulk is also reflected in the SLD profile obtained from the XRR fits, which yields an average nuclear SLD of 1.633 $r_e Å^{-3}$ ± 0.024 $r_e Å^{-3}$, compared with the theoretical value of 1.746 $r_e Å^{-3}$ for stoichiometric SRO. This significant decrease corroborates that Ru deficiency is not restricted to the interfaces but extends throughout the film thickness, indicating a generalized non-stoichiometry across the entire layer.

This observation aligns with the two types of disorder previously reported by Wakabayashi et al. [99]: (i) structural disorder, arising from Ru vacancies distributed within the crystalline lattice, which reduces the coherent thickness and perturbs long-range order, and (ii) interface-driven disorder, originating from compositional and structural inhomogeneities localized near the film–substrate interface. The former leads to a uniform reduction in the SLD, while the latter accounts for the further suppression near the interfaces observed here. In contrast to earlier reports on films grown by direct-current HOPS, where Ru deficiency was confined to interfacial regions [74, 77], the uniform SLD reduction found in the present RF–HOPS films indicates that the high oxygen pressure and plasma conditions promote Ru volatility throughout the entire growth process. As a result, the SRO layer remains structurally coherent [169], but exhibits a compositional gradient extending from surface to interface.

A slight deviation between experimental and simulated reflectivity curves was observed close to the critical angle for all models, likely originating from the use of Nb-doped STO substrates, whose slightly altered lattice parameters, SLD, and surface energies differ from those of undoped STO and are not perfectly reproduced by the standard set of model parameters.

7.1.4. Magnetic characterization

The FC magnetization curves measured with a 50 Oe magnetic field applied along the in-plane (IP) and out-of-plane (OP) directions are shown in Fig. 7.4(a). Both curves confirm the ferromagnetic nature of the Ru-deficient SRO film, with a T_{Curie} = 158.6 K ± 0.5 K, determined from the first derivative of the FC magnetization [inset of Fig. 7.4(a)]. A second anomaly appears near 90 K, corresponding to the AFD structural phase transition of the Nb:STO substrate, which slightly perturbs the magnetic response through strain-mediated coupling across the interface.

Magnetic hysteresis loops recorded at 100 K, 80 K, and 5 K are presented in Fig. 7.4(b–d). The loops reveal clear PMA, as the film saturates more easily under out-of-plane fields, whereas the in-plane configuration remains unsaturated even at 5 K. Small

step-like (bumps) features, particularly visible in the low-temperature loops, indicate a multidomain magnetic structure, commonly observed in strained SRO thin films [91, 95]. Such behavior is consistent with the coexistence of several energetically equivalent domain orientations stabilized by epitaxial strain and local structural distortions [88, 102, 108].

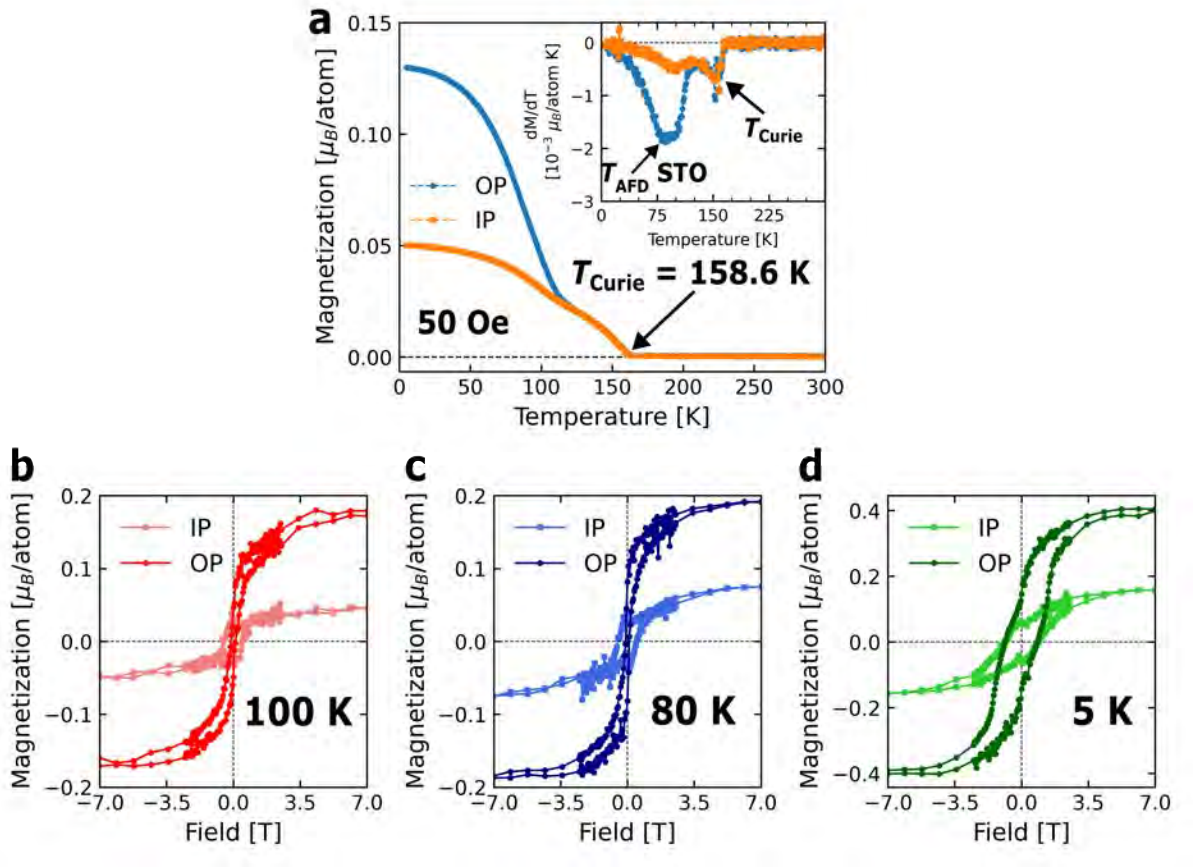

Figure 7.4.: (a) Field cooled magnetization measurement performed with 50 Oe applied perpendicular (out-of-plane – OP) and parallel (in-plane – IP) to the [001] crystallographic direction. The inset shows the first derivative of the magnetization, from where the T_{Curie} and T_{AFD} values were obtained. Magnetic hysteresis performed at (b) 100 K, (c) 80 K, and (d) 5 K.

In stoichiometric SRO, the saturation magnetization typically reaches about 1.6 μ_B/Ru at low temperature [75]. In contrast, the present Ru-deficient film exhibits a lower value of approximately 0.4 μ_B/atom at 5 K, consistent with the substantial reduction of the Ru–O–Ru exchange interaction. This suppression arises from Ru vacancies that locally disrupt the double-exchange mechanism mediating ferromagnetism in SRO, thereby weakening the long-range order [99, 169]. Nonetheless, the persistence of a finite magnetic moment demonstrates that the concentration of vacancies remains below the percolation threshold required to suppress ferromagnetism and PMA completely.

The anisotropy field in SRO can exceed 12–14 T [75], far above the maximum field applied during the SQUID (and PNR) measurements, which explains why full saturation is not achieved along the magnetic hard axes. In addition, as discussed by Ziese et al. [200], the usual subtraction of the diamagnetic background from the substrate may neglect paramagnetic contributions from the film, occasionally leading to an apparent reduction of the in-plane saturation magnetization. Structural imperfections and

local strain variations can further hinder complete alignment by promoting domain-wall pinning and small canting of the magnetization vector [102, 108, 201].

7.1.5. Neutron scattering characterization

The depth-dependent magnetic properties of the Ru-deficient SRO thin film were investigated by PNR at 100, 80, and 5 K following field cooling in a 4.8 T magnetic field applied parallel to the sample surface along the in-plane [100] direction (the magnetic hard axis of SRO). The applied field, although the maximum available at the instrument, remains below the anisotropy field of approximately 12–14 T [75], implying that complete magnetic saturation could not be reached under these conditions.

Figure 7.5(a–c) shows the experimental spin-asymmetry (SA) curves, with SA defined as:

$$\mathrm{SA} = \frac{(R+) - (R-)}{(R+) + (R-)}, \tag{7.1}$$

obtained at the three temperatures, together with the corresponding fits. The use of spin asymmetry isolates the magnetic contribution to the reflectivity by removing the purely structural background [190, 192, 194, 202]. The oscillatory behavior observed in all datasets indicates a finite magnetic contrast within the film, which increases slightly upon cooling from 100 K to 5 K. Although the amplitude of the spin asymmetry is small, consistent with the low magnetic moment determined by SQUID magnetometry, the data provide sufficient sensitivity to extract reliable depth-resolved magnetic profiles. A slight mismatch around the first minimum of the spin asymmetry is attributed to the instrumental resolution and data merging procedure during PNR data reduction, rather than to deficiencies of the structural/magnetic model.

The corresponding nuclear (nSLD) and magnetic (mSLD) density profiles derived from the fits are shown in Fig. 7.5(d). The structural parameters obtained from PNR (film thickness and interfacial roughness) agree well with those determined from XRR and AFM, confirming the internal consistency of the model (see Table 7.1). Similar to the XRR findings, the nSLD values are uniformly reduced compared with stoichiometric SRO, consistent with a generalized Ru deficiency extending throughout the film thickness.

From the magnetic point of view, the mSLD profiles reveal a finite magnetization across the entire SRO layer at all temperatures, with slightly enhanced values upon cooling. The interface regions (surface and film/substrate) exhibit a significantly reduced magnetic moment, ranging between 0.01 and 0.10 μ_B/atom, while the central region of the film retains higher values consistent with long-range ferromagnetic order. The average magnetization values extracted from the fits (0.13, 0.18, and 0.21 μ_B/atom at 100, 80, and 5 K, respectively), were calculated as the thickness-weighted mean of the layer magnetizations,

$$\langle \mu \rangle = \frac{\sum_i \mu_i t_i}{\sum_i t_i}, \tag{7.2}$$

in order to be comparable with the SQUID values, and are in excellent agreement with the macroscopic SQUID results. This consistency confirms that the reduced overall magnetization measured by SQUID arises from the depth-dependent distribution resolved by PNR rather than from incomplete magnetic ordering.

The temperature dependence of the average magnetization obtained from PNR follows the same trend as the SQUID results, but with subtle differences in magnitude that reveal an evolution of the magnetization orientation. At 100 and 80 K, the $\langle \mu \rangle$ values derived

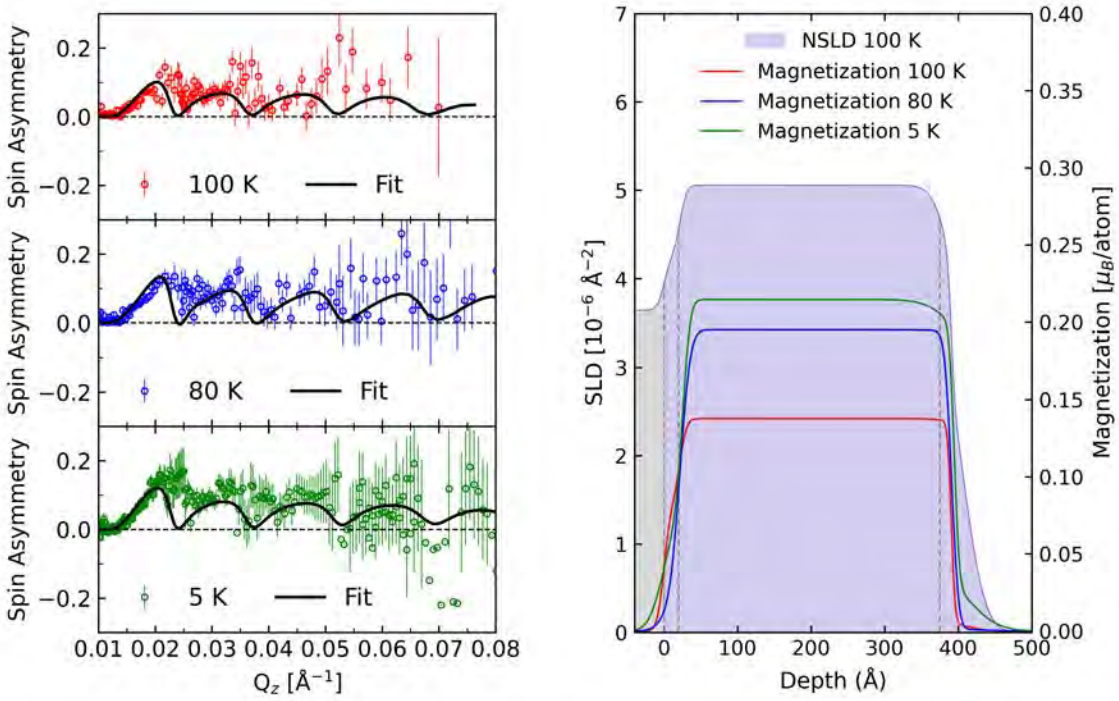

Figure 7.5.: Spin asymmetry $[(R^+)-(R^-)]/[(R^+)+(R^-)]$ measured at (a) 100 K, (b) 80 K, and (c) 5 K after field cooling the sample in a 4.8 T in-plane magnetic field. Open symbols represent experimental data and solid lines the best-fit curves obtained from the refined model. (d) Corresponding nuclear (nSLD, left axis) and magnetic (mSLD, right axis) scattering length density profiles extracted from the fits. The dotted vertical lines indicate the approximate positions of the film interfaces and layer boundaries. The reduced nSLD relative to the theoretical value for stoichiometric SRO indicates Ru deficiency extending throughout the film thickness, while the mSLD profiles reveal finite magnetization across all temperatures, slightly suppressed near the interfaces.

Table 7.1.: Structural and magnetic parameters obtained from XRR, PNR, and SQUID magnetometry. t denotes the total film thickness, σ_{eff} the RMS interfacial roughness, and $\langle\mu\rangle$ the average magnetization from PNR fits in μ_B/atom. M^{OP} and M^{IP} correspond to the saturation magnetization obtained by SQUID with the field applied out-of-plane and in-plane, respectively.

T (K)	t (Å)	σ_{eff} (Å)	$\langle\mu\rangle$ (μ_B/at.)	M^{OP} (μ_B/at.)	M^{IP} (μ_B/at.)
XRR (300)	382 (3)	13.7 (2)	–	–	–
PNR (100)	406 (20)	15.6 (5)	0.13 (0.02)	0.174	0.045
PNR (80)	406 (20)	28.6 (5)	0.18 (0.02)	0.191	0.073
PNR (5)	407 (20)	28.6 (5)	0.21 (0.06)	0.412	0.154

from PNR (0.13 and 0.18 μ_B/atom, respectively) closely match the out-of-plane (M^{OP}) magnetization obtained from SQUID, indicating that the magnetization vector remains predominantly perpendicular to the film plane in this temperature range. However, at 5 K, the PNR-derived value (0.21 μ_B/atom) approaches the in-plane (M^{IP}) component measured by SQUID, suggesting a partial reorientation of the magnetization vector toward the film plane upon cooling. This temperature-driven canting behavior reflects the competition between the strong PMA inherent to the strained SRO film and the Zeeman energy associated with the large in-plane magnetic field applied during the PNR experiment. Such reorientation of the magnetization is further supported by the off-specular scattering data discussed below.

Complementary OSS maps (Fig. 7.6) reveal a central specular line at $K_i - K_f = 0$ and diffuse scattering along the diagonals, characteristic of lateral roughness and interfacial inhomogeneity. The diffuse intensity remains nearly constant with temperature, but a slight broadening at 5 K indicates subtle modifications in the lateral magnetic correlations. This evolution can be attributed to a gradual canting of the magnetization vector toward the film plane as temperature decreases. In this scenario, the strong PMA constrains a finite out-of-plane component, while the in-plane field promotes the formation of canted magnetic domains with locally varying orientations. The coexistence of these domains, each contributing differently to the in-plane projection of magnetization, explains the broadening of the diffuse scattering without a corresponding increase in total intensity.

Given the substantial reduction in interfacial magnetization revealed by the PNR fits, it is reasonable to consider whether the top and bottom regions of the film behave as magnetically inactive, or "dead" layers. Similar interfacial magnetic suppression has been widely reported in correlated oxide thin films such as $La_{0.7}Sr_{0.3}MnO_3$ (LSMO), where non-magnetic layers of 0.8–1.5 nm were observed depending on substrate type and film thickness [186]. In SRO, Horiuchi *et al.* [187] also identified a ~3 nm region near the SRO/STO interface exhibiting reduced magnetization and conductivity. Other studies have also reported that near-interface regions in SRO exhibit diminished ferromagnetism or even non-magnetic behavior associated with disorder, stoichiometric deviations, or strain effects [188, 189]. Such effects are typically attributed to a combination of structural disorder, stoichiometric deviations, orbital reconstruction, or strain-driven distortions at the interfaces [5, 203].

To evaluate whether the interfaces could be considered magnetically "dead", an alternative model was tested in which the interfacial magnetization was constrained to zero. However, this configuration did not yield reliable results compared to the model presented here, where both interfaces retain a small but finite magnetic moment ranging from 0.01 to 0.10 μ_B/Ru. Although both models reproduce the general trend of the spin-asymmetry curves, the "dead" layer model fails to capture the oscillation minima with the same accuracy and shifts the position of the maxima, as seen by comparing the two cases in the Appendix D. Furthermore, this model requires interfacial layers significantly thicker than those determined by XRR, STEM–EDS, and the ones reported by Młynarczyk et al. [74, 77], reinforcing that such a description is not physically consistent. Therefore, the model including minimally magnetic interfaces provides a more realistic representation of the experimental data.

The strongly reduced interfacial magnetization inferred from this model could also arise from an enhanced PMA near the interfaces, which would tilt the magnetic moments further out of the film plane. Since PNR is primarily sensitive to the in-plane magnetization

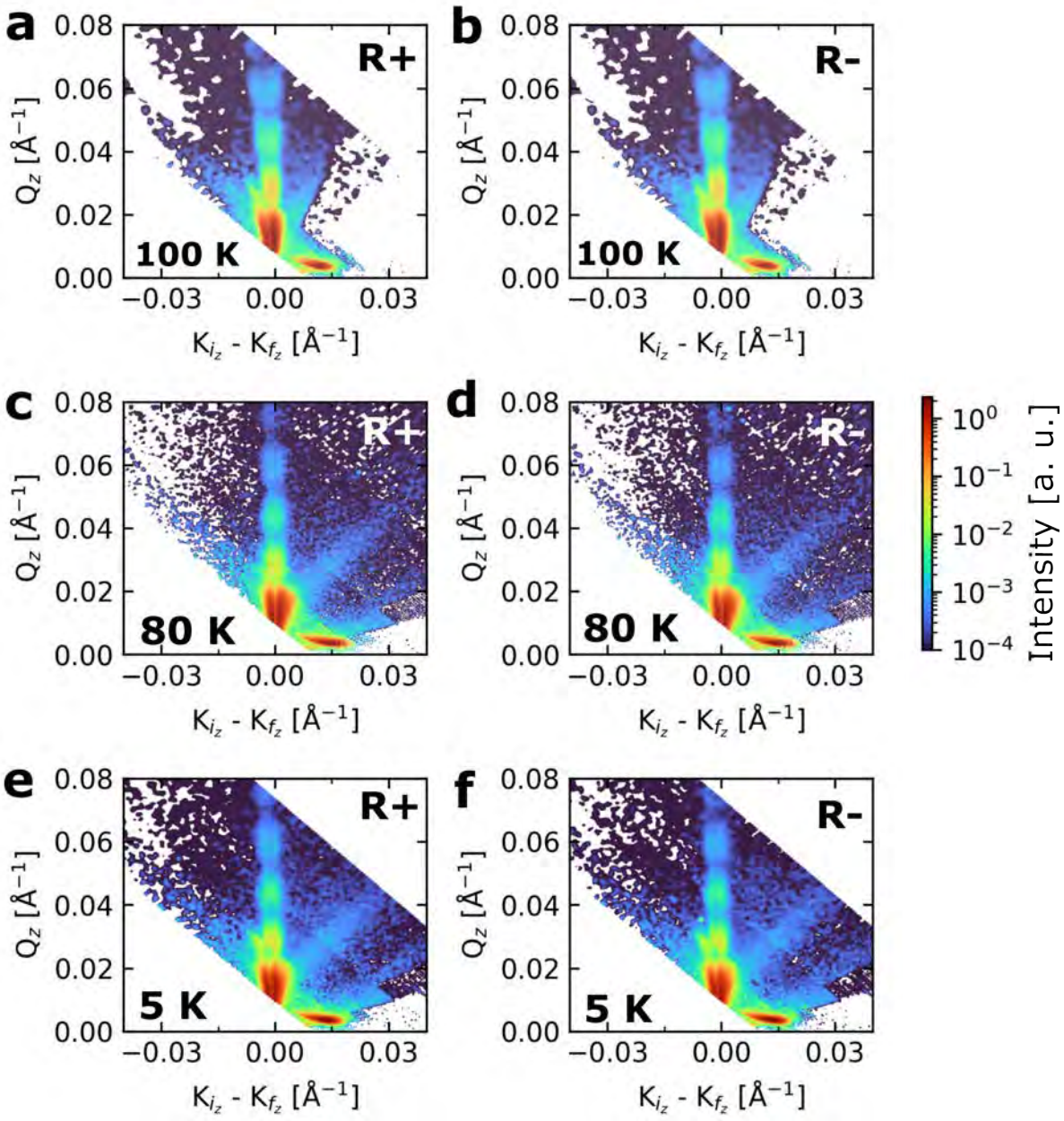

Figure 7.6.: Off-specular neutron scattering maps acquired at (a) 100 K, (b) 80 K, and (c) 5 K for both spin channels (R^+ and R^-). The maps display the central specular line at $K_i - K_f = 0$ and diffuse diagonal bands associated with lateral roughness and interfacial inhomogeneity. The diffuse features broaden slightly at low temperature, indicating modifications of the lateral magnetic correlations within the film.

component, this effect would manifest as a reduced interfacial magnetic signal even if the total magnetic moment were not substantially diminished. For these reasons, the fully "dead" layer scenario cannot be sustained. Nevertheless, the intrinsically weak magnetization of Ru-deficient SRO and the strong PMA of the material impose clear limitations on the sensitivity of PNR, meaning that the differences between the two models should be interpreted within the experimental uncertainty of the technique.

7.1.6. Conclusions

The combined XRR, STEM–EDS, SQUID magnetometry, and PNR results provide a consistent microscopic picture of the structural and magnetic properties of Ru-deficient SRO thin films grown by HOPS on Nb-doped STO substrates. Despite the 20–25% Ru deficiency, the films maintain high crystalline quality, coherent epitaxy, and well-defined PMA. The reduced nuclear SLD extracted from XRR and PNR, together with the STEM–EDS mapping, reveals that the Ru deficiency is not confined to the interfaces but extends through the entire film thickness, giving rise to a depth-dependent compositional gradient.

Magnetization measurements confirm robust ferromagnetic order with a T_{Curie} near 159 K, but a strongly reduced saturation moment (0.4 μ_B/atom at 5 K) was observed, consistent with disrupted Ru–O–Ru exchange interactions. PNR provides depth-resolved evidence that the magnetization is not uniform, with interfacial regions exhibiting a significantly smaller magnetic moment (0.01–0.10 μ_B/atom) than the film interior. The analysis shows that a model with minimally magnetic interfaces reproduces the data most accurately, while models with fully non-magnetic interfaces lead to unrealistic interfacial thicknesses and degraded fits. This suggests that the interfacial magnetization, although severely reduced, does not vanish entirely.

The temperature-dependent PNR and OSS data reveal a progressive canting of the magnetization vector toward the film plane upon cooling, driven by the competition between strong PMA and the in-plane magnetic field applied during the experiment. Such canting, combined with the compositional gradient and local strain, likely enhances the magnetic anisotropy near the interfaces, further reducing the in-plane magnetization component detected by PNR. These results indicate that the interfaces are not magnetically "dead" but rather exhibit an enhanced PMA, which cannot be directly probed by PNR since this technique is sensitive only to the in-plane component of the sample magnetization.

In summary, these findings demonstrate that Ru deficiency in SRO not only diminishes the total magnetic moment but also induces a pronounced magnetic depth modulation governed by interfacial disorder and anisotropy effects. The results clarify the microscopic origin of the reduced magnetization in non-stoichiometric SRO and establish a reliable framework for interpreting interfacial magnetic coupling in $YBa_2Cu_3O_{7-x}/SrRuO_3$ heterostructures discussed in the following section.

7.2. Investigation of magnetic proximity effects in $YBa_2Cu_3O_{7-x}/SrRuO_3$ heterostructure

7.2.1. Scientific context

Epitaxial heterostructures combining complex oxide superconductors and ferromagnets provide a versatile platform for investigating the interplay between competing order parameters at the atomic scale. When superconductivity and ferromagnetism coexist within nanometer-scale proximity, various proximity effects can arise, giving rise to unconventional interfacial states [19, 23, 26]. The manifestation of these effects depends sensitively on the magnetic anisotropy, electronic correlations, and atomic structure at the interface, offering opportunities to engineer spin-polarized transport and superconducting spintronic functionalities [4, 30].

In oxide-based superconductor/ferromagnet systems, such as $YBa_2Cu_3O_{7-x}/SrRuO_3$ (YBCO/SRO), the strong spin–orbit coupling and perpendicular magnetic anisotropy (PMA) of SRO contrast with the d-wave superconductivity and anisotropic coherence length of YBCO ($\xi_{ab} \gg \xi_c$). This combination allows the exploration of both the conventional direct proximity effect, in which superconducting correlations penetrate into the ferromagnetic layer, and the reverse or indirect proximity effects, in which magnetic correlations and spin fluctuations at the interface can modify the superconducting condensate [24, 28, 29, 31, 204]. Understanding how these correlations influence the superconducting order parameter is essential for elucidating the interfacial coupling mechanisms in complex oxides.

In this work, we investigate proximity effects in a YBCO(22 nm)/SRO(22 nm) bilayer epitaxially grown on $SrTiO_3$ (001) substrates. Building upon the results presented in Section 7.1, which established the depth-resolved magnetic structure of Ru-deficient SRO thin films, we focus here on whether the interfacial coupling between the superconducting and ferromagnetic layers can give rise to detectable modifications in the magnetic depth profile near the interface. To probe these phenomena with nanometer-scale resolution, we employ polarized neutron reflectometry (PNR), which provides quantitative information on both nuclear and magnetic scattering length densities (SLD) profiles. This technique allows us to search for superconductivity-induced changes in the magnetic scattering potential and to identify possible signatures of interfacial magnetic correlations within the YBCO/SRO heterostructure.

7.2.2. Experimental details

The YBCO/SRO heterostructures investigated in this work were fabricated following the same HOPS procedure described in Chapter 6. The main difference lies in the reduced total thickness of the layers, with both YBCO and SRO films deposited to a nominal thickness of approximately 22 nm. The heterostructures were grown on single-crystalline $SrTiO_3$ (STO) (001) substrates that had been chemically etched and thermally annealed to obtain atomically flat TiO_2-terminated surfaces.

The SRO bottom layer was first deposited from a stoichiometric ceramic target under optimized growth conditions similar to those discussed in Section 7.1.2, ensuring epitaxial growth with pronounced PMA. Subsequently, the YBCO top layer was deposited under conditions optimized to preserve oxygen stoichiometry and high crystallinity. The bilayers were cooled down to room temperature in an oxygen-rich atmosphere to promote full

oxygenation of the YBCO layer.

The structural and morphological characterizations were performed using high-resolution X-ray diffraction (HR-XRD), X-ray reflectivity (XRR), and atomic force microscopy (AFM), following the same methodologies detailed in Chapter 6. Cross-sectional Transmission Electron Microscopy (TEM) was performed on lamella prepared along the film/substrate [110] crystallographic direction using a FEI Tecnai G2 F20 microscope to verify interface sharpness. Magnetic and transport measurements were carried out using a superconducting quantum interference device (SQUID) magnetometer and a standard four-probe geometry, respectively, to confirm the presence of superconductivity and to assess the magnetic response of the bilayers.

PNR measurements were performed under the same experimental conditions described in subsection 7.1.2. The experiments were conducted at the Magnetism Reflectometer of SNS–ORNL, using an in-plane magnetic field of 4.8 T applied along the [100] crystallographic direction. The samples were field-cooled in this field to the desired measurement temperatures. The reflectivities for the spin-up (R+) and spin-down (R−) neutron polarizations were recorded at various temperatures above and below the superconducting transition temperature of YBCO.

7.2.3. Morphological and structural characterization

Figure 7.7(a) shows a topographical AFM micrograph of the STO substrate demonstrating the adequate TiO_2 surface termination. Local roughness values for the substrates are in the sub-nanometer range. AFM topography [Fig. 7.7(b)] and phase [Fig. 7.7(c)] micrographs of the YBCO/SRO heterostructure deposited on the STO substrate suggest the *c*-axis-oriented epitaxial growth of the YBCO layer, as indicated by the presence of spiral features on the surface, more clearly visible in phase micrograph [71, 72, 160, 163, 164, 174]. CuO and BaCuO precipitates/nanoparticles formed during the YBCO post-growth annealing can be observed on the YBCO film surface as bright round features in the AFM phase micrograph [168, 175, 205]. Local roughness value of 1.9 nm ± 0.7 nm were obtained by AFM in 2.5 × 2.5 μm^2.

The YBCO *c*-axis orientation is further confirmed in the XRD pattern, shown in Fig. 7.7(d), where only YBCO (00*l*) crystallographic reflections were observed, with no detectable contributions from YBCO (*h*00) orientations. Additionally, Laue oscillations around the STO (002) peak are observed in Fig. 7.7(e), the highlighted region in Fig. 7.7(d), suggesting the high structural quality with a large coherent volume for this heterostructure. A sharp interface between the YBCO and SRO films can be observed in cross-sectional TEM micrograph [Fig. 7.7(f)], confirming the *c*-axis oriented growth and epitaxial quality of each layer.

Interestingly, when comparing the YBCO/SRO heterostructures presented in this thesis, the thicker one discussed in Chapter 6 and the thinner one analyzed in this section, a subtle variation in the density of spiral-growth features, associated with *c*-axis oriented YBCO, is observed as a function of the YBCO thickness. This behavior differs from that typically found in YBCO films directly grown on STO or MgO substrates, where the development of spiral morphology and misfit-relief mechanisms strongly depend on film thickness and oxygenation conditions [71, 161, 162]. In the present case, the underlying SRO layer deposited on STO appears to act as a structural buffer layer, partially accommodating the lattice mismatch and thereby influencing the nucleation and growth mode of the overlying YBCO. For thinner YBCO layers, a higher density of *c*-axis-oriented

growth spirals is observed, while thicker layers tend to exhibit a mixed *a*– and *c*-axis orientation. The AFM micrographs, particularly the phase images, clearly show that the surface morphology of these films differs markedly, supporting this interpretation. Unfortunately, the limited number of samples with systematically varied thicknesses prevents a quantitative correlation between the spiral-growth density and YBCO thickness for films grown on SRO/STO.

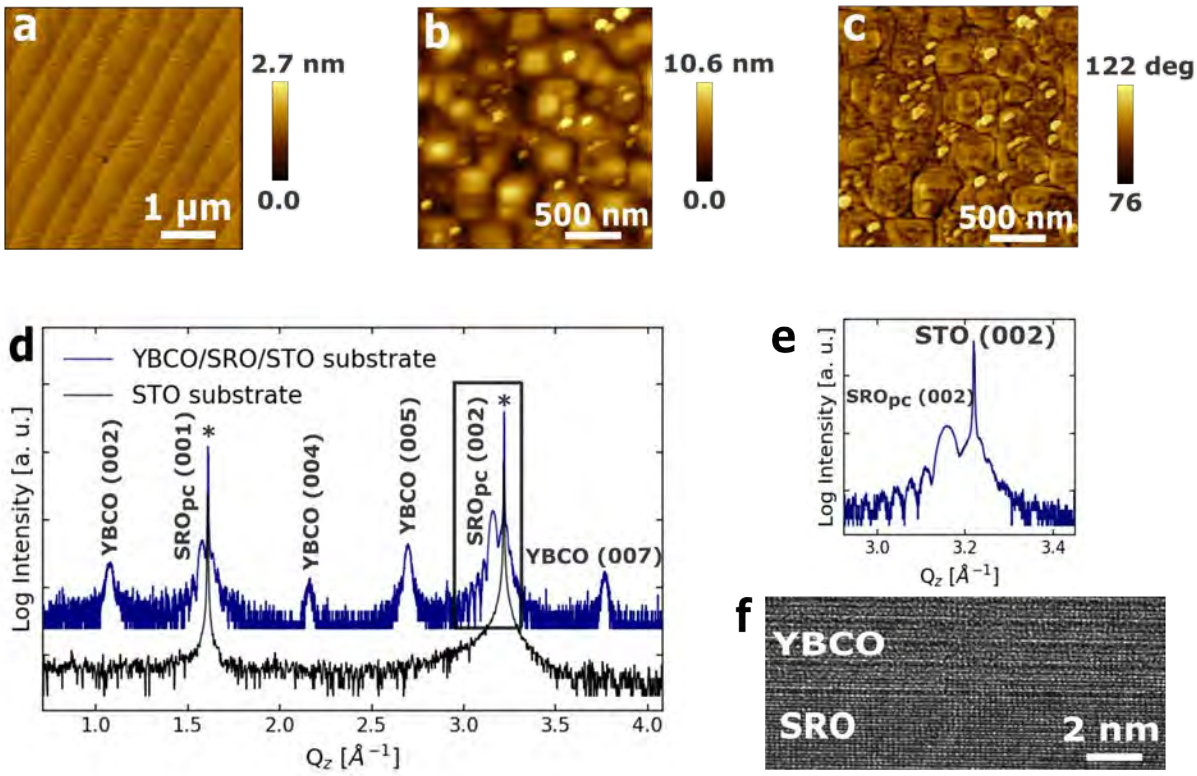

Figure 7.7.: (a) Atomic force microscopy (AFM) micrograph of STO substrate prior the YBCO/SRO heterostructure growth. Topography (b) and phase (c) AFM micrographs of the YBCO surface. (d) X-ray diffraction pattern around STO $\{00l\}$ family of planes. The highlighted region in (d) is presented in (e), showing the heterostructure Laue oscillations around the STO (002). (f) Transmission electron micrograph of the YBCO/SRO interface.

Given the small total thickness of the heterostructure and the low local roughness obtained from AFM measurements, it was possible to characterize the YBCO/SRO bilayer by XRR. The experimental XRR pattern is shown in Fig. 7.8.

For the fitting procedure, performed with GenX, we initially adopted the optimized block-like model for the SRO layer obtained in Section 7.1, which includes a reduced electronic SLD throughout the film thickness and, more prominently, at the surface and buried interfaces. The color scheme representing each layer follows that used in the previous subsection 7.1.3. On top of this structure, a YBCO layer was added, resulting in the configuration referred to as Model 1 [Fig. 7.8(a)]. However, this model did not satisfactorily reproduce the Kiessig fringes and interfacial roughness, yielding a relatively high figure of merit (FOM) of the order of 10^{-1} and noticeable residuals [Fig. 7.8(b)]. From the simulation using model 1, a total thickness of 398 Å ± 12 Å and an effective interfacial roughness of 11 Å ± 7 Å were obtained.

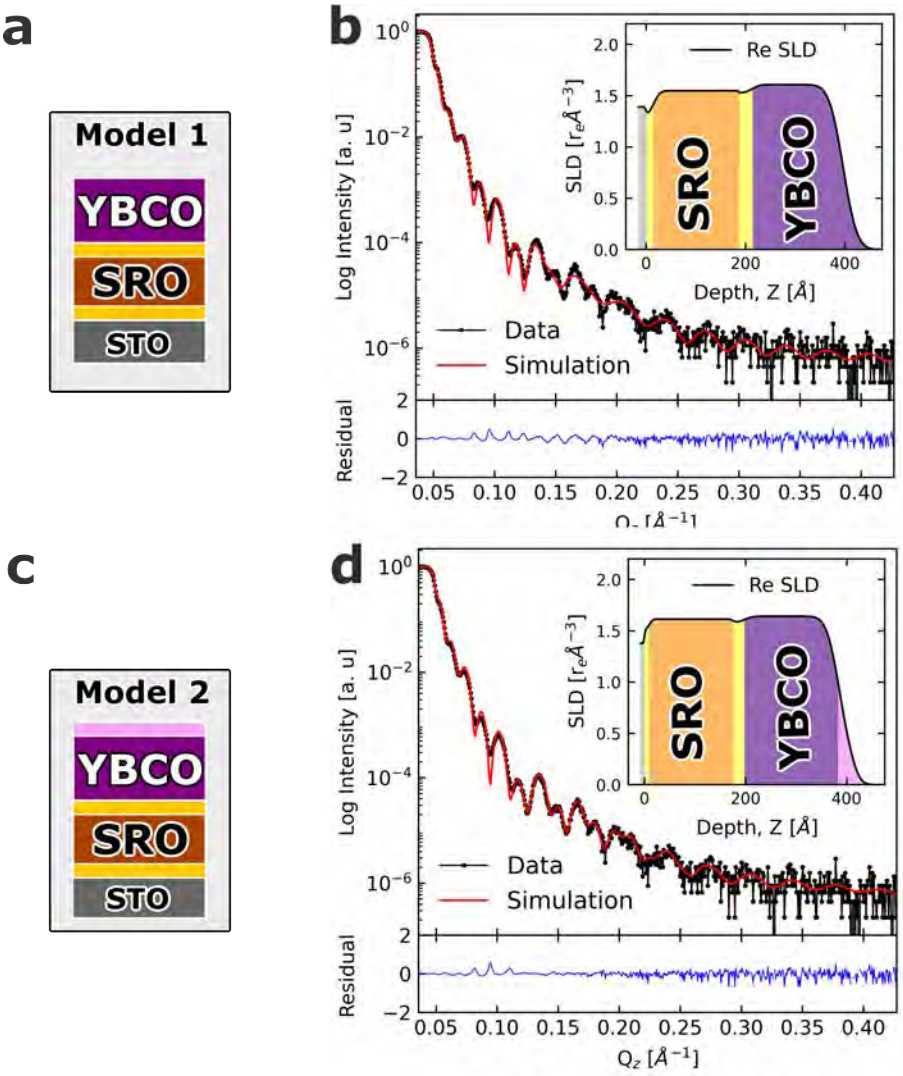

Figure 7.8.: (a) Structural model (Model 1) used to fit the X-ray reflectivity (XRR) data of the YBCO/SRO bilayer on STO substrate. (b) Experimental XRR data (black symbols) and corresponding simulation (red line) obtained using Model 1, with the residuals shown below. The inset shows the corresponding real part of the scattering length density (SLD) profile. (c) Modified structural model (Model 2) including an additional low-density surface layer to account for CuO and BaCuO surface grains observed in AFM. (d) Experimental XRR data (black symbols) and simulation (red line) obtained using Model 2, together with the residuals. The inset shows the SLD profile associated with this model.

To improve the fit, Model 1 was modified by introducing an additional low-density surface layer of YBCO (light purple) with a thickness of approximately 40 Å, forming Model 2 [Fig. 7.8(c)]. This layer was included to account for the presence of fine particulates and surface grains observed in the AFM micrographs [Fig.7.7(c)]. These features are attributed to secondary YBCO phases, such as CuO- or BaCuO-rich clusters not incorporated into the epitaxial lattice, which are expected to have a SLD value close to, but slightly lower, the bulk YBCO. Model 2 provides a significantly improved fit quality compared with Model 1, accurately reproducing both the Kiessig fringes and the overall interfacial roughness, as reflected by the lower FOM values (≈ 0.1) and smaller residuals [Fig. 7.8(d)].

From the simulation using Model 2, a total thickness of 415 Å ± 9 Å and an effective interfacial roughness of 12 Å ± 4 Å were obtained. The extracted thickness agrees well with the nominal value estimated from the deposition rate, while the roughness is within the same order of magnitude as the surface variations observed by AFM, though the two quantities are not directly comparable since XRR provides an average effective roughness over the entire interface, whereas AFM measures local topographic fluctuations on the film surface.

7.2.4. Magnetic and electrical transport characterization

Figure 7.9(a-b) displays the temperature-dependent magnetization curves measured under zero-field cooled (ZFC) and FC protocols for the YBCO/SRO heterostructure. The measurements were performed under an external magnetic field of 10 Oe applied either parallel (in-plane) or perpendicular (out-of-plane) to the film surface.

In the ZFC measurement [Fig. 7.9(a)], the sample was cooled to 5 K in the absence of an external field, after which the field was applied and the magnetization was recorded during warming. A clear diamagnetic response appears below $T_c \approx 87$ K, consistent with the SC transition of the YBCO layer. The diamagnetic response is strongly anisotropic, being significantly weaker for the in-plane configuration compared with the out-of-plane direction, as shown in the inset of Fig. 7.9(a). This behavior is consistent with the expected anisotropic screening currents in thin superconducting films, where the shielding is more efficient for fields applied perpendicular to the film surface. This behavior reflects the geometric confinement of the Meissner currents: the in-plane field configuration leads to weaker diamagnetic screening due to the geometry of the thin film. Importantly, no significant contribution from the ferromagnetic SRO layer is observed in the ZFC curves below its $T_{\mathrm{Curie}} \approx 160$ K, in either field orientation. This absence of a magnetic signal is attributed to the lack of net domain alignment in the SRO film during the ZFC procedure. In this regime, the weak applied field (10 Oe) is insufficient to align the ferromagnetic domains, particularly in a thin SRO films with a substantially reduced magnetic moment.

In contrast, the FC curves [Fig. 7.9(b)] acquired after cooling the sample under the applied field reveal a clear magnetic contribution from the SRO layer. The out-of-plane component shows a significantly larger magnetization, indicating a preferential orientation of the magnetic moment perpendicular to the film plane. This observation is consistent with the known PMA of SRO films grown on STO (001) substrates, where the compressive strain and tetragonal distortion stabilize an out-of-plane magnetic easy axis. The ferromagnetic contribution becomes discernible below T_{Curie}, as highlighted in the inset of Fig. 7.9(b), where both in-plane and out-of-plane signals rise with decreasing temperature.

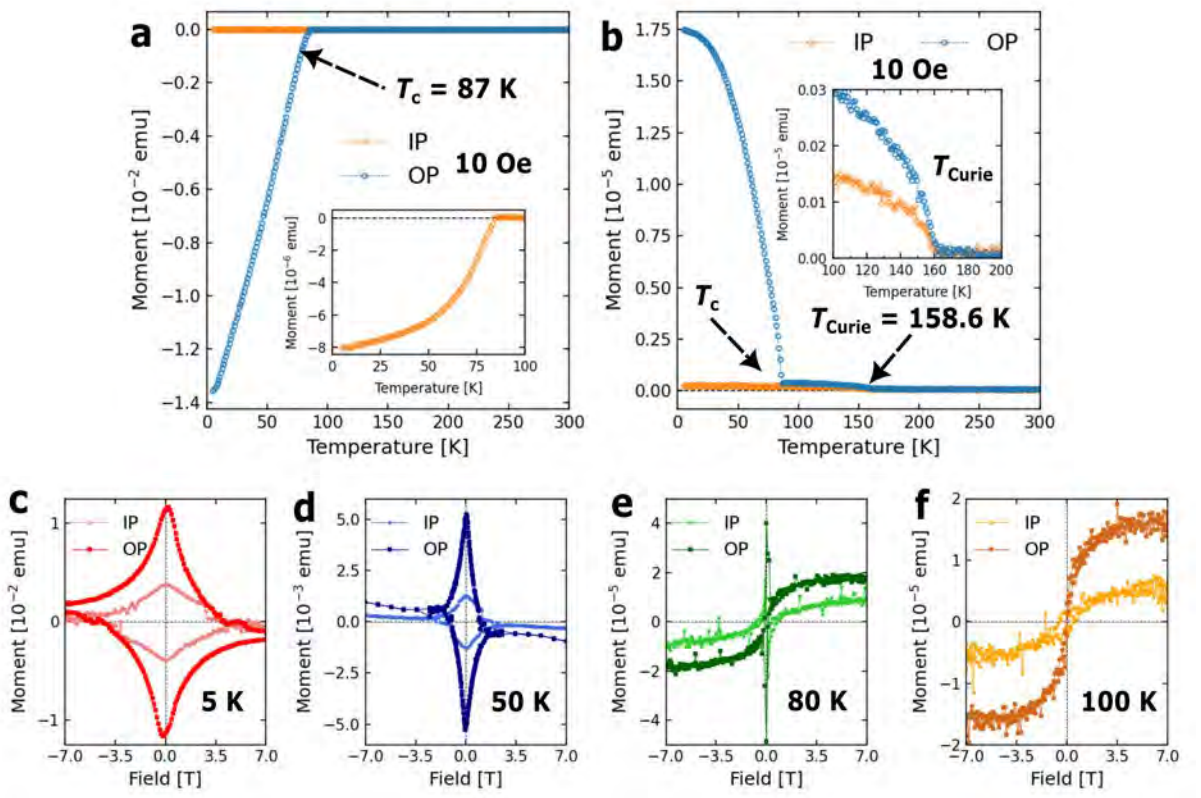

Figure 7.9.: (a) Zero-field-cooled and (b) field-cooled magnetization curves measured under an applied magnetic field of 10 Oe parallel (in-plane, IP) and perpendicular (out-of-plane, OP) to the sample surface. The superconducting transition temperature of YBCO (T_c = 87 K ± 0.5 K) and the Curie temperature of SRO (T_{Curie} = 158.6 K ± 0.5 K) are indicated. Insets show magnified views of the corresponding transitions. (c–f) Magnetic hysteresis loops acquired at 5 K, 50 K, 80 K, and 100 K for both field orientations. The diamagnetic contribution from the STO substrate was subtracted from the curves measured at 80 K and 100 K.

Complementary insight into the magnetic anisotropy and superconducting–ferromagnetic coupling behavior in the YBCO/SRO heterostructure is provided by the magnetic hysteresis loops shown in Figs. 7.9(c–f), measured at 5, 50, 80, and 100 K. At low temperatures (5 K and 50 K), a pronounced PMA is clearly observed: the out-of-plane hysteresis loops exhibit larger coercive fields and remanent magnetization compared with their in-plane counterparts. In this temperature range, the diamagnetic background from the substrate and the superconductor could not be reliably separated, as their contributions overlap and remain nearly field-symmetric; therefore, the curves are presented in raw magnetic moment (emu) units. A strong diamagnetic curvature superimposed on the OP loops evidences the dominance of superconducting screening currents in this geometry at low temperature.

At 80 K and 100 K, above or near T_c, the diamagnetic background originating from the STO substrate was subtracted by fitting the high-field region of the magnetization curves, where the superconducting contribution vanishes. After this correction, the loops reveal that the magnetic response is dominated by the SRO layer, albeit reduced in magnitude near T_c. At 100 K, above the superconducting transition but still below T_{Curie}, only a

weak ferromagnetic component remains, more pronounced in the OP configuration. The reduced net moment at this temperature is consistent with the suppressed magnetization expected for Ru-deficient SRO thin films, and the M_{OP} and M_{IP} values in μ_B/atom agree well with those obtained for the SRO film discussed in Section 7.1.

A similar T_c was obtained from zero-field cooled electrical transport measurements of the YBCO/SRO heterostructure, in agreement with the value extracted from magnetization data, as shown in Fig. 7.10(a). Field-dependent resistivity measurements with the magnetic field applied parallel [Fig. 7.10(b)] and perpendicular [Fig. 7.10(c)] to the surface of the YBCO/SRO heterostructure demonstrate the suppression of T_c under applied field, a characteristic behavior of superconductors.

The field-dependent response demonstrates the intrinsic anisotropy of YBCO, which originates from its anisotropic superconducting coherence length ξ, significantly larger in the *ab* crystallographic plane than along the *c*-axis. This anisotropy directly affects the upper critical field (H_{c2}), leading to a higher H_{c2}^{ab} compared to H_{c2}^{c}, as clearly evidenced by the more robust superconducting state when the magnetic field is applied parallel to the planes.

In summary, the magnetization and electronic transport results demonstrate that the thinner YBCO/SRO heterostructure exhibits the coexistence of superconductivity and ferromagnetism within the same temperature range. This coexistence, together with the pronounced PMA of the SRO layer, provides favorable conditions for the emergence of proximity effects at the nanometer scale. These findings motivated the PNR measurements presented in the following section, aimed at probing possible depth-resolved magnetic correlations at the YBCO/SRO interface.

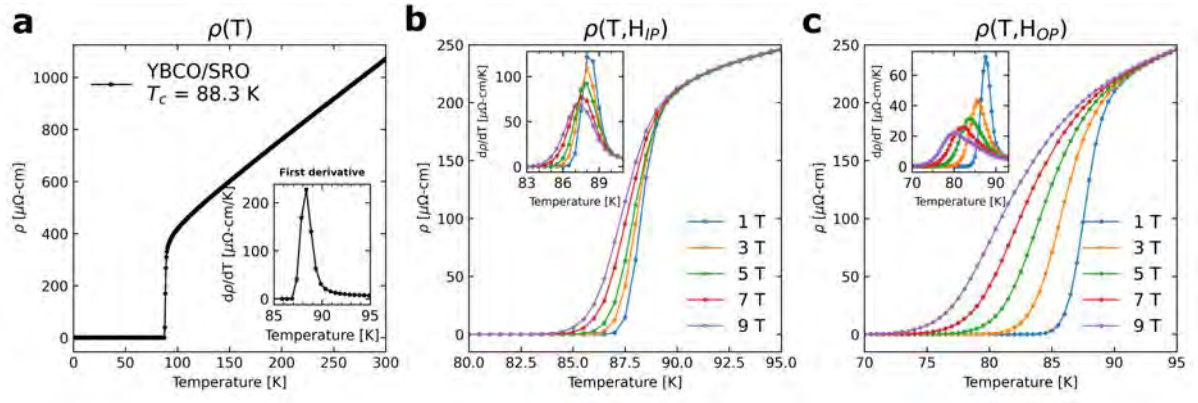

Figure 7.10.: (a) Temperature-dependent resistivity of the YBCO/SRO heterostructure measured in zero magnetic field. The superconducting transition temperature (T_c = 88.3 K ± 1.8 K) was determined from the maximum in the first derivative of $\rho(T)$, shown in the inset. (b) Resistivity curves measured under magnetic fields up to 9 T applied parallel (in-plane) and (c) perpendicular (out-of-plane) to the sample surface. The insets display the corresponding $d\rho/dT$ curves, highlighting the shift and broadening of the superconducting transition with increasing field intensity and different field orientations.

7.2.5. Neutron scattering characterization

To investigate the depth-dependent magnetic structure of the YBCO/SRO heterostructure and to search for possible signatures of an induced magnetic moment within the YBCO layer, PNR measurements were carried out after field-cooling the sample in a 4.8 T in-plane magnetic field. The applied field was maintained during the entire measurement, following the same procedure described in Section 7.1. The spin-dependent reflectivities, R+ and R−, were recorded at 100 K, 80 K, and 5 K, temperatures selected to probe the system above and below both the superconducting T_c of YBCO and below the T_{Curie} of SRO.

Given the low magnetization of the YBCO/SRO heterostructure, the splitting between the spin-up and spin-down reflectivities is very small. Therefore, it is more convenient to represent the data in terms of the spin asymmetry (SA), defined in Eq. 7.1. The resulting SA curves and corresponding fits are shown in Fig. 7.11(a–c), together with the nuclear (nSLD) and magnetization profiles in Fig. 7.11(d).

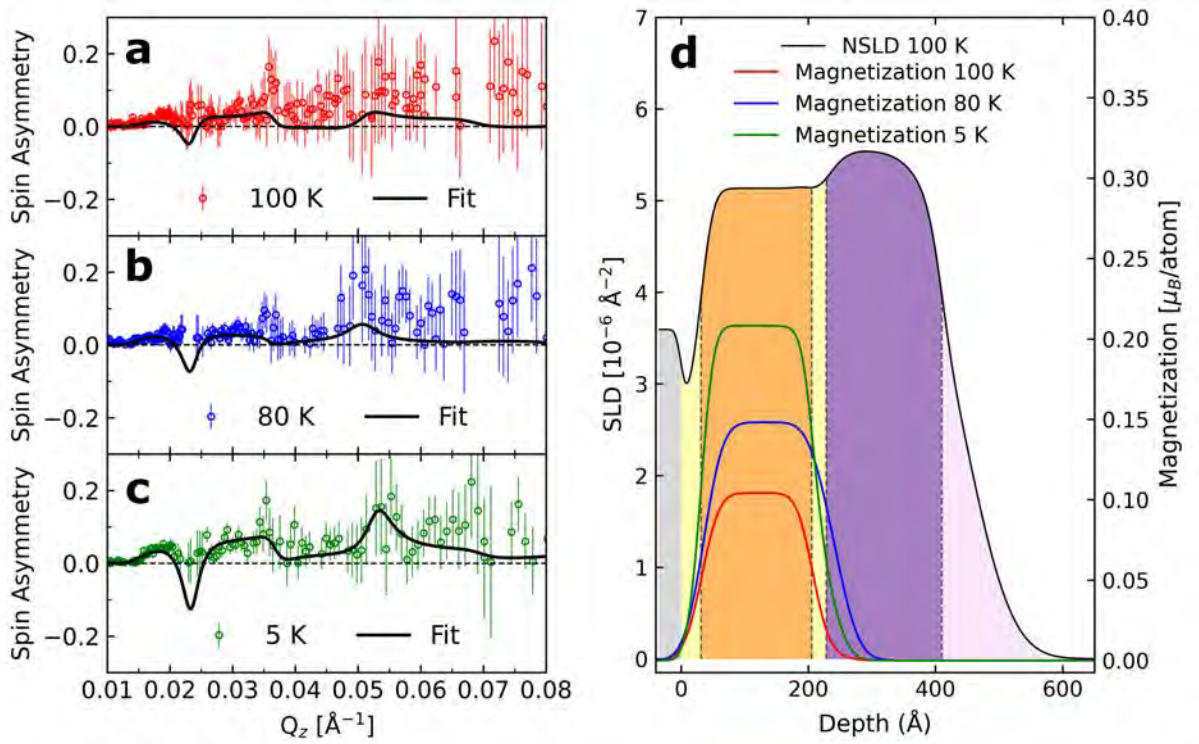

Figure 7.11.: Spin asymmetry $[(R^+) - (R^-)]/[(R^+) + (R^-)]$ measured at (a) 100 K, (b) 80 K, and (c) 5 K after field-cooling the YBCO/SRO heterostructure in a 4.8 T in-plane magnetic field. Open symbols represent the experimental data, and solid lines correspond to the best-fit curves obtained using Model 2. (d) Corresponding nuclear (nSLD, left axis) and magnetic (mSLD, right axis) scattering length density profiles extracted from the fits. The dotted vertical lines indicate the approximate positions of the film interfaces and layer boundaries. The fitting model does not include any induced magnetic moment within the YBCO layer, but provides the best agreement with the experimental data, capturing the magnetic response of the SRO layer and the interfacial structural parameters.

The simulations were performed using Model 2, previously validated by the XRR analysis (subsection 7.2.3), in which the SRO layer is described by a reduced nuclear SLD and smooth interfacial transitions to both the substrate and the YBCO layer. No induced magnetic moment was included within the superconducting layer in this model. The SA signal exhibits small amplitude and oscillates around zero, due to the low magnetic contrast as expected for a weakly magnetized system. The fits accurately reproduce the position and relative amplitude of the local minima and maxima in the SA curves, indicating that the model reliably captures the subtle magnetic contribution of the SRO layer. The negative SA values observed in certain Q_z regions simply reflect that $R^- > R+$, which results from the chosen spin convention and from interference between the nuclear and magnetic scattering terms.

The vertical dotted lines in Fig. 7.11(d) mark the approximate positions of the film interfaces, while the apparent attenuation of the mSLD near these boundaries reflects interfacial magnetic roughness rather than any induced magnetization within YBCO. The average magnetic moment extracted from the fits agrees, within the experimental uncertainty, with the values obtained from SQUID magnetometry above T_c, consistent with the low-moment behavior characteristic of Ru-deficient SRO.

To evaluate whether a magnetic moment could be induced within the superconducting layer by magnetic proximity coupling, the PNR model was refined by introducing a possible magnetized interfacial region on the YBCO side of the YBCO/SRO interface, as indicated by the shaded region in Fig. 7.12(a). This region represents a hypothetical layer affected by the magnetic proximity effect. Its thickness was varied within the range of 10–30 Å, corresponding to a thin interfacial region on the length scale over which proximity-induced effects could reasonably be expected in the highly anisotropic YBCO layer.

Two configurations were tested. In the first model, this interfacial YBCO region was allowed to carry a small finite magnetic moment. In the second model, the same region was constrained to remain non-magnetic. This comparative approach was used to evaluate the sensitivity of the PNR fits to a possible proximity-induced magnetization at the YBCO/SRO interface and to determine whether the experimental data can distinguish between these two physical scenarios within the uncertainty limits of the measurement. In Fig. 7.12(b, c), the solid black line corresponds to the fit obtained when the interfacial YBCO region is allowed to be magnetized, whereas the dashed red line corresponds to the fit in which this region is constrained to have zero magnetization. The corresponding nSLD and magnetization profiles are shown in Fig. 7.12(d) and Fig. 7.12(e), respectively.

In general, the calculated SA curves obtained from both models are nearly identical and reproduce the experimental data at 80 K and 5 K with good accuracy. The positions and relative amplitudes of the minima and maxima are well captured, confirming the weak magnetic contrast of the heterostructure. In both cases, the nSLD profile reproduces the expected YBCO/SRO/STO stacking sequence, confirming the structural integrity of the heterostructure. The magnetization profiles show that the magnetic signal is predominantly confined to the SRO layer, with a gradual decay toward the YBCO/SRO interface due to magnetic roughness and interfacial broadening. Allowing a finite magnetization in the interfacial YBCO region produces only a minor modification of the magnetization profile near the interface, without leading to a significant improvement in the spin-asymmetry fit.

A subtle difference can be observed between the mSLD profiles obtained at 80 K and 5 K. At 80 K, just below T_c, the magnetic contrast at the YBCO/SRO interface ap-

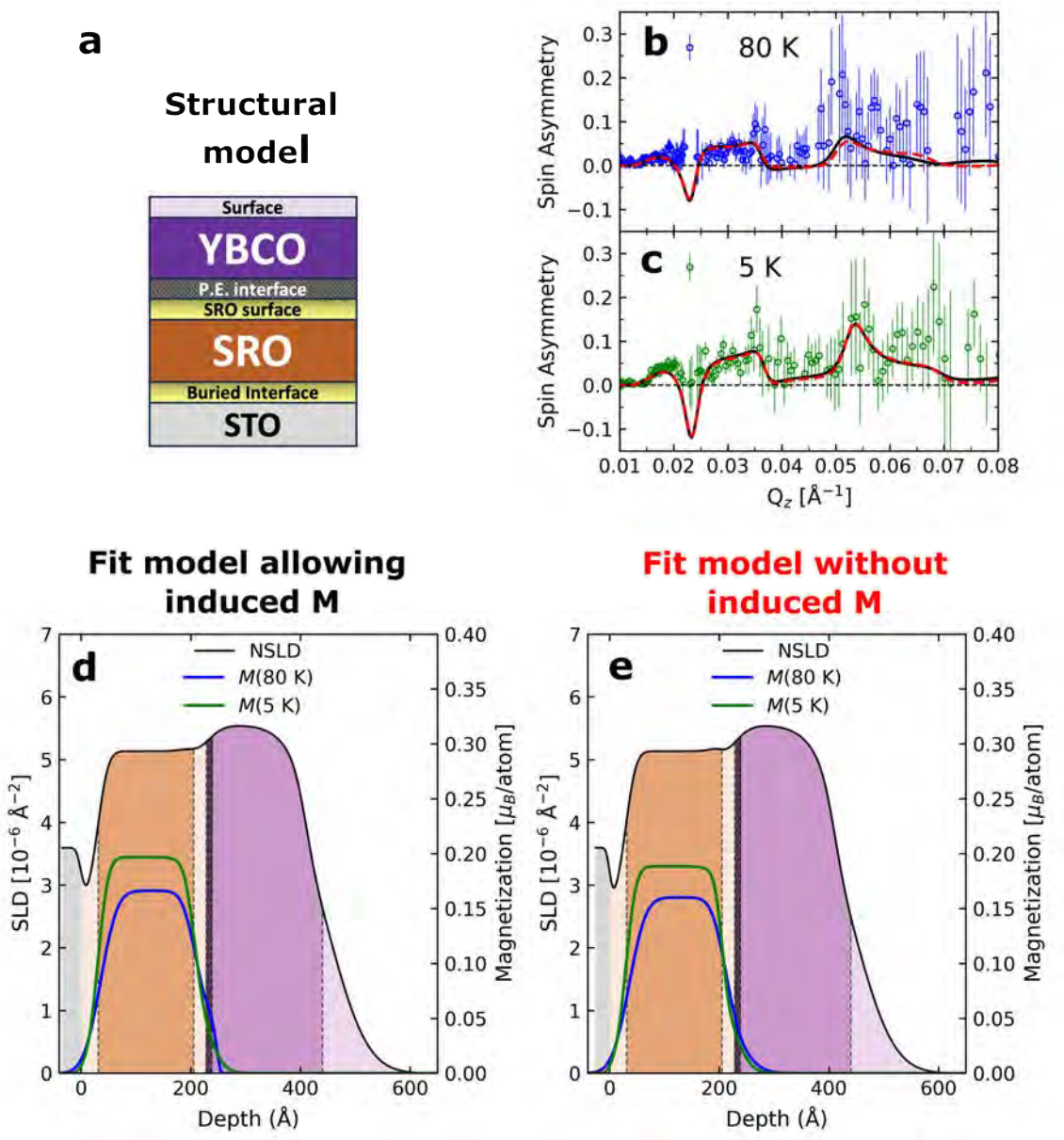

Figure 7.12.: Refined polarized neutron reflectometry (PNR) analysis used to test for a possible proximity-induced magnetic moment in the YBCO layer. (a) Structural model of the YBCO/SRO/STO heterostructure used in the fits, including the proximity-effect interface, defined as the interfacial region on the YBCO side of the YBCO/SRO interface where a possible induced magnetization was tested. (b, c) Spin asymmetry measured at 80 K and 5 K, respectively. Open symbols represent the experimental data, while the solid black and dashed red lines correspond to the calculated spin-asymmetry curves obtained from the two refined models, allowing or excluding an induced magnetic moment in the interfacial YBCO region. (d) Nuclear SLD (nSLD) and magnetization profiles for the model in which the interfacial YBCO region was allowed to carry a finite magnetic moment. (e) Corresponding profiles for the model in which this region was constrained to be non-magnetic. Both models reproduce the experimental spin asymmetry with nearly identical quality, indicating that the present PNR data cannot unambiguously resolve a proximity-induced magnetic moment in YBCO.

pears slightly enhanced compared with that at 5 K, as indicated by the small variation between the blue and green curves in Fig. 7.12(d). This effect could suggest that, in the temperature range where superconductivity is not yet fully established, the ferromagnetic order in SRO is comparatively stronger and may more effectively influence the interfacial region. At 5 K, where superconductivity dominates, the mSLD profile becomes smoother and the apparent interfacial contribution is further suppressed, consistent with the screening of magnetic fields by superconducting currents in YBCO. Although this behavior qualitatively aligns with the expected competition between superconductivity and ferromagnetism at the interface, the differences remain within the uncertainty of the fit and cannot be taken as direct evidence of an induced magnetic moment.

Within the experimental sensitivity of PNR, no unambiguous evidence of a proximity-induced magnetic moment in the YBCO layer was observed. This result is consistent with the intrinsically weak magnetization of the Ru-deficient SRO layer and the strongly anisotropic superconducting properties of YBCO ($\xi_{ab} \gg \xi_c$), which likely confine any possible magnetic correlations to a region below the spatial resolution of the technique. Despite this limitation, the present study provides a valuable experimental benchmark for investigating magnetic proximity effects in complex oxide heterostructures with PMA, highlighting the challenges associated with detecting such subtle interfacial phenomena and offering a reference for future studies employing stoichiometric SRO layers with higher magnetization and improved interfacial sharpness.

7.2.6. Conclusions

The combined structural, magnetic, transport, and neutron reflectometry results provide a comprehensive microscopic picture of the YBCO/SRO heterostructure and its interfacial behavior. AFM and HR-XRD confirmed the epitaxial c-axis-oriented growth of YBCO on SRO/STO with sharp interfaces and low roughness, while the XRR analysis demonstrated that a two-layer YBCO model including a thin low-density surface region best represents the experimental data.

Magnetization and resistivity measurements revealed the coexistence of superconductivity and ferromagnetism within the same temperature range. The SRO layer retains its PMA despite the reduced Ru content and exhibits $T_{\mathrm{Curie}} \approx 159$ K, while the YBCO layer shows a sharp superconducting transition at $T_{\mathrm{c}} \approx 87$ K. The coexistence of both order parameters establishes favorable conditions for investigating magnetic proximity effects at nanometer scales.

PNR provided depth-resolved insight into the magnetic configuration of the heterostructure. The analysis confirmed that the magnetic response arises primarily from the SRO layer, with the magnetization gradually decreasing toward the interfaces due to magnetic roughness. No unambiguous evidence of an induced magnetic moment in the YBCO layer was found within the sensitivity of the technique. The apparent temperature-dependent attenuation of the interfacial magnetic signal, from slightly stronger contrast at 80 K to smoother profiles at 5 K, suggests the expected competition between ferromagnetism and superconductivity but remains within the fitting uncertainty.

Taken together, these findings demonstrate that the magnetic and superconducting states coexist without a detectable interfacial magnetic induction in this Ru-deficient system. The results emphasize the influence of SRO stoichiometry and the anisotropic superconducting parameters of YBCO ($\xi_{ab} \gg \xi_c$) in limiting the extent of the proximity effect. The present study establishes an experimental baseline for future investigations of

magnetic proximity coupling in YBCO/SRO heterostructures employing stoichiometric SRO layers with higher magnetization and improved interfacial sharpness.

Chapter 8

Summary and Outlook

This thesis presents a comprehensive study on the growth, structural and magnetic optimization, and interfacial phenomena of complex oxide thin films and heterostructures based on $YBa_2Cu_3O_{7-x}$ (YBCO) and $SrRuO_3$ (SRO). The work combines high oxygen pressure sputtering (HOPS) deposition with advanced structural, magnetic, and neutron scattering characterization techniques to investigate the coexistence and interplay between superconductivity and ferromagnetism at the nanometer scale.

The study begins with the growth and characterization of YBCO thin films deposited by HOPS. A detailed investigation was conducted to understand the growth mechanisms and epitaxial relationships, including the coexistence of *a*- and *c*-axis oriented grains as a function of deposition conditions and substrates used. Electrical resistivity and magnetoresistance measurements demonstrated high-quality superconducting behavior, while magnetic characterization provided insight into vortex dynamics and flux pinning. These results not only clarified the growth mechanisms of YBCO under high-oxygen-pressure sputtering but also established a reliable baseline for integrating YBCO with ferromagnetic layers.

The second part addressed the optimization of SRO thin films. The effects of deposition temperature, oxygen partial pressure, and target–substrate distance were systematically evaluated. Despite exhibiting partial Ru deficiency under oxidizing conditions, the SRO films maintained excellent epitaxy and displayed pronounced perpendicular magnetic anisotropy (PMA). Combined X-ray reflectivity, scanning transmission electron microscopy with energy-dispersive X-ray spectroscopy (STEM-EDS), Rutherford backscattering spectrometry (RBS), and polarized neutron reflectometry (PNR) revealed a non-uniform magnetic depth profile, with reduced magnetization at both the film surface and the substrate interface. These results indicate that Ru deficiency modifies the local magnetic environment while preserving long-range ferromagnetic order. The transport properties showed insulating or bad-metal-like behavior, consistent with a strongly correlated regime in which electron localization coexists with weak ferromagnetism. The persistence of PMA, possibly enhanced at the interfaces rather than suppressed, suggests that the system can be characterized as a ferromagnetic insulator stabilized by interfacial anisotropy effects.

The investigation of magnetic proximity effects was carried out using two types of YBCO/SRO heterostructures with different layer thicknesses. In the thicker bilayers,

magnetotransport measurements revealed an anomalous magnetoresistance feature near the superconducting transition temperature, attributed to the interplay between the superconducting and ferromagnetic order parameters. The phenomenon arises from the competition between the PMA of the SRO layer and the anisotropic superconducting coherence of YBCO, demonstrating that interfacial coupling can modulate the electronic transport properties even in the absence of direct magnetic exchange.

In the thinner heterostructures, PNR was employed to probe the depth-dependent magnetic structure with nanometer resolution. These measurements aimed to detect a possible magnetic moment induced within the YBCO layer due to proximity coupling. However, no unambiguous evidence of such induced magnetization was observed, consistent with the weak magnetization of the Ru-deficient SRO layer and the short superconducting coherence length along the *c*-axis. Together, these results demonstrate that although magnetic proximity effects influence transport in thicker bilayers, their direct magnetic signature in thinner systems remains below the sensitivity limit of current neutron reflectometry measurements.

Taken together, the results demonstrate that the coexistence of superconductivity and ferromagnetism in these oxide systems can be achieved while maintaining high crystalline quality and well-defined anisotropies. The findings provide a microscopic understanding of how stoichiometry, growth conditions, and interfacial structure influence the balance between magnetic and superconducting order, establishing a solid experimental foundation for future studies of superconducting spintronic oxide heterostructures.

Future work will focus on completing and refining the ongoing optimization of SRO thin films prepared by HOPS using Ru-enriched targets. The systematic investigation aimed at minimizing Ru volatility and achieving stoichiometric films with enhanced transport and magnetic properties will be concluded. This study examines the influence of target composition, deposition temperature, pressure, and power source configuration (RF or DC), with the goal of establishing a reproducible route to high-magnetization SRO films. In parallel, the growth of SRO by oxide molecular beam epitaxy (MBE), as previously demonstrated at the institute by Dr. Markus Schmitz, or by pulsed laser deposition (PLD) in collaboration with partner laboratories, could provide complementary insights and enable direct comparison between different deposition techniques.

Once stoichiometric SRO films with robust ferromagnetism are available, the next step will be a systematic investigation of magnetic proximity effects in YBCO/SRO bilayers and multilayers with variable thicknesses. Such studies should combine the approaches developed in this thesis with element-specific techniques such as X-ray magnetic circular dichroism (XMCD) and X-ray linear dichroism (XLD), which offer greater sensitivity to ultrathin interfacial regions. These experiments would clarify the spatial extent and microscopic nature of the proximity coupling, offering a deeper understanding of how superconductivity and ferromagnetism interact across oxide interfaces.

By advancing the control of stoichiometry, film quality, and interfacial structure, these future efforts will enable the design of well-defined oxide heterostructures in which the balance between competing order parameters can be tuned with atomic precision. This represents an essential step toward realizing functional superconducting spintronic and quantum hybrid devices.

Bibliography

1. Li, W., Shi, J., Zhang, K. H. & MacManus-Driscoll, J. L. Defects in complex oxide thin films for electronics and energy applications: challenges and opportunities. *Mater. Horiz.* **7,** 2832–2859 (2020).
2. Bluhm, H., Brückel, T., Morgenstern, M., Plessen, G. & Stampfer, C. *Electrons in Solids: Mesoscopics, Photonics, Quantum Computing, Correlations, Topology* (Walter de Gruyter GmbH & Co KG, 2019).
3. Chakhalian, J., Freeland, J. W., Millis, A. J., Panagopoulos, C. & Rondinelli, J. M. Colloquium: Emergent properties in plane view: Strong correlations at oxide interfaces. *Rev. Mod. Phys.* **86,** 1189–1202 (2014).
4. Yu, P., Chu, Y.-H. & Ramesh, R. Oxide interfaces: pathways to novel phenomena. *Mater. Today* **15,** 320–327 (2012).
5. Pesquera, D. *et al.* Surface symmetry-breaking and strain effects on orbital occupancy in transition metal perovskite epitaxial films. *Nat. Comm.* **3,** 1189 (2012).
6. Li, L., Richter, C., Mannhart, J. & Ashoori, R. C. Coexistence of magnetic order and two-dimensional superconductivity at $LaAlO_3/SrTiO_3$ interfaces. *Nat. Phys.* **7,** 762–766 (2011).
7. Ahn, C. *et al.* Designing and controlling the properties of transition metal oxide quantum materials. *Nat. Mater.* **20,** 1462–1468 (2021).
8. Onnes, H. K. *Commun. Leiden Lab* 1911.
9. Meissner, W. & Ochsenfeld, R. Ein neuer effekt bei eintritt der supraleitfähigkeit. *Naturwissenschaften* **21,** 787–788 (1933).
10. Bardeen, J., Cooper, L. N. & Schrieffer, J. R. Theory of superconductivity. *Phys. Rev.* **108,** 1175 (1957).
11. Kittel, C. *Introduction to solid state physics Eighth edition* (John Wiley & Sons, Inc., 2005).
12. Tinkham, M. *Introduction to superconductivity* (Courier Corporation, 2004).
13. Bednorz, J. G. & Müller, K. A. Possible high T_c superconductivity in the Ba-La-Cu-O system. *Zeitschrift für Physik B Condensed Matter* **64,** 189–193 (1986).
14. Wu, M.-K. *et al.* Superconductivity at 93 K in a new mixed-phase Y-Ba-Cu-O compound system at ambient pressure. *Phys. Rev. Lett.* **58,** 908 (1987).

15. Blundell, S. *Magnetism in condensed matter* (American Association of Physics Teachers, 2003).

16. Lima, V. A. d. O. *Propriedades eletronicas e magneticas de filmes ultrafinos de* $La_{0.67}$ $Sr_{0.33}MnO_3$. MA thesis (Universidade Federal de Campina Grande, 2021).

17. Soltan, S. *Interaction of superconductivity and ferromagnetism in YBCO-LCMO heterostructures* (Cuvillier Verlag, 2005).

18. De Lacheisserie, E. d. T., Gignoux, D. & Schlenker, M. *Magnetism: I - Fundamentals* (Springer Science & Business Media, 2002).

19. Eschrig, M. Spin-polarized supercurrents for spintronics. *Phys. Today* **64,** 43–49 (2011).

20. Sanchez-Manzano, D. *et al.* Long-range superconducting proximity effect in $YBa_2Cu_3O_7/La_{0.7}Ca_{0.3}MnO_3$ weak-link arrays. *Appl. Phys. Lett.* **124** (2024).

21. Chou, H. *et al.* Controllable spin-triplet superconductivity states and enhanced non-dissipation spin-polarized supercurrents in $YBa_2Cu_3O_7/La_{0.7}Ca_{0.3}MnO_3$ interfaces. *Appl. Surf. Sci.* **644,** 158739 (2024).

22. Yang, Z., Lange, M., Volodin, A., Szymczak, R. & Moshchalkov, V. V. Domain-wall superconductivity in superconductor–ferromagnet hybrids. *Nat. Mater.* **3,** 793–798 (2004).

23. Chakhalian, J. *et al.* Magnetism at the interface between ferromagnetic and superconducting oxides. *Nat. Phys.* **2,** 244–248 (2006).

24. Stahn, J. *et al.* Magnetic proximity effect in perovskite superconductor/ferromagnet multilayers. *Phys. Rev. B* **71,** 140509 (2005).

25. Eschrig, M. Spin-polarized supercurrents for spintronics: a review of current progress. *Rep. Prog. Phys.* **78,** 104501 (2015).

26. Linder, J. & Robinson, J. W. Superconducting spintronics. *Nat. Phys.* **11,** 307–315 (2015).

27. Robinson, J., Witt, J. & Blamire, M. Controlled injection of spin-triplet supercurrents into a strong ferromagnet. *Science* **329,** 59–61 (2010).

28. Prajapat, C. *et al.* Proximity effects across oxide-interfaces of superconductor-insulator-ferromagnet hybrid heterostructure. *Sci. Rep.* **8,** 3732 (2018).

29. Uribe-Laverde, M. A. *et al.* Depth profile of the ferromagnetic order in a $YBa_2Cu_3O_7/La_{2/3}Ca_{1/3}MnO_3$ superlattice on a LSAT substrate: A polarized neutron reflectometry study. *Phys. Rev. B* **87,** 115105 (2013).

30. Cai, R., Žutić, I. & Han, W. Superconductor/ferromagnet heterostructures: a platform for superconducting spintronics and quantum computation. *Adv. Quantum Technol.* **6,** 2200080 (2023).

31. Cuoco, M. & Di Bernardo, A. Materials challenges for $SrRuO_3$: From conventional to quantum electronics. *APL Materials* **10** (2022).

32. Liu, Y. *et al.* Advancing Superconductivity with Interface Engineering. *Adv. Mater.* **36,** 2405009 (2024).

33. Ko, W., Song, S. Y., Yan, J., Lado, J. L. & Maksymovych, P. Atomic-Scale Andreev Probe of Unconventional Superconductivity. *Nano Letters* **23,** 8310–8318 (2023).
34. Stellhorn, A. *Interplay of proximity effects in superconductor/ferromagnet heterostructures.* PhD thesis (RWTH Aachen University, 2021).
35. Stellhorn, A. *et al.* Tailoring superconducting states in superconductor-ferromagnet hybrids. *New J. Phys.* **22,** 093001 (2020).
36. Buzdin, A. I. & Mel'nikov, A. Domain wall superconductivity in ferromagnetic superconductors. *Phys. Rev. B* **67,** 020503 (2003).
37. Aladyshkin, A. Y. *et al.* Domain-wall superconductivity in hybrid superconductor-ferromagnet structures. *Phys. Rev. B* **68,** 184508 (2003).
38. Zdravkov, V. I. *et al.* Experimental observation of the triplet spin-valve effect in a superconductor-ferromagnet heterostructure. *Phys. Rev. B* **87,** 144507 (2013).
39. Gu, Y., Halász, G. B., Robinson, J. & Blamire, M. Large superconducting spin valve effect and ultrasmall exchange splitting in epitaxial rare-earth-niobium trilayers. *Phys. Rev. Lett.* **115,** 067201 (2015).
40. Gu, J. *et al.* Magnetization-Orientation Dependence of the Superconducting Transition Temperature in the Ferromagnet-Superconductor-Ferromagnet System: CuNi/Nb/CuNi. *Phys. Rev. Lett.* **89,** 267001 (2002).
41. Di Bernardo, A. *et al.* Nodal superconducting exchange coupling. *Nat. Mater.* **18,** 1194–1200 (2019).
42. Pena, V. *et al.* Giant magnetoresistance in ferromagnet/superconductor superlattices. *Phys. Rev. Lett.* **94,** 057002 (2005).
43. Khaydukov, Y. N. *et al.* Evidence for spin-triplet superconducting correlations in metal-oxide heterostructures with noncollinear magnetization. *Phys. Rev. B* **90,** 035130 (2014).
44. Ovsyannikov, G. *et al.* Magnetic proximity effect at the interface between a cuprate superconductor and an oxide spin valve. *JETP* **122,** 738–747 (2016).
45. Ovsyannikov, G., Constantinian, K., Demidov, V. & Khaydukov, Y. N. Magnetic proximity effect and superconducting triplet correlations at the cuprate superconductor and oxide spin valve interface. *Low Temp. Phys.* **42,** 873–883 (2016).
46. Stellhorn, A. *et al.* Control of the stripe domain pattern in L10-ordered FePd thin films. *J. Magn. Magn. Mater.* **476,** 483–486 (2019).
47. Tang, M. *Study of microstructural, magnetic and electrical transport properties in YBCO/FePd heterostructures.* MA thesis (RWTH Aachen University, 2023).
48. Boschker, H. *et al.* Ferromagnetism and conductivity in atomically thin $SrRuO_3$. *Phys. Rev. X* **9,** 011027 (2019).
49. Contreras, J. R. *et al.* Improved $PbZr_{0.52}Ti_{0.48}O_3$ film quality on $SrRuO_3/SrTiO_3$ substrates. *Journal of crystal growth* **277,** 210–217 (2005).
50. Gu, Y. *et al.* An overview of $SrRuO_3$-based heterostructures for spintronic and topological phenomena. *Journal of Physics D: Applied Physics* **55,** 233001 (2022).
51. Habermeier, H., Albrecht, J. & Soltan, S. The enhancement of flux-line pinning in all-oxide superconductor/ferromagnet heterostructures. *Superconductor Science and Technology* **17,** S140 (2004).

52. Cardwell, D. A., Larbalestier, D. C. & Braginski, A. *Handbook of Superconductivity: Fundamentals and Materials, Volume One* (CRC Press, 2022).

53. Blügel, S. *Electronic oxides - correlation phenomena, exotic phases and novel functionalities: lecture notes of the 41st spring school 2010* (Forschungszentrum, Zentralbibliothek, 2010).

54. Klamut, J. *et al.* Thermal vibrations in $YBa_2Cu_3O_{6+x}$ and $PrBa_2Cu_3O_{6+x}$. *Acta physica Polonica. A* **73,** 759–765 (1988).

55. Swinnea, J. & Steinfink, H. The crystal structure of $YBa_2Cu_3O_6$, the x=1 phase of the superconductor $YBa_2Cu_3O_{7-x}$. *J. Mater. Res.* **2,** 424–426 (1987).

56. Capponi, J. *et al.* Structure of the 100 K superconductor $YBa_2Cu_3O_7$ between (5–300) K by neutron powder diffraction. *Europhys. Lett.* **3,** 1301 (1987).

57. Khallouq, K. *Exploring High-Temperature Superconductivity in the YBCO System: From Theory to Experiments* (Springer Nature, 2024).

58. Saxena, A. K. *High-temperature superconductors* (Springer Science & Business Media, 2012).

59. Damascelli, A., Hussain, Z. & Shen, Z.-X. Angle-resolved photoemission studies of the cuprate superconductors. *Rev. Mod. Phys.* **75,** 473 (2003).

60. Barthélemy, M. C. *Studies of charge density waves in cuprate superconductors.* PhD thesis (University of Bristol, 2019).

61. Tallon, J. L. & Loram, J. The doping dependence of T*–what is the real high-T_c phase diagram? *Physica C: Superconductivity* **349,** 53–68 (2001).

62. Taillefer, L. Superconductivity and quantum criticality. *La Physique au Canada* **67,** 20 (2011).

63. Sen, K. *Magnetic proximity effect in oxide-based superconductor/ferromagnet and superconductor/antiferromagnet heterostructures.* PhD thesis (University of Fribourg, 2016).

64. Li, Y. *et al.* Unusual magnetic order in the pseudogap region of the superconductor $HgBa_2CuO_{4+\delta}$. *Nature* **455,** 372–375 (2008).

65. Sonier, J. *et al.* Hole-doping dependence of the magnetic penetration depth and vortex core size in $YBa_2Cu_3O_y$: Evidence for stripe correlations near 1/8 hole doping. *Phys. Rev. B—Condensed Matter and Materials Physics* **76,** 134518 (2007).

66. Krusin-Elbaum, L., Malozemoff, A., Yeshurun, Y., Cronemeyer, D. & Holtzberg, F. Temperature dependence of lower critical fields in Y-Ba-Cu-O crystals. *Phys. Rev. B* **39,** 2936 (1989).

67. Moodera, J. *et al.* Critical-magnetic-field anisotropy in single-crystal $YBa_2Cu_3O_7$. *Phys. Rev. B* **37,** 619 (1988).

68. Alcântara, K. S. *Crescimento por laser pulsado e caracterização de filmes finos de $YBa_2Cu_3O_{7-\delta}$ e Sr_2IrO_4.* MA thesis (Universidade Estadual de Campinas - UNICAMP, 2023).

69. Davelos Bagarinao, K. & Yamasaki, H. Large area pulsed laser deposition of $YBa_2Cu_3O_{7-d}$ thin film: Microstructure and flux pinning properties. *YBCO Superconductor Research Progress,* 53 (2008).

70. Prusseit, W., Furtner, S. & Nemetschek, R. Series production of large area $YBa_2Cu_3O_7$ films for microwave and electrical power applications. *Superconductor Science and Technology* **13,** 519 (2000).

71. Poppe, U. *et al.* Low-resistivity epitaxial $YBa_2Cu_3O_7$ thin films with improved microstructure and reduced microwave losses. *J. Appl. Phys.* **71,** 5572–5578 (1992).

72. Faley, M. I. in *Applications of High-T_c Superconductivity* (IntechOpen, 2011).

73. Breternitz, J. & Schorr, S. What defines a perovskite? *Advanced Energy Materials* **8,** 1802366 (2018).

74. Młynarczyk, M. *Physicochemical properties of the $Sr_{1-x}Ca_xRuO_3$ thin films.* PhD thesis (Jagiellonian University, 2024).

75. Koster, G. *et al.* Structure, physical properties, and applications of $SrRuO_3$ thin films. *Rev. Mod. Phys.* **84,** 253–298 (2012).

76. Rodriguez Contreras, J. *Ferroelectric tunnel junctions.* PhD thesis (Cologne University, 2003).

77. Młynarczyk, M. *et al.* Surface layer of $SrRuO_3$ epitaxial thin films under oxidizing and reducing conditions. *J. Appl. Phys.* **101** (2007).

78. Wakabayashi, Y. K., Kaneta-Takada, S., Krockenberger, Y., Taniyasu, Y. & Yamamoto, H. Wide-range epitaxial strain control of electrical and magnetic properties in high-quality $SrRuO_3$ films. *ACS Applied Electronic Materials* **3,** 2712–2719 (2021).

79. Grutter, A., Wong, F., Arenholz, E., Vailionis, A. & Suzuki, Y. Evidence of high-spin Ru and universal magnetic anisotropy in $SrRuO_3$ thin films. *Phys. Rev. B—Condensed Matter and Materials Physics* **85,** 134429 (2012).

80. Grutter, A. *et al.* Enhanced magnetism in epitaxial $SrRuO_3$ thin films. *Appl. Phys. Lett.* **96** (2010).

81. Cox, P., Egdell, R., Goodenough, J., Hamnett, A. & Naish, C. The metal-to-semiconductor transition in ternary ruthenium (IV) oxides: a study by electron spectroscopy. *Journal of Physics C: Solid State Physics* **16,** 6221 (1983).

82. Allen, P. *et al.* Transport properties, thermodynamic properties, and electronic structure of $SrRuO_3$. *Phys. Rev. B* **53,** 4393 (1996).

83. Singh, D. J. Electronic and magnetic properties of the 4*d* itinerant ferromagnet $SrRuO_3$. *J. Appl. Phys.* **79,** 4818–4820 (1996).

84. Seki, Y. *et al.* Correlated Ligand Electrons in the Transition-Metal Oxide $SrRuO_3$. *Phys. Rev. Lett.* **135,** 046402 (2025).

85. Wakabayashi, Y. K. *et al.* Machine-learning-assisted thin-film growth: Bayesian optimization in molecular beam epitaxy of $SrRuO_3$ thin films. *APL Materials* **7** (2019).

86. Hölgye, Z. & Křivánek, M. On the volatility of ruthenium. *Journal of Radioanalytical and Nuclear Chemistry* **42,** 133–141 (1978).

87. Kunkemöller, S., Sauer, F., Nugroho, A. & Braden, M. Magnetic anisotropy of large floating-zone-grown single-crystals of $SrRuO_3$. *Crystal Research and Technology* **51,** 299–305 (2016).

88. Wakabayashi, Y. K. *et al.* Single-domain perpendicular magnetization induced by the coherent O 2*p*-Ru 4*d* hybridized state in an ultra-high-quality $SrRuO_3$ film. *Phys. Rev. Materials* **5,** 124403 (2021).

89. Wang, Z. *et al.* Epitaxial integration and properties of $SrRuO_3$ on silicon. *APL Materials* **6** (2018).

90. Klein, L. *et al.* Domain wall resistivity in $SrRuO_3$. *Phys. Rev. Lett.* **84,** 6090 (2000).

91. Marshall, A. *et al.* Lorentz transmission electron microscope study of ferromagnetic domain walls in $SrRuO_3$: statics, dynamics, and crystal structure correlation. *J. Appl. Phys.* **85,** 4131–4140 (1999).

92. Hong, W. *et al.* Persistent step-flow growth of strained films on vicinal substrates. *Phys. Rev. Lett.* **95,** 095501 (2005).

93. Higuchi, T. *et al.* Fabrication of pseudocubic $SrRuO_3$ (100) epitaxial thin films on Si by pulsed laser deposition. *Japanese J. Appl. Phys.* **41,** L481 (2002).

94. Rao, R. A., Gan, Q. & Eom, C.-B. Growth mechanisms of epitaxial metallic oxide $SrRuO_3$ thin films studied by scanning tunneling microscopy. *Appl. Phys. Lett.* **71,** 1171–1173 (1997).

95. Gan, Q., Rao, R. & Eom, C. Control of the growth and domain structure of epitaxial $SrRuO_3$ thin films by vicinal (001) $SrTiO_3$ substrates. *Appl. Phys. Lett.* **70,** 1962–1964 (1997).

96. Bern, F. *et al.* Structural, magnetic and electrical properties of $SrRuO_3$ films and $SrRuO_3/SrTiO_3$ superlattices. *Journal of Physics: Condensed Matter* **25,** 496003 (2013).

97. Kaneta-Takada, S. *et al.* Scattering-dependent transport of $SrRuO_3$ films: From Weyl fermion transport to hump-like Hall effect anomaly. *Phys. Rev. Materials* **7,** 054406 (2023).

98. Takiguchi, K. *et al.* Quantum transport evidence of Weyl fermions in an epitaxial ferromagnetic oxide. *Nat. Comm.* **11,** 4969 (2020).

99. Wakabayashi, Y. K. *et al.* Structural and transport properties of highly Ru-deficient $SrRu_{0.7}O_3$ thin films prepared by molecular beam epitaxy: Comparison with stoichiometric $SrRuO_3$. *AIP advances* **11** (2021).

100. Gausepohl, S., Lee, M., Char, K., Rao, R. & Eom, C. Magnetoresistance properties of thin films of the metallic oxide ferromagnet $SrRuO_3$. *Phys. Rev. B* **52,** 3459 (1995).

101. Kacedon, D., Rao, R. & Eom, C. Magnetoresistance of epitaxial thin films of ferromagnetic metallic oxide $SrRuO_3$ with different domain structures. *Appl. Phys. Lett.* **71,** 1724–1726 (1997).

102. Wang, W. *et al.* Magnetic domain engineering in $SrRuO_3$ thin films. *npj Quantum Materials* **5,** 73 (2020).

103. Sanchez, F., Ocal, C. & Fontcuberta, J. Tailored surfaces of perovskite oxide substrates for conducted growth of thin films. *Chemical Society Reviews* **43,** 2272–2285 (2014).

104. Schlom, D. G. *et al.* Strain tuning of ferroelectric thin films. *Annu. Rev. Mater. Res.* **37,** 589–626 (2007).

105. Hoppler, J. *et al.* X-ray study of structural domains in the near-surface region of $SrTiO_3$ substrates with $Y_{0.6}Pr_{0.4}Ba_2Cu_3O_7/La_{2/3}Ca_{1/3}MnO_3$ superlattices grown on top. *Phys. Rev. B* **78,** 134111 (2008).

106. Lytle, F. W. X-ray diffractometry of low-temperature phase transformations in strontium titanate. *J. Appl. Phys.* **35,** 2212–2215 (1964).

107. Gellé, F. *et al.* Guideline to atomically flat TiO_2-terminated $SrTiO_3$ (001) surfaces. *Surface Science* **677,** 39–45 (2018).

108. Zahradník, M. *et al.* Magnetic domain wall motion in $SrRuO_3$ thin films. *Materials & Design* **187,** 108390 (2020).

109. Vlasko-Vlasov, V. *et al.* Direct magneto-optical observation of a structural phase transition in thin films of manganites. *Phys. Rev. Lett.* **84,** 2239 (2000).

110. Blinc, R., Zalar, B., Laguta, V. V. & Itoh, M. Order-Disorder Component in the Phase Transition Mechanism of ^{18}O Enriched Strontium Titanate. *Phys. Rev. Lett.* **94,** 147601 (2005).

111. Schöffmann, P. *Stoichiometric control and magnetoelectric coupling in artificial multiferroic heterostructures.* PhD thesis (RWTH Aachen University, 2021).

112. Kuech, T. *Handbook of Crystal Growth: Thin Films and Epitaxy* (Elsevier, 2014).

113. Bauer, E. Phänomenologische theorie der kristallabscheidung an oberflächen. i. *Zeitschrift für Kristallographie-Crystalline Materials* **110,** 372–394 (1958).

114. Prieto, J. & Markov, I. Stranski–Krastanov mechanism of growth and the effect of misfit sign on quantum dots nucleation. *Surface Science* **664,** 172–184 (2017).

115. Poppe, U., Schubert, J. & Evers, W. *Method of fabricating thin layers from high-temperature oxide superconductors* US Patent 4,965,248. 1990.

116. Faley, M. & Poppe, U. *Sputtering sources for high-pressure sputtering with large targets and sputtering method* US Patent 9,481,928. 2016.

117. Park, S.-I. *et al.* A review on fabrication processes for electrochromic devices. *International Journal of Precision Engineering and Manufacturing-Green Technology* **3,** 397–421 (2016).

118. Schmitz, M. *Strain and electric field mediated manipulation of magnetism in* $La_{(1-x)}Sr_xMnO_3/BaTiO_3$ *heterostructures.* PhD thesis (RWTH Aachen University, 2015).

119. Vassenden, F., Linker, G. & Geerk, J. Growth direction control YBCO thin films. *Physica C: Superconductivity* **175,** 566–572 (1991).

120. De Oliveira, R., Albuquerque, D., Cruz, T., Yamaji, F. & Leite, F. Measurement of the nanoscale roughness by atomic force microscopy: basic principles and applications. *Atomic force microscopy-imaging, measuring and manipulating surfaces at the atomic scale* **3** (2012).

121. Oxford Instruments: What is Atomic Force Microscopy (AFM)? *https://afm.oxinst.com/outreach/atomic-force-microscopy* (Dec. 2024).

122. Ishida, N. & Craig, V. S. Direct measurement of interaction forces between surfaces in liquids using atomic force microscopy. *KONA Powder and Particle Journal* **36,** 187–200 (2019).

123. Park Systems: AFM imaging Modes. https://www.parksystems.com/en/products/research-afm/AFM-modes/imaging-modes (Dec. 2024).

124. Fundamentals of Contact Mode and TappingMode Atomic Force Microscopy. https://www.azonano.com/article.aspx?ArticleID=3010 (Dec. 2024).

125. Angst, M., Brückel, T., Förster, S., Friese, K. & Zorn, R. *Scattering! soft, functional and quantum materials: Lecture notes of the 50th iff spring school 2019* tech. rep. (Streumethoden, 2019).

126. Angst, M., Brückel, T., Richter, D. & Zorn, R. *Scattering methods for condensed matter research* **PreJuSER-136382** (Streumethoden, 2012).

127. Willmott, P. *An introduction to synchrotron radiation: techniques and applications* (John Wiley & Sons, 2019).

128. Calligaris, G. *Introdução a técnicas de espalhamento e difração DIF-2: Difração de raios-X em cristais* in *3rd edition of the Brazillian Synchrotron School* (2019).

129. Silva Junior, G. R. d. Mapas do espaço recíproco de camadas epitaxiais de CdTe (2017).

130. Schierle, E. *Antiferromagnetism in thin films studied by resonant magnetic soft X-ray scattering.* PhD thesis (Free University of Berlin, 2007).

131. Rai, V. *Magnetic and transport studies of the parent and Fe doped hexagonal-Mn_3Ge Weyl semimetal.* PhD thesis (RWTH Aachen University, 2023).

132. Zubayer, A. *Ion Dynamics and Magnetic Order in 2D Honeycomb Materials.* MA thesis (KTH Royal Institute of Technology - School Of Engineering Sciences, 2020).

133. Brückel, T., Heger, G., Richter, D., Zorn, R. & Roth, G. *Laboratory Course Neutron Scattering: Lectures* **PreJuSER-16299** (Streumethoden, 2011).

134. Brückel, T. Atomic and Magnetic Structures in Crystalline Materials: Neutron and X-ray Scattering. *ChemInform* **39** (2008).

135. Birkholz, M. *Thin Film Analysis by X-Ray Scattering* (Wiley-VCH Verlag GmbH & Co. KGaA, 2006).

136. De Andrade, G. C. *Modificação de hábito e análise estrutural de monocristais quase perfeitos de NaBrO3 dopados com S2O6 por difração de raios X de n-feixes e absorção* PhD thesis (Universidade Estadual de Campinas, 2018).

137. Volz, H. & Matyi, R. Triple-axis X-ray diffraction analyses of lysozyme crystals. *Acta Crystallographica Section D: Biological Crystallography* **56,** 881–889 (2000).

138. Kiessig, H. Untersuchungen zur totalreflexion von röntgenstrahlen. *Annalen der Physik* **402,** 715–768 (1931).

139. Kiessig, H. Interferenz von Röntgenstrahlen an dünnen Schichten. *Annalen der Physik* **402,** 769–788 (1931).

140. Parratt, L. G. Surface studies of solids by total reflection of X-rays. *Phys. Rev.* **95,** 359 (1954).

141. Mori, T. J. d. A. *Materiais e técnicas para nanoestruturas magnetoelétricas compósitas.* PhD thesis (Universidade Federal de Santa Maria, 2014).

142. Yasaka, M. *et al.* X-ray thin-film measurement techniques. *The Rigaku Journal* **26,** 1–9 (2010).

143. Glavic, A. & Björck, M. GenX 3: the latest generation of an established tool. *Journal of applied crystallography* **55,** 1063–1071 (2022).

144. Dhiman, I. *et al.* Setup for polarized neutron imaging using in situ ^{3}He cells at the Oak Ridge National Laboratory High Flux Isotope Reactor CG-1D beamline. *Review of Scientific Instruments* **88** (2017).

145. Hafner, A. *Full Off-Specular and Specular Reflectometry for Soft Thin Film Analysis.* PhD thesis (Université libre de Bruxelles, 2019).

146. Callori, S. J., Saerbeck, T., Cortie, D. L. & Lin, K.-W. in *Solid State Physics* 73–116 (Elsevier, 2020).

147. Lima, R. J. d. S. *et al. Efeitos de agentes quelantes no processo de crescimento de nanopartículas de* α*-*Fe_2O_3*.* PhD thesis (Universidade Federal de Sergipe, 2013).

148. Jeol. *SEM A to Z: basic knowledge for using the SEM* tech. rep. (JEOL - Serving Advance Technology, 2020).

149. Electron microscope: principles, types & real-world applications. *https://vaccoat.com/blog/electron-microscope/* (Jan. 2025).

150. Williams, D. B., Carter, C. B., Williams, D. B. & Carter, C. B. *The transmission electron microscope* (Springer, 1996).

151. Backscattering Spectrometry, W. & Chu, J. *Mayer and Marc-A. Nicolet* 1978.

152. Oura, K., Lifshits, V., Saranin, A., Zotov, A. & Katayama, M. *Surface science: an introduction* (Springer Science & Business Media, 2013).

153. Thompson, M. RUMP: Rutherford backscattering spectroscopy analysis package. *Cornell Univesity* (1983).

154. Design, Q. *Magnetic Property Measurement System MPMS XL Hardware Reference Manual* 1996.

155. McElfresh, M. Fundamentals of magnetism and magnetic measurements featuring Quantum Design's magnetic property measurement system. *Quantum Design* **11578,** 132 (1994).

156. Schmelz, M. & Stolz, R. Superconducting quantum interference device (SQUID) magnetometers. *High Sensitivity Magnetometers,* 279–311 (2017).

157. Schroder, D. K. *Semiconductor material and device characterization* (John Wiley & Sons, 2015).

158. Zhang, J., Wu, H., Zhao, G., Han, L. & Zhang, J. Progress in the study of vortex pinning centers in high-temperature superconducting films. *Nanomaterials* **12,** 4000 (2022).

159. Ambature: we make superconductors. *https://ambature.com/a-axis-versus-c-axis-materials* (Jan. 2025).

160. Suyolcu, Y. E. *et al.* a-axis $YBa_2Cu_3O_{7-x}$/$PrBa_2Cu_3O_{7-x}$/$YBa_2Cu_3O_{7-x}$ trilayers with subnanometer rms roughness. *APL materials* **9** (2021).

161. Yeadon, M., Aindow, M., Wellhöfer, F. & Abell, J. Topographical development and misfit relief in laser-ablated heteroepitaxial $YBa_2Cu_3O_{7-\delta}$ thin films. *J. Crystal Growth* **172,** 145–155 (1997).

162. Feenstra, R., Lindemer, T., Budai, J. & Galloway, M. Effect of oxygen pressure on the synthesis of $YBa_2Cu_3O_{7-x}$ thin films by post-deposition annealing. *J. Appl. Phys.* **69,** 6569–6585 (1991).

163. Faley, M., Meertens, D., Poppe, U. & Dunin-Borkowski, R. *Graphoepitaxial Josephson junctions and DC SQUIDs* in *2013 IEEE 14th International Superconductive Electronics Conference (ISEC)* (2013), 1–3.

164. Faley, M. *et al.* Meandering of the grain boundary and d-wave effects in high-T_c bicrystal Josephson junctions. *Superconductor Science and Technology* **19,** S195 (2006).

165. Dam, B., Huijbregtse, J. & Rector, J. Strong pinning linear defects formed at the coherent growth transition of pulsed-laser-deposited $YBa_2Cu_3O_{7-\delta}$ films. *Phys. Rev. B* **65,** 064528 (2002).

166. Mazini Álvarez, M. S. *Efecto del espesor en películas delgadas de $YBa_2Cu_3O_{7-\delta}$ crecidas sobre $SrLaAlO_4$* PhD thesis (Universidad de la Republica Uruguay, 2023).

167. Oliveira, F. F. M. d. *Growth of superconducting and ferroelectric heterostructures* PhD thesis (Universidade de São Paulo, 2018).

168. De Oliveira Lima, V. A. *et al.* Anomalous magnetoresistance around the critical temperature in heterostructures of high-T c superconducting $YBa_2Cu_3O_{7-x}$ and ferromagnetic $SrRuO_3$ with perpendicular magnetic anisotropy. *Phys. Scr.* **100,** 075985 (2025).

169. Siemons, W. *et al.* Dependence of the electronic structure of $SrRuO_3$ and its degree of correlation on cation off-stoichiometry. *Phys. Rev. B.* **76,** 075126 (2007).

170. Lu, H.-Z. & Shen, S.-Q. *Weak localization and weak anti-localization in topological insulators* in *Spintronics Vii* **9167** (2014), 263–273.

171. Gunnarsson, R. Anisotropic spin-orbit interaction revealed by in-plane magnetoresistance in single-oriented $SrRuO_3$ thin films. *Phys. Rev. B* **85,** 235409 (2012).

172. Pesquera, D. *et al.* X-ray interference effects on the determination of structural data in ultrathin $La_{2/3}Sr_{1/3}MnO_3$ epitaxial thin films. *Appl. Phys. Lett.* **99** (2011).

173. Miller, A. M. *et al.* Extracting information from X-ray diffraction patterns containing Laue oscillations. *Zeitschrift für Naturforschung B* **77,** 313–322 (2022).

174. Liu, L., Zhao, Z., Liu, H. & Li, Y. Effect of deposition temperature on the epitaxial growth of YBCO thin films on RABiTS substrates by pulsed laser deposition method. *IEEE Transactions on Applied Superconductivity* **20,** 1553–1556 (2010).

175. Yanmaz, E., Basoglu, M. & Grovenor, C. Anomalous ferromagnetic behaviour of Y_2O_3 and CuO nanoparticles in $YBa_2Cu_3O_y$ superconductor. *physica status solidi (a)* **206,** 2844–2850 (2009).

176. Albrecht, J., Soltan, S. & Habermeier, H.-U. Magnetic pinning of flux lines in heterostructures of cuprates and manganites. *Phys. Rev. B* **72,** 092502 (2005).

177. Jha, A. K., Khare, N. & Pinto, R. Influence of interfacial LSMO nanoparticles/layer on the vortex pinning properties of YBCO thin film. *Journal of Superconductivity and Novel Magnetism* **27,** 1021–1026 (2014).

178. Martinis, J. M., Hilton, G. C., Irwin, K. D. & Wollman, D. A. Calculation of Tc in a normal-superconductor bilayer using the microscopic-based Usadel theory. *Nuclear Instruments and Methods in Physics Research Section A: Accelerators, Spectrometers, Detectors and Associated Equipment* **444,** 23–27 (2000).

179. Aristomenopoulou, E., Zeibekis, M. & Stamopoulos, D. Optimizing the magnitude of the magnetoresistance observed in ferromagnet/superconductor/ferromagnet trilayers: A formula to combine all involved parameters. *Journal of Applied Physics* **119** (2016).

180. Asulin, I., Yuli, O., Koren, G. & Millo, O. Evidence for crossed Andreev reflections in bilayers of (100) $YBa_2Cu_3O_{7-\delta}$ and the itinerant ferromagnet $SrRuO_3$. *Phys. Rev. B* **74,** 092501 (2006).

181. Schäpers, T. *Semiconductor spintronics* (Walter de Gruyter GmbH & Co KG, 2021).

182. Kaul, P. *et al.* GeSn quantum wells as a platform for spin-resolved hole transport. *Communications Materials* **6,** 216 (2025).

183. Chen, Y. *et al.* Dirac-Like Fermions Anomalous Magneto-Transport in a Spin-Polarized Oxide 2D Electron System. *Advanced Materials* **37,** 2410354 (2025).

184. Yoo, Y. *et al.* Contribution of oxygen partial pressures investigated over a wide range to $SrRuO_3$ thin-film properties in laser deposition processing. *J. Appl. Phys.* **97** (2005).

185. Palai, R., Huhtinen, H., Scott, J. & Katiyar, R. Observation of spin-glass-like behavior in $SrRuO_3$ epitaxial thin films. *Phys. Rev. B.* **79,** 104413 (2009).

186. Porter, S. *et al.* Magnetic dead layers in $La_{0.7}Sr_{0.3}MnO_3$ revisited. *IEEE Trans. Magn.* **53,** 1–4 (2017).

187. Horiuchi, H. *et al.* Single-Layer Spin-Orbit-Torque Magnetization Switching Due to Spin Berry Curvature Generated by Minute Spontaneous Atomic Displacement in a Weyl Oxide. *Adv. Mater.,* 2416091 (2025).

188. Ali, Z. *et al.* Origin of insulating and nonferromagnetic $SrRuO_3$ monolayers. *Phys. Rev. B* **105,** 054429 (2022).

189. Falsetti, E. *et al.* High conductivity of ultrathin nanoribbons of $SrRuO_3$ on $SrTiO_3$ probed by infrared spectroscopy. *Sci. Rep.* **8,** 15217 (2018).

190. Lauter, V., Ambaye, H., Goyette, R., Lee, W.-T. H. & Parizzi, A. Highlights from the magnetism reflectometer at the SNS. *Phys. Rev. B.* **404,** 2543–2546 (2009).

191. Lauter-Pasyuk, V. Neutron grazing incidence techniques for nano-science. *Collect. SFN* **7,** s221–s240 (2007).

192. Daillant, J. & Gibaud, A. *X-ray and neutron reflectivity: principles and applications* (Springer, 2008).

193. Toperverg, B. P. & Zabel, H. in *Exp. Methods Phys. Sci.* 339–434 (Elsevier, 2015).

194. Ott, F. & Kozhevnikov, S. Off-specular data representations in neutron reflectivity. *J. Appl. Crystallogr.* **44,** 359–369 (2011).

195. Kentzinger, E., Rücker, U., Toperverg, B., Ott, F. & Brückel, T. Depth-resolved investigation of the lateral magnetic correlations in a gradient nanocrystalline multilayer. *Phys. Rev. B.* **77,** 104435 (2008).

196. Zhang, Z. *et al.* Manipulating the carrier concentration and phase transition via Nb content in $SrTiO_3$. *Sci. Rep.* **12,** 2499 (2022).

197. McCalla, E., Walter, J. & Leighton, C. A unified view of the substitution-dependent antiferrodistortive phase transition in $SrTiO_3$. *Chem. Mater.* **28,** 7973–7981 (2016).

198. Iles, N., Finocchi, F. & Khodja, K. D. A systematic study of ideal and double layer reconstructions of ABO_3 (001) surfaces (A = Sr, Ba; B = Ti, Zr) from first principles. *J. Phys. Condens. Matter.* **22,** 305001 (2010).

199. Jiang, J., Tian, W., Pan, X., Gan, Q. & Eom, C. Domain structure of epitaxial $SrRuO_3$ thin films on miscut (001) $SrTiO_3$ substrates. *Appl. Phys. Lett.* **72,** 2963–2965 (1998).

200. Ziese, M., Vrejoiu, I. & Hesse, D. Structural symmetry and magnetocrystalline anisotropy of $SrRuO_3$ films on $SrTiO_3$. *Phys. Rev. B.* **81,** 184418 (2010).

201. Goossens, A. S., Leiviskä, M. & Banerjee, T. Anisotropy and current control of magnetization in $SrRuO_3/SrTiO_3$ heterostructures for spin-memristors. *Front. Nanotechnol.* **3,** 680468 (2021).

202. Zabel, H. & Theis-Bröhl, K. Polarized neutron reflectivity and scattering studies of magnetic heterostructures. *Journal of Physics: Condensed Matter* **15,** S505 (2003).

203. Trappen, R. *Depth dependent atomic valence determination in $La_{0.7}Sr_{0.3}MnO_3$ thin films using synchrotron techniques* (West Virginia University, 2019).

204. Bhatt, H. *et al.* Correlation of Magnetic and Superconducting Properties with the Strength of the Magnetic Proximity Effect in $La_{0.67}Sr_{0.33}MnO_3/SrTiO_3/YBa_2Cu_3O_{7-\delta}$ Heterostructures. *ACS Applied Materials & Interfaces* **14,** 8565–8574 (2022).

205. Kim, Y. *et al.* CuO formation control as a function of mixed ratio of Cu-free powders in the synthesis of YBCO superconductors on Cu substrates. *Journal of electroceramics* **17,** 1063–1067 (2006).

Appendix A

High Oxygen Pressure Sputtering system – User guide and growth protocol

This protocol and user guide were developed collaboratively by Vitor Alexandre de Oliveira Lima and Prof. Dr. Michael Faley (ER-C-1), ensuring a comprehensive approach. Dr. Nileena Nandakumaran and Dr. Ankita Singh assisted with the images and provided valuable feedback on the guide. As of the writing of this thesis, the protocol and guide are in version 3.0.

Introduction

High Oxygen Pressure Sputtering (HOPS) is a technique for growing thin films at oxygen pressures higher than 0.5 mbar. This contrasts with conventional sputtering processes, which usually operate at much lower pressures. Thin films prepared by HOPS exhibit good homogeneity across the substrate surface, and their stoichiometry is predetermined by the composition of the target.

In a sputtering process, atoms are ejected from a target made of the material to be deposited. These atoms are released when the target is bombarded by ionized atoms of a process gas. The sputtered material forms a plasma or plume, which is directed toward a heated substrate to initiate film growth. Magnets mounted behind the target can further direct the plasma toward the substrate, a process known as magnetron sputtering [116, 118].

The HOPS systems at Forschungszentrum Jülich (FZJ) were developed in the early 1980s by Prof. Dr. Ulrich Poppe and Prof. Dr. Michael Faley for the preparation of high-temperature superconductors such as $YBa_2Cu_3O_{7-x}$ [71, 115, 116]. Over time, these machines have also been used for the deposition of other materials, including complex oxides and multiferroic systems [111, 118]. These instruments are patented, and therefore any technical drawings or related material must not be distributed to third parties outside FZJ.

The HOPS system described in this manual is located in laboratory room 65 of the Jülich Centre for Neutron Science (JCNS-2), part of FZJ. The laboratory supervisors are Oleg Petracic (JCNS-2) and technician Frank Gossen (JCNS-2), who is responsible for

the HOPS machines.

The system consists of several interconnected instruments that operate together during thin-film deposition. The deposition chamber (Fig. A.1) is maintained at a base pressure between the low 10^{-5} and $\approx 10^{-6}$ mbar range with the help of a Pfeiffer HiPace 80 turbo pump and a screw-type backing pump. Thin films can be grown in pure oxygen (99.99% purity) at pressures ranging from 0.5 mbar to 2.5 mbar.

Oxygen pressure is regulated using an MKS Type 250E pressure/flow controller, a self-contained PID module that provides optimized closed-loop control of total gas pressure or flow. The substrate heater is managed by a Eurotherm model 2404, which allows deposition at temperatures up to 1100 °C. The heater is connected to a computer via iTools software, which enables complex temperature processes such as ramps and post-annealing treatments. The Eurotherm heater is shown in Fig. A.2, together with the vacuum measurement system (turbo pump, backing pump, bypass, and leak test) controller and the MKS pressure/flow controller.

This HOPS machine can generate plasma using either radio-frequency (RF) or direct-current (DC) sputtering. In practice, RF sputtering is most commonly used, since the available target configuration is optimized for this method. In RF mode, a frequency of 13.56 MHz is applied to enhance electron–ion collisions and increase the sputtering rate. The RF power supply is a Hüttinger PGF 300 RF generator, which enables plasma powers up to 150 W. The RF generator is shown in Fig. A.3.

Figure A.1.: The JCNS-2 HOPS system.

The following sections provide detailed step-by-step instructions for safely operating, maintaining, and documenting experiments with the HOPS system.

Safety: Always wear gloves, goggles, and use oxygen carefully to avoid rapid venting accidents.

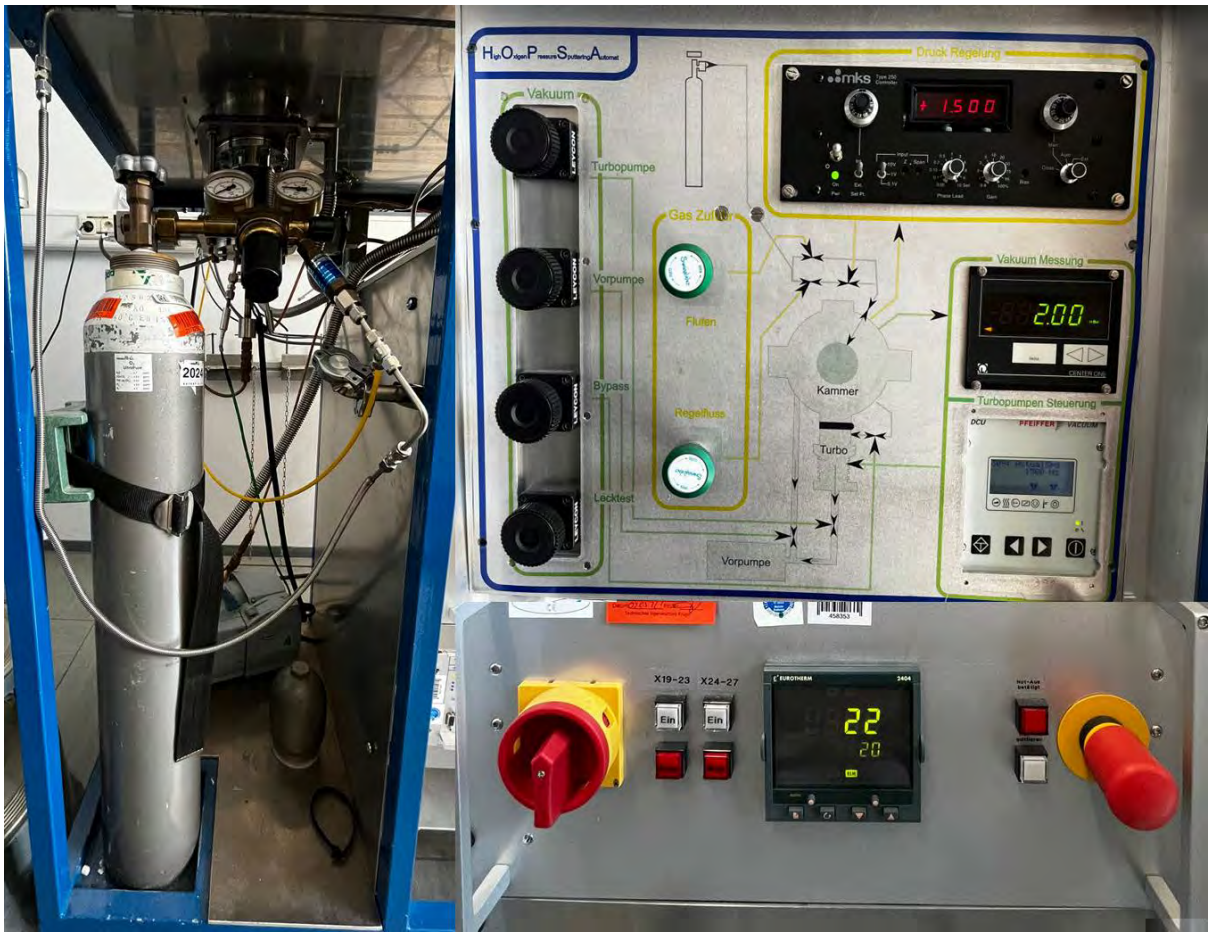

Figure A.2.: Vacuum measurement system and Eurotherm heater controller.

Figure A.3.: Radio Frequency generator.

Opening the deposition chamber

The deposition chamber (Fig. A.4) is kept under high vacuum (10^{-6} mbar) and high oxygen pressure during deposition. Follow the steps below to open it safely:

Figure A.4.: Deposition chamber.

1. Close the gate valve (Fig. A.5). Pull the pin, turn the valve to the left, and lock it with the pin.
2. Close the three knobs for the turbo pump, pre-pump (*vorpump*), and bypass (Fig. A.6).
3. Hold the chamber lid with your left hand (Fig. A.7).
4. With your right hand, slowly open the venting valve (Fig. A.7, bottom) to admit pure oxygen.
5. Vent gradually with periodic movements (3–5 s). Stop when the chamber reaches 1 bar.
6. **Caution:** If vented too quickly, the lid may fly open and cause injury. Always hold the lid securely.
7. Use a screwdriver in the lid gap if needed to help release pressure.
8. Remove the external ring and the lid (Fig. A.8).
9. Wait about 3 minutes for the oxygen to disperse.
10. The chamber is now open.

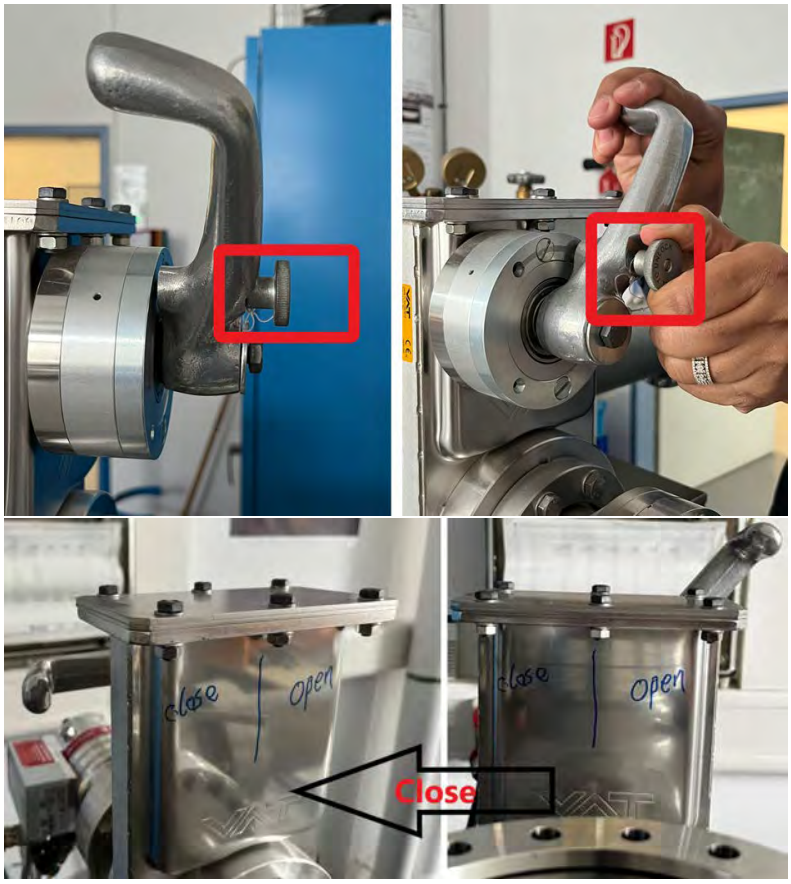

Figure A.5.: Closing the gate valve: pull the pin and turn the valve to the left. Lock it with the pin.

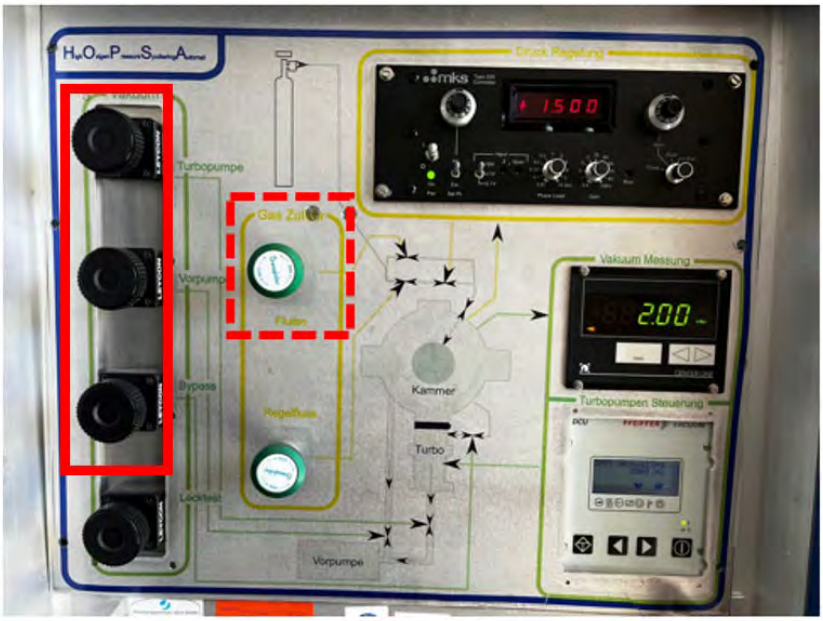

Figure A.6.: Turbo-pump (turbopumpe), pre-pump (vorpumpe, screw-pump) and Bypass valves/knobs panel.

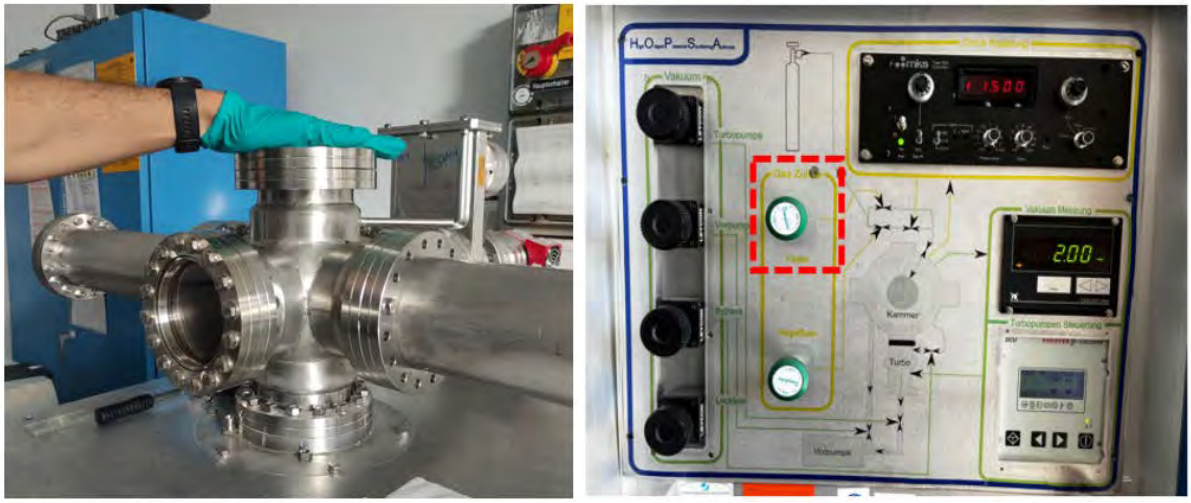

Figure A.7.: Use the left hand to hold the lid of the chamber and the right hand to vent the chamber with pure oxygen.

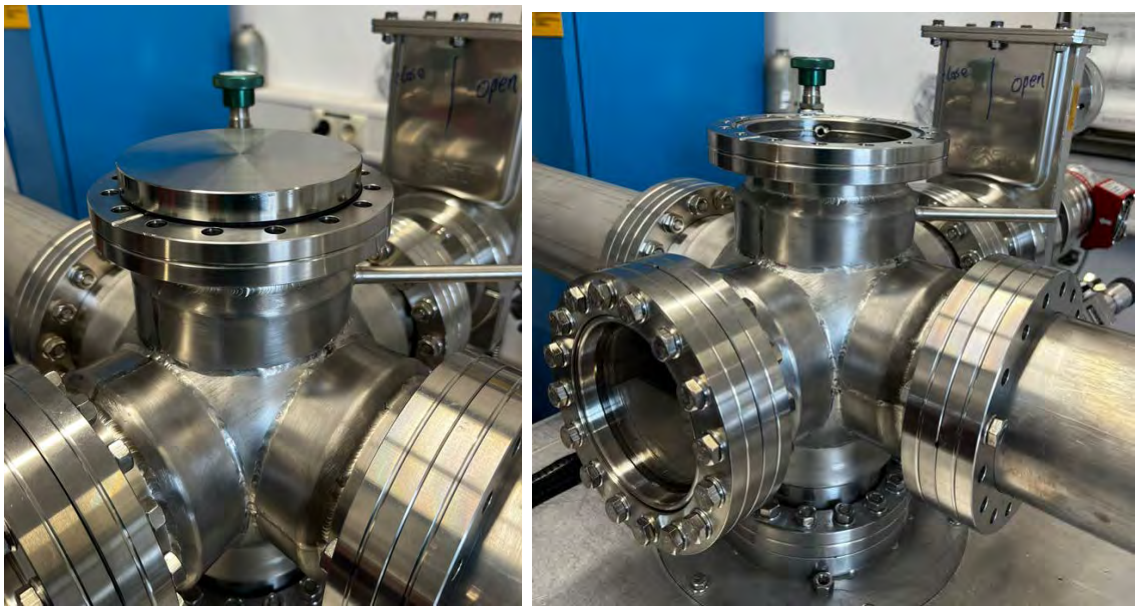

Figure A.8.: Chamber lid without the external ring and open.

Closing the deposition chamber

Close the chamber as follows:

1. Place the chamber lid back in position (Fig. A.9).
2. Open the screw pump (red box in Fig. A.10) until the vacuum gauge (green LED) reads 10^{-2} mbar.
3. Close the screw pump knob. Then open the bypass and turbo pump knobs/valves (blue boxes in Fig. A.10).
4. Open the gate valve: pull the pin, turn to the right, and lock it with the pin (Fig. A.11).

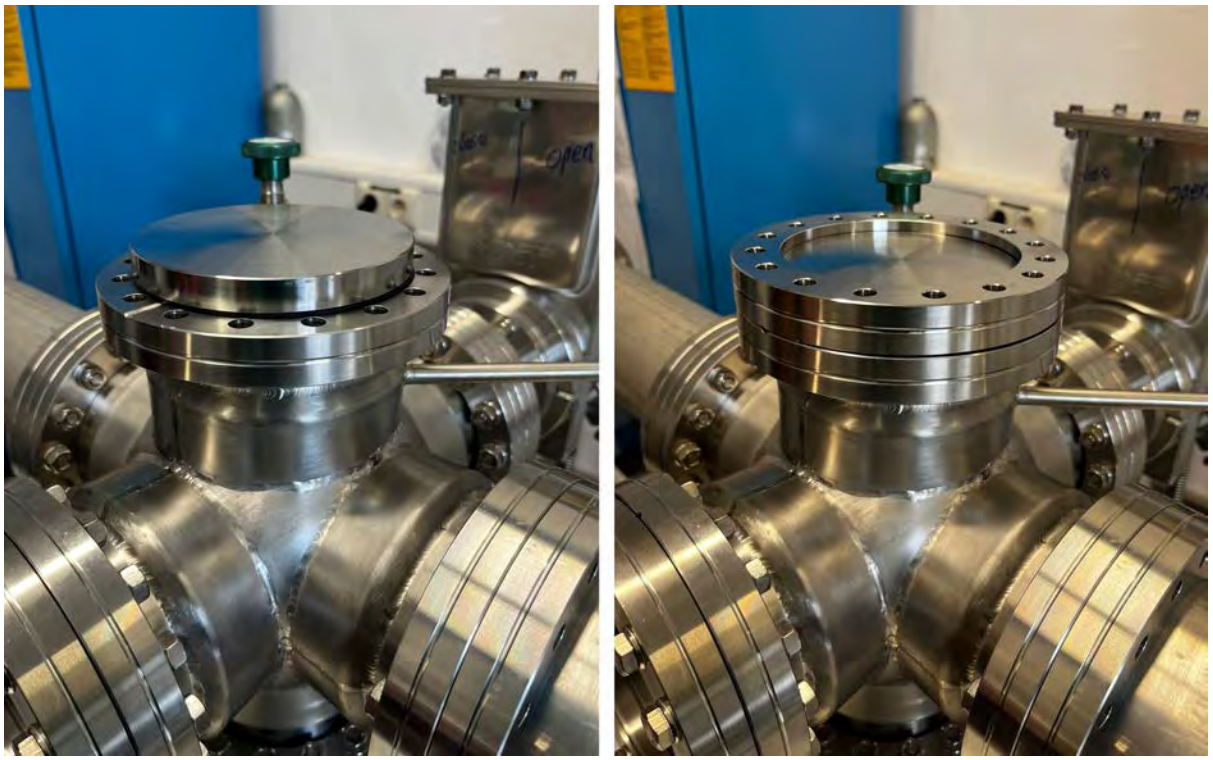

Figure A.9.: Closing the deposition chamber.

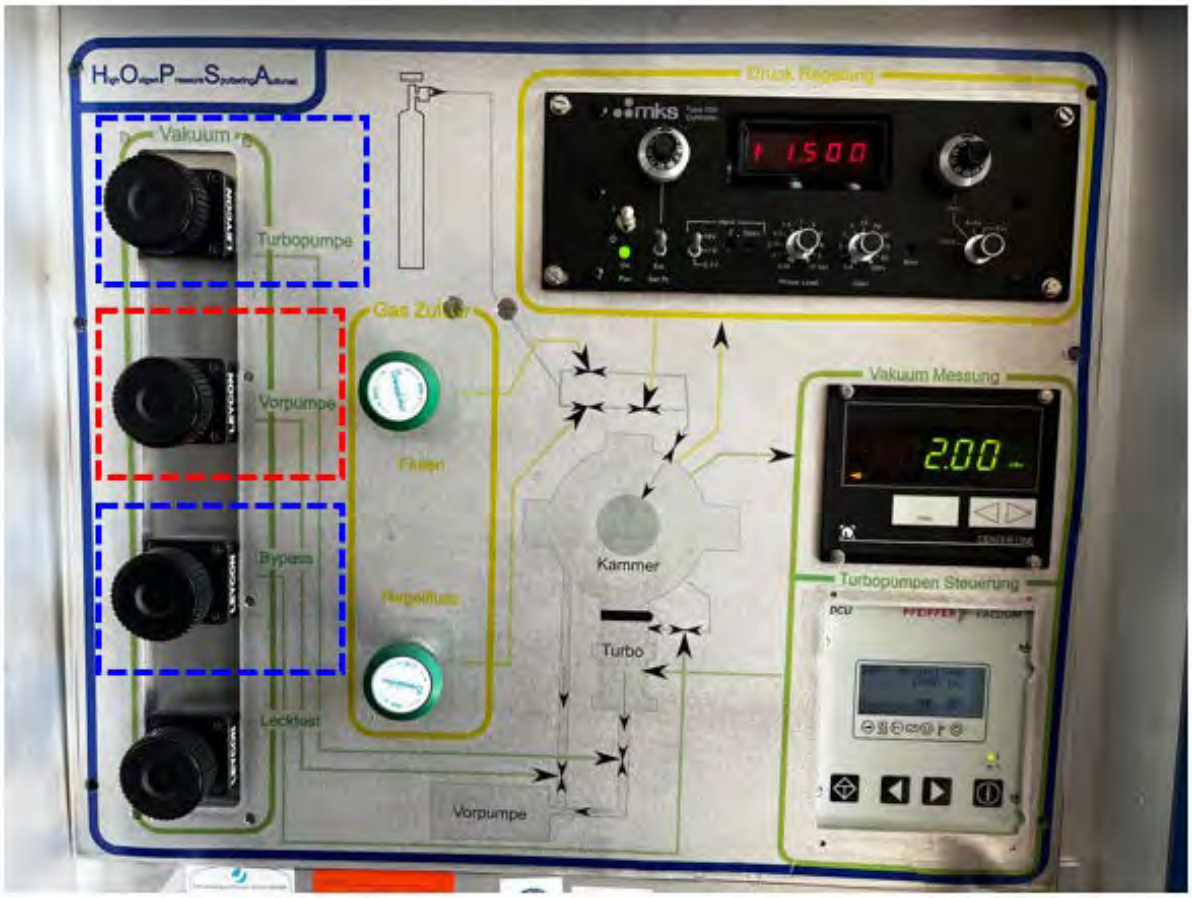

Figure A.10.: Vacuum measurement is the green LED. Turbo and screw pump nobs/valves and by pass knob/valve.

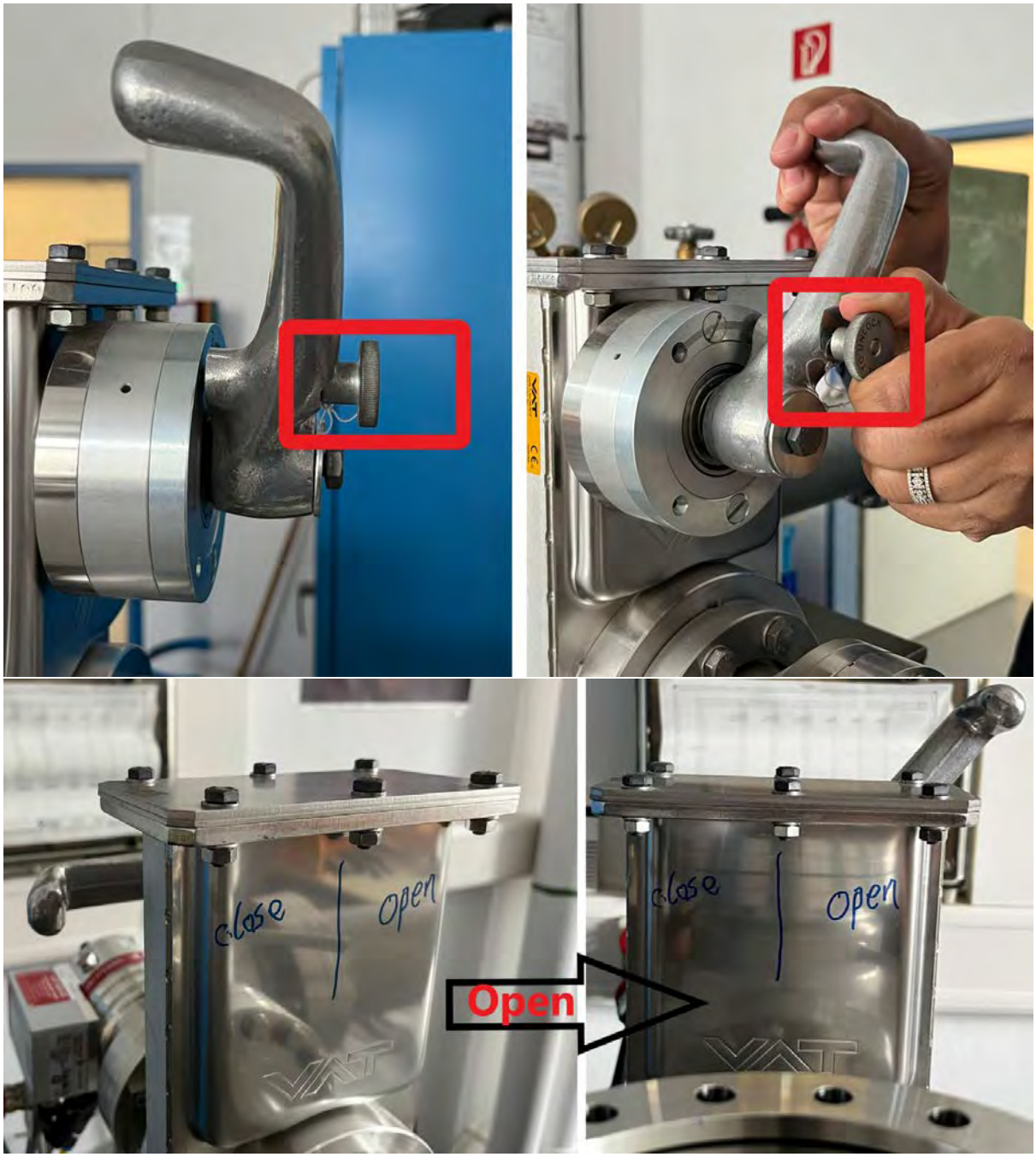

Figure A.11.: Opening the gate valve: pull the pin and turn the valve to the right. Lock it with the pin.

Loading the substrate/sample in the deposition chamber

Load the substrate as follows:

1. Wearing gloves, place the frame on top of the heater block.
2. Hold the substrate with tweezers and insert it into the frames (Fig. A.12).
3. **Note:** Select the correct frame size for your substrate (5 mm × 5 mm or 10 mm × 10 mm).
4. Adjust the frame to avoid deposition on the heater block (Fig. A.13).

Removing the substrate/sample from the deposition chamber

Remove the substrate as follows:

1. Open the deposition chamber (see Section A.2).
2. Move the frame aside on the heater block (left in Fig. A.13).
3. Wearing gloves, take the substrate from the heater using tweezers.
4. Place the substrate securely in the frame (Fig. A.12).
5. Close the chamber (see Section A.3).

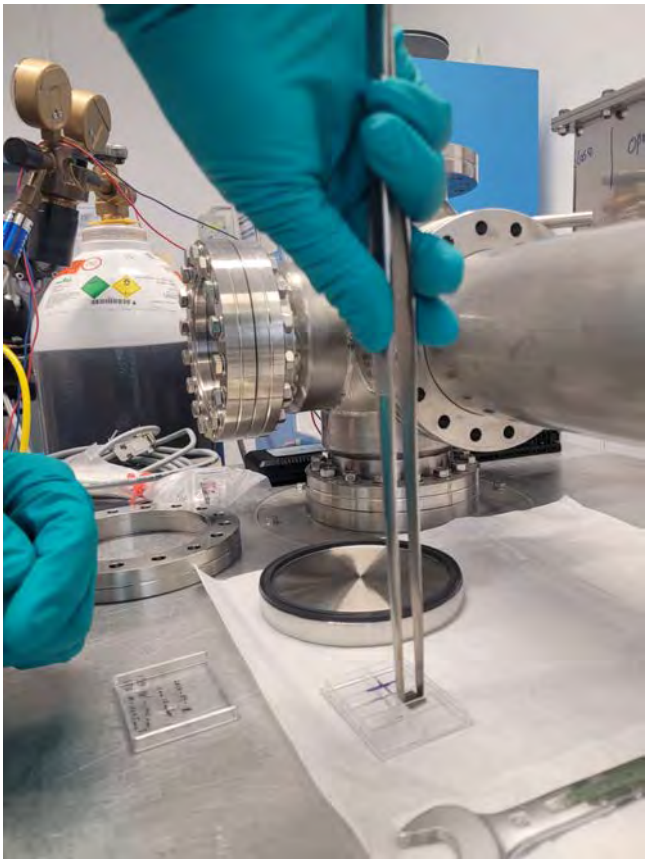

Figure A.12.: Hold the substrate/sample tight, to not lose it.

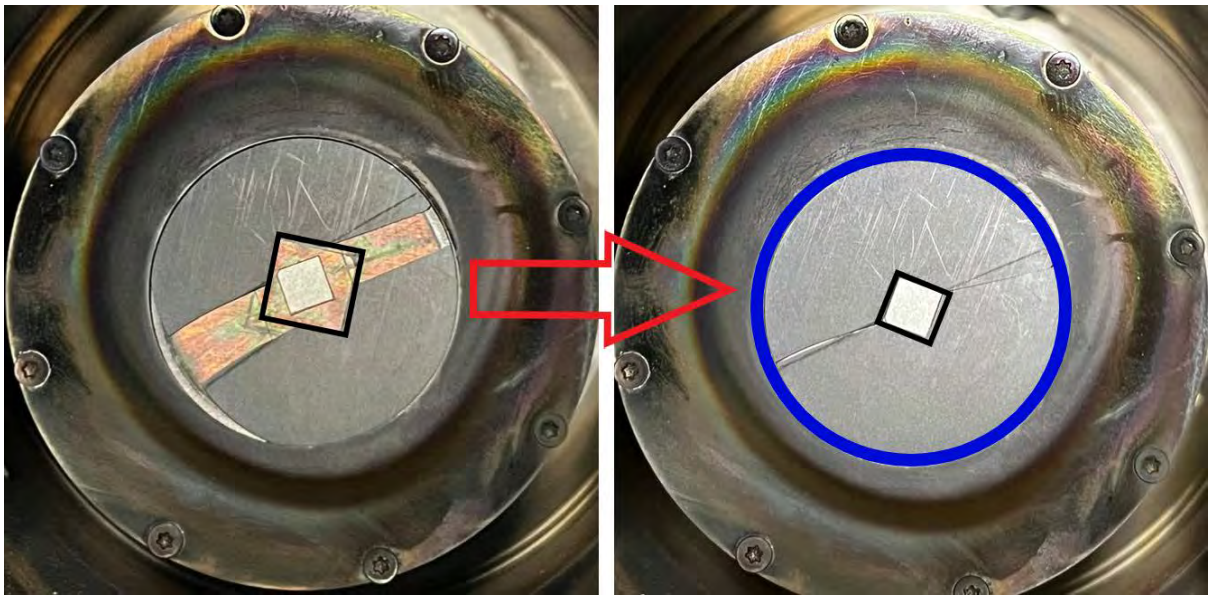

Figure A.13.: Substrate adjusted on the frames on the heater block.

Target positioning

The HOPS system has slots for five targets, spaced by ≈ 67.5 mm (Fig. A.14). Each target is identified by its position (e.g., Target 1 = Position 1). The list of mounted targets, including material, formula, and position, is available on the board at the back of the HOPS lab door.

At Position 0, no target is placed above the substrate/heater block (Fig. A.15). Move the desired target into position manually or using computer control.

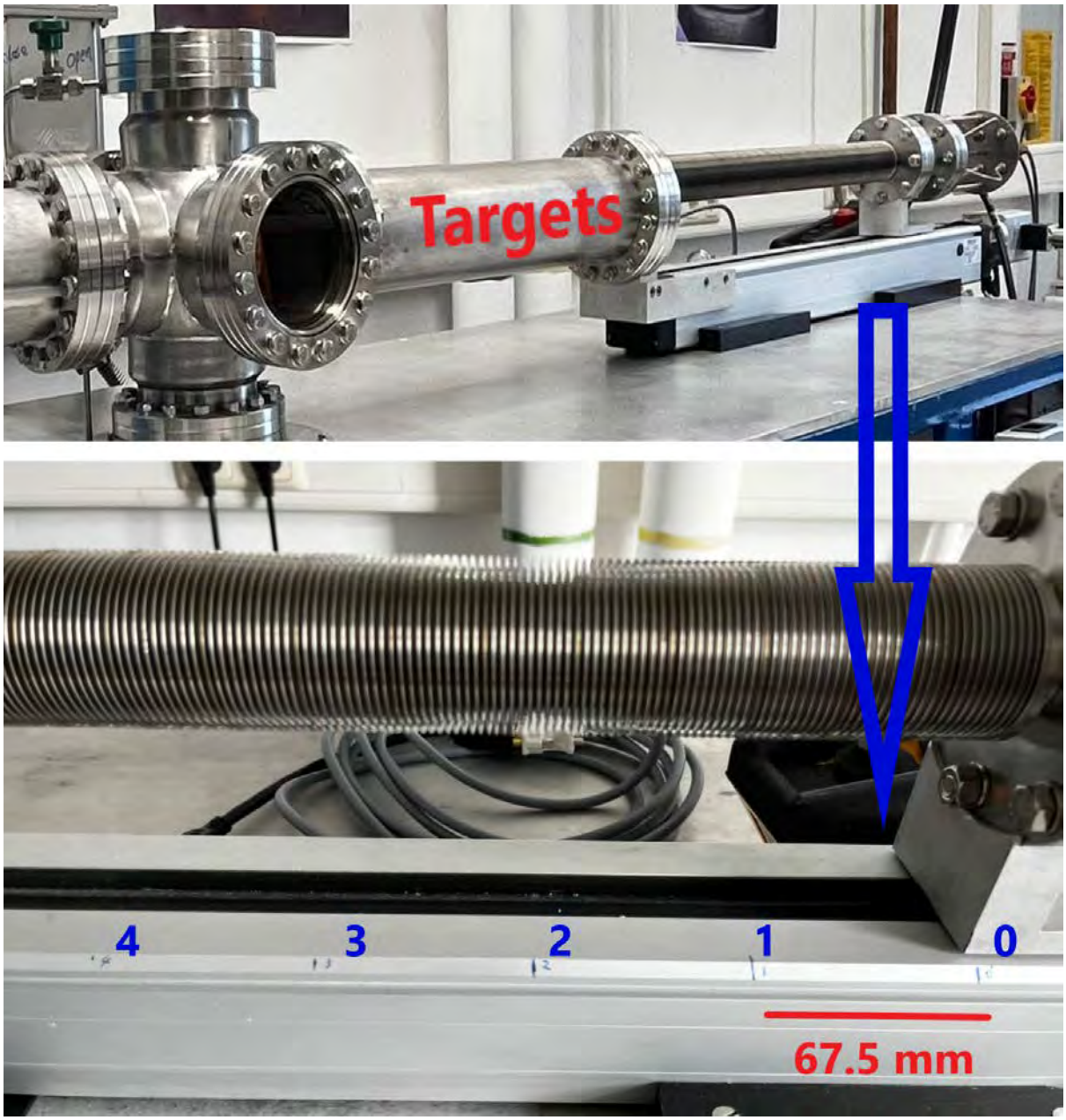

Figure A.14.: Distance between targets slots.

Manual positioning:

1. Ensure the motor is switched off.
2. Rotate the wheel clockwise (Fig. A.16) until the desired position is reached.
3. To return to Position 0, rotate counterclockwise.

Computer positioning:

1. Open the MiniMove software (Fig. A.17, left).
2. Press *Homing* (red, 1).
3. Immediately press *Stop* (blue, 2).
4. Enter the position value (in tenths of a millimeter) corresponding to the target. Example: for Target 1, use 675.
5. Click *Move to Pos* (Fig. A.17, right).
6. To return to Position 0, set the position value to 0.

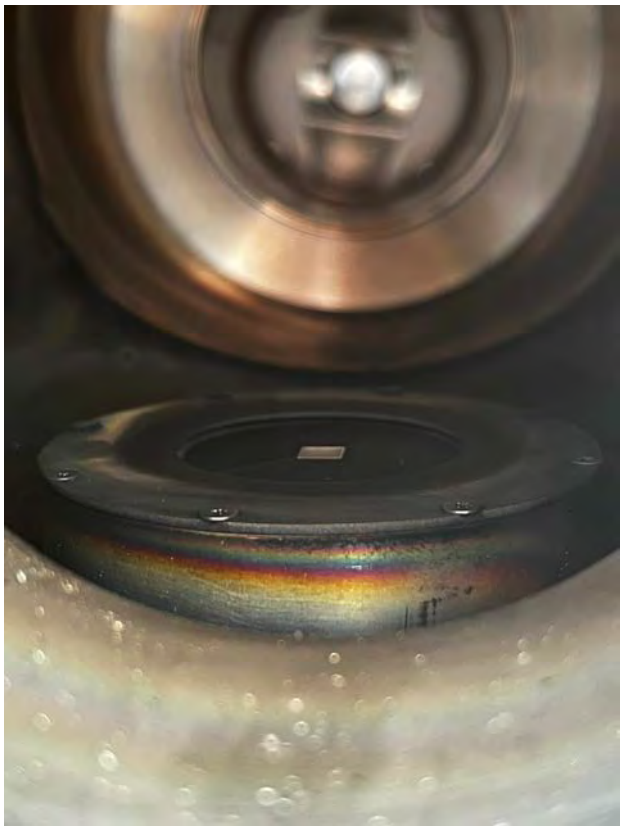

Figure A.15.: Position 0. No target positioned above the substrate/sample in the heater block.

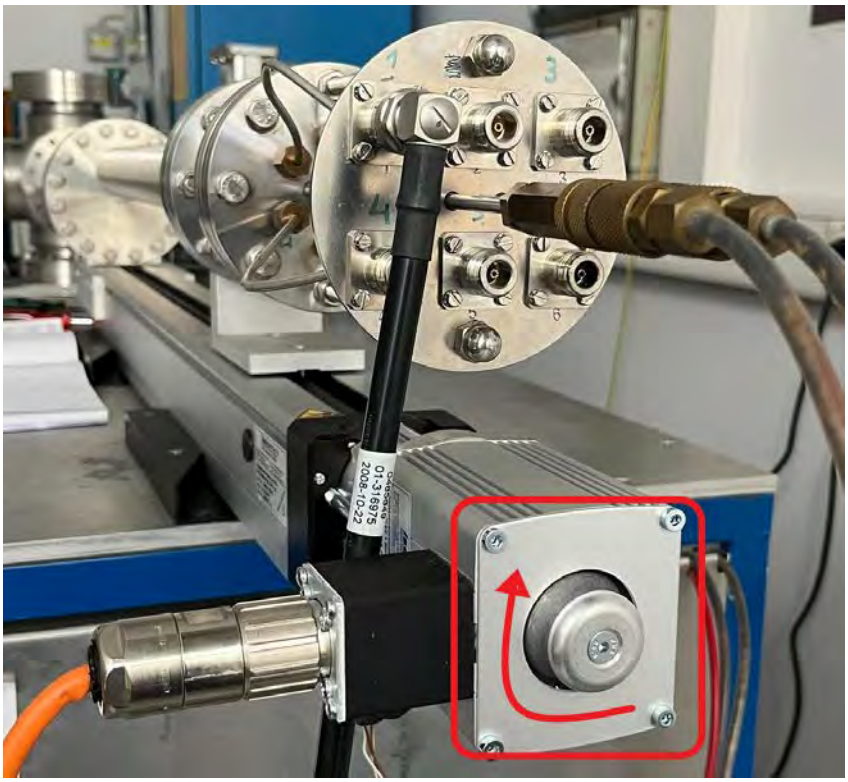

Figure A.16.: Rotate clockwise to move forward a desired target to the deposition position. Rotate counter-clockwise to return the target back.

Figure A.17.: MiniMove software interface for automated target positioning.

Adjusting the target–sample distance

Adjust the target–substrate distance (D_{TS}) before growth. This parameter directly influences the growth rate and film quality.

1. Use a screwdriver and a ruler to adjust the distance (Fig. A.18).
2. Refer to Table A.1 for correspondence between D_{TS} and ruler values.
3. Examples of different D_{TS} are shown in Fig. A.19.

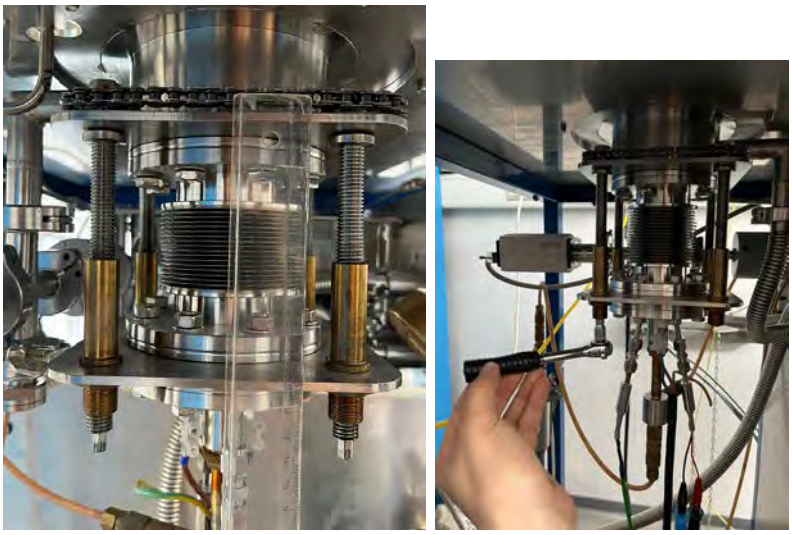

Figure A.18.: Adjusting the target–substrate distance.

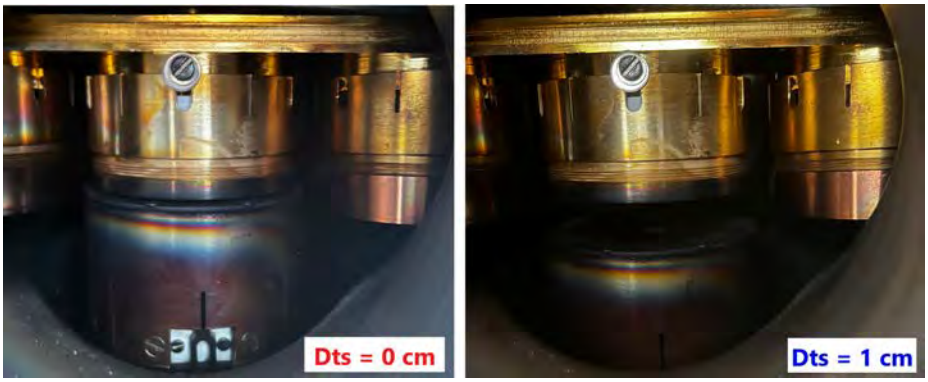

Figure A.19.: Example of $D_{TS} = 0$ cm (left) and $D_{TS} = 1$ cm (right).

Table A.1.: Relation between the D_{TS} and the ruler values in cm.

D_{TS} (cm)	0.0	1.0	1.5	2.0	2.5	3.0
Ruler (cm)	10.0	11.0	11.5	12.0	12.5	13.0

Adjusting the oxygen pressure

Set the oxygen pressure only when the chamber is under vacuum with the following state:

- Gate valve: open
- Turbo pump and bypass knobs: open
- Pre-pump knob: closed

To set the pressure (Fig. A.20):

1. Close the gate valve. Keep turbo pump and bypass knobs open. Keep pre-pump knob closed.
2. Open the controlled flow valve (blue box). A half turn is sufficient.
3. Set the desired pressure using the valve in the green box.
4. Switch from *Close* to *Auto* (red box) to start oxygen flow at the set pressure.
5. Record the oxygen pressure values (setpoint, MKS reading, and VM) in the logbook.
6. **Note:** For pressures above 2.25 mbar, slightly close the bypass valve (Fig. A.21).

After the experiment:

1. Switch from *Auto* back to *Close* (red box).
2. Close the controlled flow valve (blue box).
3. Open the chamber following Section A.2.

Figure A.20.: Vacuum measurement and MKS panel. Follow the instructions to insert oxygen into the chamber under a controlled value of pressure.

Figure A.21.: Remember to close the bypass valve for sputtering experiment with pressures bigger than 2.25 mbar.

Adjusting the radio-frequency (RF) generator

Oxygen is used as the process gas, and the RF generator supplies the plasma power. A stable plasma requires both pressure and RF power. **Caution: Never switch on the RF generator while the chamber is under vacuum.**

To turn on the RF generator (Fig. A.22):

1. Press the green button on the RF generator panel.
2. Increase forward power (FWDP) by turning the wheel or using the +/− buttons.
3. Keep reflected power (REFP) at 0.
4. If REFP ≠ 0, adjust the variable capacitor C_l and C_t values.

To tune C_l and C_t:

1. Press F3 on the RF panel.
2. Press F2 to select either C_l or C_t.
3. Adjust values with the wheel or +/− buttons until REFP = 0.
4. Press F3 or F4 to exit.
5. Record FWDP, REFP, DC-BIAS, C_l, and C_t values in the logbook.

To turn off the RF generator:

1. Reduce FWDP to 0 using the wheel or +/− buttons.
2. Press the red button on the RF panel.

Figure A.22.: RF generator panel.

Controlling the heater temperature

The growth temperature can be controlled either by computer or manually (in case of computer malfunction). The HOPS computer remains on at all times. Restart the computer or the iTools program before starting any process.

To start a temperature program:

1. Open the iTools interface.
2. On the welcome page, select the second option in German: *Existierend Clone Datei bearbeiten (offline Konfiguration).*
3. Open the file *alte Config.uic* (Fig. A.23).
4. In the iTools interface, click *Abfrage* to connect to the Eurotherm controller. Synchronization takes 2–3 minutes.
   a) After synchronization, a Eurotherm icon will appear at the bottom of the interface, showing temperature and setpoint (Fig. A.24).
   b) Press *Abfrage* again if needed.
5. Click *Programmgeber* to open the temperature program editor.
6. Review the loaded temperature program (Fig. A.24).
   a) RMP.T = temperature ramp (target setpoint and time to reach it).
   b) DWEL = dwell step (constant temperature for a set time).
7. Configure a temperature recipe suited to your growth. Respect the heater limits.
   a) Typical heating ramp: 11.7°C/min.
   b) Typical cooling ramp: 23.3°C/min.
8. **Note:** The heater has no active cooling system. To accelerate cooling after growth, close all valves and fill the chamber with 800 mbar of oxygen. This improves heat transfer and allows sample removal on the same day.
9. Upload the recipe to the Eurotherm controller by clicking the third icon above *Program parameter.*
10. On the Eurotherm controller, press *Run.*
11. Monitor the program by selecting *Operator* → *Run.* The programmer tab will display the steps (Fig. A.25).
12. Do not change the program once it is running. To modify parameters, first stop the program.
13. To stop, press and hold *Run* on the Eurotherm controller. Then reconfigure as needed.

Tuning the temperature feedback

Perform this step only if the heater is unstable (temperature oscillates around the setpoint).

1. Run a program with a setpoint above 700°C and a DWEL step of 3 hours.
2. Once the setpoint is reached, activate the *ATUN* function by enabling the *tunE* parameter.
3. The heater will oscillate around the setpoint in a controlled way to adjust the PID constants.
4. After tuning, the heater will stabilize at the setpoint (Fig. A.26).

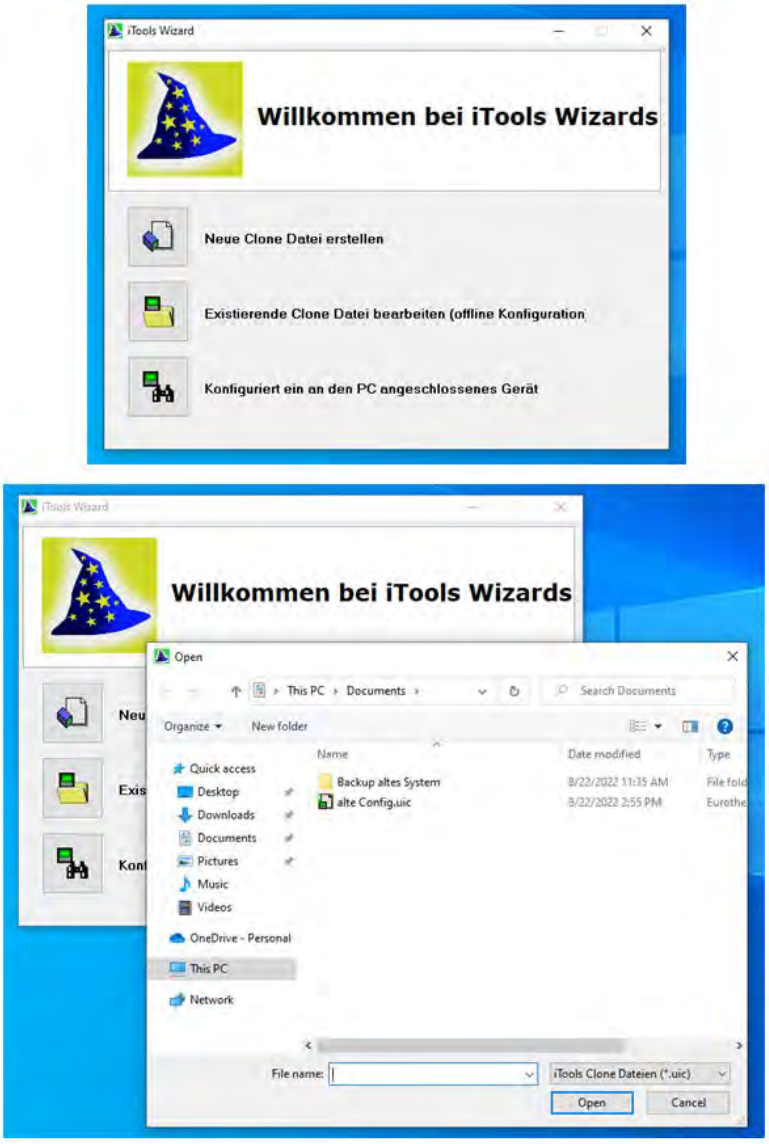

Figure A.23.: Opening the iTools program.

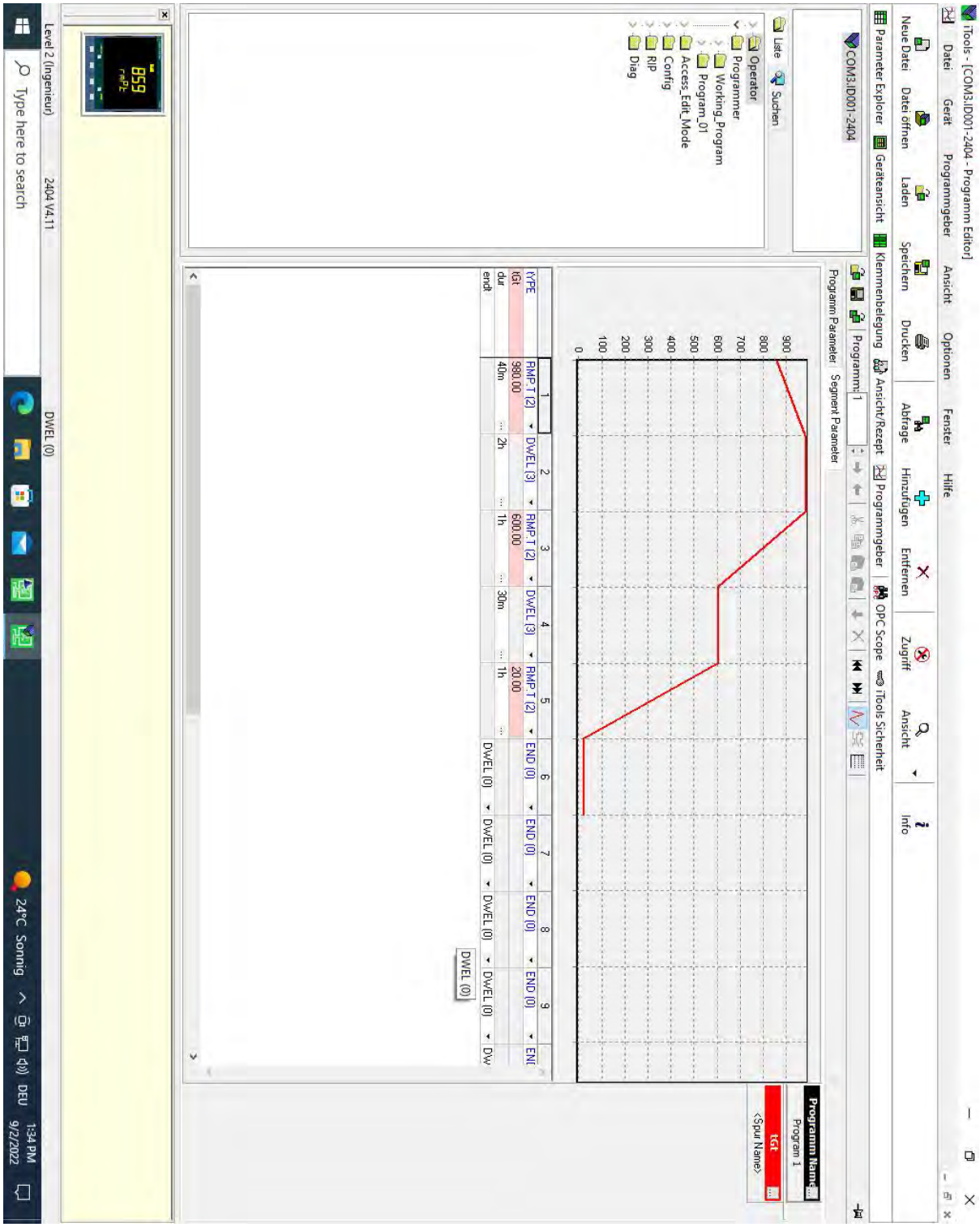

Figure A.24.: iTools interface.

Figure A.25.: Operator tab.

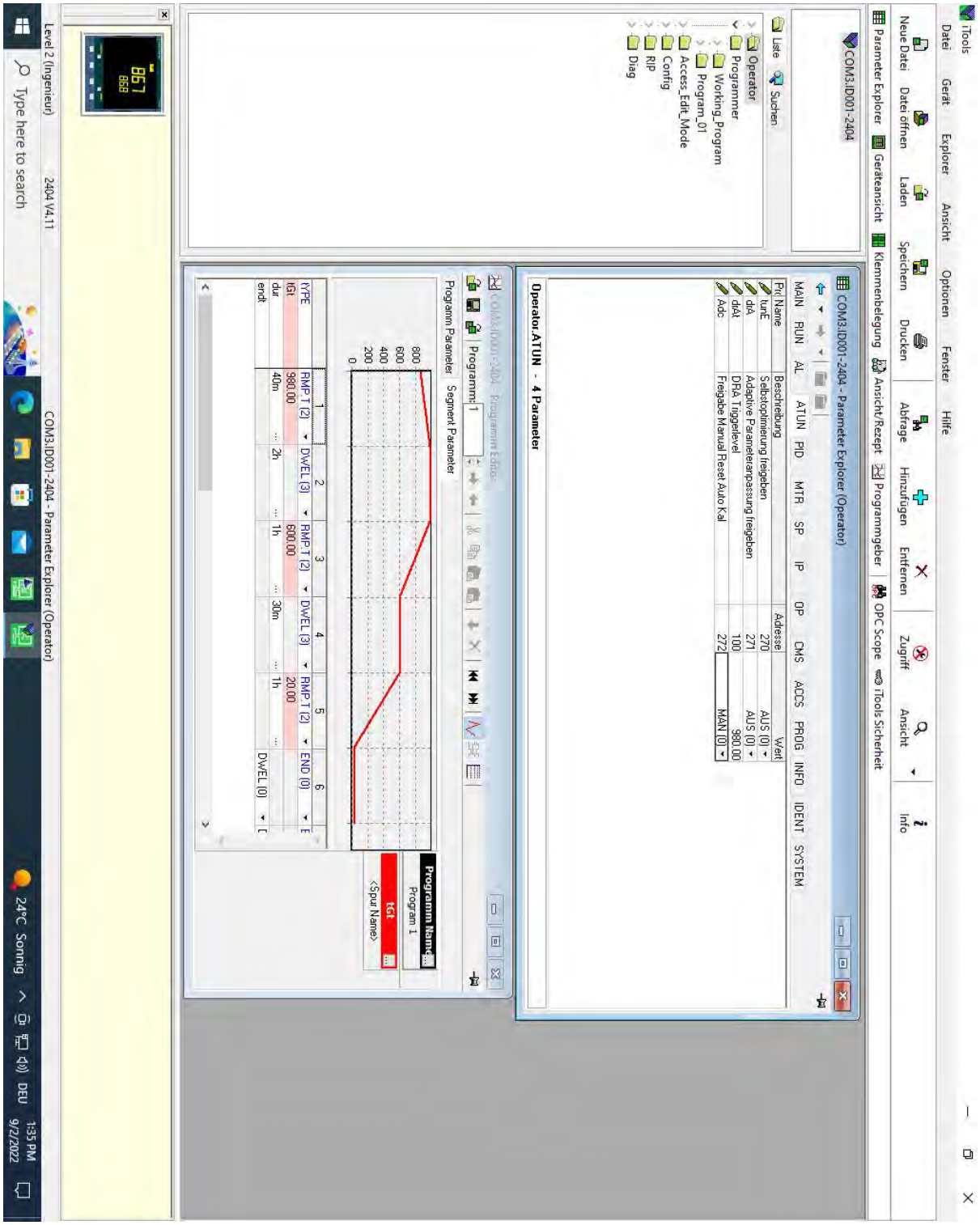

Figure A.26.: Tuning the temperature feedback.

Suggested protocol for sample growth

1. Insert the substrate into the deposition chamber and set the target–substrate distance (D_{TS}).

2. Pump down the system overnight.

3. Pre-sputter the target for at least 24 hours before growth. This cleans the target and ensures stable conditions (substrate temperature, RF power, oxygen pressure).

4. Pump down the system overnight again.

5. Start the growth:

   a) Set the oxygen pressure.

   b) Switch on the RF generator.

   c) Raise the heater to the growth temperature (this acts as a short pre-sputtering).

6. Allow the sample to cool to room temperature before removal.

7. Record all parameters used during each stage in both the HOPS logbook and the IFF samples database (https://iffsamples.fz-juelich.de).

Organization of the HOPS logbook

Always document experiments clearly, legibly, and with as much detail as possible in both the HOPS logbook and the IFF samples database (https://iffsamples.fz-juelich.de). Include:

1. Date and description of the experiment (e.g., annealing a substrate, growth of YBCO on MgO (100)).

2. Base pressure at the beginning of the experiment.

3. Process gas information (setpoint, MKS reading, VM values).

4. RF generator parameters: target material and position, Forward Power (FWDP), Reflected Power (REFP), DC-BIAS, and capacitor constants C_l and C_t.

5. Temperature recipe (include a quick sketch/graph if possible).

6. Start and end times of the process.

7. Date and time when the chamber was closed and pumping resumed after the experiment.

Maintenance

Specifying the targets

The targets used in the HOPS machine consist of 2″ diameter × 0.125″ thick material, bonded with Indium to a 2″ diameter × 5 mm thick Copper backing plate. The backing plate is used to avoid any target damage during the shipment and should be removed. The target is then bonded on the target holder, with are magnets inside, by the responsible technician. The target holder and the magnets arrangement are shown in Fig. A.27.

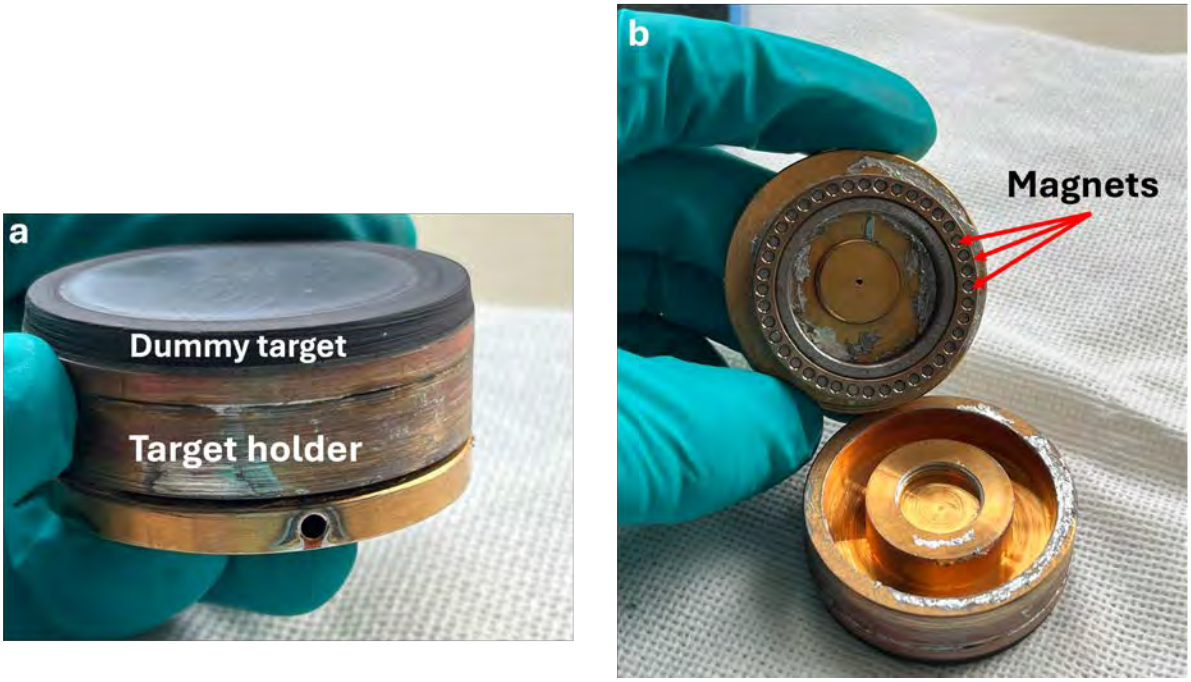

Figure A.27.: (a) Dummy target mounted in the target holder. (b) Target holder parts, illustrating the magnets inside it.

Mounting the target

Once the target is bonded to the target holder, it can be mounted on the HOPS machine. Make sure the machine is switched off and that the RF generator is also switched off. Then, disconnect the RF generator cable from the target arm, as shown in Fig. A.28.

After that, vent and open the HOPS machine as described in Section A. Once the deposition chamber is open [Fig. A.29(a)], remove the screws [Fig. A.29(b–d)] and pull out the part where the targets are mounted inside [Fig. A.29(e–f)] far enough to provide sufficient working space. If necessary, manually move the target arm to position 3 or 4 to create more space.

The target can now be connected to the target arm using rubber and Al_2O_3 insulating rings. The arrangement of these insulating parts depends on the plasma type (RF or DC), as illustrated in Fig. A.30.

Mounting procedure:

1. Connect the pin and insert the screws of the target arm on the backside of the target [Fig. A.31(a–b)].

2. Ensure that the rubber and Al_2O_3 rings are properly cut and aligned with the screws and screw holes so that the target fits correctly [Fig. A.31(c)].

3. Tighten the screws on the top of the target arm [highlighted in red in Fig. A.31(d)], securing the target in place.

4. Tighten the screw inside the target [highlighted in blue in Fig. A.31(d)] to fix the connection between the target arm and the target.

5. After these steps, the target should be properly mounted, as shown in Fig. A.31(e).

Final assembly of the target holder:
To finalize the mounting, attach the final structure of the target holder [Fig. A.32(a)] to the target arm. This structure consists of two independent parts [Fig. A.32(b)], which must be properly connected with several Al_2O_3 rings placed internally. These rings have specific diameters and thicknesses [Fig. A.32(c)] and must be arranged alternately at the bottom of the structure [Fig. A.32(d)]. Finally, add a hollow Al_2O_3 cylinder [Fig. A.32(e)] and connect the structure to the target arm by tightening the screws [Fig. A.33(a-c)]. If necessary, tighten up the bottom part of the external structure of the target to have it more adjusted [Fig. A.33(d)].

Disassembling the target
To disassemble the target, simply follow the steps described above in reverse order.

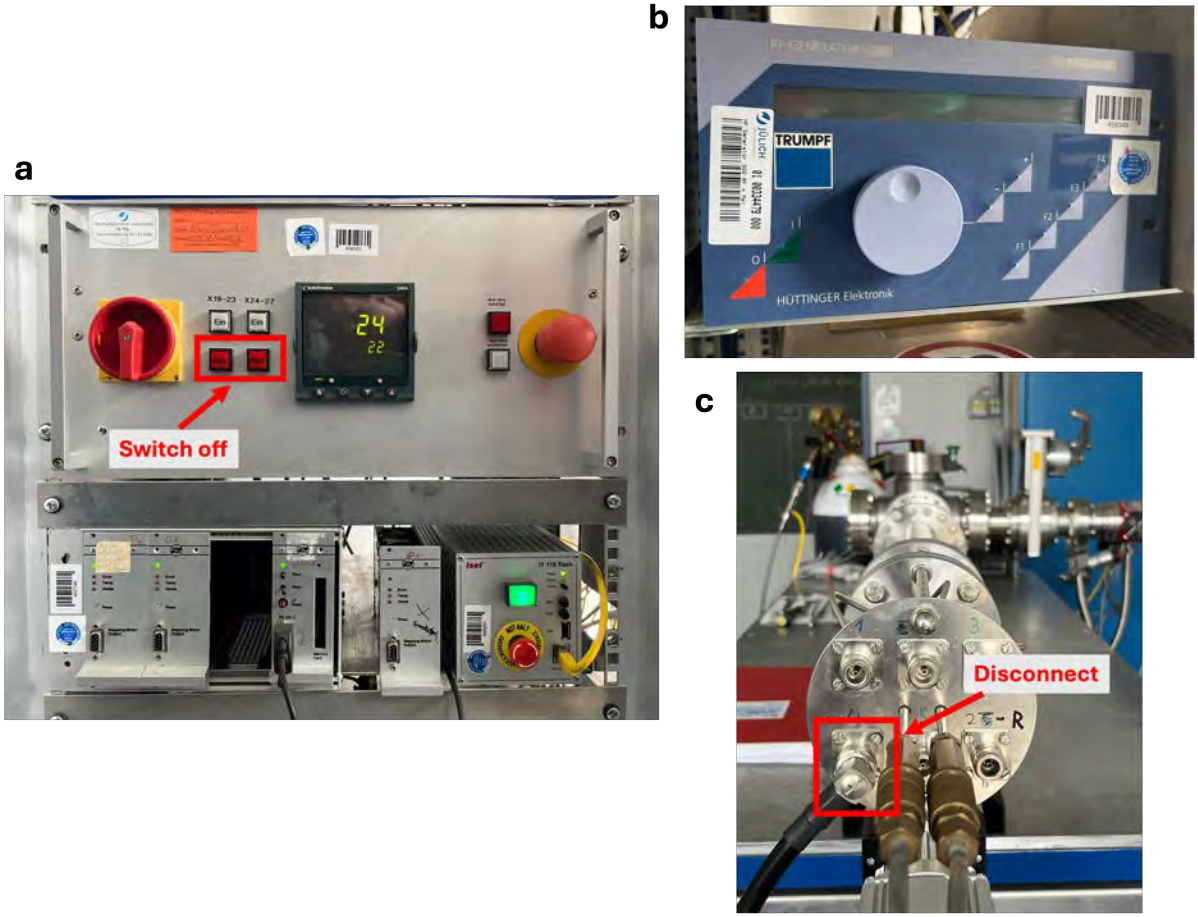

Figure A.28.: (a) Switch off the power supply of the HOPS machine. (b) Make sure that the RF generator is switched off. (c) Disconnect the RF generator cable from the target arm.

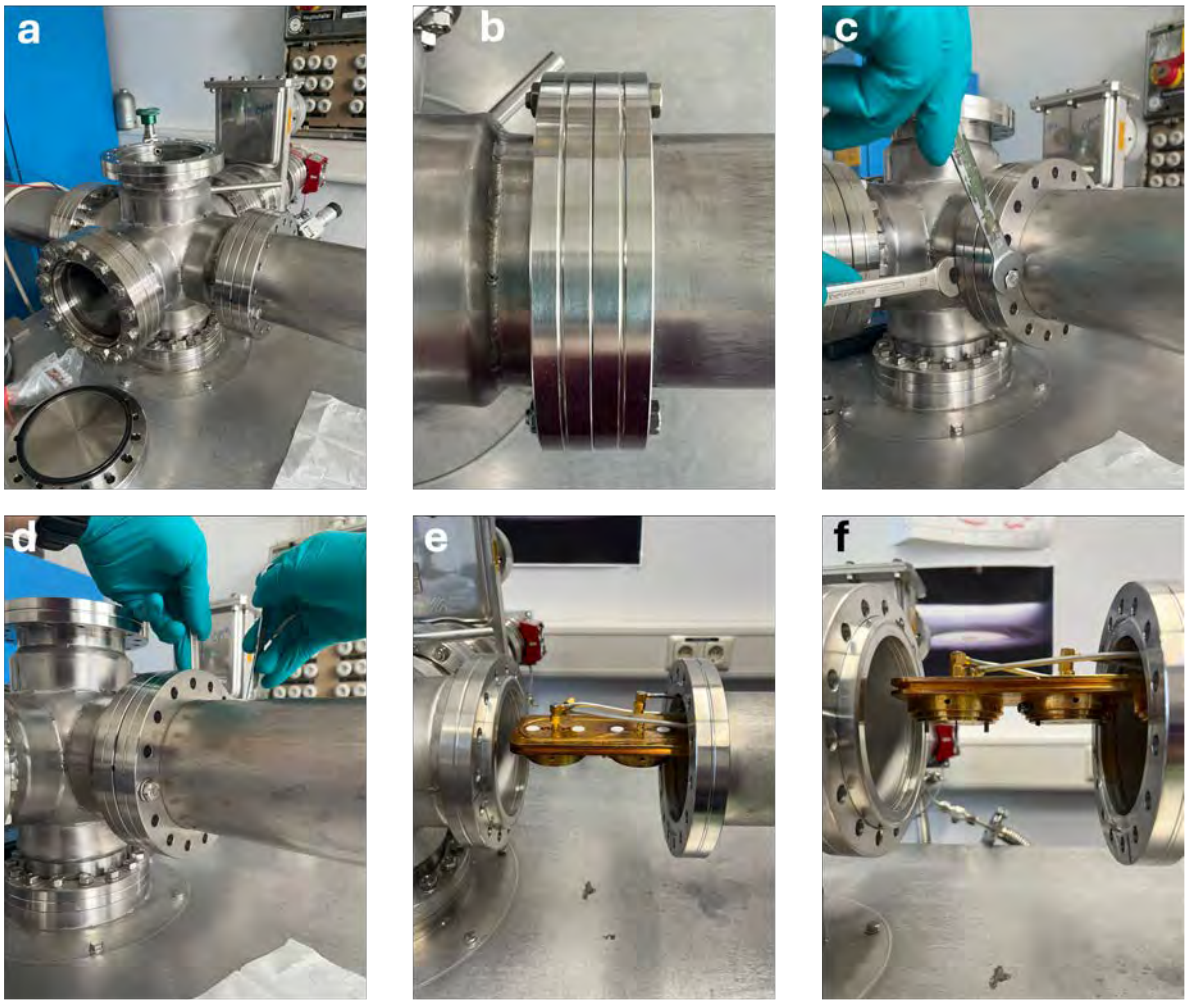

Figure A.29.: (a) Vent the deposition chamber and remove the lid. (b–d) Completely remove these screws. (e) Pull the assembly to the right to access the target arm. (f) Free target slots.

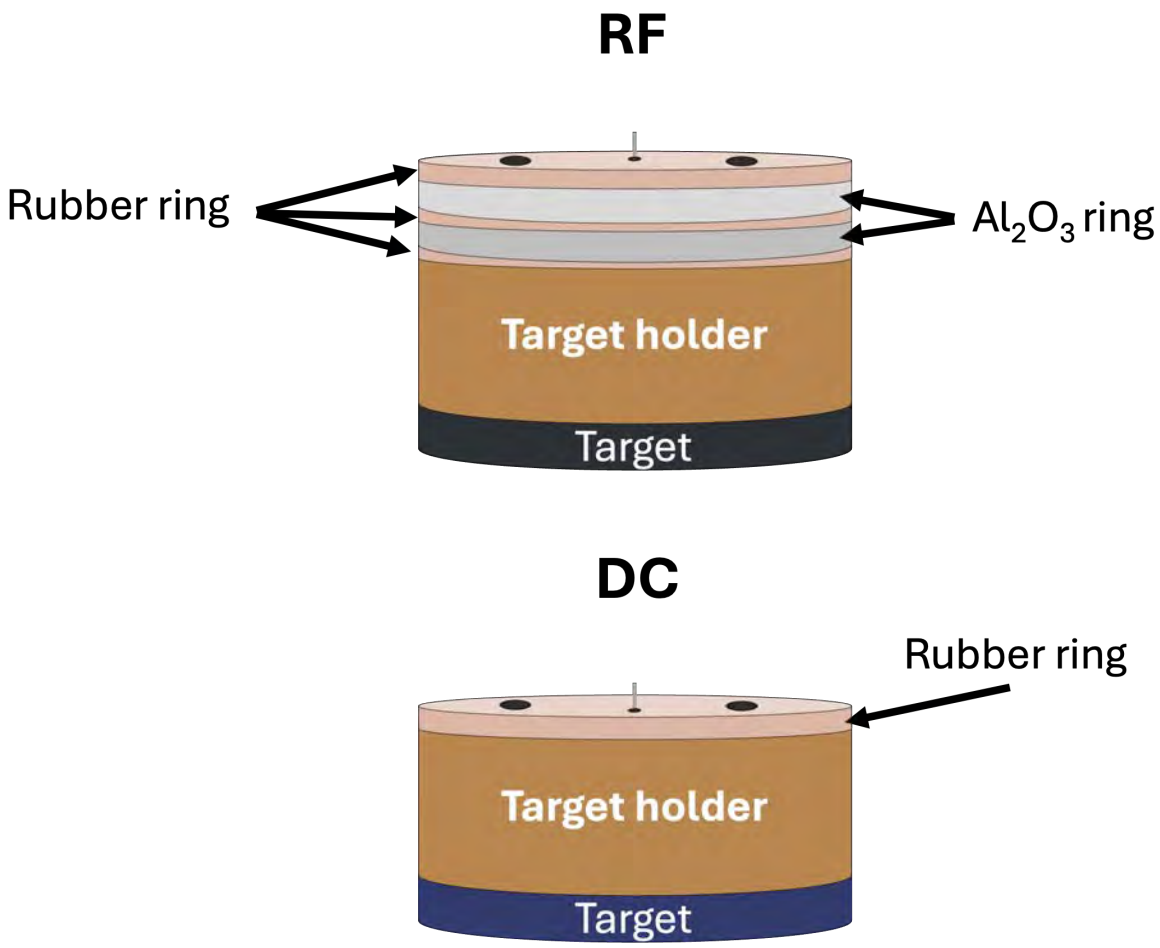

Figure A.30.: Arrangement of rubber rings and Al_2O_3 rings for RF plasma (top) and DC plasma (bottom).

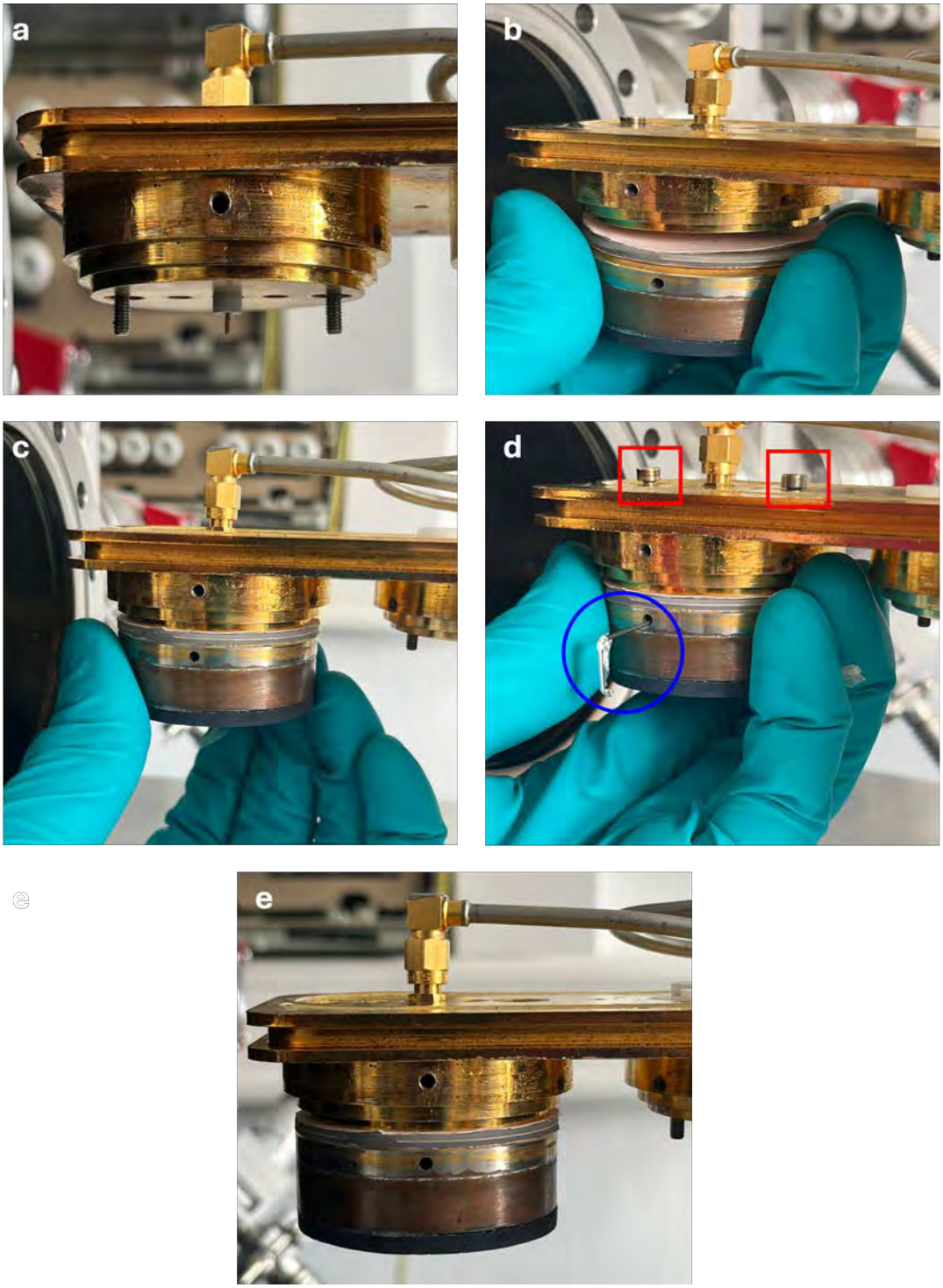

Figure A.31.: (a–c) Insert the target into the target arm with the appropriate rubber and Al_2O_3 rings. (d) First tighten the screws of the target arm, then secure the connecting pin. (e) Final view of the mounted target.

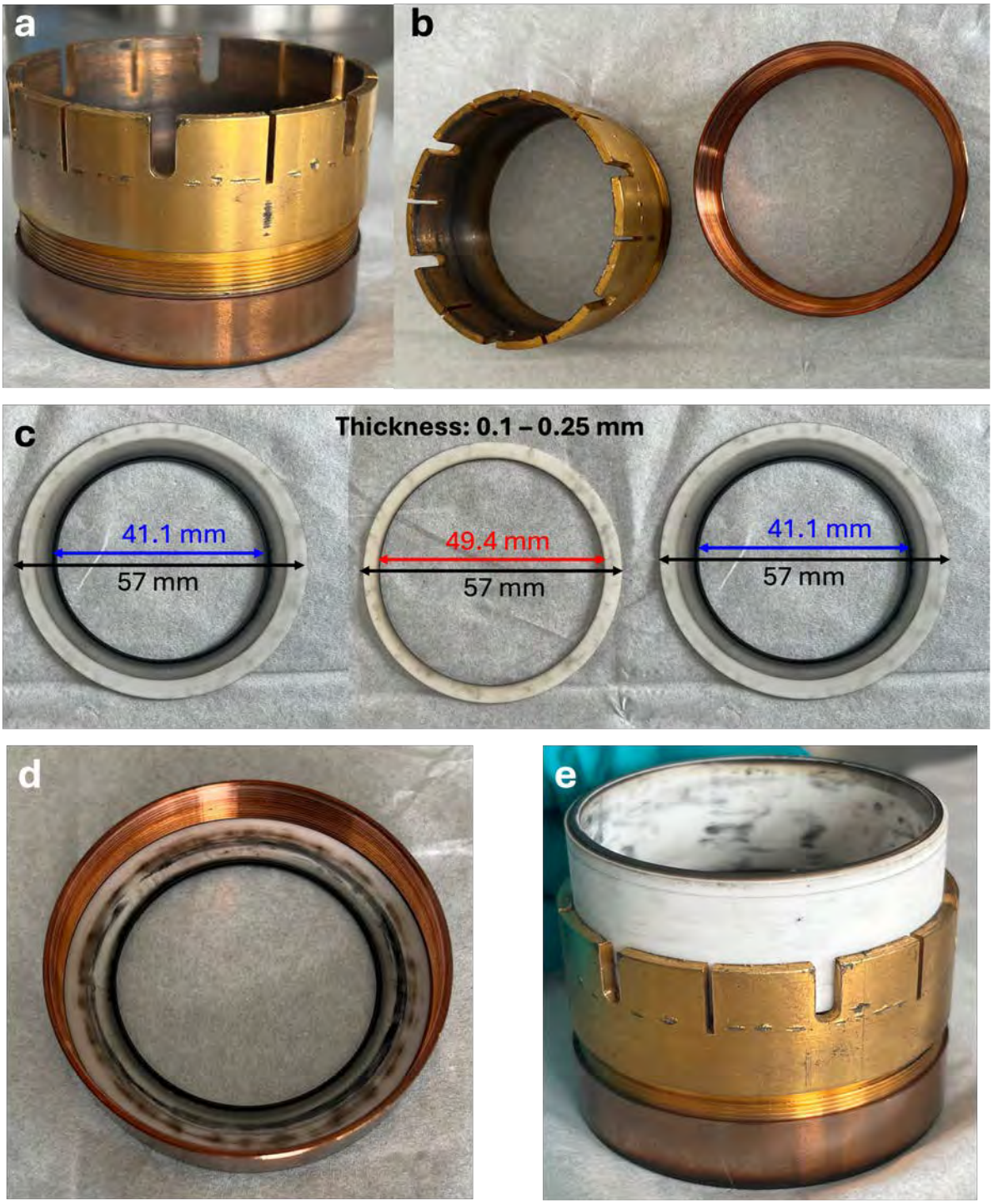

Figure A.32.: (a-b) External structure of the target holder. (c-d) Diameter and thickness of Al_2O_3 rings that should be mounted on the bottom part of the external structure. (e) Hollow Al_2O_3 cylinder.

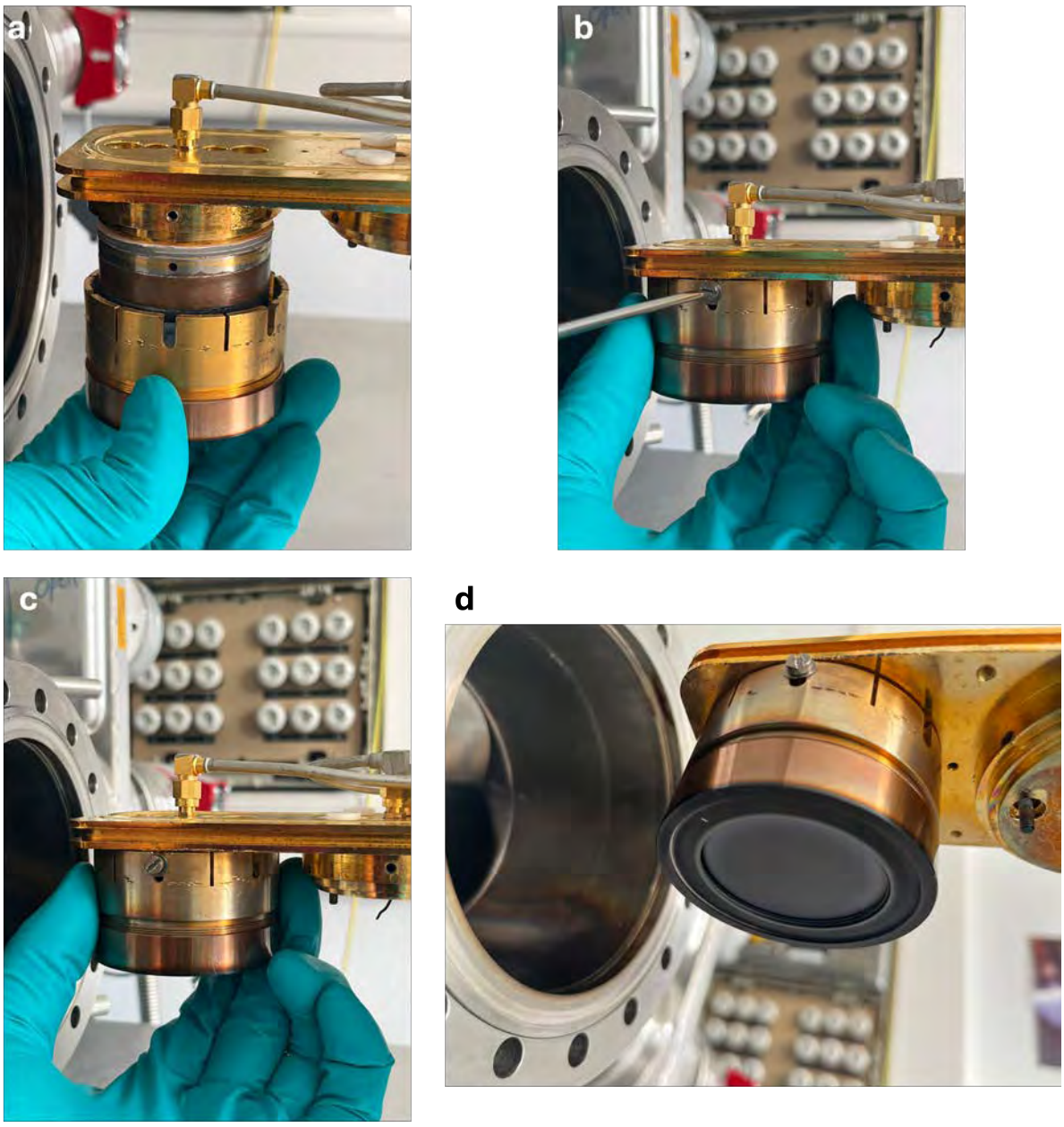

Figure A.33.: (a-c) Connect the structure to the target arm by tightening the screws. (d) If necessary, tighten up the bottom part of the external structure of the target to have it more adjusted.

Appendix B

X-ray and Neutron calculated/theoretical Scattering Length Densities

The scattering length density (SLD) describes how the material interacts with incident X-rays or neutrons, providing information about electron density (X-rays) or nuclear/magnetic contrast (neutrons). It is a fundamental factor used for modeling reflectivity profiles or interfaces. The SLD is a measure of the material's scattering power per unit of volume.

For X-rays, the SLD is proportional to the number of electrons in the atom (approximated by the atomic form factor) while for neutrons it is the average of the scattering length of atoms in the material (usually approximated by the coherent scattering length). Table B.1 provides the X-ray form factor (f_0) and the neutron coherent scattering length (b) for the elements present in the $SrTiO_3$, $SrRuO_3$ and $YBa_2Cu_3O_{7-x}$.

Table B.1.: X-ray form factor (f_0) and the neutron coherent scattering length (b) present in the $SrTiO_3$, $SrRuO_3$ and $YBa_2Cu_3O_{7-x}$.

Element	X-ray form factor [dimensionless]	Neutron [fm]
Sr	38	7.02
Ti	22	-3.4
O	8	5.8
Ru	44	7.03
Y	39	7.75
Ba	56	5.07
Sr	29	7.72

Therefore, we can calculate the Scattering Length Densities (SLD) for X-rays and Neutrons accordingly to the equations below.

$$\mathrm{SLD}_{\text{X-rays}} = \sum_{i}^{atoms} \frac{r_e f_{0,i}}{\text{Vol. Unit Cell}} \quad \text{and} \tag{B.1}$$

$$\mathrm{SLD}_{\mathrm{Neutrons}} = \sum_{i}^{atoms} \frac{b_i}{\mathrm{Vol.\ Unit\ Cell}}. \tag{B.2}$$

The calculated SLD values for $SrTiO_3$, $SrRuO_3$ and $YBa_2Cu_3O_{7-x}$ are shown in Tab. B.2.

Table B.2.: X-ray and Neutron calculated SLD values for the materials in study.

Material	$\mathrm{SLD}_{\mathrm{X\text{-}Rays}}$ $[r_e\,\text{Å}^{-3}]$	$\mathrm{SLD}_{\mathrm{Neutrons}}$ $[10^{-6}\ \text{Å}^{-2}]$
$SrTiO_3$	1.410	3.53
$SrRuO_3$	1.746	5.181
$YBa_2Cu_3O_{7-x}$	1.6939	4.704

Appendix C

Samples prepared in the optimization process

This appendix summarizes the structural and morphological parameters obtained from atomic force microscopy (AFM), High-resolution X-ray diffraction (HR-XRD), and X-ray reflectivity (XRR) for the Ru-deficient $SrRuO_3$ (SRO) thin films prepared during the optimization of the growth conditions.

The first set of tables compiles the results for films grown at room temperature, which were used to evaluate the plasma stoichiometry and verify the composition of different sputtering targets. The extracted parameters include the film thickness, interfacial roughness, and scattering length density (SLD) obtained from the XRR fits.

In GenX, the figure of merit (FOM) quantifies the deviation between the experimental and simulated reflectivity curves, with values on the order of 10^{-2} typically indicating good agreement (see Ref. [143] and the GenX user guide for additional details). It is important to note that GenX does not provide the statistical uncertainty (standard deviation) of the fitted parameters, such as thickness, roughness, and SLD. Therefore, to estimate the uncertainty of a given parameter, it must be manually varied around its best-fit value while monitoring the degradation of the FOM. For the SLD values, the resulting deviations are extremely small and are therefore not included in the tables presented in this appendix.

Subsequent tables present the optimization of the target–substrate distance (D_{TS}) and its effect on the film thickness and surface morphology, as determined by AFM and XRR, followed by the study of the deposition temperature (T_{dep}) and the influence of the forward sputtering power (FWDP) and oxygen partial pressure (P_{O_2}) on the layer density and interfacial roughness. In all these series, the other growth parameters were kept constant, and the films were deposited using a stoichiometric SRO target.

Finally, the last table summarizes the temperature-optimization results for films grown from the Ru-deficient SRO-143 target. In this case, AFM, XRD, and XRR data, including the fit of the Laue oscillations observed in the HR-XRD patterns, are presented together, showing the evolution of the film thickness, crystallinity, and roughness as a function of T_{dep}.

For reference, the optimized parameters (Opt. Params.) in each optimization process are indicated in the corresponding tables. The term Sample structure (or simply

Structure) represents the block-like stack of layers on the substrate used to model the XRR data. The local roughness (σ_{AFM}), corresponding to the RMS roughness, was calculated over 2×2 μm^2 scan areas across the sample surface. The film thickness (t_{XRR}), interfacial roughness (σ_{XRR}), SLD, and FOM are reported in all tables, illustrating the gradual reduction of SLD across the film and particularly at the interfaces (surface and film–substrate interface).

The thickness values extracted from the fit of the Laue oscillations in the HR-XRD patterns of the films grown from the SRO-143 target further demonstrate the high structural coherence of these samples, despite the considerable Ru deficiency.

Table C.1.: XRR parameters for SRO thin films deposited from stoichiometric SRO target on Si substrates at room temperature. D_{TS}, P_{O_2} and FWDP were kept at 2.5 cm, 1.5 mbar and 100 W, respectively.

Sample structure	t **[Å]**	$\sigma_{\mathbf{XRR}}$ **[Å]**	**SLD** [r_e **Å**$^{-3}$]	**FOM**
Surface	1 ± 0.5	7.7 ± 0.2	0.868	
SRO film	366 ± 4	16.3 ± 4.3	1.277	5.96×10^{-2}
Si substrate	—	8.3 ± 2.1	0.855	

Table C.2.: XRR parameters for the SRO thin film deposited from the SRO-143 target on Si substrate. D_{TS}, P_{O_2} and FWDP were kept at 2.5 cm, 1.5 mbar and 100 W, respectively.

Sample structure	t **[Å]**	$\sigma_{\mathbf{XRR}}$ **[Å]**	**SLD** [r_e **Å**$^{-3}$]	**FOM**
Surface	5.6 ± 4.4	17.8 ± 1.2	1.087	
SRO film	667 ± 3	4.6 ± 0.4	1.509	7.13×10^{-2}
Interface	15 ± 3	14.8 ± 0.2	1.214	
Si substrate	—	5 ± 3	1.250	

Table C.3.: AFM and XRR parameters of SRO thin films grown at 785 °C with different target–substrate distances (D_{TS}). T_{dep}, P_{O_2} and FWDP were kept at 785 °C, 1.5 mbar and 100 W, respectively.

Opt. Params.	**Structure**	$\boldsymbol{\sigma}_{AFM}$ [nm]	$\boldsymbol{t}$ [Å]	$\boldsymbol{\sigma}_{XRR}$ [Å]	**SLD** [r_e Å^{-3}]	**FOM**
D_{TS} = 1.5 cm	Surface		2.5 ± 5.9	21.3 ± 5.7	1.150	
	SRO film	1.42 ± 0.01	1430 ± 200	4.2 ± 0.9	1.636	7.56×10^{-2}
	Interface		42.5 ± 22.8	20.6 ± 5.0	1.541	
	STO substrate	—	—	14 ± 7	1.500	
D_{TS} = 2.0 cm	Surface		14.4 ± 5.9	10.8 ± 0.7	1.372	
	SRO film	0.21 ± 0.01	941 ± 11	2.4 ± 1.1	1.604	1.16×10^{-1}
	Interface		21.7 ± 22.8	7.8 ± 8.0	1.563	
	STO substrate	—	—	10 ± 2	1.430	
D_{TS} = 2.5 cm	Surface		30.2 ± 4.6	9.3 ± 0.3	1.583	
	SRO film	0.23 ± 0.01	549 ± 35	6.8 ± 6.1	1.636	9.37×10^{-2}
	Interface		21.4 ± 6.1	1.0 ± 0.5	1.626	
	STO substrate	—	—	7 ± 2	1.530	

Table C.4.: AFM and XRR parameters of SRO thin films grown at different deposition temperatures (T_{dep}) with D_{TS} = 2.5 cm and (P_{O_2}, FWDP) = (1.5 mbar, 100 W).

Opt. Params.	**Structure**	$\boldsymbol{\sigma}_{AFM}$ [nm]	$\boldsymbol{t}$ [Å]	$\boldsymbol{\sigma}_{XRR}$ [Å]	**SLD** [r_e **Å**$^{-3}$]	**FOM**
T_{dep} = 560 °C	Surface	0.24 ± 0.01	12.3 ± 2.5	7.0 ± 5.0	0.885	1.10×10^{-1}
	SRO film		142 ± 6	7.0 ± 5.0	1.699	
	Interface		7.0 ± 5.0	1.0 ± 0.5	2.048	
	STO substrate	—	—	5 ± 1	1.480	
T_{dep} = 673 °C	Surface	3.2 ± 1.1	25 ± 3	9.0 ± 1.0	1.415	8.92×10^{-2}
	SRO film		432 ± 7	3.5 ± 2.5	1.623	
	Interface		7.5 ± 6.5	6.0 ± 4.0	1.552	
	STO substrate	—	—	12 ± 5	1.510	
T_{dep} = 897 °C	Surface	3.3 ± 0.8	8.0 ± 5.0	18.2 ± 2.1	1.183	7.15×10^{-2}
	SRO film		184 ± 200	7.0 ± 1.0	1.647	
	STO substrate	—	—	7 ± 1	1.50	

Table C.5.: XRR parameters of SRO thin films grown at 785 °C with D_{TS} = 2.5 cm for different forward powers (FWDP) and oxygen pressures (P_{O_2}).

Opt. Params.	**Structure**	$\boldsymbol{t}$ [Å]	$\boldsymbol{\sigma}_{\mathrm{XRR}}$ [Å]	**SLD** [r_e **Å**$^{-3}$]	**FOM**
FWDP = 150 W	Surface	27.3 ± 3.5	8.0 ± 2.0	0.481	5.72×10^{-2}
PO_2 = 2.5 mbar	SRO film	344 ± 3.0	6.4 ± 0.8	1.678	
	STO substrate	—	6 ± 3	1.450	
FWDP = 125 W	Surface	1.3 ± 0.5	14.7 ± 5.5	1.183	6.91×10^{-2}
PO_2 = 2.0 mbar	SRO film	406 ± 10	6.0 ± 3.0	1.648	
	STO substrate	—	7 ± 1	1.530	

Table C.6.: AFM, XRD, and XRR parameters of SRO thin films grown from the SRO-143 target at different deposition temperatures (T_{dep}) with D_{TS} = 2.5 cm and (P_{O_2}, FWDP) = (1.5 mbar, 100 W).

Opt. Params.	**Structure**	$\boldsymbol{\sigma}_{AFM}$ [nm]	$\boldsymbol{t}_{XRD}$ [Å]	$\boldsymbol{t}_{XRR}$ [Å]	$\boldsymbol{\sigma}_{XRR}$ [Å]	**SLD** [r_e Å^{-3}]	**FOM**
T_{dep} = 975 °C	Surface	2.9 ± 0.4	180 ± 3	3 ± 1	6 ± 3	0.512	8.92×10^{-2}
	SRO film			183 ± 3	27 ± 3	1.730	
	Interface			12 ± 5	7 ± 3	1.640	
	STO substrate	—	—	—	4 ± 2	1.540	
T_{dep} = 897 °C	Surface	2.2 ± 0.5	155 ± 3	1 ± 0.5	17.5 ± 0.5	0.134	9.07×10^{-2}
	SRO film			171 ± 3	1 ± 0.5	1.681	
	STO substrate	—	—	—	10 ± 3	1.480	
T_{dep} = 785 °C	Surface	0.28 ± 0.04	183 ± 3	1 ± 0.5	12 ± 2	0.072	1.21×10^{-1}
	SRO film			195 ± 5	1 ± 0.5	1.680	
	STO substrate	—	—	—	8 ± 3	1.490	
T_{dep} = 673 °C	Surface	0.34 ± 0.01	163 ± 3	1 ± 0.5	5 ± 4	0.131	1.41×10^{-1}
	SRO film			178 ± 3	15 ± 3	1.670	
	STO substrate	—	—	—	2 ± 1	1.430	
T_{dep} = 560 °C	Surface	0.70 ± 0.10	166 ± 3	3 ± 1	2 ± 1	0.071	9.45×10^{-2}
	SRO film			170.5 ± 6	15 ± 2	1.620	
	STO substrate	—	—	—	12 ± 1	1.010	

Appendix D

Comparison between models used in PNR data analysis

To evaluate the sensitivity of the polarized neutron reflectometry (PNR) analysis to the interfacial magnetic configuration, an alternative fitting approach (Model 4B) was implemented, in which the magnetization at both interfaces was constrained to zero. This contrasts with the model discussed in the main text (Model 4A), where the interfaces retain a small but finite magnetic moment. The purpose of this test was to examine whether a magnetically *dead* layer scenario could also reproduce the reflectivity data with comparable quality.

Figures D.1 and D.2 display the reflectivity fits obtained using both configurations at 100, 80, and 5 K. Although the dead-layer model reproduces the global amplitude of the curves, it fails to capture the fine oscillation structure with the same accuracy, particularly in the $\vec{Q}_z$ range of 0.04–0.06 Å^{-1}, where the maxima are shifted while the minima remain nearly fixed (see the insets). This discrepancy becomes more pronounced at low temperature. Moreover, the best-fit structural parameters for Model 4B required significantly thicker and more diffuse interfacial regions than those obtained from XRR and STEM–EDS analyses, or those reported in similar sputtered SRO films [74, 77]. These inconsistencies indicate that the assumption of completely non-magnetic interfaces does not provide a physically sound description of the experimental data.

The corresponding nuclear SLD and magnetization profiles obtained from Model 4B are shown in Fig. D.3. In this configuration, the complete suppression of the interfacial magnetization produces broader and more diffuse transition regions in both the nuclear and magnetic SLDs, indicating that the model compensates for the absence of interfacial moments by artificially increasing the interface thickness. In contrast, the model with partially magnetic interfaces (Model 4A) reproduces the reflectivity periodicity and amplitude more accurately while yielding structural parameters consistent with complementary measurements.

It is worth noting, however, that the intrinsically low magnetic moment of the Ru-deficient SRO film and its pronounced perpendicular magnetic anisotropy (PMA) limit the sensitivity of the PNR measurements. Under these conditions, distinguishing between truly non-magnetic interfaces and regions where the magnetization is strongly canted or locally enhanced in the out-of-plane direction becomes challenging. Therefore, the

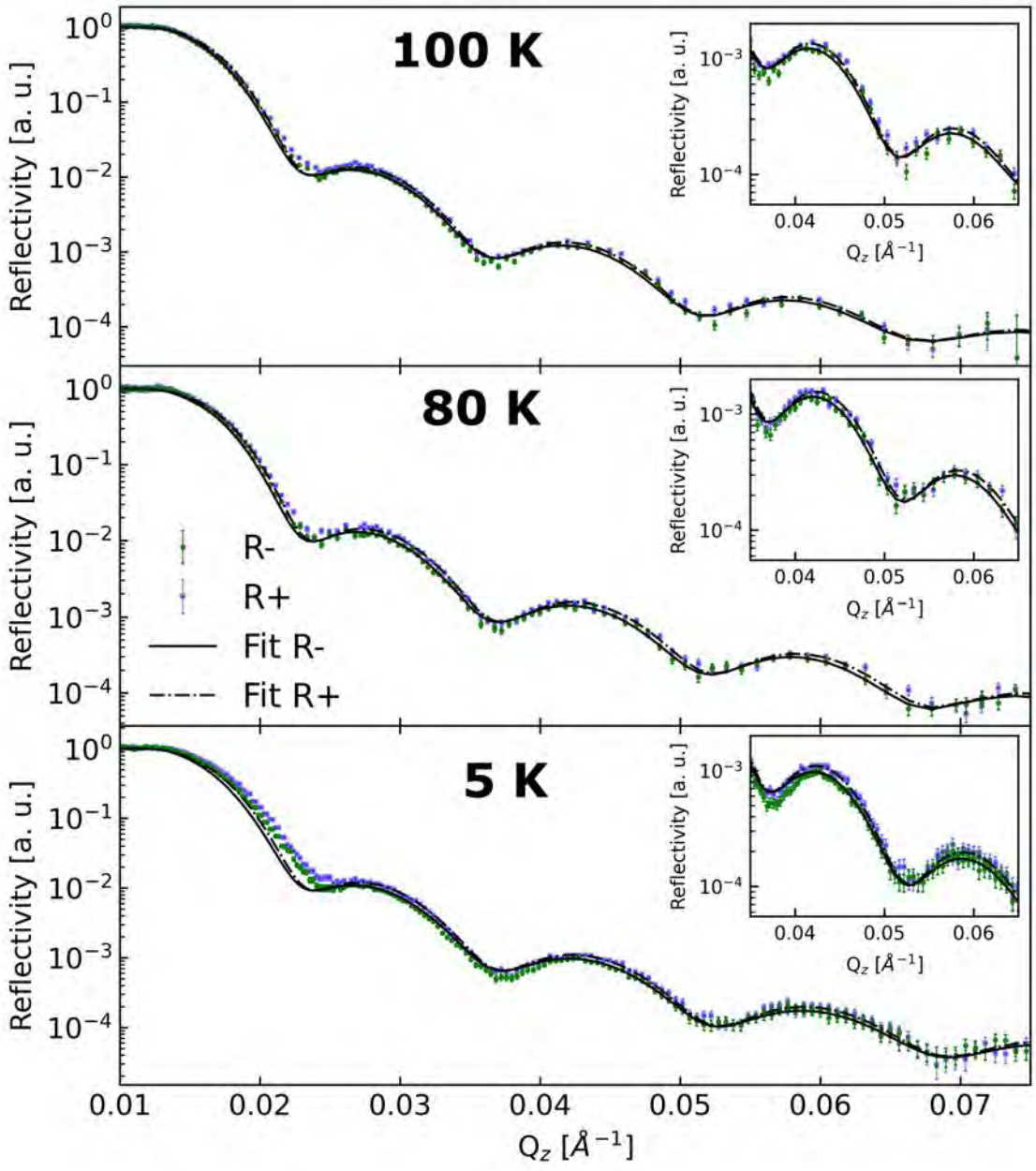

Figure D.1.: Polarized neutron reflectivity curves (R+ and R–) and corresponding fits using Model 4A, in which the interfacial regions retain a small finite magnetization. Insets highlight the oscillation minima region in $\vec{Q}_z$.

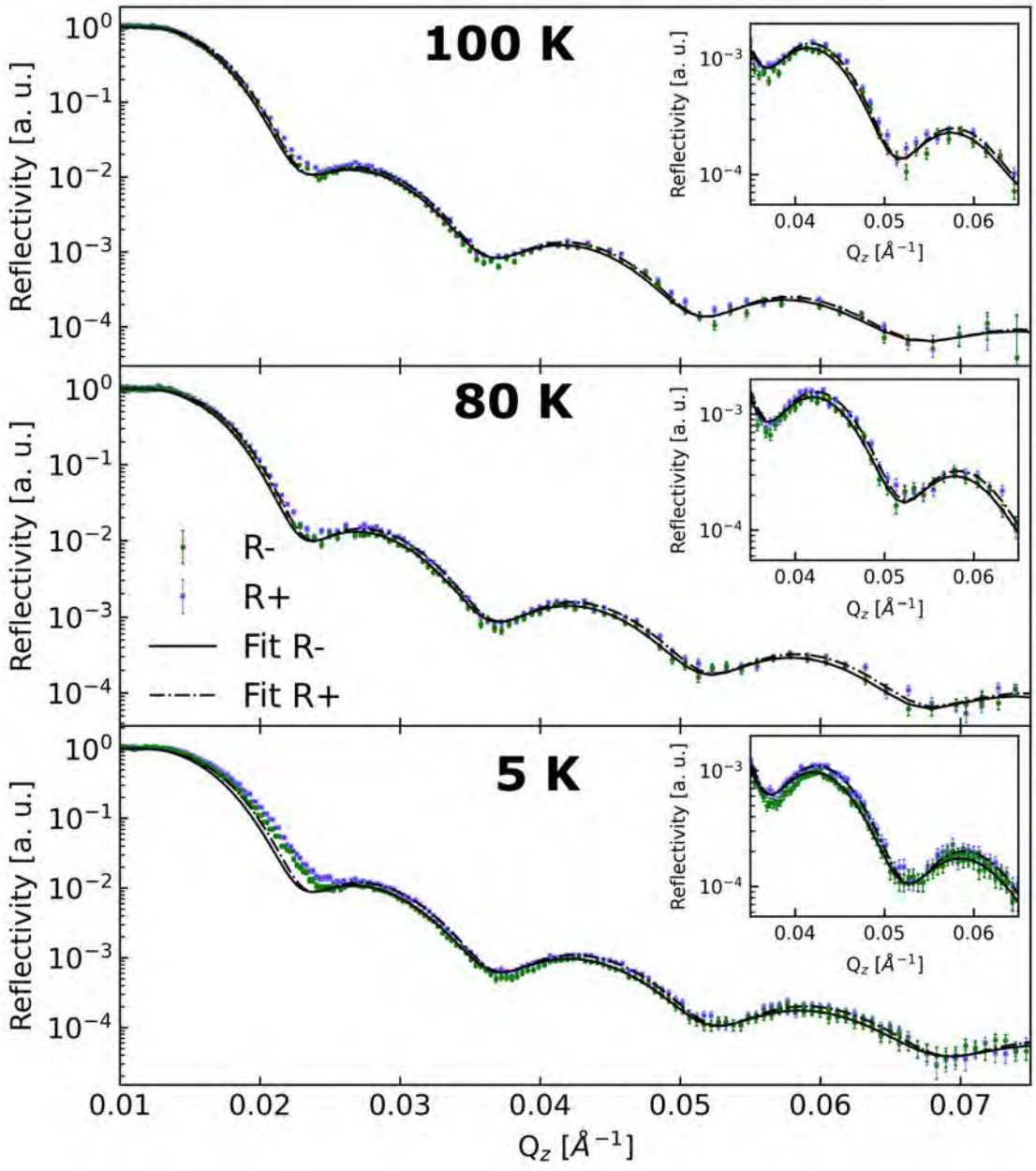

Figure D.2.: Same data as in Fig. D.1 fitted using Model 4B, where the interfacial magnetization is constrained to zero. Note the shift in the oscillation maxima and the poorer agreement near the first minimum.

subtle differences observed between Models 4A and 4B should be interpreted within the experimental resolution of the technique.

The analysis presented in this appendix demonstrates that enforcing magnetically dead interfaces leads to a slightly inferior description of the reflectivity data and to structural parameters inconsistent with independent measurements. The adopted model (Model 4A), which incorporates finite interfacial magnetization, provides a more robust and physically meaningful representation of the depth-dependent magnetic structure of Ru-deficient $SrRuO_3$ thin films. These results highlight the importance of considering interfacial magnetic contributions even in systems with low overall magnetization, as they can play a decisive role in shaping the measured PNR response.

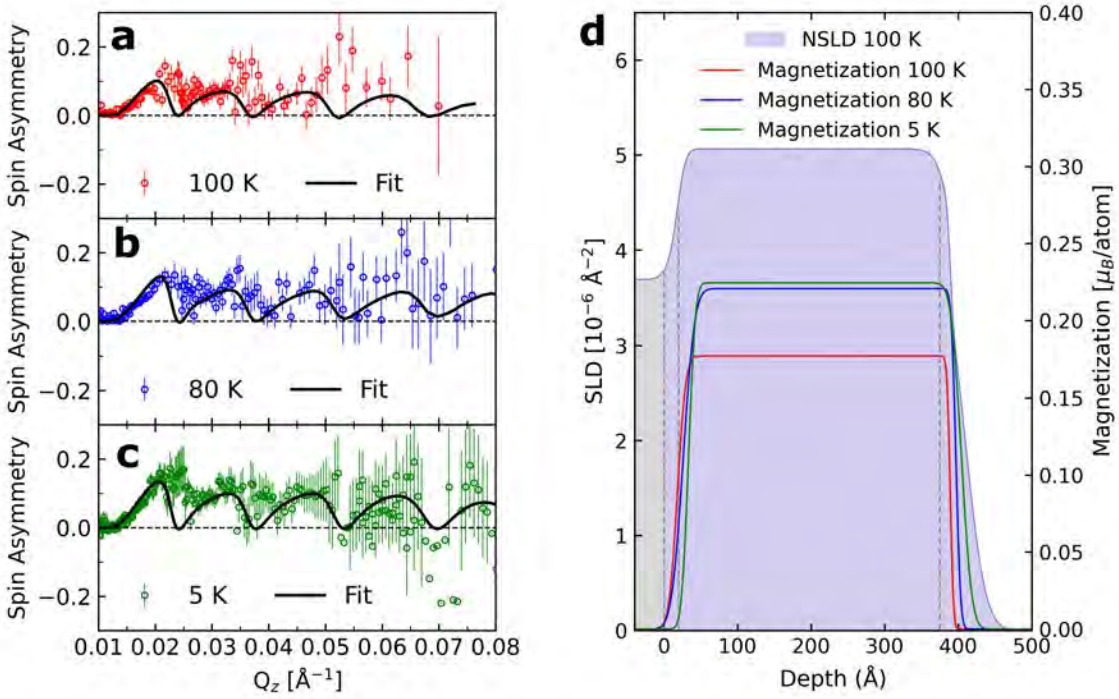

Figure D.3.: (a–c) Spin-asymmetry curves measured at (a) 100 K, (b) 80 K, and (c) 5 K, together with the best-fit simulations obtained using Model 4B, in which the magnetization at both interfaces was constrained to zero. Open symbols represent experimental data and solid lines the corresponding fits. Although the overall oscillation amplitude is reproduced, the model with magnetically *dead* interfaces fails to capture the periodicity and intensity of the first minima and maxima with the same accuracy as the model presented in the main text (Model 4A). (d) Nuclear (nSLD, left axis) and magnetic (magnetization, right axis) scattering-length-density profiles obtained from the fits at 100, 80, and 5 K.

Appendix E

List of publications

Papers related to this thesis:

- **Paper I:**
  Anomalous magnetoresistance around the critical temperature in heterostructures of high-T_c superconducting $YBa_2Cu_3O_{7-x}$ and ferromagnetic $SrRuO_3$ with perpendicular magnetic anisotropy.

  V. A. de Oliveira Lima, M. I. Faley, O. Concepción, S. Nandi, P. Prakash, M. H. Hamed, E. Kentzinger, Th. Brückel and C. Bednarski-Meinke

  Physica Scripta, **100** 075985, 2025
  DOI: https://doi.org/10.1088/1402-4896/ade7f7

  My contribution: Conceptualization. Preparation of the thin film heterostructures. Characterization of the samples using Atomic Force Microscopy (AFM), SQUID magnetometry, and electron transport and magnetotransport measurements. Data curation for all measurements included in the paper. Investigation of the proposed proximity effect through comprehensive analysis of all results. Writing and editing of the manuscript.

- **Paper II:**
  Anisotropy-driven interfacial magnetism in Ru-deficient $SrRuO_3$ thin films.

  V. A. de Oliveira Lima, M. I. Faley, A. Qdemat, H. Ambayed, V. Lauter, O. Concepción, A. Singh, S. Nandi, E. Kentzinger, Th. Brückel and C. Bednarski-Meinke

  Accepted in APL Materials.
  Submitted version DOI: https://doi.org/10.48550/arXiv.2602.14932

  My contribution: Conceptualization. Preparation of the samples. Characterization of the samples using Atomic Force Microscopy (AFM), SQUID magnetometry, polarized neutron reflectometry (PNR), and off-specular neutron scattering (OSS). Data curation for all measurements included in the paper. Investigation of the proposed interfacial effect through comprehensive analysis of all experimental results. Writing and editing of the manuscript.

Papers published in collaboration:

- **Paper I:**
  Increased reflectivity, polarization, reduced stress, and diminished spin-flip reflectivity in stacked multilayers of Fe/Si by incorporating $^{11}B_4C$

  A. Zubayer, N. Ghafoor, A. Devishvili, A. Vorobiev, A. Glavic, J. Stahn, T. Hanashima, J. Sugiyama, **V. A. de Oliveira Lima**, J. Birch, F. Eriksson

  Materials Today Advances, **26** 100578, 2025,
  DOI: https://doi.org/10.1016/j.mtadv.2025.100578

  My contribution: In this work, I was responsible for performing the SQUID magnetometry measurements of the samples. I analyzed the resulting data and actively contributed to the discussion and interpretation of the findings with the other authors. I was also involved in the writing and editing of the manuscript.

- **Paper II:**
  Magnetic domain texture in Fe_3O_4 thin films on SiO_2 nanospheres.

  M. H. Hamed, Y. Xu, H. Elnaggar, M. Zaghloul, A. M. Mio, A. Backs, A. Stellhorn, **V. A. de Oliveira Lima**. C. Yin, C. Bednarski-Meinke, N.j. Steinke, O. Petracic, Th. Brückel, T. Saerbeck, A. Qdemat

  Advanced Materials, **2025**, e13849.
  DOI: https://doi.org/10.1002/adma.202513849

  My contribution: In this work, I participated in the X-ray Photoemission Electron Microscopy (XPEEM) beamtime. During the experiment, I initiated the X-ray Absorption Spectroscopy (XAS) and X-ray Magnetic Circular Dichroism (XMCD) data plotting, and started developing Python scripts for XPEEM data visualization.

- **Paper III:**
  Incorporating B_4C into Fe/Cr Multilayers to Achieve Improved Interfaces and Stress-Free Films

  A. Zubayer, M. Lorentzon, N. Ghafoor, T. Hanashima, **V. A. de Oliveira Lima**, J. Sugiyama, J. Birch, D. E. Bürgler, R. Maruyama, F. Eriksson

  In preparation for submission.

  My contribution: In this work, I performed the magnetoresistance measurements and actively contributed to the discussion and interpretation of the findings with the other authors. I was also involved in the writing and editing of the manuscript.

- **Paper IV:**
  Magnetic domain walls in FePd thin films: CD-X-ray Surface Scattering and Microscopy

  A. Stellhorn, A. Backs, C. Bednarski-Meinke, E. Kentzinger, P. Steadman, M. Valvidares, D. Vasiukov, O. Stepancic, S. Tober, **V. A. de Oliveira Lima**, J. Schwenke, E. Blackburn

  In preparation for submission.

  My contribution: In this work, I participated in the X-ray Resonant Magnetic Scattering (XRMS) and X-ray Magnetic Circular Dichroism (XMCD) beamtime and have revised the manuscript.

Eidesstattliche Erklärung

Declaration of Authorship

I, Vítor Alexandre de Oliveira Lima,

declare that this thesis and the work presented in it are my own and has been generated by me as the result of my own original research.

Hiermit erkläre ich an Eides statt / I do solemnely swear that:

1. This work was done wholly or mainly while in candidature for the doctoral degree at this faculty and university;

2. Where any part of this thesis has previously been submitted for a degree or any other qualification at this university or any other institution, this has been clearly stated;

3. Where I have consulted the published work of others or myself, this is always clearly attributed;

4. Where I have quoted from the work of others or myself, the source is always given. This thesis is entirely my own work, with the exception of such quotations;

5. I have acknowledged all major sources of assistance;

6. Where the thesis is based on work done by myself jointly with others, I have made clear exactly what was done by others and what I have contributed myself;

7. Part of this work have been published before as:
V. A. de Oliveira Lima *et al* 2025 *Phys. Scr.* **100** 075985 (2025)
[DOI: 10.1088/1402-4896/ade7f7]

19.11.2025

Vítor A O Lima

signature